PHYSICAL PROPERTIES AND TRANSFORMATIONS OF LOW-DIMENSIONAL SYSTEMS

By

Dan Liu

A DISSERTATION

Submitted to
Michigan State University
in partial fulfillment of the requirements
for the degree of

Physics – Doctor of Philosophy

2019

ABSTRACT

PHYSICAL PROPERTIES AND TRANSFORMATIONS OF LOW-DIMENSIONAL SYSTEMS

By

Dan Liu

Evolving from the macroscopic scale to the nanometer scale, in particular by reducing the dimensionality, fundamental properties (such as electronic and mechanical properties) of certain systems exhibit dramatic changes, which not only give rise to a wide range of emergent phenomena, but also boost technology development including nanoelectronics, optoelectronics and catalysis. In this thesis, I utilized combined techniques including density functional theory (DFT), molecular dynamic simulations (MD), continuum elasticity approach, and the tight-binding model to conduct a systematic study on low-dimensional nanostructures regarding their electronic and mechanical properties as well as underlying microscopic transformation mechanisms between different structural allotropes.

First, I briefly introduce the motivation and background of this thesis. Then, in Chapter 2, I describe the computational techniques, mainly the DFT approach, on which most of my thesis is based.

In Chapters 3 and 4, I apply the continuum elasticity method to study the phonon spectrum of two-dimensional (2D) and one-dimensional (1D) systems. My results highlight advantages of the continuum elasticity approach especially for the flexural acoustic phonon modes close to the Γ point, which are otherwise extremely hard to converge in atomistic calculations that use very large supercell sizes.

From Chapter 5 to Chapter 7, I focus on allotropes of group III, V and VI elements and study both their stability and microscopic transformation mechanisms from one allotrope

to another. First, I predicted a stable phosphorus coil structure, which may form by reconstruction of red phosphorous, and which was synthesized by filling a carbon nanotube with sublimed red phosphorus. Second, I proposed two stable 2D allotropes of Se and Te. I also suggested and evaluated a promising fabrication approach starting from natural 1D structures of these elements. After considering low-dimensional charge neutral systems, I changed my focus to study the effect of net charge on the equilibrium structure. Considering a heterostructure of alternating electron donor layers an monolayers of boron, I have identified previously unknown stable 2D boron allotropes that may change their structure under different levels of charge transfer.

From Chapter 8 to Chapter 10, I focus mainly on carbon-based nanomaterials and their properties. In Chapter 8, I proposed a way to enhance the density of states at the Fermi level in doped C_{60} crystals in order to increase their superconducting critical temperature to room temperature. In Chapter 9, I have investigated a shear instability twisted bilayer graphene using the tight binding model. This system is susceptible to very small structural changes, since it becomes superconducting in a very narrow range of twist angles near the 'magic angle'. In Chapter 10, I introduced the cause of an unusual negative Poisson ratio and a shape-memory behavior in porous graphene with an artificially designed pattern.

In Chapter 11, I finally present general conclusions of my PhD Thesis.

To all people whom I love and respect.

ACKNOWLEDGMENTS

During the five and a half years of my Ph.D. study at Michigan State University, many things happened, including not only happiness, but also embarrassment. Fortunately, I have a family, friends, and colleagues to share the joy and to help me to get through tough times. In retrospect, I consider my five years at MSU to be valuable. What I gained is not only a more profound understanding of Physics, but also a more in-depth knowledge of what a meaningful life should be, and what a valuable person should be like.

The thing I need to appreciate is the difficulties. Solving the challenges I met in Physics and life help me to grow up, become humble, and let me know that nothing is easy in the life of a mature person. I want to quote a sentence from the movie 'Angel has Fallen': 'It's our moment of struggle that defines us'. It is defining who I am now and will determine who I will be. The first person I should appreciate is my Ph.D. advisor Professor David Tomanek. He is not just my advisor in Physics but also my friend in life. According to his advice, I decided to stay in Physics even though it is not a field that can bring me wealth quickly. And because of him, I know a scientist should value what he is doing and should not look down at other people's work. From him, I saw what integrity and selflessness is. For me, he is very strict in Physics but very kind in life. He set a standard for me to be an instructor in the future.

I need to thank all of my classmates and friends, including Kuan Zhu, Xingze Mao, Hao Lin, Liangji Zhang, Faran Zhou, Shuyue Xue, Mengze Zhu, Didi Luo, we have a good time together in MSU. Especially, I want to thank Professor Xianqinq Lin of Zhejiang University of Technology, Professor Jie Guan of Southeast University and Jingwei Jiang of UC Berkeley, we discussed lots of intriguing projects and collaborated on several publications. I also need

to appreciate the help from Professor Vincent Meunier of Rensselaer Polytechnic Institute and Professor Arthur Every of the University of the Witwatersrand for understanding the fundamental physics of nanomaterials and also for their recommendation letters that have provided strong support for me when applying for a Postdoc position.

I acknowledge financial support from the National Science and Engineering Center for High-Rate Nanomanufacturing (NSEC) program, grant number $\#EEC - 0832785$, and the NSF/AFOSR EFRI 2-DARE program, grant number $\#EFMA - 1433459$. I also acknowledge partial financial support by the Physics and Astronomy Department, and the Dissertation Completion Fellowship from College of Natural Science, which has supported me financially during the last semester of my Ph.D. study.

Last but not least, I want to apologize to my parents, my wife, and my daughter. As a son, I have obtained much support from my parents, but I can not give them a hand now when they become old and need my help. As a husband, I feel the respect and understanding of my wife even though we are living apart on two continents. Still, I feel bad that I am not available to her when she is sick. As a father, I have not seen my daughter for more then one year (expect on we-chat in cyberland) and miss seeing her grow for close-up. For the next two years, I still will unlikely stay with them and can not contribute my share to being a warm-hearted family. I believe this is a temporary situation. In the near future, I will do my best in being responsible as a son to my parents, a husband to my wife, and a father to my daughter.

TABLE OF CONTENTS

LIST OF TABLES . . . . **x**

LIST OF FIGURES . . . . **xi**

Chapter 1 Introduction **1**
- 1.1 Continuum approach of long-wavelength acoustic phonon modes of quasi-2D and 1D nanomaterials 1
- 1.2 Microscopic mechanism of structural transitions in 2D and 1D systems . . . 2
- 1.3 Mechanical and electronic properties of novel carbon-based nanomaterials . . 3
- 1.4 Outline of the dissertation 5

Chapter 2 From Hartree-Fock to Density Functional Theory **7**
- 2.1 The Born-Oppenheimer approximation 7
- 2.2 Hartree-Fock equation 8
- 2.3 Density Functional Theory 10
- 2.4 Exchange-correlation functionals 15
- 2.5 Basis sets and pseudopotentials 16

Chapter 3 Continuum approach for long-wavelength acoustic phonons in quasi-2D structures **18**
- 3.1 Introduction 18
- 3.2 Continuum approach for long-wavelength acoustic modes of an elastic membrane 21
- 3.3 Calculation of acoustic phonon modes of an elastic membrane in the continuum limit 22
- 3.4 Computational approach to determine the elastic constants 24
- 3.5 Results 25
  - 3.5.1 Graphene 25
  - 3.5.2 Phosphorene 26
  - 3.5.3 Vibration spectra of carbon fullerenes and nanotubes 28
- 3.6 Discussion 29
- 3.7 Summary and Conclusions 31
- 3.8 Related Information 32
  - 3.8.1 Lagrange function of an infinitely thin elastic plate under strain . . . 32
    - 3.8.1.1 Stretching 32
    - 3.8.1.2 Shearing 33
    - 3.8.1.3 Bending 34
  - 3.8.2 Derivation of Euler-Lagrange equations of motion for deformations of an infinitely thin elastic plate using Hamilton's principle 35
    - 3.8.2.1 Stretching 35
    - 3.8.2.2 Shearing 37
    - 3.8.2.3 Bending 37

3.8.3 Radial breathing mode of spherical fullerenes 39
3.8.4 Radial breathing mode of carbon nanotubes 41

Chapter 4 Long-wavelength deformations and vibrational modes in empty and liquid-filled microtubules and nanotubes: A theoretical study 44
4.1 Introduction 44
4.2 Continuum elasticity approach 46
4.2.1 Vibrational Modes of empty Nanotubes 47
4.2.2 Vibrational Modes of Liquid-Filled Nanotubes 50
4.3 Vibrational Modes of Nanotubes in a Surrounding Liquid 51
4.4 Computational Approach to Determine the Elastic Response of Carbon Nanotubes 54
4.5 Results 54
4.5.1 Carbon Nanotubes 55
4.5.2 Tubulin-Based Microtubules 57
4.6 Discussion 60
4.7 Summary 62
4.8 Related Information 63
4.8.1 Lagrange Function of a Strained Nanotube 64
4.8.1.1 Stretching 64
4.8.1.2 Torsion 65
4.8.1.3 Bending 65
4.8.2 Derivation of Euler-Lagrange Equations of Motion for Deformations of a Nanotube using Hamilton's Principle 68
4.8.2.1 Stretching 68
4.8.2.2 Torsion 70
4.8.2.3 Bending 70
4.8.3 Coupling Between a Travelling Pressure Wave and the RBM in a Liquid-Filled Carbon Nanotube 71
4.8.4 Coupling Between the LA Mode and the RBM in Carbon Nanotubes 75

Chapter 5 Unusually stable helical coil allotrope of phosphorus 79
5.1 Introduction 79
5.2 Computational methods 81
5.3 Results and discussion 81
5.4 Summary 89

Chapter 6 Microscopic Mechanism of the Helix-to-Layer Transformation in Elemental Group VI Solids 90
6.1 Introduction 90
6.2 Computational techniques 92
6.3 Results and discussions 94
6.4 Summary 108

Chapter 7 Effect of Net Charge on the Relative Stability of 2D Boron Allotropes **110**
7.1 Introduction 110
7.2 Computational techniques 113
7.3 Results and discussions 113
7.4 Summary 128

Chapter 8 Towards room-temperature superconductivity in low-dimensional C_{60} nanoarrays: An *ab-initio* study **129**
8.1 Introduction 129
8.2 Computational methods 130
8.3 Results and discussions 131
8.4 Summary 138

Chapter 9 Shear instability in twisted bilayer graphene **140**
9.1 Introduction 140
9.2 Computational methods 141
9.3 Results and discussions 142
  9.3.1 Deformation Modes in Bilayer Graphene 142
  9.3.2 Relaxations in Sheared and Twisted Bilayer Graphene 143
  9.3.3 Electronic Structure of Sheared, Twisted and Relaxed Bilayer Graphene 147
9.4 Summary 150
9.5 Related Information 151
  9.5.1 Mathematical formulation of the rigid shear-twist deformation in bilayer graphene 151
  9.5.2 Mathematical background of the relaxation treatment in sheared and twisted bilayer graphene 153
  9.5.3 Local relaxation in sheared and twisted bilayer graphene 157
  9.5.4 Electronic structure changes in sheared and twisted bilayer graphene 157
  9.5.5 Value of the magic angle in unsheared and sheared twisted bilayer graphene 158

Chapter 10 Two-dimensional Mechanical Metamaterials with Unusual Poisson Ratio Behavior **159**
10.1 Introduction 159
10.2 Computational methods 160
10.3 Results and discussions 162
10.4 Summary 168
10.5 Related Information 169
  10.5.1 Deformation behavior in 2D isosceles triangle assemblies 169
  10.5.2 Deformations in a 2D assembly of rigid equilateral triangles 170

Chapter 11 Conclusions **172**

BIBLIOGRAPHY **175**

LIST OF TABLES

Table 4.1: Summary of expressions derived for the vibrational frequencies ω of 1D tubules and 2D plates. $\tilde{\omega}$ denotes the frequency of liquid-filled tubules. Equation numbers refer to the present publication. 52

Table 4.2: Elastic behavior of a 2D graphene monolayer. c_{11}, c_{22}, c_{66} are 2D elastic stiffness constants defined in Eq. (4.1). α is the in-plane Poisson ratio, D is the flexural rigidity, and ρ_{2D} is the areal mass density. These values can be used directly to calculate long-wavelength acoustic frequencies $\omega(k)$ using the expressions in Table 4.1 and the speed of sound v_{LA} and v_{TA}. Present values are compared to published data. 56

Table 6.1: Cohesive energy E_{coh} of various Se and Te allotropes in [eV/atom] units, obtained using DFT-LDA and DFT-PBE calculations. 95

Table 7.1: Cohesive energy E_{coh} of selected neutral borophene allotropes, obtained using DFT-PBE calculations. n is the number of boron atoms per unit cell and Z is the coordination number of individual atoms in the unit cell. . . 115

LIST OF FIGURES

Figure 3.1: (a) Schematic representation of possible distortions of an elastic membrane. (b) Schematic dependence of the longitudinal acoustic (LA), inplane transverse acoustic (TA) and the flexural acoustic (ZA) mode vibration frequencies on the crystal momentum near the center of the Brillouin zone. 19

Figure 3.2: Phonon spectra of (a) graphene, reproduced from Reference [1] and (b) phosphorene, a monolayer of black phosphorus, reproduced from Reference [2], shown by solid lines. Superposed to the spectra are continuum results for the three acoustic phonon modes in different high-symmetry directions, evaluated near Γ, with the longitudinal acoustic (LA, dashed lines), in-plane transverse acoustic (TA, dotted lines), and the flexural acoustic (ZA, solid lines) modes. Ball-and-stick models of the structure, including the primitive unit cells, are shown in the top panels. The Brillouin zones are shown as insets in the phonon spectra. 27

Figure 3.3: Radial breathing mode (RBM) in (a) fullerenes and (b) carbon nanotubes as a function of their diameter d. The prediction is shown by the solid line. Experimental and theoretical RBM frequencies for the only observed fullerene with spherical symmetry, C_{60}, are shown by the data points in (a). The experimentally well-established relationship [3, 4] $\omega = 248\ \mathrm{cm}^{-1} \times (1\ \mathrm{nm}/d)$ in nanotubes in (b) is represented by the dashed line and the calculation is shown by the solid line. 28

Figure 4.1: Schematic representation of important deformations of a tubular structure. (a) Longitudinal acoustic (LA, stretching), (b) torsional acoustic (TA, torsion), (c) flexural acoustic (doubly degenerate ZA, bending), and (d) the radial breathing mode (RBM). (e) Schematic dispersion relations of the corresponding long-wavelength phonon modes. The tilde denotes liquid-filled tubules. 46

Figure 4.2: (a) Frequency of vibrational modes depicted in Fig. 4.1(a) in empty and water-filled carbon nanotubes. (b) Dependence of the flexural coefficient $c_{ZA}(R)$, defined in Eq. (4.9), on the radius R of empty and water-filled carbon nanotubes. The tilde denotes liquid-filled nanotubes. 55

Figure 4.3: (a) Frequency of vibrational modes depicted in Fig. 4.1(a) in empty and water-filled tubulin-based microtubules. (b) Dependence of the flexural coefficient $c_{ZA}(R)$, defined in Eq. (4.9), on the radius R of empty and water-filled tubulin-based microtubules. The tilde denotes liquid-filled tubules. 57

Figure 4.4: Nature and coupling of vibration modes $\omega(k)$ of a carbon nanotube that may be filled with water. (a) Coupling between the dispersionless RBM of a CNT, shown by the black line, and the pressure wave of water enclosed in the CNT, shown by the green dotted line. (b) Coupling between the RBM of a CNT, shown by the black line, and the longitudinal acoustic mode of the CNT, shown by the green dotted line. Results are presented for a CNT with a radius of 1 nm. 72

Figure 5.1: (a) Optimum structure of an isolated, straight 1D P_{∞} chain with the P_{10} unit cell of length L. (b) Optimized P_{18}, P_{28} and P_{38} segments of the isolated chain, indicating the tendency to form rings with a radius $R\approx 2.4$ nm. (c) The optimum structure of a single coil. (d) Optimum structure of a 2D assembly of P_{∞} chains separated by the distance d. (e) Possible scenario for the formation of helical coils by connecting finite-length chain segments inside a cylindrical cavity. The unit cells are indicated by dashed lines in (a) and (d). 80

Figure 5.2: (a) Strain energy ΔE per atom as a function of the radius R of an isolated P coil. (b) Inter-chain interaction energy ΔE per atom in a 2D assembly of phosphorus chains, depicted in Fig. 5.1(d), as a function of the inter-chain distance d. (c) Interaction energy ΔE per phosphorus atom between a P chain and a graphene monolayer as a function of the adsorption height h. PBE results are shown by the solid red lines, LDA results by the dashed blue lines. 82

Figure 5.3: Electronic structure of (a) an isolated P chain and (b) a 2D layer of P chains, shown in Figs. 5.1(a) and 5.1(d). Left panels depict the electronic band structure based on PBE and the middle panels the corresponding density of states. The Brillouin zone is shown as inset of the left panel in (b). The right panels depict the charge distribution associated with frontier states in the valence band region, indicated by the green hashed region in (a) and (b), which extends from E_F to 0.2 eV below the top of the valence band. Charge density contours are superposed to structural models, with the unit cells indicated by the dashed lines. Due to differences in the density of states between these systems, the contours are presented at the electron density 0.008 e/Å^3 in (a) and 0.002 e/Å^3 in (b). 85

Figure 6.1: Stable 1D and 2D structural allotropes of Se and Te. 1D structures of the (a) a helix and (b) b chain and their 2D counterparts, the (c) δ and (d) η allotrope. The δ allotrope is a covalently bonded 2D assembly of b chains. The unit cells of the 2D structures are highlighted by the transparent green areas in (c) and (d). 91

Figure 6.2: Phonon spectra of (a) δ-Se and (b) η-Se calculated using the DFT-LDA energy functional. The Brillouin zones and high-symmetry points are shown schematically in the insets. Continuum elasticity results for long-wavelength longitudinal acoustic modes are shown by the blue dash-dotted lines, for transverse acoustic modes by the dotted green lines, and for flexural modes by the dashed red parabolas. 92

Figure 6.3: (a) Schematic growth mechanism of the energetically stable 2D δ structure by zipper-like attachment of the b chain, which is being formed locally locally at a defect in the native a helix and propagates by dislocation motion. (b) Bond length d, bond angle θ and dihedral angle ψ used to characterize chalcogen structures. (c) DFT-LDA based energy differences ΔE encountered during the stepwise conversion from 1D a-Se to b-Se as a function of the reaction coordinate. The system is represented by a finite Se_9H_2 chain, passivated by hydrogen at both ends, and the total energy is given with respect to the final state. The dotted line is guide to the eye. The energy of a 9-atom long segment of the defect-free infinite a-Se and b-Se chains is indicated by asterisks. Ball-and-stick models show stable Se_9H_2 geometries, labeled by A-D, and the transition states T. Location of the unusually small dihedral angle in the transition states is indicated by shaded triangles. 94

Figure 6.4: Transformation of 1D to 2D structures of elemental Se. (a) Perspective and end-on view of the initial 2D assembly of 1D a-chains. (b) End-on view of the structure after artificial confinement to an infinitely thin slab. (c) End-on view of the 2D δ-Se allotrope that formed spontaneously after the structure in (b) was relaxed. 97

Figure 6.5: Structural transformation between the 2D δ and the η allotropes by a series of reflections in planes normal to the picture plane. (a)-(c) Schematic side view of the initial and intermediate structures. Atoms in a plane normal to the lattice are shown by $\bigcirc$ and atoms in front of these by $\odot$. Atoms in one unit cell are labeled by the numbers $1-6$. Primed numbers are used to label atoms in neighboring cells. Perspective views of (d) the initial δ and (e) the final η structure. 98

Figure 6.6: (a) Potential energy E as a function of the optimum reaction coordinate during the A-D transformation. (b) Schematic transformation from the a-helix to the b-chain by dislocation motion.Schematic geometry of hydrogen terminated 9-atom segments of (c) the a-helix and (d) the b-chain. Atoms are labeled for later use. 102

Figure 6.7: (a,c) Dihedral angle ψ and (b,d) potential energy E of the Se system during (a,b) CG optimization and (c,d) MD calculations starting in transition point T_{AB}, identified energetically in Fig. 6.6(a). Atomic positions used to define ψ_{6789} are identified in Fig. 6.6(c) and 6.6(d). 103

Figure 6.8: (a,c) Dihedral angle ψ and (b,d) potential energy E of the Se system during (a,b) CG optimization and (c,d) MD calculations starting in transition point T_{BC}, identified energetically in Fig. 6.6(a). Atomic positions used to define ψ_{2345} are identified in Fig. 6.6(c) and 6.6(d). 104

Figure 6.9: (a,c) Dihedral angle ψ and (b,d) potential energy E of the Se system during (a,b) CG optimization and (c,d) MD calculations starting in transition point T_{CD}, identified energetically in Fig. 6.6(a). Atomic positions used to define $\psi_{789,10}$ are identified in Fig. 6.6(c) and 6.6(d). 105

Figure 6.10: Electronic band structure of an isolated (a) a-Se helix, (b) b-Se chain, isolated (c) δ-Se and (d) η-Se monolayers. GW results, shown by solid red lines, are compared to LDA results, shown by the black dashed lines. . . 106

Figure 6.11: Electronic band structure of an isolated (a) a-Te helix, (b) b-Te chain, isolated (c) δ-Te and (d) η-Te monolayers obtained using DFT-LDA. . . 107

Figure 7.1: Previously unexplored neutral borophene allotropes formed by spontaneous conversion of an artificial honeycomb lattice: (a) ϵ-B and (b) ω-B. The structures are shown in top and side view. The lattice vectors $\vec{a}_1$ and $\vec{a}_2$, shown in red, delimit the highlighted primitive unit cells. 114

Figure 7.2: Electron doped 2D borophene structures obtained by optimizing a distorted boron honeycomb superlattice with 32 atoms per unit cell. The average excess charge $\langle \Delta Q \rangle$ per boron atom, specified in the panels, increases from (a) ϵ_1-B to (f) ϵ_6-B. The structures are shown in top and side view. The lattice vectors $\vec{a}_1$ and $\vec{a}_2$, shown in red, delimit the highlighted unit cells. 116

Figure 7.3: Electron doped 2D borophene structures obtained by optimizing a distorted boron honeycomb superlattice with 32 atoms per unit cell. The average excess charge $\langle \Delta Q \rangle$ per boron atom, specified in the panels, increases from (a) to (c). The structures are shown in top view (upper panels) and side view (lower panels). The lattice vectors $\vec{a}_1$ and $\vec{a}_2$, shown in red, delimit the highlighted unit cells. 117

Figure 7.4: Charge redistribution in 2D borophene layers induced by extra electrons or by contact with monolayers of Ca_2N electride. Charge density difference $\Delta\rho$ caused by placing an excess charge (a) $\langle \Delta Q \rangle = -0.406$ e/atom on ϵ_3-B and (b) $\langle \Delta Q \rangle = -1.0$ e/atom on ϵ_6-B. Charge density redistribution $\Delta\rho = \rho(\mathrm{B/Ca_2N}) - \rho(\mathrm{B}) - \sum \rho(\mathrm{Ca_2N})$ in the bilayer structures (c) ϵ_3-B/Ca_2N and (d) ϵ_6-B/Ca_2N as well as in the sandwich structures (e) Ca_2N/ϵ_3-B/Ca_2N and (f) Ca_2N/ϵ_6-B/Ca_2N. $\Delta\rho$ is shown by isosurfaces bounding regions of electron excess at $+7\times10^{-3}$ e/Å^3 (yellow) and electron deficiency at -2×10^{-3} e/Å^3 (blue). $\langle \Delta\rho(z) \rangle$ is averaged across the $x-y$ plane of the layers. 118

Figure 7.5: Changes in the interlayer interaction energy ΔE and net average charge $\langle \Delta Q \rangle$ on borophene in the Ca_2N/B/Ca_2N sandwich geometry as a function of the interlayer distance d. Results for ϵ_3-B in (a) and (c) are compared to those for ϵ_6-B in (b) and (d). 119

Figure 7.6: Electron flow between borophene and bilayers of the Ca_2N electride. Charge density redistribution $\Delta\rho = \rho(\mathrm{B/[Ca_2N]_2}) - \rho(\mathrm{B}) - \sum \rho(\mathrm{Ca_2N})$ in (a) ϵ_3-B/$[Ca_2N]_2$ and (b) ϵ_6-B/$[Ca_2N]_2$ triple-layer heterostructures. $\Delta\rho$ is shown by isosurfaces bounding regions of electron excess at $+7\times10^{-3}$ e/Å^3 (yellow) and electron deficiency at -2×10^{-3} e/Å^3 (blue). $\langle \Delta\rho(z) \rangle$ is averaged across the $x-y$ plane of the layers. 120

Figure 7.7: Effect of net charge on the equilibrium geometry of ϵ-B. (a) Effect of the net average charge $\langle \Delta Q \rangle$ on the orthogonal lattice constants a_i with $i = 1, 2$. Plotted are charge-induced relative changes $\Delta a_i / a_i^0$, where a_i^0 are the lattice constants in the neutral ϵ-B allotrope. (b) Strain energy ΔE as a function of in-layer strain σ at different levels of extra electrons $\langle \Delta Q \rangle$. 121

Figure 7.8: Electronic band structure of (a) neutral ϵ-B, (b) ϵ_1-B with $\langle \Delta Q \rangle = -0.156$ e/B, (c) ϵ_3-B with $\langle \Delta Q \rangle = -0.406$ e/B, (d) ϵ_4-B with $\langle \Delta Q \rangle = -0.500$ e/B, (e) ϵ_5-B with $\langle \Delta Q \rangle = -0.750$ e/B, and (f) ϵ_6-B with $\langle \Delta Q \rangle = -1.000$ e/B, calculated using the DFT-PBE functional. The indirect fundamental band gap is indicated by the red arrow in (a). 122

Figure 7.9: Electronic band structure of ϵ-B subject to in-layer strain of (a) -6%, (b) -4%, (c) +4%, and (d) +6% along the $\vec{a}_1$ direction, and (e) -3%, (f) -1%, (g) +1%, and (h) +3% along the $\vec{a}_2$ direction. The fundamental band gap is indicated by the red arrows in semiconducting systems. 123

Figure 7.10: Charge density difference $\Delta\rho$ caused by placing an excess charge $\langle\Delta Q\rangle = -0.0625$ e/atom on selected borophene structures characterized in Figure 7.2 of the main manuscript and in Figure 7.3. (a) ϵ_1-B of Figure 7.2(a), (b) ϵ_2-B of Figure 7.2(b), (c) ϵ_3-B of Figure 7.2(c), (d) ϵ_4-B of Figure 7.2(d), as well as B structures shown in (e) Figure 7.3(b) and (f) Figure 7.3(c). $\Delta\rho$ is shown by isosurfaces bounding regions of electron excess at $+2.5\times10^{-3}$ e/Å^3 (yellow). 125

Figure 8.1: Schematic arrangement of C_{60} molecules in (a) a 3D fcc crystal, (b) a 2D triangular lattice, and (c) a 1D array inside a $(10, 10)$ carbon nanotube peapod. (d) Width of the t_{1u}-derived band in a 1D, 2D and 3D arrangement of C_{60} molecules as a function of the C_{60}-C_{60} center-to-center separation d_{cc}. The equilibrium value of d_{cc} depends on the C_{60} orientation and is indicated by the gray strip in (d) for undoped structures. The 'error bars' reflect the effect of changing the C_{60} orientation on the bandwidth. (e) Schematic arrangement of dopant atoms outside the 1D peapod (▲), inside the nanotube but outside the fullerene (■), and inside the fullerene (+). Dark spheres in (a) represent clusters other than C_{60} that separate quasi-1D percolating arrays of fullerenes from the surrounding matrix. The planes in (b) are only a visual aid. 132

Figure 8.2: Density of states (DOS) and charge redistribution in doped C_{60} crystals. (a) DOS of the t_{1u} LUMO-derived bands of C_{60} in 1D, 2D and 3D periodic C_{60} arrangements for the C_{60}-C_{60} separation $d_{cc} = 9.8$ Å. (b) Total and projected DOS of a C_{60}@$(10, 10)$ CNT peapod doped externally by 7 K donor atoms per C_{60}. (c) Charge density difference $\Delta\rho = \rho_{tot}(C_{60}@CNT+7K) - \rho_{tot}(C_{60}@CNT) - \sum_{at}\rho_{tot}(\text{K atom})$. (d) DOS of the h_u HOMO-derived bands of C_{60} in 1D, 2D and 3D periodic C_{60} arrangements for the C_{60}-C_{60} separation $d_{cc} = 9.8$ Å. (e) Total and projected DOS of a C_{60}@$(10, 10)$ CNT peapod doped externally by 8 F acceptor atoms per C_{60}. (f) Counterpart of (c) for C_{60}@CNT+8F. In (c) and (f), blue contours for electron deficit are shown for $\Delta\rho = -3.0\times10^{-3}$ e/bohr^3 and red contours for electron excess are shown for $\Delta\rho = +3.0\times10^{-3}$ e/bohr^3. All energies are with respect to E_F. 133

Figure 8.3: Properties of 1D arrays of C_{60} molecules found in CNT peapods. (a) Ball-and-stick models of different atomic arrangements at the C_{60}-C_{60} interface. Considered are double-bonds facing double-bonds (d), hexagons facing hexagons (h), pentagons facing pentagons (p). α and β arrangements are obtained by a 90° rotation of C_{60} molecules in p arrangement about two different axes that are orthogonal to the chain axis and to each other. (b) DOS of the t_{1u} LUMO-derived bands of C_{60} for the C_{60} orientations, defined in (a), at the C_{60}-C_{60} separation $d_{cc} = 9.8$ Å. All energies are with respect to E_F. (c) Maximum DOS value of t_{1u}-derived bands in 1D, 2D and 3D crystals of C_{60}. The 'error bars' reflect the effect of changing the C_{60} orientation. (d) Critical temperature for superconductivity T_c based on the McMillan equation (8.1) and using $N(E_F)$ from (c). The lines in (c) and (d) are guides to the eye. 137

Figure 9.1: Shear and twist in bilayer graphene (BLG). (a) Definition of shear and twist operations in BLG, initially a bilayer in AA stacking indicated by the honeycomb lattice. A rectangular segment of the top layer, with one side closing the angle β with respect to the highlighted armchair direction, is indicated in yellow and surrounded by the dotted line. The segment is first sheared by the angle α and subsequently rotated by the angle θ. (b) Schematic top view of a uniformly twisted and sheared monolayer graphene (MLG) on top of an undeformed MLG. The resulting relaxed Moiré pattern contains regions of AA stacking, highlighted by the white circles, and those of AB or BA stacking. (c) Dark-field TEM image of bilayer graphene reproduced from Ref. [[5]]. (d) Schematic side view of a relaxed sheared and twisted BLG with locally varying stacking. 143

Figure 9.2: (a) Energy difference ΔE caused by shearing the top layer of BLG, which had been twisted by $\theta_m = 1.08°$, by varying the shear angle α along the $\beta = 0°$ direction. Results for the BLG with unrelaxed atomic positions in planar, sheared monolayers are shown by the red dotted line and for the BLG with relaxed atomic positions by the black solid line. Contour plots of the local shift vector length $\delta = |\boldsymbol{\delta}|$ in the BLG structure, which had been twisted by $\theta_m = 1.08°$ and sheared by $\alpha = 0.08°$ along the $\beta = 0°$ direction, (b) in absence and (c) in presence of lattice relaxation. 144

Figure 9.3: Electronic density of states (DOS) in the BLG structure subject to the magic twist angle $\theta_m = 1.08°$. Results for the unsheared structure are shown in panels (a) and (c), and those for the top layer sheared by $\alpha = 0.08°$ along the $\beta = 0°$ direction in (b) and (d). Results for the unrelaxed structure in (a) and (b) are compared to those for the relaxed structure in (c) and (d). 149

Figure 9.4: Contour plots of the local shift vector length $\delta = |\boldsymbol{\delta}|$ in the BLG structure, which had been twisted by $\theta = 0.4^\circ$ and sheared by $\alpha = 0.08^\circ$ along the $\beta = 0^\circ$ direction, (a) in absence and (b) in presence of lattice relaxation. 155

Figure 9.5: Electronic density of states (DOS) in the BLG structure subject to the magic angle twist $\theta_m = 1.08^\circ$. Results for the unsheared structure are shown in panels (a) and (c), and those for the top layer sheared by $\alpha = 0.08^\circ$ along the $\beta = 0^\circ$ direction in (b) and (d). Results for the unrelaxed structure in (a) and (b) are compared to those for the relaxed structure in (c) and (d). The energy scale is extended in comparison to Fig. 9.3. . 156

Figure 9.6: The width of the 'flat band' in a relaxed twisted bilayer graphene structure as a function of the twist angle θ. Data points for commensurate, relaxed structures in the vicinity of the observed value $\theta_m = 1.08^\circ$ are presented by the black diamonds (◆) for the unsheared lattice and by the red circles (●) for the structure with the top layer sheared by $\alpha \approx 0.08^\circ$ along the $\beta = 0^\circ$ direction. The dotted and dashed lines are guides to the eye. . . 157

Figure 10.1: Deformations in a 2D assembly of rigid isosceles triangles. (a) Adjacent triangles with opening angle α and mutual orientation defined by the closing angle β, hinged tip-to-corner, forming the primitive unit cell. The triangle height x_0 and the length y_0 of its base define the horizontal and vertical length scales. (b) Snap shots of the $\alpha = 120^\circ$ triangle assembly for different values of β. The conventional rectangular unit cell is twice the size of the primitive unit cell. (c) Contour plot of the Poisson ratio $\nu_{xy} = -(dy/y)/(dx/x)$ as a function of α and β. The dotted red line highlights behavior of the $\alpha = 120^\circ$ triangle assembly. (d) Poisson ratio ν_{xy} as a function of β in the $\alpha = 120^\circ$ system. (e) Changes in the scaled width x/x_0 and height y/y_0 of the conventional unit cell for $\alpha = 120^\circ$ caused by changing the angle β. 161

Figure 10.2: Deformations in porous graphene, a phenanthrene-based 2D mechanical metamaterial. (a) Structure of the $C_{14}H_{10}$ phenanthrene molecule and its relation to an isosceles $\alpha = 120^\circ$ triangle of Fig. 10.1. (b) Equilibrium structure of 2D porous graphene consisting of polymerized phenanthrene molecules with $\beta = 70^\circ$. Saturating hydrogen atoms are shown by the lighter and smaller spheres. Changes in the scaled width x/x_0 (c) and height y/y_0 (d) of the conventional unit cell in the triangle assembly and porous graphene as a function of the closing angle β. (e) Poisson ratio ν_{xy} in porous graphene as a function of β. (f) Strain energy in the $C_{56}H_{28}$ conventional unit cell as a function of β. The dashed and dotted lines connecting data points for porous graphene in (c)-(f) are guides to the eye. 162

Figure 10.3: Electronic structure of porous graphene, a phenanthrene-based 2D mechanical metamaterial, based on DFT-PBE calculations. (a) Band structure of the equilibrium structure with $\beta = 70^\circ$ obtained using the rectangular $C_{56}H_{28}$ unit cell. High-symmetry points in the rectangular Brillouin zone are shown in the inset. (b) Fundamental band gap E_g as a function of the angle β. 166

Figure 10.4: Changes in the scaled width x/x_0 and height y/y_0 of the conventional unit cell for different values of the opening angle α as a function of the closing angle β. The relevant quantities are defined in Fig. 10.1. 170

Figure 10.5: Deformations in a 2D assembly of rigid equilateral triangles. (a) Adjacent triangles with mutual orientation defined by the closing angle β, hinged at the corners, forming the primitive unit cell. The triangle height x_0 and the length y_0 of its base define the horizontal and vertical length scales. (b) Snap shots of the triangle assembly for different values of β. The conventional unit cells of width x and height y are indicated. 171

Chapter 1

Introduction

There are three main projects related to low-dimensional systems on the nanoscale in this thesis. First of all, the continuum elasticity method was utilized to successfully solve a very common problem, namely the occurrence of unphysical imaginary frequencies in long-wavelength flexural acoustic phonon modes of 2D and 1D systems. The second topic mainly addresses the stability and electronic properties, as well as a microscopic mechanism behind structural transformations between different low-dimensional systems. The last topic are electronic and mechanical properties of carbon-based materials. All of these topics have been motivated by a desire to solve long-standing problems in the specific field and to explore the bright future that may benefit from unique properties of 2D and 1D nanostructures.

1.1 Continuum approach of long-wavelength acoustic phonon modes of quasi-2D and 1D nanomaterials

Atomistic calculations of phonon spectra based on *ab initio* density functional theory (DFT) start with the calculation of the force-constant matrix, which is associated with finite displacements of atoms in the unit cell. While addressing long-wavelength acoustic phonon modes, this approach reaches it practical limitations in a computer calculation. For long-wavelength vibration modes, especially as the wave number k is close to zero, a very large supercell is typically required to obtain an accurate result. However, the computer limitations lead to numerical inaccuracies in the force-constant matrix which usually cause imaginary frequencies in the acoustic phonon modes near the Γ point.

In this case, imaginary frequencies are numerical artifacts that differ fundamentally from the case, where imaginary frequencies indicate real structural instabilities. Imaginary frequencies appearing as artifacts also affect related simulations that depend on a correct phonon spectrum, such as thermal conductivity, charge transport, and others. Here, I propose a continuum elasticity approach to solve the problem, which does not suffer from the large supercell sizes in 2D/1D systems. In this thesis, I introduced a 3×3 2D elastic stiffness matrix, complemented by the flexural rigidity D, which describes the elastic behavior of 2D/1D systems in the linear regime. Independent of thickness of the 2D/1D system, all acoustic phonon modes can be determined using elements of the 2D elastic matrix. These elements can be calculated using very few static *ab initio* density functional theory calculations or relaxed and distorted structures in a much more reliable and straight-forward way, or can be obtained experimentally.

1.2 Microscopic mechanism of structural transitions in 2D and 1D systems

Low-dimensional nanostructures receive growing attention due to their different physical properties in comparison with those of macroscopic 3D systems. These include high flexibility, charge carrier mobility, tunable electronic structure, and others. Exploring 2D and 1D nanomaterials beyond those, which have been synthesised in experiment, plays an important role in developing electronic devices. Recent developments including data mining and machine learning appear to have accelerated the process of predicting low dimensional nanomaterials. However, many of such predicted nanomaterials are hard to synthesis and some may only occur under extreme synthesis conditions. To quote one example, 2D allotropes of elemental boron need a special substrate to grow. It is thus not only the stability of a nanostructure in vacuum, but also the likely formation formation mechanism that is essential to provide a guideline for future experiments.

In this thesis, I predicted previously unknown stable allotropes of elements in groups III, V and VI. I found these allotropes, often with a peculiar structural symmetry, to be at least as stable as existing materials. I also investigate the electronic properties of these allotropes to explore their application prospect. More importantly, I studied the transformation mechanism between different allotropes, and proposed critical information about the synthesis conditions under which these allotropes could be formed in the experiment. I found that the most efficient transformation from a 1D helix of Se/Te to a 2D allotrope involves only changes in the dihedral angle, while the bond lengths and bond angles are not affected. I also found that when carrying one extra electron per atom, elemental boron will mimic carbon in both its atomic and electronic structure. In reality, such a large electron charge can be provided when in contact with a 2D electride such as Ca_2N.

1.3 Mechanical and electronic properties of novel carbon-based nanomaterials

Carbon is one of the most abundant elements on earth. Reducing dimensionality from 3D to 0D, we find many stable carbon allotropes, such as diamond in 3D, graphene/graphite in 2D, nanotubes in 1D, and fullerenes in 0D. Different carbon allotropes also exhibit a rich spectrum of physical properties. For example, twisted bilayer graphene will turn superconducting at a special twist angle. Carbon nanotubes can be used for medication delivery. Functionalized fullerenes are valuable candidate drugs. The high number os structurally stable 0D-3D allotropes provides nanomaterials based on elemental carbon with a wide range of unexpected properties and promises new fundamental physics insight.

I will discuss carbon materials from three aspects. First, the 3D alkali-metal-doped C_{60} crystal is a superconductor with T_c around 30 K, and T_c can be well explained based on McMillan equation in theory. One critical factor, which determines the value of T_c, is the density of state at the Fermi level. Instead of changing the Fermi level by doping, my calculation shows that the critical superconducting temperature of doped C_{60} crystals can be elevated near to room temperature simply by reducing the dimensionality from 3D to quasi-1D.

Pristine carbon has never been observed to superconduct. It is only in an alkali-metal-doped C_{60} crystal that superconductivity has been observed and explained within the framework of BCS theory. On the other hand, the Physics underlying the recently reported emerging superconductivity in twisted bilayer graphene at the 'magic angle' remains unclear. Conventional DFT calculations fail to reproduce the electronic structure for lack of periodicity or in view of very large Moiré supercells with a large number of atoms. Here, by using the tight-binding model, I succeeded in exploring the importance of in-plane shear and atomic relaxation in the bilayer graphene system. Both effects stabilize the system and enhance the density of states at Fermi level.

Finally, I study an unexpected behavior of an important mechanical property, namely the Poisson ratio ν, which can become negative and change sign in a designer carbon metamaterial. ν is positive in ordinary materials, which means that stretching the material in one direction will shrink the material in an orthogonal direction. In previously proposed auxetic materials with a particular atomic structure, the Poisson ratio is negative, meaning that stretching in one direction causes expansion in an orthogonal direction. Graphene is a promising candidate from this perspective given the possibility to modify its structure, which may be achieved by supramolecular assembly in the experiment. Here I propose that a structurally tailored graphene, which could form by polymerization of phenanthrene molecules, exhibits both a negative Poisson ration and a shape-memory effect, which changing reversibly its fundamental band gap at will.

1.4 Outline of the dissertation

This thesis contains 11 Chapters in total. The introduction to all my Ph.D. research is described in Chapter 1, and computational methods I used for most of my work are described in Chapter 2.

In Chapters 3 and 4, I introduced the continuum elasticity approach to study acoustic phonon modes of one-dimensional and two-dimensional systems. I have developed expressions for the momentum-dependent frequencies of long-wavelength acoustic phonon modes in terms of the 2D elastic constants of the system. My approach solves the problem of numerical artifacts in atomistic calculations that result in imaginary frequencies near the Γ.

In Chapter 5 to Chapter 7, I predicted a variety of previously unknown stable low-dimensional allotropes of elements in group III, V and VI. The stability of these allotropes turns out to be comparable to the existing materials. In particular, a one-dimensional phosphorus coil, which can be formed inside carbon nanotubes, is as stable as black phosphorus. As for Se/Te, I have predicted two previously unknown, stable allotropes. In Chapter 6, I study the transformation of Se/Te allotropes from 1D to 2D structures and identify the reaction coordinates for this transformation. My general findings should be of value to other, related systems. Unlike other elements, boron is very sensitive to doping. Thus searching for stable 2D electron-doped boron allotropes is of practical importance. Here I predict different stable allotropes at different level of net charging. More importantly, I also discuss the mechanism of forming such allotropes in detail.

In Chapter 8, I focused on the properties of carbon based materials, including the superconductivity of C_{60} crystals, the shear-induced instability of twisted bilayer graphene, and the negative Poisson ratio of porous graphene. For the first topic, heavy alkali atoms have been used to dope the C_{60} crystal and increase its lattice constant to increase its critical temperature for superconductivity. I propose an alternative approach by reducing the coordination number of C_{60} in 2D and quasi-1D systems, which promises an even more significant in increasing T_c to close to room temperature. The second topic relates to twisted bilayer graphene which is aperiodic in the most general case. By using the tight-binding model, I found that during the twist, an in-plane shear provides further stabilization for the system. This appears to be confirmed by dark-field transmission electron microscopy images. Finally, I studied the peculiar negative Poisson ratio ν of porous graphene with specific structure. I found that the designed metamaterial shows not only a negative value ν, but that ν may change sign and even diverge for specific structural arrangements in the 2D metamaterial.

Chapter 2

From Hartree-Fock to Density Functional Theory

In this Chapter, I will start with the Hatree-Fock approximation that begins with the Schrodinger equation for a one-electron system and antisymmetrizes the many-electron wavefunction represented by a Slater determinant. Then I will introduce the Density Functional Theory (DFT) where the density of electrons is the fundamental property that determines the properties of ground state of the system. In most cases, self-consistency in DFT is obtained by solving a set of Kohn-Sham equations.

2.1 The Born-Oppenheimer approximation

For a material containing atoms and electrons, the Hamilton operator of the system is following:

$$\hat{H} = \sum_I -\frac{\hbar^2}{2M}\nabla_I^2 + \sum_i -\frac{\hbar^2}{2m}\nabla_i^2 + \frac{1}{2}\sum_{I\neq J}\frac{Z_I Z_J e^2}{|\mathbf{R_I}-\mathbf{R_J}|} + \frac{1}{2}\sum_{i\neq j}\frac{e^2}{|\mathbf{r_i}-\mathbf{r_j}|} - \sum_{I,i}\frac{Z_I e^2}{|\mathbf{r_i}-\mathbf{R_I}|} \tag{2.1}$$

This Hamiltonian contains five parts, namely the kinetic and interaction energy of electrons, kinetic and interaction energy of ions, and the interaction between electrons and ions. Uppercase indices refer to ions and lowercase indices to electrons. $\mathbf{R_I}$ and $\mathbf{R_J}$ denote the ion positions and $\mathbf{r_i}$ and $\mathbf{r_j}$ denote the electron positions. Since the mass of the nucleus is thousands times higher than that of electron, the nucleus can be treated as static while the electrons are moving. This is the Born-Oppenheimer approximation [6]. With this approximation, the Hamiltonian can be written as:

$$\hat{H} = \sum_i -\frac{\hbar^2}{2m}\nabla_i^2 + \frac{1}{2}\sum_{i\neq j}\frac{e^2}{|\mathbf{r_i} - \mathbf{r_j}|} - \sum_{I,i}\frac{Z_I e^2}{|\mathbf{r_i} - \mathbf{R_I}|} = \hat{H}_i + \frac{1}{2}\sum_{i\neq j}\frac{e^2}{|\mathbf{r_i} - \mathbf{r_j}|}. \tag{2.2}$$

Here, $\hat{H}_{ii}$ is the Hamiltonian of a single electron.

2.2 Hartree-Fock equation

In order to get the ic wavefunction in a one-electron system, we need to solve the Schrödinger equation

$$\hat{H}\Psi(\mathbf{r}) = E\Psi(\mathbf{r}). \tag{2.3}$$

The total energy of the system is

$$E = \langle \Psi^*(\mathbf{r}) \mid \hat{H} \mid \Psi(\mathbf{r})\rangle. \tag{2.4}$$

In a many-electron system, if we do not consider the electron-electron interaction as described as the second term in Eq. (2.2), the wavefunction of the whole system can be written as the product of the one-electron wave functions for each electron. Since electrons are fermions, exchange of two fermions will result in a sign change of the wavefunction. In that case, the wave function of the whole system can be written as a Slater determinant,

$$\Psi(\mathbf{r}) = \frac{1}{\sqrt{N!}} \begin{vmatrix} \Phi_1(\mathbf{r_1}) & \Phi_1(\mathbf{r_2}) & \cdots & \Phi_1(\mathbf{r_N}) \\ \Phi_2(\mathbf{r_1}) & \Phi_2(\mathbf{r_2}) & \cdots & \Phi_2(\mathbf{r_N}) \\ \vdots & \vdots & & \vdots \\ \Phi_N(\mathbf{r_1}) & \Phi_N(\mathbf{r_2}) & \cdots & \Phi_N(\mathbf{r_N}) \end{vmatrix}.$$

Here, $\Phi_i(\mathbf{r_j})$ represents the orthonormal orbital of electron i at the position $\mathbf{r_j}$,

$$\int \Phi_i^*(\mathbf{r})\Phi_j(\mathbf{r}) = \delta_{ij}. \tag{2.5}$$

The third term in Eq. (2.2) represents the crystal potential of the electron and can be written as

$$V(\mathbf{r}) = \sum_I v(\mathbf{r} - \mathbf{R_I}) = -\sum_I \frac{Z_I e^2}{|\mathbf{r} - \mathbf{R_I}|}. \tag{2.6}$$

By substituting the Hamiltonian and the wave function into Eq. (2.6), we can get the average energy

$$\begin{aligned} E &= \sum_i \int \mathrm{d}\mathbf{r}\Phi_i^*(\mathbf{r})\hat{H}_i\Phi_i(\mathbf{r}) + \frac{1}{2}\sum_{i\neq j}\int \mathrm{d}\mathbf{r}d\mathbf{r}'|\Phi_i(\mathbf{r})|^2\frac{e^2}{|\mathbf{r}-\mathbf{r}'|}|\Phi_j(\mathbf{r}')|^2 - \\ &\quad \frac{1}{2}\sum_{i\neq j}\int \mathrm{d}\mathbf{r}d\mathbf{r}'\Phi_i^*(\mathbf{r})\Phi_j^*(\mathbf{r}')\frac{e^2}{|\mathbf{r}-\mathbf{r}'|}\Phi_j(\mathbf{r})\Phi_i(\mathbf{r}'). \end{aligned} \tag{2.7}$$

The energy of the ground state can be obtained by applying the variational principle on Eq. (2.7). This leads to the Hartree-Fock equation:

$$[-\frac{\hbar^2}{2m}\nabla^2 + V(\mathbf{r}) + \sum_j \int \mathrm{d}\mathbf{r}' |\mathit{\Phi}_j(\mathbf{r}')|^2 \frac{e^2}{|\mathbf{r}-\mathbf{r}'|}]\mathit{\Phi}_i(\mathbf{r}) - \sum_j \int \mathrm{d}\mathbf{r}' \frac{e^2 \mathit{\Phi}_j^*(\mathbf{r}')\mathit{\Phi}_i(\mathbf{r}')}{|\mathbf{r}-\mathbf{r}'|}\mathit{\Phi}_j(\mathbf{r}) = \epsilon_i \mathit{\Phi}_i(\mathbf{r}). \tag{2.8}$$

The Hartree-Fock equation is a wavefunction-based equation. Since the size of the Slater determinant increases with the size of the system, this approach is not suited for infinite solids.

2.3 Density Functional Theory

Two remarkable theorems form the exact basis of density functional theory (DFT). The first theorem states that the total energy of the system in the ground state is a functional of only the electron density $\rho(\mathbf{r})$. The second theorem states that the ground-state charge density is the one that minimizes the total energy.

While both theorems are exact, finding the energy functional $E[\rho]$, which relates the total energy to the charge density in the ground state, is a challenging problem. Minimization of $E[\rho]$ is achieved by solving

$$\delta \left\{ E[\rho] - \epsilon \int \rho(\mathbf{r}) d\mathbf{r} \right\} = 0, \tag{2.9}$$

where ϵ is a Lagrange multiplier that keeps the total charge constant. This expression implies that for the correct charge density,

$$\delta E[\rho]/\delta\rho(\mathbf{r}) = \epsilon. \tag{2.10}$$

$E[\rho]$ is usually separated into several terms:

$$E[\rho] = T[\rho] + V_s[\rho], \tag{2.11}$$

where $T[\rho]$ is the kinetic energy functional and $V_s[\rho]$ is a potential energy functional. The potential energy functional is usually separated as

$$V_s[\rho] = V_c + V_H + V_{XC}, \tag{2.12}$$

where V_c is the crystal potential energy describing the interaction of the electron with the nuclei or external fields. $V_H[\rho]$ is the Hartree energy functional describing the Coulomb repulsion between electrons. All other energy terms except for $T[\rho]$, V_c and V_H are combined in the last potential energy term V_{XC}, which describes all other contributions to $E[\rho]$, mostly related to electron exchange, correlation, relativistic effects, etc.

We may define an energy functional

$$G[\rho] = T[\rho] + V_{XC}, \tag{2.13}$$

leading to the expression

$$E[\rho] = V_c + V_H + G[\rho]. \tag{2.14}$$

All potential energy functionals may be represented by specific potentials. $V_c[\rho]$ can be written as

$$V_c[\rho] = \int \mathrm{d}\mathbf{r} v_c(\mathbf{r})\rho(\mathbf{r}).$$

The space integral describes the interaction of the electron with the potential $v_c(\mathbf{r})$ that is dominated by the Coulomb potential of the nuclei.

$V_H[\rho]$ is the Hartree energy that can be expressed as

$$V_H[\rho] = \frac{1}{2}\int \mathrm{d}\mathbf{r}\mathrm{d}\mathbf{r}'\rho(\mathbf{r})\frac{e^2}{|\mathbf{r}-\mathbf{r}'|}\rho(\mathbf{r}') = \int \mathrm{d}\mathbf{r}\rho(\mathbf{r})v_H.$$

where

$$v_H = \frac{1}{2}\int \mathrm{d}\mathbf{r}'\frac{e}{|\mathbf{r}-\mathbf{r}'|}\rho(\mathbf{r}').$$

Then, the total electrostatic potential in the system is given by

$$v(\mathbf{r}) = v_c(\mathbf{r}) + v_H(\mathbf{r}). \tag{2.15}$$

Similarly,

$$V_{XC}[\rho] = \int \mathrm{d}\mathbf{r}v_{XC}(\mathbf{r})\rho(\mathbf{r}),$$

where $v_{XC}[\rho]$ is the so-called exchange-correlation potential.

So, the total energy can be written as:

$$E[\rho] = \int \mathrm{d}\mathbf{r}v(\mathbf{r}) + G[\rho]. \tag{2.16}$$

Inserting Eq. (2.16) to Eq. (2.10), we can get

$$v(\mathbf{r}) + \delta G[\rho]/\delta\rho(\mathbf{r}) = \epsilon. \tag{2.17}$$

It is also not easy to solve the above equation. To solve this problem, Kohn and Sham mapped the real system of interacting electrons to a system of non-interacting quasielectrons with the same charge density. For the quasielectron system, they derived a set of single-particle Schrödinger equations. The self-consistent solution for the occupied states would provide the same charge density as found in the interacting many-electron system.

First let us consider a system of N non-interacting quasi-electrons, which move in a static external potential $v_{ext}(\mathbf{r})$. The kinetic energy of this noninteracting system is

$$T[\rho] =< \Psi| - \frac{\hbar^2}{2m}\nabla^2|\Psi > . \tag{2.18}$$

For this noninteracting system, instead of Eq. (2.17), we will get:

$$v_{ext}(\mathbf{r}) + \delta T[\rho]/\delta\rho(\mathbf{r}) = \epsilon. \tag{2.19}$$

If we know the form of $T[\rho]$, we can get the $\rho(\mathbf{r})$ for solving Eq. (2.19), however, we can find the charge density in an easier way.

Since it is a system of noninteracting fermions, the wave function will be the Slater determinant of single-particle wave functions ψ_i of the Schrödinger equation

$$[-\frac{\hbar^2}{2m}\nabla^2 + v_{ext}(\mathbf{r})]\psi_i(\mathbf{r}) = \epsilon_i\psi_i(\mathbf{r}). \tag{2.20}$$

The electron density is given by

$$\rho(\mathbf{r}) = \sum_i \psi_i^*(\mathbf{r})\psi_i(\mathbf{r}). \tag{2.21}$$

Comparing with Eq. (2.19), it is much easier to solve Eq. (2.21) self-consistently.

Now, let us go back to the interacting electron system. Using Eq. (2.13), Eq. (2.17) can be reformulated as

$$v(\mathbf{r}) + \delta V_{XC}[\rho]/\delta\rho(\mathbf{r}) + \delta T[\rho]/\delta\rho(\mathbf{r}) = v(\mathbf{r}) + v_{XC}(\mathbf{r}) + \delta T[\rho]/\delta\rho(\mathbf{r}) = \epsilon. \tag{2.22}$$

Next, we define the effective potential $v_{eff}(\mathbf{r})$,

$$v_{eff}(\mathbf{r}) = v(\mathbf{r}) + v_{XC}(\mathbf{r}). \tag{2.23}$$

Then, Eq. (2.22) can be written as

$$v_{eff}(\mathbf{r}) + \delta T[\rho]/\delta\rho(\mathbf{r}) = \epsilon, \tag{2.24}$$

which is similar to Eq. (2.19) by relating $v_{ext}(\mathbf{r})$ to $v_{eff}(\mathbf{r})$. As a result, Eq. (2.20) becomes the so-called Kohn-Sham equation

$$[-\frac{\hbar^2}{2m}\nabla^2 + v_{eff}(\mathbf{r})]\psi_i(\mathbf{r}) = \epsilon_i\psi_i(\mathbf{r}). \tag{2.25}$$

The charge density is then given by

$$\rho(\mathbf{r}) = \sum_{occ} \psi_i^*(\mathbf{r})\psi_i(\mathbf{r}). \tag{2.26}$$

Equations (2.25) and (2.26) are solved self-consistently to obtain the correct charge density $\rho(\mathbf{r})$ in the ground state. Once $\rho(\mathbf{r})$ is established, the total energy of the many-electron system is obtained using Eq. (2.11) and the proper expressions for the potential energy functional $V_s[\rho]$.

2.4 Exchange-correlation functionals

As mentioned above, the properties of the system is the functional of electron density $\rho(\mathbf{r})$, also the exchange-correlation energy does. One frequently uses the Local Density Approximation (LDA) [7,8] which works especially very well for carbon systems. This approximation depends only on the value of the electron density, not on the derivatives of the density. Within this approximation, the exchange-correlation is:

$$V_{XC}^{LDA}[\rho] = \int \mathrm{d}\mathbf{r}\rho(\mathbf{r})v_{xc}(\rho). \tag{2.27}$$

where ρ is the electron density and $v_{xc}(\rho) = v_x(\rho) + v_c(\rho)$ is the exchange and correlation potential per particle in a homogeneous electron gas.

For the homogenous electron gas, the exchange energy is:

$$v_x(\rho) = -\frac{3}{4}\left(\frac{3}{\pi}\right)^{\frac{1}{3}} \rho(\mathbf{r})^{\frac{1}{3}}. \tag{2.28}$$

The precise value of the correlation energy v_c has been established by Quantum Monte Carlo calculations [8] for a homogenous electron gas with different electron densities.

LDA is based on the homogenous electron gas, in which the electron density is the same. In the more common case, the electron density is not constant. LDA works well for systems, where the electron density does not change dramatically in space. It may not be correct in systems with a strongly varying electron density. For solving this problem, other approximations for V_{xc} have been introduced that consider charge density gradients. They are usually called the Generalized Gradient Approximation (GGA). In GGA, the exchange-correlation energy can be written as

$$V_{xc}^{GGA}[\rho] = \int \mathrm{d}\mathbf{r} f(\rho(\mathbf{r}), \nabla\rho(\mathbf{r})). \tag{2.29}$$

There are different functions $f(\rho, \nabla\rho)$ for different systems. Currently, most commonly used is the PBE [9] functional proposed by Perdew, Burke and Ernzerhof in 1996.

LDA and GGA can give the information of structure and energy, but none of them can describe the long distance interaction, like van der Waals (VDW), very well. In layered systems, the interlayer interaction is important, which will be overestimated by LDA and underestimated by GGA-PBE. Various corrections have been applied for layered systems, like the DFT-D2 [10] and optB86b-vdW [11, 12] functionals.

2.5 Basis sets and pseudopotentials

In quantum mechanics, a basis set $\{\chi_\nu(\mathbf{r})\}$ is needed to solve the Kohn-Sham equations Eqs. (2.25) and (2.26). The single quasi-electron wave function $\psi_i(\mathbf{r})$ can be represented by the basis functions:

$$\psi_i(\mathbf{r}) = \sum_\nu c_{\nu i}\chi_\nu(\mathbf{r}). \tag{2.30}$$

Here $c_{\nu i}$ are expansion coefficients.

Usually there are two methods used to construct the basis. One is using the linear combination of atomic orbitals to build the molecular orbitals in quantum chemistry; this method is so-called LCAO-MO approximation. Such basis of atomic orbitals is used in DFT implemented in the SIESTA code [13]. The other basis, more proper for infinite systems, is the plane wave basis which is used in DFT implemented in VASP code [14–17].

In DFT, there is also a approximation about the atomic potential, since most of the properties of the system are determined by the valence electrons. The effect of the nucleus and core electrons on the valence electrons are reproduced by a pseudopotential which replace the atomic all-electron potential. With pseudopotential, the wave function of valence electrons have significantly fewer nodes, which result in the reducing of the computational effort. In this thesis, norm-conserving pseudopotentials are used in the SIESTA code and projector augmented wave (PAW) pseudopotentials [17, 18] are used in the VASP code.

Chapter 3

Continuum approach for long-wavelength acoustic phonons in quasi-2D structures

The following discussion is my original contribution to the related publication by Dan Liu, Arthur G. Every, and David Tománek, Phys. Rev. B **94**, 165432 (2016) [19].

3.1 Introduction

Since graphene has become one of the hottest research topic in recent years, interest in quasi-2D materials has been rising steadily. Phonon spectra are one of the important characteristics. State-of-the-art atomistic calculations of phonon frequencies based on *ab initio* Density Functional Theory (DFT) start with the calculation of the Hessian (or force-constant) matrix using energy differences associated with finite displacements of all atoms in the unit cell. The eigenvalues of the dynamical matrix constructed from the Hessian matrix. This gives phonon frequencies. This approach works very well for all phonons except for long-wavelength acoustic modes in quasi-2D systems. There, all practical implementations require the use of very large supercells, dense k-meshes, and a highly converged basis to obtain a sufficiently ac-

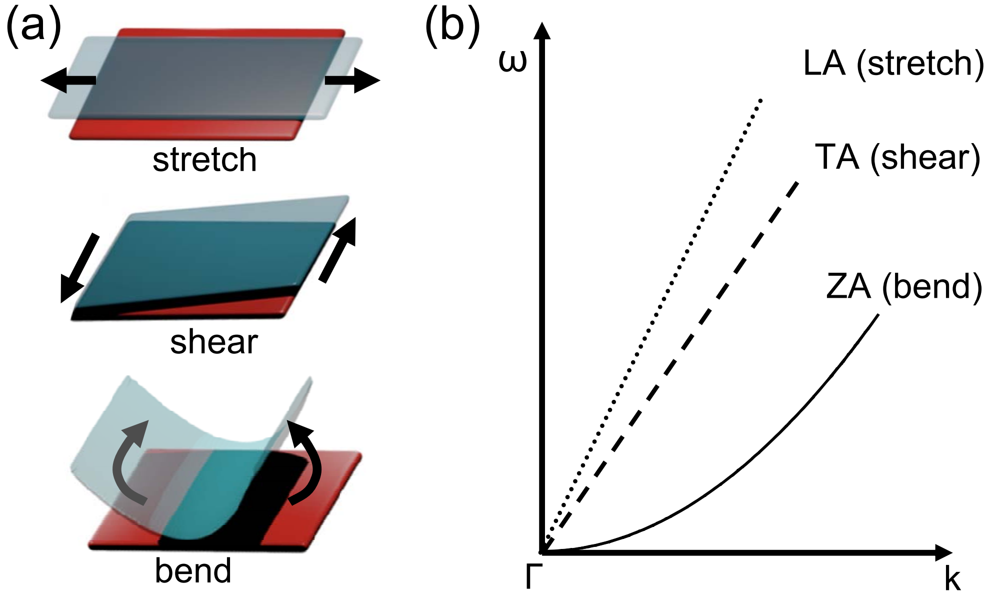

Figure 3.1: (a) Schematic representation of possible distortions of an elastic membrane. (b) Schematic dependence of the longitudinal acoustic (LA), in-plane transverse acoustic (TA) and the flexural acoustic (ZA) mode vibration frequencies on the crystal momentum near the center of the Brillouin zone.

curate dynamical matrix. Even small inaccuracies caused by computer resource limitations commonly lead to imaginary frequencies in long-wavelength flexural ZA modes [20,21]. This artifact does not mean the structure is instable, but relates to the way the dynamical matrix is constructed and diagonalized. Even though this shortcoming does not affect other modes much, its unphysical consequences will affect the subsequent calculation. So far, no practicable, predictive and accurate alternative approach has been proposed to determine the frequency of long-wavelength ZA modes, which – among others – play an important role in thermal conductivity of graphene nanoribbons [22].

In order to address the long-standing problem with the computation of long-wavelength flexural ZA modes in atomically thin layers, I propose a quantitatively predictive and physically intuitive approach based on continuum elasticity theory. I use a (3×3) elastic matrix as well as the flexural rigidity D to describe elastic behavior of a layer, independent of its thickness, by a membrane. In the thesis, I present simple quantitative expressions for frequencies of long-wavelength acoustic ZA and also for the longitudinal acoustic (LA) and transverse acoustic (TA) modes, which I determine using 2D elastic constants calculated by *ab initio* Density Functional Theory. The calculated spectra accurately reproduce observed and calculated long-wavelength phonon spectra of graphene and monolayer of black phosphorus. This approach also describes the observed dependence of the radial breathing mode frequency on the diameter of carbon fullerenes and nanotubes very well.

Using continuum elasticity theory to determine the frequencies of long-wavelength acoustic phonons is well established [23], including its extension to plates of finite thickness [24,25]. Elastic constants have also been related to specific phonon modes in graphene [26–29]. Independent of thickness, any plate can be mapped onto a 2D elastic membrane. Here, I introduce a (3×3) elastic stiffness matrix for 2D membranes which relate to the commonly used (6×6) elastic matrix for 3D systems. I then derive simple expressions for long-wavelength acoustic phonon frequencies in these structures based on the 2D elastic constants and flexural rigidity D, which determined using static DFT calculations for the deformation energy of unit cells with few atoms. The quadratic frequency dependence on the crystal momentum for ZA and the linear dependence for LA and TA modes is quantitatively reproduced near the Brillouin zone center using these 2D elastic constants and D. Clearly, this approach is limited to long-wavelength acoustic modes. For the full phonon spectrum, these results can be combined with those of atomistic DFT calculations, which do not have the convergence problem for optical and short-wavelength acoustic modes.

3.2 Continuum approach for long-wavelength acoustic modes of an elastic membrane

Independent of the thickness, a free-standing thin slab of any substance can be mapped onto an elastic membrane that resists deformations, as illustrated in Fig. 3.1(a). Within the harmonic region, a (3×3) 2D elastic stiffness matrix describe the elastic response of this two-dimensional system,which lie in the $x-y$ plane, the matrix is given in Voigt notation by

$$\begin{pmatrix} c_{11} & c_{12} & 0 \\ c_{12} & c_{22} & 0 \\ 0 & 0 & c_{66} \end{pmatrix} . \tag{3.1}$$

c_{11} and c_{22} describe the longitudinal strain-stress relationship along the $x-$ and $y-$direction, respectively. c_{66} describes the elastic response to in-plane shear. In an elastic isotropic plate, $c_{11} = c_{22}$, $c_{66} = (c_{11} - c_{12})/2$, and the Poisson ratio $\alpha = c_{12}/c_{11}$. In a 2D plate represented by a membrane, the dimension of the elastic stiffness constants c_{ij} is (N/m).

The individual coefficients c_{ij} are obtained by subjecting the equilibrium 2D structure to particular distortions in the harmonic regime, typically $\sigma < 1\%$. For c_{11} as an example, a unit square of the system would be stretched and compressed along the same direction. The energies of the compressed and the stretched structure should be equal in the harmonic regime and higher than that of the equilibrium structure. Three points of $E(\sigma)$ define a parabola and its curvature is the particular elastic constant, which is c_{11} in our example.

The elastic response of the corresponding 3D system consisting of weakly interacting layers separated by interlayer spacing d_{il} is described in Voigt notation by a (6×6) C_{ij}

matrix of elastic stiffness constants with the dimension (N/m^2). The relation between the two elastic matrices is given by $c_{ij} = d_{il} \cdot C_{ij}$.

The flexural response to out-of-plane stress is described by the flexural rigidity D of the plate, which may be anisotropic. D can be calculated by considering the energy cost associated with rolling up a rectangle of length L to a tube with diameter d. Assuming that L and d are large enough to ignore edge effects, I obtain

$$D = \frac{1}{2}\epsilon_b d^2 \,, \tag{3.2}$$

where ϵ_b is the bending strain energy divided by the surface area of the tube, which is close to the area of the initial rectangle.

3.3 Calculation of acoustic phonon modes of an elastic membrane in the continuum limit

Near the of the Brillouin zone center, it is well established that the frequency of LA and TA show a linear dependence on the crystal momentum k, whereas the ZA mode frequency increases as k^2, as seen in Fig. 3.1(b). As shown in the Related Information section, the frequencies of the three acoustic modes of an elastic membrane can be determined quantitatively using only the elastic constants c_{11}, c_{22}, c_{66} and D. These elastic constants can be either calculated or obtained experimentally. Also needed is the 2D mass density ρ_{2D}, which is easily determined using the atomic mass numbers and the area of the optimized unit cell.

For acoustic modes with linear dispersion, I get

$$\omega_{LA,1} = \sqrt{\frac{c_{11}}{\rho_{2D}}}\, k \tag{3.3}$$

for the longitudinal acoustic (LA) mode along the $x-$direction, with the value of the square root giving the longitudinal speed of sound in the $x-$direction. Similarly, I get

$$\omega_{LA,2} = \sqrt{\frac{c_{22}}{\rho_{2D}}}\, k \tag{3.4}$$

for the LA mode along the $y-$direction, with the value of the square root giving the longitudinal speed of sound in the $y-$direction. Finally, I get

$$\omega_{TA} = \sqrt{\frac{c_{66}}{\rho_{2D}}}\, k \tag{3.5}$$

for the in-plane transverse acoustic (TA) modes in the $x-$ and $y-$ directions, with the value of the square root giving the transverse speed of sound in those directions. In anisotropic plates, acoustic modes in an arbitrary in-plane direction have mixed LA and TA character, and their speed varies in a complicated way with the direction [24].

As shown in the Related Information section, the flexural ZA mode displays an unusual quadratic frequency dependence on the crystal momentum. Its frequency is given by

$$\omega_{ZA} = \sqrt{\frac{D}{\rho_{2D}}}\, k^2\,, \tag{3.6}$$

where the value of the flexural rigidity D depends on the bending direction in an anisotropic material.

The schematic dependence of the acoustic mode frequencies ω of a zero-thickness plate on the crystal momentum $\mathbf{k}$, given by Eqs. (3.3)-(3.6), is shown in Fig. 3.1(b). I note that these expressions, albeit not in the notation of the 2D elastic matrix, have been obtained previously [29–31].

Expressions describing the deformation of an elastic membrane can also be used the determine the frequency of the radial breathing mode (RBM). Previously derived theoretical expressions [32] and experimental observations are being used commonly as an indirect way to determine the diameter of carbon fullerenes and nanotubes [4].

As shown in the Related Information section, I obtain

$$\omega_{C_n} = \frac{2}{d}\sqrt{\frac{2c_{11}}{\rho_{2D}}}\,, \tag{3.7}$$

for the RBM frequency of a spherical C_n fullerene with diameter d. Similarly, the RBM frequency of a carbon nanotube (CNT) of radius d is given by

$$\omega_{CNT} = \frac{2}{d}\sqrt{\frac{c_{11}}{\rho_{2D}}}\,. \tag{3.8}$$

3.4 Computational approach to determine the elastic constants

I determine the elastic response of atomically thin graphene and phosphorene monolayers using *ab initio* density functional theory (DFT) as implemented in the SIESTA [13] code. I used the Perdew-Burke-Ernzerhof (PBE) [9] exchange-correlation functional, norm-conserving Troullier-Martins pseudopotentials [33], and a double-ζ basis including polarization orbitals. To determine the energy cost associated with in-plane distortions, I sampled the Brillouin zone of a 3D superlattice of non-interacting layers by a 20×20×1 k-point grid [34]. To determine the strain energy associated with flexural motion, I constructed and optimized single-wall nanotubes and sampled their 3D superlattice by a 20×1×1 k-point grid. I used a mesh cutoff energy of 180 Ry and an energy shift of 10 meV in the self-consistent total energy calculations, which has provided us with a precision in the total energy of $\leq$2 meV/atom.

3.5 Results

3.5.1 Graphene

Graphene is known to display isotropic elastic behavior. The DFT calculations yield the (3×3) 2D elastic stiffness matrix of Eq. (3.1)

$$\begin{pmatrix} c_{11} & c_{12} & 0 \\ c_{12} & c_{22} & 0 \\ 0 & 0 & c_{66} \end{pmatrix} = \begin{pmatrix} 352.6 & 59.6 & 0 \\ 59.6 & 352.6 & 0 \\ 0 & 0 & 146.5 \end{pmatrix} N/m\,. \tag{3.9}$$

These values are in very good agreement with experimental and other theoretical results [35], including the value of the Poisson ratio $\alpha = c_{12}/c_{11} = 0.17$, which is very close to the observed value of 0.19 based on HREELS [36].

The calculated 2D mass density of graphene is $\rho_{2D} = 0.743 \cdot 10^{-6}$ kg/m^2 and the calculated value of the flexural rigidity $D = 1.40$ eV$=$ 0.224 GPa·nm^3 lies close to the previously estimated value [29] $D \approx 1.0$ eV. Using the numerical values listed in Eq. (3.9) and the above value of D, I can determine the three acoustic branches of graphene near the Γ point using

Eqs. (3.3)-(3.6). The results are presented in Fig. 3.2(a), superposed to those of a more recent *ab initio* calculation [1] that agrees very well with with the observed and fitted phonon spectrum of graphene [37].

First of all, I notice an excellent agreement with the linear LA and TA modes, which indicate that the calculated speed of sound agrees with the observation. Specifically, the calculated speed of sound with in-plane longitudinal polarization, $v_{LA,th} = 22.1$ km/s, agrees very well with the observed value $v_{LA,expt} = 22.0$ km/s obtained using HREELS [36]. Similarly, the speed of sound with in-plane transverse polarization, $v_{TA,th} = 14.2$ km/s, agrees very well with the observed value [36] of $v_{TA,expt} = 14.0$ km/s.

Agreement between calculated and observed ZA modes indicates that the calculated flexural rigidity value correctly reproduces the elastic response of graphene to bending.

3.5.2 Phosphorene

Unlike graphene, phosphorene is strongly anisotropic. It is much softer under compression along the $x-$ (or $\mathbf{a_1}-$) direction than along the $y-$ (or $\mathbf{a_2}-$) direction. The optimized rectangular unit cell is defined by $a_1 = 4.63$ Å and $a_2 = 3.35$ Å according to the DFT studies. With 4 atoms per unit cell, the 2D mass density of phosphorene is $\rho_{2D} = 1.34 \cdot 10^{-6}$ kg/m^2. The numerical values $c_{11} = 24.4$ N/m and $c_{22} = 94.6$ N/m reflect the strong anisotropy in the in-plane longitudinal elastic response. The calculated speed of sound with LA polarization is $v_{LA_X,th} = 4.3$ km/s along the soft $\Gamma - X$ direction and $v_{LA_Y,th} = 8.4$ km/s along the stiff $\Gamma - Y$ direction.

The transverse acoustic phonon frequency depends on the in-plane shear and is described by the calculated value $c_{66} = 22.1$ N/m. The corresponding speed of sound with TA polarization is $v_{TA,th} = 4.1$ km/s.

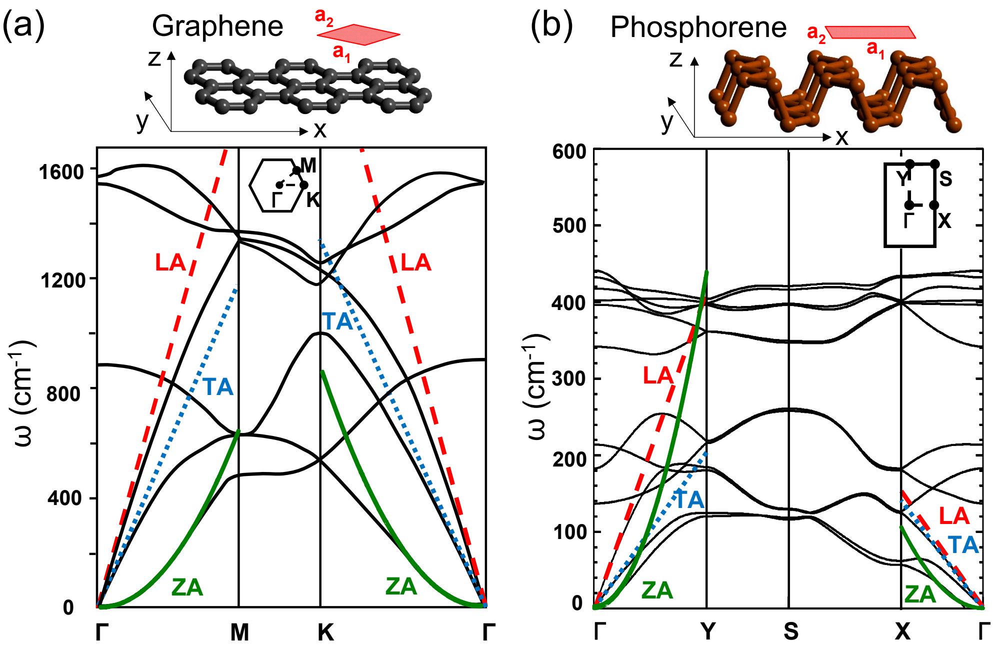

Figure 3.2: Phonon spectra of (a) graphene, reproduced from Reference [1] and (b) phosphorene, a monolayer of black phosphorus, reproduced from Reference [2], shown by solid lines. Superposed to the spectra are continuum results for the three acoustic phonon modes in different high-symmetry directions, evaluated near Γ, with the longitudinal acoustic (LA, dashed lines), in-plane transverse acoustic (TA, dotted lines), and the flexural acoustic (ZA, solid lines) modes. Ball-and-stick models of the structure, including the primitive unit cells, are shown in the top panels. The Brillouin zones are shown as insets in the phonon spectra.

Finally, I find also the flexural rigidity to be highly anisotropic. I find $D(\Gamma - X) = 1.55$ eV= 0.248 GPa·nm^3 when bending phosphorene along the $x-$ (or $\mathbf{a_1}-$) direction, yielding a tube with its axis aligned along the $y-$ (or $\mathbf{a_2}-$) direction. Bending along the $y-$ (or $\mathbf{a_2}-$) direction, I find $D(\Gamma - Y) = 7.36$ eV= 1.179 GPa·nm^3.

These data are sufficient to reproduce the three acoustic branches of phosphorene along the $\Gamma - X$ and $\Gamma - Y$ direction near Γ using Eqs. (3.3)-(3.6) and are presented in Fig. 3.2(b). In analogy to graphene, the results are superposed to phonon spectra , which – in absence of experimental phonon spectra – are based on atomistic DFT calculations of phosphorene [2]. I notice a particularly good agreement between the two approaches along the stiff $\Gamma - Y$ direction. As I expand in the Discussion, the continuum results deviate from those of the

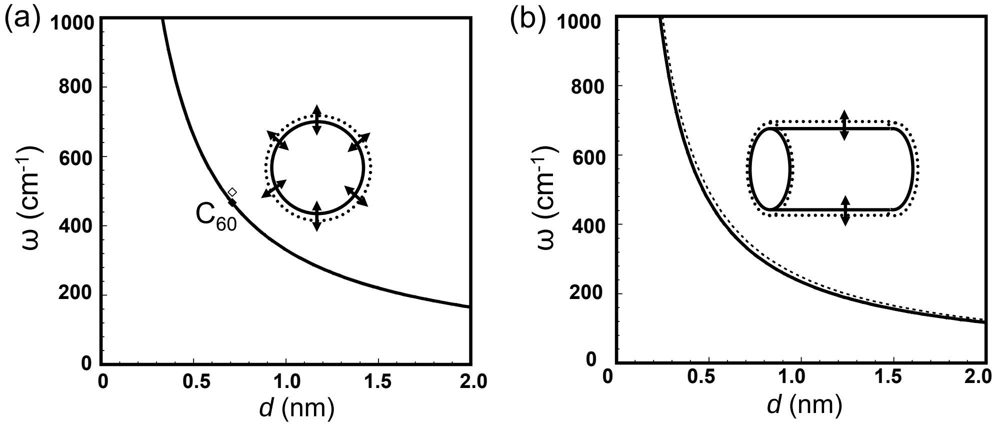

Figure 3.3: Radial breathing mode (RBM) in (a) fullerenes and (b) carbon nanotubes as a function of their diameter d. The prediction is shown by the solid line. Experimental and theoretical RBM frequencies for the only observed fullerene with spherical symmetry, C$_{60}$, are shown by the data points in (a). The experimentally well-established relationship [3,4] $\omega = 248$ cm$^{-1}\times(1$ nm$/d)$ in nanotubes in (b) is represented by the dashed line and the calculation is shown by the solid line.

atomistic study along the soft $\Gamma - X$ direction, which – at close inspection – predicts small imaginary ZA frequencies near Γ.

3.5.3 Vibration spectra of carbon fullerenes and nanotubes

The radial breathing mode (RBM) frequency ω_{RBM} of C$_n$ fullerenes may be calculated using Eq. (3.7) and that of carbon nanotubes using Eq. (3.8), in combination with the elastic constants provided in the section on graphene. The expected dependence of ω_{RBM} on the diameter d is displayed in Fig. 3.3(a) for fullerenes and in Fig. 3.3(b) for carbon nanotubes (CNTs). The RBM mode is Raman active and its frequency is known to depend primarily on the diameter. Thus, the RBM frequency is commonly used to judge the diameter of carbon nanostructures.

According to Eq. (3.7), the RBM frequency of spherical fullerenes should scale inversely with their diameter. But only one spherical fullerene, namely C$_{60}$ with $d = 7.1$ Å, forms a molecular solid. I find the predicted value $\omega_{RBM,th}(\mathrm{C}_{60}) = 467\ \mathrm{cm}^{-1}$ to lie very close to the observed RBM frequency $\omega_{RBM,expt}(\mathrm{C}_{60}) = 497\ \mathrm{cm}^{-1}$.

The well-documented observed diameter dependence of the RBM in nanotubes [4], $\omega_{RBM,expt}(\mathrm{CNT}) = 248\ \mathrm{cm}^{-1}\times(1\ \mathrm{nm}/d)$, is reproduced by the dashed line in Fig. 3.3(b). Based on continuum theory and Eq. (3.8), I find $\omega_{RBM,th}(\mathrm{CNT}) = 234\ \mathrm{cm}^{-1}\times(1\ \mathrm{nm}/d)$ in very good agreement with the observed behavior.

3.6 Discussion

So far, the most common description of a layer by continuum elasticity theory has been that of a finite-thickness plate consisting of a material characterized by a (6×6) elastic stiffness matrix. As I show here, this approach is unnecessarily cumbersome, since every 2D system of finite thickness may be mapped onto an elastic membrane with the same mass density. The resistance of the realistic system, such as graphene or phosphorene, to stretching, shear and bending becomes that of the elastic membrane. The advantage of this approach, which does not suffer from ambiguities about the "real" thickness of an atomic layer, has been discussed before [26, 27]. The unconventional units of the 2D elastic stiffness matrix in Eq. (3.1) are well adapted to ultra-thin layers.

The approach appears particularly suitable when describing the ZA mode in soft, atomically thin atomic layers such as phosphorene. As mentioned earlier during the discussion of Fig. 3.2(b), the required precision of the dynamical matrix has not been reached in the calculation of phonon modes near *Gamma* along the $\Gamma - X$ direction [2]. This is a common shortcoming of *ab initio* phonon calculations in layered solids. Among the eigenvalues of the dynamical matrix, which are proportional to ω^2, the one associated with the ZA mode often turns out to be negative, yielding nominally an imaginary frequency, as a numerical artifact. The small error in the ZA frequency eigenvalue is also reflected in other close-lying eigenvalues, such as those of the LA and TA modes, at the same crystal momentum. This is clearly reflected in Fig. 3.2(b). I believe that the present continuum approach is much better adapted to describe long-wavelength acoustic modes and should be preferred to atomistic phonon calculations near Γ.

As seen in Fig. 3.2(b), the LA and TA mode frequencies are very similar along the soft $\Gamma - X$ direction in phosphorene. This is unusual, but not unexpected in view of the accordion-like structure depicted in the ball-and-stick model in the top panel of Fig. 3.2(b). Making an analogy to a real accordion, it appears equally easy to produce a longitudinal and a transversal motion while the instrument is being played. Since the TA speed of sound is the same along the $\Gamma - X$ and the $\Gamma - Y$, the TA mode is clearly distinguished in its softness from the LA mode along the hard $\Gamma - Y$ direction. In this rigid direction in space, small imprecisions in the dynamical matrix play a much less important role than along the soft direction. Therefore, the continuum results agree well with the phonon frequencies obtained using the atomistic approach for all three acoustic branches.

In the Section on the radial breathing motion of carbon nanostructures, I have shown in Eq. (3.61) that the RBM frequency of nanotubes does not show a pure $1/d$ behavior as a function of the nanotube diameter. For single-wall carbon nanotubes with typical diameters between $1 - 2$ nm, the value of the correction $4D/(c_{11}d^2)$ is indeed negligibly small in comparison to 1. This need not be the case in nanotubes of other substances with large values of D and small values of c_{11}. In postulated phosphorene nanotubes [38], c_{11} differs significantly from c_{22}, and D is strongly anisotropic.

Finally, I have shown in Eq. (3.2) how to estimate the value of D in a layered material by calculating the strain energy in nanotubes with a very large diameter d. Optimizing wide nanotubes using *ab initio* techniques is non-trivial. The values for D quoted in the Section on phosphorene required DFT calculations containing more than 14 unit cells along the perimeter of phosphorene nanotubes bent along the soft $x-$ (or $\mathbf{a_1}-$) direction. For nanotubes bent along the rigid $y-$ (or $\mathbf{a_2}-$) direction, $D(d{\rightarrow}\infty$ was extrapolated using 10, 12, 14, 16 and 18 unit cells along the perimeter of the corresponding phosphorene nanotubes.

3.7 Summary and Conclusions

In conclusion, as a viable alternative to atomistic calculations of long-wavelength acoustic modes of atomically thin layers, which are known to converge very slowly, I have proposed a quantitatively predictive and physically intuitive approach based on continuum elasticity theory. I describe a layer, independent of its thickness, by a membrane, and characterize its elastic behavior by a (3×3) elastic matrix as well as the flexural rigidity D. I have derived simple quantitative expressions for frequencies of long-wavelength acoustic ZA and – for the sake of completeness – also for the longitudinal acoustic (LA) and transverse acoustic (TA) modes. These frequencies are determined using 2D elastic constants obtained from *ab initio* DFT calculations for the deformation energy of unit cells with few atoms. I found that the calculated spectra accurately reproduce observed and calculated long-wavelength phonon spectra of graphene and phosphorene, the monolayer of black phosphorus. The approach also correctly describes the observed dependence of the radial breathing mode frequency on the diameter of carbon fullerenes such as C_{60} and carbon nanotubes.

3.8 Related Information

The most fundamental way to determine vibration motion in any system starts with a Lagrangian, from which the Euler-Lagrange equations of motion can be derived by applying Hamilton's principle of least action. In the following, I determine the Lagrangians that describe stretching, shearing and bending of an infinitely thin elastic plate. Using these Lagrange functions, I derive the equations of stretching, shearing and bending motion of the plate. Finally, I derive the Lagrangian describing the radial breathing motion of carbon fullerenes and nanotubes and determine the corresponding equations of motion for the RBM in these nanostructures.

3.8.1 Lagrange function of an infinitely thin elastic plate under strain

3.8.1.1 Stretching

Let us consider a thin plate suspended in the $xy-$plane and its response to in-plane tensile strain applied uniformly along the $x-$direction,

$$\frac{du_x}{dx} = \text{const.} \tag{3.10}$$

The resulting energy density caused by tensile strain along the $x-$direction is then given by

$$U = \frac{1}{2}c_{11}\left(\frac{du_x}{dx}\right)^2 , \tag{3.11}$$

where c_{11} describes the elastic stiffness to tensile strain. In the harmonic regime, I will consider only small strain values. Releasing the strain will cause a vibration in the x-direction with the velocity $v_x = du_x/dt$. Then, the kinetic energy density will be given by

$$T = \frac{1}{2}\rho_{2D}\left(\frac{du_x}{dt}\right)^2 , \tag{3.12}$$

where ρ_{2D} is the 2D mass density. The Lagrangian density is then given by

$$\mathcal{L}\left(\frac{du_x}{dx}, \frac{du_x}{dt}, x, t\right) = T - U = \frac{1}{2}\left[\rho_{2D}\left(\frac{du_x}{dt}\right)^2 - c_{11}\left(\frac{du_x}{dx}\right)^2\right] . \tag{3.13}$$

In an anisotropic plate, the $x-$ and $y-$directions are not equivalent. To describe the $y-$response to in-plane tensile strain applied uniformly along the $y-$direction, I have to replace x by y and c_{11} by c_{22} in Eqs. (A1)-(A4), yielding the Lagrangian density

$$\mathcal{L}\left(\frac{du_y}{dy}, \frac{du_y}{dt}, y, t\right) = T - U = \frac{1}{2}\left[\rho_{2D}\left(\frac{du_y}{dt}\right)^2 - c_{22}\left(\frac{du_y}{dy}\right)^2\right] . \tag{3.14}$$

3.8.1.2 Shearing

The derivation of the Euler-Lagrange equation for the shear motion is very similar to that for the stretching motion. The main difference is that the displacement u is normal to the propagation direction. To obtain the corresponding equations, I need to replace u_x by u_y and c_{11} by c_{66} in Eqs. (A1)-(A4). The Lagrangian density is then given by

$$\mathcal{L}\left(\frac{du_y}{dx}, \frac{du_y}{dt}, x, t\right) = T - U = \frac{1}{2}\left[\rho_{2D}\left(\frac{du_y}{dt}\right)^2 - c_{66}\left(\frac{du_y}{dx}\right)^2\right] . \tag{3.15}$$

3.8.1.3 Bending

Bending a thin plate suspended in the xy-plane plane in order to to achieve a radius of curvature R requires displacements $u_z(x)$ along the normal z-direction that are described by

$$\frac{d^2u_z}{dx^2} = \frac{1}{R}\,. \tag{3.16}$$

The resulting bending energy density is then given by

$$U = \frac{1}{2}D\left(\frac{d^2u_z}{dx^2}\right)^2\,, \tag{3.17}$$

where D is the flexural rigidity. In the harmonic regime, I will consider only small strain values corresponding to $R{\rightarrow}\infty$. Releasing the strain will cause a vibration in the z-direction with the velocity $v_z = du_z/dt$. Then, the kinetic energy density will be given by

$$T = \frac{1}{2}\rho_{2D}\left(\frac{du_z}{dt}\right)^2\,, \tag{3.18}$$

where ρ_{2D} is the 2D mass density. This leads to the Lagrangian density

$$\mathcal{L}\left(\frac{d^2u_z}{dx^2}, \frac{du_z}{dt}, x, t\right) = T - U = \frac{1}{2}\left[\rho_{2D}\left(\frac{du_z}{dt}\right)^2 - D\left(\frac{d^2u_z}{dx^2}\right)^2\right]\,. \tag{3.19}$$

3.8.2 Derivation of Euler-Lagrange equations of motion for deformations of an infinitely thin elastic plate using Hamilton's principle

3.8.2.1 Stretching

The Lagrangian specified in Eq. (3.13) has the form $\mathcal{L}(du_x/dx, du_x/dt, x, t)$. In this case, I have two independent variables, x and t, and can define the action S by

$$S = \int_{t_1}^{t_2} dt \int_{x_1}^{x_2} dx \mathcal{L}(\frac{du_x}{dx}, \frac{du_x}{dt}, x, t) \,. \tag{3.20}$$

Hamilton's principle of least action yields

$$\delta S = \delta \int_{t_1}^{t_2} dt \int_{x_1}^{x_2} dx \mathcal{L}(\frac{du_x}{dx}, \frac{du_x}{dt}, x, t) = 0 \,. \tag{3.21}$$

This can be modified to

$$\delta S = \int_{t_1}^{t_2} dt \int_{x_1}^{x_2} dx [\mathcal{L}(\frac{du_x}{dx} + \delta\frac{du_x}{dx}, \frac{du_x}{dt} + \delta\frac{du_x}{dt}, x, t) - \mathcal{L}(\frac{du_x}{dx}, \frac{du_x}{dt}, x, t)] \,. \tag{3.22}$$

and

$$\delta S = \int_{t_1}^{t_2} dt \int_{x_1}^{x_2} dx \, \left[\frac{\partial \mathcal{L}}{\partial \frac{du_x}{dx}} \delta\frac{du_x}{dx} + \frac{\partial \mathcal{L}}{\partial \frac{du_x}{dt}} \delta\frac{du_x}{dt}\right] \,. \tag{3.23}$$

This expression can be reformulated to

$$\delta S = \int_{t_1}^{t_2} dt \int_{x_1}^{x_2} dx \left[\frac{d}{dt}\left(\frac{\partial \mathcal{L}}{\partial \frac{du_x}{dt}}\right) + \frac{d}{dx}\left(\frac{\partial \mathcal{L}}{\partial \frac{du_x}{dx}}\right)\right] \delta u_x \,. \tag{3.24}$$

For δS to vanish, the quantity in the square brackets in Eq. (3.24) must vanish. This leads to the Euler-Lagrange equation

$$\frac{d}{dt}\left(\frac{\partial \mathcal{L}}{\partial \frac{du_x}{dt}}\right) + \frac{d}{dx}\left(\frac{\partial \mathcal{L}}{\partial \frac{du_x}{dx}}\right) = 0\,. \tag{3.25}$$

Inserting the Lagrangian of Eq. (3.13) in the Euler-Lagrange Eq. (3.25) yields the wave equation for longitudinal in-plane vibrations

$$\rho_{2D}\frac{d^2u_x}{dt^2} - c_{11}\frac{d^2u_x}{dx^2} = 0\,. \tag{3.26}$$

This wave equation can be solved using the ansatz

$$u_x = u_{x,0}e^{i(kx-\omega t)} \tag{3.27}$$

to yield

$$\rho_{2D}\omega^2 = c_{11}k^2\,. \tag{3.28}$$

This finally translates to the desired form

$$\omega = \sqrt{\frac{c_{11}}{\rho_{2D}}}k\,, \tag{3.29}$$

which is identical to Eq. (3.3).

In an anisotropic plate, I need to use the Lagrangian of Eq. (3.14) to describe motion along the $y-$direction and obtain

$$\omega = \sqrt{\frac{c_{22}}{\rho_{2D}}}k\,, \tag{3.30}$$

which is identical to Eq. (3.4).

3.8.2.2 Shearing

The Lagrangian $\mathcal{L}(du_y/dx, du_y/dt, x, t)$ in Eq. (3.15), which describes the shearing motion, has the same form as the Lagrangian in Eq. (3.13). To obtain the equations for shear motion from those for stretching motion, I need to replace u_x by u_y and c_{11} by c_{66} in Eqs. (3.20)-(3.29). Thus, the equation for shear motion becomes

$$\omega = \sqrt{\frac{c_{66}}{\rho_{2D}}}k\,, \tag{3.31}$$

which is identical to Eq. (3.5).

3.8.2.3 Bending

The Lagrangian specified in Eq. (3.19) has the unconventional form $\mathcal{L}(d^2u_z/dx^2, du_z/dt, x, t)$. In this case, I have two independent variables, namely x and t, and can define the action S by

$$S = \int_{t_1}^{t_2} dt \int_{x_1}^{x_2} dx\ \mathcal{L}(\frac{d^2u_z}{dx^2}, \frac{du_z}{dt}, x, t)\,. \tag{3.32}$$

Hamilton's principle of least action yields

$$\delta S = \delta \int_{t_1}^{t_2} dt \int_{x_1}^{x_2} dx\ \mathcal{L}(\frac{d^2u_z}{dx^2}, \frac{du_z}{dt}, x, t) = 0\,. \tag{3.33}$$

This can be modified to

$$\delta S = \int_{t_1}^{t_2} dt \int_{x_1}^{x_2} dx[\mathcal{L}(\frac{d^2u_z}{dx^2} + \delta\frac{d^2u_z}{dx^2}, \frac{du_z}{dt} + \delta\frac{du_z}{dt}, x, t) - \mathcal{L}(\frac{d^2u_z}{dx^2}, \frac{du_z}{dt}, x, t)]\,. \tag{3.34}$$

and

$$\delta S = \int_{t_1}^{t_2} dt \int_{x_1}^{x_2} dx \; \left[\frac{\partial \mathcal{L}}{\partial \frac{d^2 u_z}{dx^2}} \delta \frac{d^2 u_z}{dx^2} + \frac{\partial \mathcal{L}}{\partial \frac{du_z}{dt}} \delta \frac{du_z}{dt} \right] . \tag{3.35}$$

Finally, I can rewrite this expression as

$$\delta S = \int_{t_1}^{t_2} dt \int_{x_1}^{x_2} dx \left[\frac{d}{dt} \left(\frac{\partial \mathcal{L}}{\partial \frac{du_z}{dt}} \right) - \frac{d^2}{dx^2} \left(\frac{\partial \mathcal{L}}{\partial \frac{d^2 u_z}{dx^2}} \right) \right] \delta u_z \, . \tag{3.36}$$

For δS to vanish, the quantity in the square brackets in Eq. (3.36) must vanish. This leads to the Euler-Lagrange equation

$$\frac{d}{dt} \left(\frac{\partial \mathcal{L}}{\partial \frac{du_z}{dt}} \right) - \frac{d^2}{dx^2} \left(\frac{\partial \mathcal{L}}{\partial \frac{d^2 u_z}{dx^2}} \right) = 0 \, . \tag{3.37}$$

Inserting the Lagrangian of Eq. (3.19) for flexural motion in the Euler-Lagrange Eq. (3.37) yields the wave equation for flexural vibrations

$$\rho_{2D} \frac{d^2 u_z}{dt^2} + D \frac{d^4 u_z}{dx^4} = 0 \, . \tag{3.38}$$

This wave equation can be solved using the ansatz

$$u_z = u_{z,0} e^{i(kx - \omega t)} \tag{3.39}$$

to yield

$$\rho_{2D} \omega^2 = D k^4 \, . \tag{3.40}$$

This finally translates to the desired form

$$\omega = \sqrt{\frac{D}{\rho_{2D}} k^2} \,, \tag{3.41}$$

which is identical to Eq. (3.6).

3.8.3 Radial breathing mode of spherical fullerenes

Let us consider a spherical fullerene molecule with the equilibrium radius R, such as C_{20}, C_{60}, ... Except for the presence of 12 pentagons, the surface is covered by hexagonal carbon rings, so that the 2D mass density ρ_{2D} can be taken as that of graphene. Similarly, R can be estimated using the number of C atoms in the fullerene and the unit cell area in graphene. According to continuum elasticity theory, the total bending strain energy of any such spherical fullerene, independent of R, is given by [39]

$$U_b = 4\pi D(1+\alpha) \,, \tag{3.42}$$

where D is the flexural rigidity and α is the Poisson ratio of graphene. In other words, changing the radius of the fullerene by δR will not affect the total bending energy.

Allowing the equilibrium radius R of the fullerene to change by δR results, on the other hand, in a quadratic increase of the tensile strain energy

$$U_t = 2 \times \frac{1}{2} \left[4\pi R^2 c_{11} \right] \left(\frac{\delta R}{R} \right)^2 \,. \tag{3.43}$$

The (radial) kinetic energy of a radially expanding or contracting fullerene, shown schematically in the inset of Fig. 3.3(a), is given by

$$T = \frac{1}{2}\left[4\pi R^2 \rho_{2D}\right]\left(\frac{d}{dt}\delta R\right)^2 \tag{3.44}$$

and the Lagrangian by

$$\begin{aligned}
\mathcal{L} &= T - U = T - U_t \qquad (3.45)\\
&= \frac{1}{2}\left[4\pi R^2 \rho_{2D}\right]\left(\frac{d}{dt}\delta R\right)^2 - \left[4\pi R^2 c_{11}\right]\left(\frac{\delta R}{R}\right)^2 \\
&= 4\pi R^2\left[\frac{1}{2}\rho_{2D}\left(\frac{d}{dt}\delta R\right)^2 - c_{11}\left(\frac{\delta R}{R}\right)^2\right].
\end{aligned}$$

Hamilton's principle of least action

$$\frac{\partial \mathcal{L}}{\partial(\delta R)} - \frac{d}{dt}\left(\frac{\partial \mathcal{L}}{\partial(\frac{d}{dt}\delta R)}\right) = 0 \tag{3.46}$$

leads, with the Lagangian of Eq. (3.45), to the Euler-Lagrange equation

$$-c_{11}\frac{2\delta R}{R^2} = \rho_{2D}\frac{d^2}{dt^2}\delta R\,. \tag{3.47}$$

With the ansatz

$$\delta R = \delta R_0 \; e^{i\omega t} \tag{3.48}$$

I obtain

$$\omega = \frac{1}{R}\sqrt{\frac{2c_{11}}{\rho_{2D}}}\,, \tag{3.49}$$

which is identical to Eq. (3.7).

3.8.4 Radial breathing mode of carbon nanotubes

Let us now consider a carbon nanotube that has been rolled up from a rectangular graphene nanoribbon of width $2\pi R_0$, length L, and the 2D mass density ρ_{2D}. According to continuum elasticity theory, the total bending strain energy of any such nanotube is given by [39]

$$U_b = \frac{\pi D L}{R_0}\,, \tag{3.50}$$

where D is the flexural rigidity of graphene. Increasing the radius by the small amount δR, while still $\delta R/R_0 << 1$, changes the potential energy of the nanotube with respect to the value at R_0 by

$$\Delta U_b(\delta R) = \frac{\pi D L}{R_0}\left[-\frac{\delta R}{R_0} + \left(\frac{\delta R}{R_0}\right)^2\right]\,, \tag{3.51}$$

where higher than quadratic terms have been neglected in the Taylor expansion.

I consider the initial nanotube of radius R_0 to be free of tensile strain energy. In this case, the change in tensile strain energy associated with the radius increase by δR is

$$\Delta U_t(\delta R) = \frac{1}{2}\left[2\pi R_0 c_{11}\right] L \left(\frac{\delta R}{R_0}\right)^2\,. \tag{3.52}$$

The equilibrium value of δR can be obtained by minimizing $\Delta U_b + \Delta U_t$,

$$\frac{\partial(\Delta U_b + \Delta U_t)}{\partial(\delta R)} = 0\,. \tag{3.53}$$

This leads to

$$\delta R \approx \frac{D}{2c_{11}R_0} \tag{3.54}$$

and the equilibrium value of the nanotube radius becomes $R = R_0 + \delta R$

$$R = R_0 \left(1 + \frac{D}{2c_{11}R_0^2} \right) . \tag{3.55}$$

R is the radius, around which the RBM vibrations take place. I use the total potential energy U of the nanotube at the equilibrium radius R as the reference energy. Then, changing the equilibrium nanotube radius R by an arbitrarily small value δR increases the potential energy of the nanotube by

$$U = \frac{1}{2}[2\pi RL] \left(\frac{D}{R^4} + \frac{c_{11}}{R^2} \right) (\delta R)^2 . \tag{3.56}$$

The (radial) kinetic energy of a radially expanding or contracting nanotube, shown schematically in the inset of Fig. 3.3(b), is given by

$$T = \frac{1}{2} \left[2\pi R\rho_{2D}L\right] \left(\frac{d}{dt}\delta R \right)^2 . \tag{3.57}$$

The Lagrangian for this motion is

$$\mathcal{L} = T - U = [\pi R\rho_{2D}L] \left(\frac{d}{dt}\delta R \right)^2 - [\pi RL] \left(\frac{D}{R^4} + \frac{c_{11}}{R^2} \right) (\delta R)^2 . \tag{3.58}$$

Using Hamilton's principle of Eq. (3.46), I get the Euler-Lagrange equation

$$\rho_{2D}\frac{d^2(\delta R)}{dt^2} = -\left(\frac{D}{R^4} + \frac{c_{11}}{R^2} \right) \delta R . \tag{3.59}$$

Using the ansatz

$$\delta R = \delta R_0 \; e^{i\omega t} \tag{3.60}$$

and referring to the nanotube diameter $d = 2R$, I obtain

$$\omega = \frac{2}{d}\sqrt{\frac{c_{11}}{\rho_{2D}}\left(1 + \frac{D}{c_{11}R^2}\right)}\,. \tag{3.61}$$

For a nanotube with a typical diameter $d = 1$ nm, using the values of c_{11} and D for graphene, I find that the bending correction $4D/(c_{11}d^2)\approx 1\times 10^{-3}$ is negligibly small. In this case, I obtain

$$\omega = \frac{2}{d}\sqrt{\frac{c_{11}}{\rho_{2D}}}\,, \tag{3.62}$$

which is identical to Eq. (3.8).

Chapter 4

Long-wavelength deformations and vibrational modes in empty and liquid-filled microtubules and nanotubes: A theoretical study

The following discussion is my original contribution to the related publication by Dan Liu, Arthur G. Every, and David Tománek, Phys. Rev. B **95**, 165432 (2017) [40].

4.1 Introduction

There are plenty of tubular structures with diameters ranging from nanometers to meters in nature to fill various functions. Low-frequency flexural acoustic (ZA) modes dominate the elastic response of most tubular structures. Much attention has been paid on the nanometer-wide carbon nanotubes (CNTs) [41], which are extremely stiff [42], and on their flexural modes [42–45]. Correct description of soft flexural modes in stiff quasi-1D systems like nanotubes and nanowires is essential for calibrating nanoelectromechanical systems used for ultrasensitive mass detection and radio-frequency signal processing [43, 46]. In CNTs and in related graphene nanoribbons, flexural ZA modes have also been shown to significantly influence the unsurpassed lattice thermal conductivity [22]. Much softer microtubules formed of tubulin proteins, with a diameter $d{\approx}20$ nm, are key factors of the cytoskeleton and help to maintain the shape of cells in organisms. Although they are important, there are little experimental data available describing the elastic behavior of microtubules. The conventional approach to calculate the frequency spectrum is based on an atomistic calculation of the force-constant matrix. This approach often fails for long-wavelength acoustic modes, in particular the soft flexural ZA modes, due to an excessive demand on supercell size and basis convergence. Typical the failure of atomistic calculation will results in numerical artifacts such as imaginary vibration frequencies [47].

Like Chapter 3, in this chapter, I also offer an alternative way based on continuum elasticity theory [23] and its extension to planar [19] and tubular structures [48–50], to predict the frequency of acoustic modes in quasi-1D structures such as empty and liquid-filled tubes consisting of stiff graphitic carbon or soft tubulin proteins. While the approach works very well for long-wavelength acoustic modes, the accuracy of vibration frequencies calculated using the simple expressions I derive surpasses that of conventional atomistic *ab initio* calculations. The approach covers longitudinal and torsional modes, flexural modes, as well as the radial breathing mode. The longitudinal and flexural acoustic modes of tubules are simply related to those of an elastic beam resembling a nanowire. Since the native environment of tubulin nanotubes contains water, I specifically consider the effect of a liquid on the vibrational modes of tubular structures. The numerical results for tubulin microtubules and carbon nanotubes agree with available experimental data.

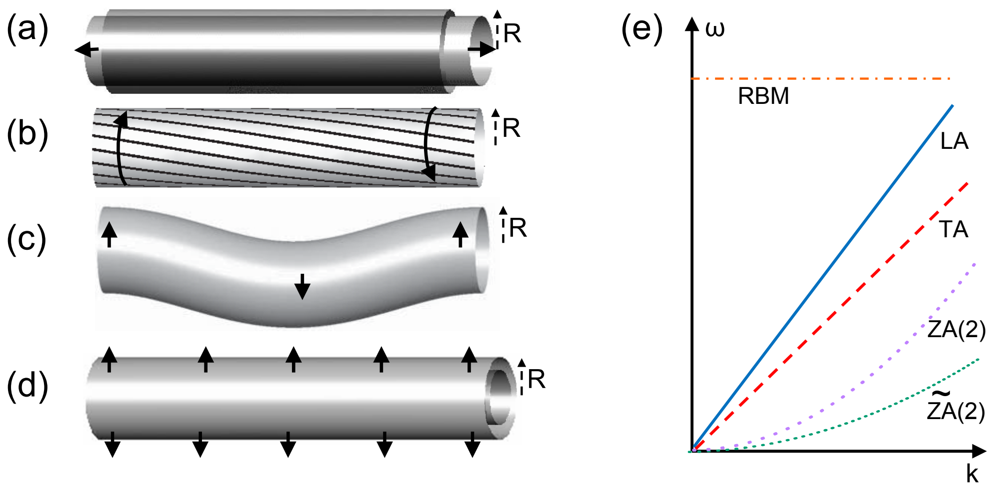

Figure 4.1: Schematic representation of important deformations of a tubular structure. (a) Longitudinal acoustic (LA, stretching), (b) torsional acoustic (TA, torsion), (c) flexural acoustic (doubly degenerate ZA, bending), and (d) the radial breathing mode (RBM). (e) Schematic dispersion relations of the corresponding long-wavelength phonon modes. The tilde denotes liquid-filled tubules.

4.2 Continuum elasticity approach

A 1D tubular structure of radius R can be thought of as a rectangular 2D plate of width 2πR that is rolled up to a cylinder. Consequently, the elastic response of 1D tubules to strain, illustrated in Figs. 4.1(a)-4.1(d), is related to that of the constituting 2D plate. To describe this relationship in the linear regime and calculate the frequency of long-wavelength vibrational modes in 1D tubular structures, I take advantage of a continuum elasticity formalism that has been successfully adapted to 2D structures [19].

As shown earlier [19], elastic in-plane deformations of a plate of indefinite thickness may be described by the (3×3) 2D elastic stiffness matrix, which is given in Voigt notation by

$$\begin{pmatrix} c_{11} & c_{12} & 0 \\ c_{12} & c_{22} & 0 \\ 0 & 0 & c_{66} \end{pmatrix} . \tag{4.1}$$

Resistance of a plate to bending is determined by the flexural rigidity D. For a plate suspended in the $x-y$ plane, c_{11} and c_{22} describe the longitudinal strain-stress relationship along the $x-$ and $y-$direction, respectively. c_{66} describes the elastic response to in-plane shear. For an isotropic plate, which I consider here, $c_{11} = c_{22}$, $c_{66} = (c_{11} - c_{12})/2$, and the in-plane Poisson ratio $\alpha = c_{12}/c_{11}$. Considering a 3D plate of finite thickness h, characterized by the (6×6) elastic stiffness matrix C_{ij}, the coefficients of the 2D elastic stiffness matrix c_{ij} for the equivalent plate of indefinite thickness are related by $c_{ij} = h{\cdot}C_{ij}(1 - \alpha_{\perp}^2)$. This expression takes account of the fact that stretching a finite-thickness slab of isotropic material not only reduces its width by the in-plane Poisson ratio α, but also its thickness by the out-of-plane Poisson ratio $\alpha_{\perp}$. For the weak inter-layer coupling layered compound such as graphite, this consideration is not needed, so that $c_{ij} = h{\cdot}C_{ij}$. In near-isotropic materials like tubulin, however, $\alpha_{\perp}{\approx}\alpha$ and $c_{ij} = h{\cdot}C_{ij}(1 - \alpha^2)$.

4.2.1 Vibrational Modes of empty Nanotubes

Now considering an infinitely thin 2D plate of finite width $2\pi R$ and an areal mass density ρ_{2D} rolled up to a nanotube of radius R that is aligned with the $x-$axis. The linear mass density of the nanotube is related to that of the plate by

$$\rho_{1D} = 2\pi R \rho_{2D} \, . \tag{4.2}$$

In the long-wavelength limit, represented by $k = (2\pi/\lambda){\to}0$, the longitudinal acoustic mode of a tubular structure, depicted in Fig. 4.1(a), resembles the stretching mode of a 2D plate [19]. As mentioned above, the equivalent plate I consider here is a strip of finite width that is reduced during stretching due to the nonzero in-plane Poisson ratio α.

In the following, I illustrate the computational approach for a tubular structure by focussing on its longitudinal acoustic mode. The derivation, which is described in more detail in Related Information sections 4.8.1 and 4.8.2, starts with the Lagrange function density

$$\begin{aligned}\mathcal{L}\left(\frac{du_x}{dx},\frac{du_x}{dt},x,t\right) &= T-U \\ &= \frac{1}{2}\left[\rho_{2D}\left(\frac{du_x}{dt}\right)^2 - c_{11}\left(1-\alpha^2\right)\left(\frac{du_x}{dx}\right)^2\right]2\pi R \\ &= \frac{1}{2}\left[\rho_{1D}\left(\frac{du_x}{dt}\right)^2 - c_{LA}\left(\frac{du_x}{dx}\right)^2\right],\end{aligned} \tag{4.3}$$

where

$$c_{LA} = c_{11}\left(1-\alpha^2\right)2\pi R \tag{4.4}$$

is the longitudinal force constant of a 1D nanowire equivalent to the tubule, and the relation between ρ_{1D} and ρ_{2D} is defined in Eq. (4.2). The resulting Euler-Lagrange equation is

$$\frac{d}{dt}\left(\frac{\partial\mathcal{L}}{\partial\frac{du_x}{dt}}\right)+\frac{d}{dx}\left(\frac{\partial\mathcal{L}}{\partial\frac{du_x}{dx}}\right)=0\,. \tag{4.5}$$

Using the ansatz

$$u_x = u_{x,0}e^{i(kx-\omega t)} \tag{4.6}$$

I obtain the vibration frequency of the longitudinal acoustic (LA) mode of the nanotube or nanowire from

$$\omega_{LA} = \sqrt{\frac{c_{11}(1-\alpha^2)}{\rho_{2D}}}\,k = \sqrt{\frac{c_{LA}}{\rho_{1D}}}\,k\,. \tag{4.7}$$

The prefactor of the crystal momentum k is the longitudinal speed of sound. As already noted in Ref. [[51]], the frequency of the LA mode is independent of the nanotube radius.

The torsional mode, depicted in Fig. 4.1(b), is very similar to the shear mode of a plate. Consequently, as shown in Related Information section 4.8.2, the vibration frequency of the torsional acoustic (TA) mode of the nanotube and the transverse acoustic mode of the plate should be the same. With c_{66} describing the resistance of the equivalent plate to shear, I obtain

$$\omega_{TA} = \sqrt{\frac{c_{66}}{\rho_{2D}}}\; k \,. \tag{4.8}$$

Again, prefactor of the crystal momentum k is the corresponding speed of sound. Similar to the LA mode, the frequency of the TA mode is independent of the nanotube radius [51].

The doubly degenerate flexural acoustic (ZA) mode, depicted in Fig. 4.1(c), differs significantly from the corresponding bending mode of a plate [19] that involves the plate's flexural rigidity D. The continuum elasticity treatment of the bending deformation, described in Related Information sections 4.8.1 and 4.8.2, leads to

$$\omega_{ZA} = \sqrt{\frac{\pi R^3 c_{11}}{\rho_{1D}}\left(1+\frac{D}{c_{11}R^2}\right)}\; k^2 = \sqrt{\frac{D_b}{\rho_{1D}}}\; k^2 = c_{ZA}(R)\; k^2 \,. \tag{4.9}$$

Here, c_{ZA} is the effective bending force constant and D_b is the effective beam rigidity of a corresponding nanowire, defined in Eq. (4.36).

Finally, the radial breathing mode (RBM) of the nanotube, depicted Fig. 4.1(d), has a nearly $k-$independent frequency given by [19]

$$\omega_{RBM} = \frac{1}{R}\sqrt{\frac{c_{11}}{\rho_{2D}}} \,. \tag{4.10}$$

The four vibration modes described above and their functional dependence on the momentum k and radius R have been partially described before using an elastic cylindrical shell model [49, 50]. The schematic dependence of the vibration frequencies of these modes on k is shown in Fig. 4.1(e). The main expressions for the vibration frequencies of both 2D and tubular 1D structures are summarized in Table 4.1.

4.2.2 Vibrational Modes of Liquid-Filled Nanotubes

Next, I consider the nanotubes completely filled with a compressible, but viscosity-free liquid that can slide without resistance along the nanotube wall [52]. Since the nanotubes remain straight and essentially maintain their radius during stretching and torsion, the frequency $\tilde{\omega}$ of the LA and TA modes is not affected by the liquid inside, which remains immobile during the vibrations. I thus obtain

$$\tilde{\omega}_{LA}(k) \approx \omega_{LA}(k) \tag{4.11}$$

and

$$\tilde{\omega}_{TA}(k) = \omega_{TA}(k) \,, \tag{4.12}$$

where the tilde refers to filling by a liquid.

The only effect of filling by a liquid on the flexural modes is an increase in the linear mass density to

$$\tilde{\rho}_{1D} = \rho_{1D} + \pi R^2 \rho_l \,, \tag{4.13}$$

where ρ_l denotes the gravimetric density of the liquid. In comparison to an empty tube, described by Eq. (4.9), I observe a softening of the flexural vibration frequency to

$$\begin{aligned} \tilde{\omega}_{ZA} &= \sqrt{\frac{\pi R^3 c_{11}}{\tilde{\rho}_{1D}} \left(1 + \frac{D}{c_{11} R^2}\right)} \, k^2 = \sqrt{\frac{D_b}{\tilde{\rho}_{1D}}} \, k^2 \\ &= \tilde{c}_{ZA}(R) \, k^2 \,. \end{aligned} \tag{4.14}$$

Finally, as I expand in Related Information section 4.8.3, the effect of the contained liquid on the RBM frequency will depend on the stiffness of the tubular container. For stiff carbon nanotubes, the RBM mode is nearly unaffected, whereas the presence of an incompressible liquid increases $\tilde{\omega}_{RBM}$ in soft tubules. Thus,

$$\tilde{\omega}_{RBM} \leq \omega_{RBM} \, . \tag{4.15}$$

The schematic dependence of the four vibration modes on the momentum k in liquid-filled nanotubes is shown in Fig. 4.1(e). The main expressions for the vibration frequencies of liquid-filled tubular 1D structures are summarized in Table 4.1.

4.3 Vibrational Modes of Nanotubes in a Surrounding Liquid

From among the four long-wavelength vibrational modes of nanotubes illustrated in the left panels of Fig. 4.1, the stretching and the torsional modes are not affected by the presence of a liquid surrounding the nanotube. I expect the radial breathing mode in Fig. 4.1(d) to couple weakly and be softened by a small amount in the immersing liquid. The most important effect of the surrounding liquid is expected to occur for the flexural mode shown in Fig. 4.1(c).

The following arguments and expressions have been developed primarily to accommodate soft biological structures such as tubulin-based microtubules, which require an aqueous environment for their function. I will describe the surrounding liquid by its gravimetric density ρ_l and viscosity η. As suggested above, I will focus the concern on the flexural long-wavelength

Table 4.1: Summary of expressions derived for the vibrational frequencies ω of 1D tubules and 2D plates. $\tilde{\omega}$ denotes the frequency of liquid-filled tubules. Equation numbers refer to the present publication.

Mode	1D Tubules	Equation	2D Plates[1]
LA	$\omega_{LA} = \sqrt{\frac{c_{11}(1-\alpha^2)}{\rho_{2D}}}\ k$	Eq. (4.7)	$\omega_{LA} = \sqrt{\frac{c_{11}}{\rho_{2D}}}\ k$
	$\omega_{LA} = \sqrt{\frac{c_{LA}}{\rho_{1D}}}\ k$	Eq. (4.7)	
	$\tilde{\omega}_{LA} = \omega_{LA}$		
TA	$\omega_{TA} = \sqrt{\frac{c_{66}}{\rho_{2D}}}\ k$	Eq. (4.8)	$\omega_{TA} = \sqrt{\frac{c_{66}}{\rho_{2D}}}\ k$
	$\tilde{\omega}_{TA} = \omega_{TA}$		
ZA	$\omega_{ZA} = \sqrt{\frac{\pi R^3 c_{11}}{\rho_{1D}}\left(1 + \frac{D}{c_{11}R^2}\right)}\ k^2$	Eq. (4.9)	$\omega_{ZA} = \sqrt{\frac{D}{\rho_{2D}}}$
	$\omega_{ZA} = \sqrt{\frac{\pi R^3 c_{11}}{\rho_{1D}}\left(1 + \frac{D}{c_{11}R^2}\right)}\ k^2$	Eq. (4.9)	$\omega_{ZA} = \sqrt{\frac{D}{\rho_{2D}}}$
	$\omega_{ZA} = \sqrt{\frac{D_b}{\rho_{1D}}}\ k^2$	Eq. (4.9)	
	$\tilde{\omega}_{ZA} = \sqrt{\frac{\pi R^3 c_{11}}{\tilde{\rho}_{1D}}\left(1 + \frac{D}{c_{11}R^2}\right)}\ k^2$	Eq. (4.14)	
	$\tilde{\omega}_{ZA} = \sqrt{\frac{D_b}{\tilde{\rho}_{1D}}}\ k^2$	Eq. (4.14)	
RBM	$\omega_{RBM} = \frac{1}{R}\sqrt{\frac{c_{11}}{\rho_{2D}}}$	Eq. (4.10)	
	$\tilde{\omega}_{RBM} \geq \omega_{RBM}$	Eq. (4.15)	

vibrations of such structures.

I will show later on, the flexural modes of idealized, free-standing biological microtubules are extremely soft. In that case, the velocity of transverse vibrations will also be very small and definitely lower than the speed of sound in the surrounding liquid. Under these conditions, the motion of the rod-like tubular structure will only couple to the evanescent sound waves in the surrounding liquid and there will be no radiation causing damping. The main effect of the immersion in the liquid will be to increase the effective inertia of the rod. I may assume that the linear mass density ρ_{1D} of the tubule in vacuum may increase to $\tilde{\rho}_{1D} = \rho_{1D} + \Delta\rho_{1D}$ in the surrounding liquid. I can estimate $\Delta\rho_{1D} = \Delta A \rho_l$, where ΔA

describes the increase in the effective cross-section area of the tubule due to the surrounding liquid that is dragged along during vibrations. I expect $\Delta A \lesssim \pi R^2$, where R is the radius of the tubule. The softening of the flexural mode frequency $\tilde{\omega}_{ZA}$ due to the increase in ρ_{1D} is described in Eq. (4.14).

Next I consider the effect of viscosity of the surrounding liquid on long-wavelength vibrations of a tubular structure that will resemble a rigid rod for $k \to 0$. Since – due to Stoke's paradox – there is no closed expression for the drag force acting on a rod moving through a viscous liquid, I will approximate the rod by a rigid chain of spheres of the same radius, which are coupled to a rigid substrate by a spring. The motion for a rigid chain of spheres is the same as of a single sphere, which is damped by the drag force $F = 6\pi\eta R v$ according to Stoke's law, where v is the velocity.

The damped harmonic motion of a sphere of radius R and mass m is described by

$$m\frac{d^2u}{dt^2} = -m\omega_0^2 u - 6\pi\eta R\frac{du}{dt}\,. \tag{4.16}$$

With the ansatz $u(t) = u_0 e^{i\omega t}$, I get

$$-m\omega^2 = -m\omega_0^2 - i\omega 6\pi\eta R \tag{4.17}$$

and thus

$$\omega = \pm\sqrt{\omega_0^2 - \left(\frac{3\pi\eta R}{m}\right)^2} + i\frac{3\pi\eta R}{m}\,. \tag{4.18}$$

Assuming that the damping is small, I can estimate the energy loss described by the $Q-$factor

$$Q = \omega_0\frac{m}{3\pi\eta R} = \frac{2}{3}\frac{m}{R}\frac{f_0}{\eta}\,, \tag{4.19}$$

where $f_0 = \omega_0/(2\pi)$ is the harmonic vibration frequency. In a rigid string of masses separated by the distance $2R$, the linear mass density is related to the individual masses by $\rho_{1D} = m/(2R)$. Then, the estimated value of the $Q-$factor will be

$$Q = \frac{4}{3}\rho_{1D}\frac{f_0}{\eta}\,. \tag{4.20}$$

4.4 Computational Approach to Determine the Elastic Response of Carbon Nanotubes

I use *ab initio* density functional theory (DFT) as implemented in the SIESTA [13] code to determine the elastic response and elastic constants of an atomically thin graphene monolayer, the constituent of CNTs. The exchange-correlation functional is Perdew-Burke-Ernzerhof (PBE) [9] with norm-conserving Troullier-Martins pseudopotentials [33], and a double-ζ basis including polarization orbitals. To determine the energy cost associated with in-plane distortions, I sampled the Brillouin zone of a 3D superlattice of non-interacting layers by a $20\times20\times1$ k-point grid [34]. I used a mesh cutoff energy of 180 Ry and an energy shift of 10 meV in the self-consistent total energy calculations, which has provided us with a precision in the total energy of $\leq$2 meV/atom. The same static approach can be applied to other layered materials that form tubular structures.

4.5 Results

I selected two extreme examples to show the usefulness of the approach for all tubular structures. One is nanometer-wide CNTs which have been characterized well as rigid structures

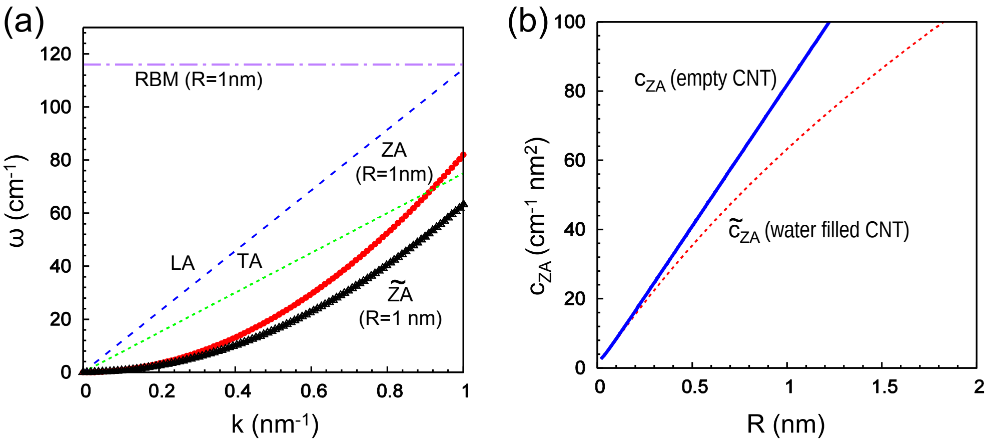

Figure 4.2: (a) Frequency of vibrational modes depicted in Fig. 4.1(a) in empty and water-filled carbon nanotubes. (b) Dependence of the flexural coefficient $c_{ZA}(R)$, defined in Eq. (4.9), on the radius R of empty and water-filled carbon nanotubes. The tilde denotes liquid-filled nanotubes.

able to support themselves in vacuum. The other example is tubulin-based microtubules, which are significantly wider and softer than carbon nanotubes. These biological structures require an aqueous environment for their function.

4.5.1 Carbon Nanotubes

The elastic behavior of carbon nanotubes can be described using quantities previously obtained using DFT calculations for graphene [19]. The calculated elements of the elastic stiffness matrix (4.1) are $c_{11} = c_{22} = 352.6$ N/m, $c_{12} = 59.6$ N/m, and $c_{66} = 146.5 N/m$, all in very good agreement with experimental results [53]. The calculated in-plane Poisson ratio $\alpha = c_{12}/c_{11} = 0.17$ is also close to the experimentally estimated value for graphene [53] of $\alpha_{expt} = 0.19$. The calculated flexural rigidity of a graphene plate is $D = 0.22$ GPa·nm^3. The calculated 2D mass density of graphene $\rho_{2D} = 0.743{\cdot}10^{-6}$ kg/m^2 translates to $\rho_{1D} = 0.743{\cdot}10^{-6}$ kg/m$^2{\cdot}2\pi R$ for nanotubes of radius R.

The phonon dispersion relations $\omega(k)$ depend primarily on the radius and not the specific

Table 4.2: Elastic behavior of a 2D graphene monolayer. c_{11}, c_{22}, c_{66} are 2D elastic stiffness constants defined in Eq. (4.1). α is the in-plane Poisson ratio, D is the flexural rigidity, and ρ_{2D} is the areal mass density. These values can be used directly to calculate long-wavelength acoustic frequencies $\omega(k)$ using the expressions in Table 4.1 and the speed of sound v_{LA} and v_{TA}. Present values are compared to published data.

Quantity	Present result	Literature values
$c_{11} = c_{22}$	352.6 N/m	342 N/m [2]
c_{66}	146.5 N/m	144 N/m [a]
α	0.17	0.19 [a]
D	0.22 GPa·nm^3	0.225 GPa·nm^3 [3]
$R\ \omega_{RBM} = \sqrt{c_{11}/\rho_{2D}}$	116 cm^{-1}nm	116 cm^{-1}nm [4] 108 cm^{-1}nm [5]
v_{LA}	21.5 km/s	22 km/s [a] ≈21 km/s [6]
v_{TA}	14.1 km/s	14 km/s [a,b]

chiral index (n, m) of carbon nanotubes and are presented in Fig. 4.2(a) for the different polarizations. The LA and TA mode frequencies are almost independent of the nanotube radius for a given k. The corresponding group velocities at $k \to 0$ give the longitudinal speed of sound of $v_{LA} = d\omega_{LA}/dk = 21.5$ km/s and the speed of sound with torsional polarization of $v_{TA} = d\omega_{TA}/dk = 14.1$ km/s.

The flexural or bending ZA mode does depend on the nanotube radius through the proportionality constant $c_{ZA}(R)$, defined in Eq. (4.9), which is plotted as a function of R in Fig. 4.2(b). The dispersion of the ZA mode in a CNT of radius $R = 1$ nm is shown in Fig. 4.2(a). Also the RBM frequency depends on the nanotube radius according to Eq. (4.10). I find the value $\sqrt{c_{11}/\rho_{2D}} = 116$ cm^{-1}nm of the prefactor of R^{-1} in Eq. (4.10) to agree well with the published theoretical value [55] of 116 cm^{-1}nm and with the value of 108 cm^{-1}nm, obtained by fitting a set of observed Raman frequencies [56]. The calculated value $\omega_{RBM} = 116$ cm^{-1} for CNTs with $R = 1$ nm is shown in Fig. 4.2(a).

Filling the CNT with a liquid of density ρ_l increases its linear density ρ_{1D} according to

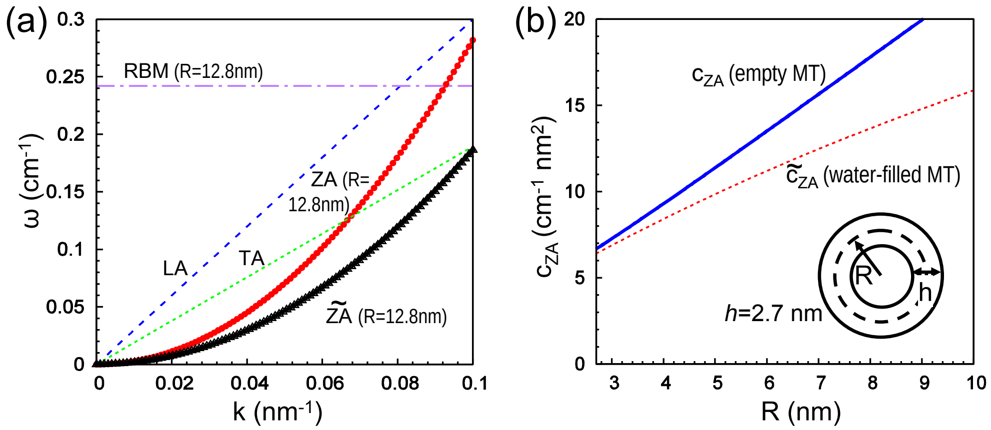

Figure 4.3: (a) Frequency of vibrational modes depicted in Fig. 4.1(a) in empty and water-filled tubulin-based microtubules. (b) Dependence of the flexural coefficient $c_{ZA}(R)$, defined in Eq. (4.9), on the radius R of empty and water-filled tubulin-based microtubules. The tilde denotes liquid-filled tubules.

Eq. (4.13). For a nanotube filled with water of density $\rho_l = 1$ g/cm^3, the radius-dependent quantity $\tilde{c}_{ZA}(R)$, defined in Eq. (4.14), is plotted as a function of R in Fig. 4.2(b). The dispersion of the $\tilde{\text{ZA}}$ mode in a water-filled CNT of radius $R = 1$ nm is shown in Fig. 4.2(a).

Elastic constants calculated in this work, and results derived using the present continuum elasticity approach are listed and compared to literature data in Table 4.2.

4.5.2 Tubulin-Based Microtubules

To describe phonon modes in tubulin-based microtubules, I used published experimental data [57] for microtubules with an average radius $R = 12.8$ nm and a wall thickness $h = 2.7$ nm. The observed density of the tubule wall material $\rho = 1.47$ g/cm^3 translates to $\rho_{2D} = 4.0{\cdot}10^{-6}$ kg/m^2. The estimated Young's modulus of the wall material is $E = 0.5$ GPa and the flexural beam rigidity of these microtubules with $R = 12.8$ nm is $D_b = 0.9{\cdot}10^{-23}\ N{\cdot}m^2$. Using the relationship between D_b and D, defined in Eq. (4.35), to map these values onto the elastic 2D wall material and obtain $c_{11} = E{\cdot}h = 1.4$ N/m and $D = 2.71$ GPa·nm^3. In a rough approximation, tubulin can be considered to be isotropic, with a Poisson ratio $\alpha = 0.25$. Further assuming that $c_{11} = c_{22}$, I estimate $c_{66} = (c_{11} - c_{12})/2 = c_{11}(1 - \alpha)/2 = 0.5$ N/m.

There is one fundamental difference between tubulin-based microtubules and systems such as CNTs is that the former necessitate an aqueous environment for their shape and function. So, the correct description of microtubule deformations and vibrations need to address the complete microtubule-liquid system, which would exceed the scope of this study. I rather resorted to the expressions derived in the Subsection on nanotubes in a surrounding liquid to at least estimate their $Q-$factor in an aqueous environment. I used $\rho_{1D} = 7 \times 10^{-13}$ kg/m for a water-filled microtubule, $\eta = 10^{-3}$ Pa·s and $f_0 = 10^9$ Hz, which provided us with the value $Q \approx 1.2$. In other words, the aqueous environment highly damped flexural vibrations in microtubules, as a result, their frequency should be very hard to measure. Consequently, the only available comparison between the calculations and experimental data should be made for static measurements.

An appropriate way to experimentally determine the effective beam rigidity of individual tubulin-based microtubules involves the measurement of buckling caused by applying an axial buckling force using optical tweezers. Experimental results for the effective beam rigidity have been obtained in this way for microtubules that are free of the paclitaxel stabilizing agent and contain 14 tubulin protofilaments, which translates to the effective radius $R \approx 9.75$ nm. The observed values range from $D_b = 3.7 \pm 0.8 \times 10^{-24}$ Nm^2 [58] to $D_b = 7.9 \pm 0.7 \times 10^{-24}$ Nm^2 [59], in good agreement with the calculated value $D_b = 4.2 \times 10^{-24}$ Nm^2. The estimated value $D_b = 6.2 \times 10^{-24}$ Nm^2 for wider tubules with 16 protofilaments is 49% larger than for the narrower tubules with 14 protofilaments. The corresponding increase by 49% has been confirmed in a corresponding experiment [59].

Next, I still use the oversimplifying assumption that tubulin microtubules which may exist in the vacuum and could be described by the above-derived continuum values [50]. In this way, I compare the results to published theoretical results. The calculated phonon dispersion relations $\omega(k)$ for most common microtubules with the radius $R = 12.8$ nm are presented in Fig. 4.3(a). The LA and TA mode frequencies are independent of the tubule radius. The longitudinal speed of sound $v_{LA} = d\omega_{LA}/dk = 0.56$ km/s and the speed of sound with torsional polarization $v_{TA} = d\omega_{TA}/dk = 0.36$ km/s are got from the slope. In order to compare, I extracted the v_{LA} value based on the elastic cylindrical shells model with $E = 2.0$ GPa from Ref. [50]. Extrapolating to the value $E = 0.5$ GPa in the set of parameters using the relationship $v_{LA} \propto \sqrt{E}$, I obtained $v_{LA} = 0.59$ km/s, in excellent agreement with the calculated value.

The flexural or bending ZA mode depends on the tubule radius through the proportionality constant $c_{ZA}(R)$, defined in Eq. (4.9), which is plotted as a function of R in Fig. 4.3(b). The dispersion of the ZA mode in a microtubule of radius $R = 12.8$ nm is shown in Fig. 4.3(a).

Also the RBM frequency depends on the nanotube radius according to Eq. (4.10). For $R = 12.8$ nm, I obtain $\omega_{RBM} = 0.24$ cm^{-1}, as seen in Fig. 4.3(a).

For describing the increase in the linear density ρ_{1D} of a microtubule filled with a liquid of density ρ_l, I need to account for the finite thickness h of the wall and replace the radius R by $R - h/2$ in Eq. (4.13). Considering water of density $\rho_l = 1$ g/cm^3 as the filling medium, I plot the radius-dependent quantity $\tilde{c}_{ZA}(R)$, defined in Eq. (4.14), as a function of R in Fig. 4.3(b). The dispersion of the $\tilde{\text{ZA}}$ mode in a water-filled CNT of radius $R = 12.8$ nm is shown in Fig. 4.3(a).

The results in Fig. 4.3(a) suggest soft vibration in the GHz range, in agreement with other theoretical estimates [49, 50]. As mentioned above, all these vibrations will be hight damped in an aqueous environment to the low $Q-$factor.

4.6 Discussion

Although the atomistic approach which is based on an atomistic calculation of the force-constant matrix, is quite adequate to determine frequencies of the optical and of short-wavelength acoustic modes. This approach for calculating the frequency spectrum, does not provide accurate frequencies for long-wavelength soft acoustic modes in quasi-1D tubular structures, the excessive demand on supercell size and basis convergence often yields imaginary vibration frequencies as an artifact of insufficient convergence.

An alternative to tedious atomistic calculations of the force-constant matrix of complex tubular systems, I propose here a continuum elasticity approach to determine the frequency of long-wavelength acoustic modes in tubular structures that does not require the thickness of the wall as an input. The approach for quasi-1D structures is based on the successful description of corresponding modes in 2D structures [19]. Using this approach, I obtain for the first time quantitative results for systems ranging from stiff CNTs to much wider and softer protein microtubules.

The elastic behavior of the wall material can be determined accurately by static calculations of 2D plate subjected to small deformation or by elastic measurements. This approach works very well for long-wavelength vibrations and large-radius nanotubes, both of which require extraordinary computational resources in atomistic calculations. In particular, the flexural ZA modes with their $\omega \propto k^2$ momentum dependence are known to be very hard to reproduce by *ab initio* calculations near the Γ point [47].

For the sake of completeness, I have also derived the Euler-Lagrange equations of motion required to describe all long-wavelength acoustic modes and present the detailed derivation in the Related Information section.

Of course, the frequency of the ZA modes is expected to be much softer than that of the LA mode in any nanotube or nanowire. Since $\omega_{ZA} \propto k^2$ whereas $\omega_{LA} \propto k$, expressions derived here for the long-wavelength limit would lead to the unrealistic behavior $\omega_{ZA} > \omega_{LA}$ for large values of k. This limits the $k-$range, for which the formalism is valid in the dispersion relations presented in Figs. 4.2(a) and 4.3(a). In a crystalline tubule, k is restricted to typically an even smaller range given by the size of the 1D Brillouin zone.

The radial breathing mode (RBM) should be decoupled from the longitudinal acoustic or stretching mode in systems with a vanishing Poisson ratio α. However, most systems have a non-vanishing value of α as discussed in Related Information section 4.8.4. In that case, these two modes mix and change their character beyond the wavevector $k = 1/R$, where $\omega_{LA}(k) \approx \omega_{RBM}$, as discussed previously [50]. For k with smaller values, coupling between the LA mode and the RBM modifies the frequency of these modes by only $\approx 1\%$ in CNTs.

The model allows a simple extension from empty to liquid-filled nanotubes. As shown in Related Information section 4.8.4, I find that presence of a filling liquid does not affect longitudinal acoustic and torsional acoustic modes to a significant extent, but softens the flexural modes. I also expect the pressure wave of the liquid to couple to the RBM beyond the wavevector $k \approx \omega_{RBM}/v_p$, where v_p is the speed of the propagating pressure wave.

To demonstrate the validity of the approach, I also considered microtubules formed of the proteins α- and β-tubulin. These are responsible for maintaining the shape and elasticity of cells, but are too complex for an atomistic description to predict vibration spectra. The necessity to include the aqueous environment in the description of tubulin-based microtubules makes the problem becomes more complex for computation.

The basic finding that microtubule motion and vibrations are overdamped in the natural aqueous environment, with a $Q-$factor of the order of unity, naturally explains the absence of experimental data reporting observation of motion, dynamical shape changes and vibrations in these protein-based systems. Among static measurements of the elastic behavior of microtubules, optical tweezers appear to be the optimum way to handle and deform individual microtubules in order to determine their effective beam rigidity D_b. In this static scenario, I find the description of the beam rigidity precise enough to compare with experimental data. The reported dependence of D_b on the cube of the radius [59] is reflected in the corresponding expression for D_b in Eq. (4.35). In the case of tubulin-based microtubules, I find the leading term in D_b to be indeed proportional to R^3 and to be much larger than the second term, which is proportional to R.

4.7 Summary

For addressing the shortcoming of conventional atomistic calculations of long-wavelength acoustic frequencies in tubular structures, I have developed an alternative computational approach based on continuum elasticity theory to 2D and 1D structures. Since 1D tubular structures can be viewed as 2D plates of finite width rolled up to a cylinder, I have taken advantage of the correspondence between 1D and 2D structures to determine their elastic response to strain. In the approach, computation of long-wavelength acoustic frequencies does not require the determination and diagonalization of a large, momentum-dependent dynamical matrix. Instead, the simple expressions I have derived for the acoustic frequencies $\omega(k)$ depends only four elements of a $k-$independent 2D elastic matrix, namely c_{11}, c_{22}, c_{12}, and c_{66}, as well as the value of the flexural rigidity D of the 2D plate constituting the wall. These five numerical values can easily be obtained using static calculations for a 2D plate. The scope of the approach is limited to long-wavelength acoustic modes, but the accuracy of the calculated vibration frequencies surpasses that of conventional atomistic *ab initio* calculations. Starting with a Lagrange function describing longitudinal, torsional, flexural and radial deformations of empty or liquid-filled tubular structures, I have derived corresponding Euler-Lagrange equations to obtain simple expressions for the vibration frequencies of the corresponding modes. I have furthermore shown that longitudinal and flexural acoustic modes of tubules are well described by those of an elastic beam resembling a nanowire. Using the simple expressions, I were able to show that a pressure wave in the liquid contained in a stiff carbon nanotube has little effect on its RBM frequency, whereas the effect of a contained liquid on the RBM frequency in much softer tubulin tubules is significant. I found that presence of water in the native environment of tubulin microtubules reduces the $Q-$factor to such a degree that flexural vibrations can hardly be observed. I also showed that the coupling between long-wavelength LA modes and the RBM can be neglected. I have found general agreement between the numerical results for biological microtubules and carbon nanotubes and available experimental data.

4.8 Related Information

Material in the Related Information section provides detailed derivation of expressions used in the main text and considers specific limiting cases. In Related Information section 4.8.1, I derive the Lagrange function for stretching, torsional and bending modes of tubular structure. In Related Information section 4.8.2, I derive analytical expressions for the frequencies of the corresponding vibration modes using the Euler-Lagrange equations. The effect of a liquid contained inside a CNT on its RBM frequency is investigated in Related Information section 4.8.3. The coupling between the longitudinal acoustic mode and the RBM in a CNT due to its non-vanishing Poisson ratio is discussed in Related Information section 4.8.4.

4.8.1 Lagrange Function of a Strained Nanotube

4.8.1.1 Stretching

Let us consider a nanotube of radius R aligned with the $x-$axis and its response to tensile strain du_x/dx applied uniformly along the $x-$direction. The strain energy will be the same as that of a 2D strip of width $y = 2\pi R$ lying in the $xy-$plane that is subject to the same condition.

Assuming that the width of the strip is constrained to be constant, the strain energy per length is given by

$$U_x = \frac{1}{2}\, c_{11} \left(\frac{du_x}{dx} \right)^2 2\pi R\,. \tag{4.21}$$

For a nonzero Poisson ratio α, stretching the strip by du_x/dx will reduce its width by $du_y/dy = \alpha du_x/dx$ and its radius R, as shown in Fig. 4.1(a). Releasing the constrained width will release the energy $U_y = -\alpha^2 U_x$. The total strain energy per length of a nanotubule or an equivalent 1D nanowire is the sum $U = U_x + U_y$ and is given by

$$U = \frac{1}{2} c_{11} \left(1 - \alpha^2\right) \left(\frac{du_x}{dx} \right)^2 2\pi R = \frac{1}{2} c_{LA} \left(\frac{du_x}{dx} \right)^2 . \tag{4.22}$$

Here, $c_{LA} = 2\pi R c_{11}(1-\alpha^2)$ is the the longitudinal force constant of a 1D nanowire equivalent to the tubule, defined in Eq. (4.4).

In the harmonic regime, I will consider only small strain values. Releasing the strain will cause a vibration in the x-direction with the velocity $v_x = du_x/dt$. Then, the kinetic energy density of the strip will be given by

$$T = \frac{1}{2}\rho_{2D}\left(\frac{du_x}{dt}\right)^2 2\pi R = \frac{1}{2}\rho_{1D}\left(\frac{du_x}{dt}\right)^2 , \tag{4.23}$$

where ρ_{2D} is the areal mass density of the equivalent strip that is related to ρ_{1D} by Eq. (4.2). The Lagrangian density is then given by

$$\begin{aligned} \mathcal{L}\left(\frac{du_x}{dx}, \frac{du_x}{dt}, x, t\right) &= T - U \\ &= \frac{1}{2}\left[\rho_{2D}\left(\frac{du_x}{dt}\right)^2 - c_{11}\left(1-\alpha^2\right)\left(\frac{du_x}{dx}\right)^2\right] 2\pi R\,, \\ &= \frac{1}{2}\left[\rho_{1D}\left(\frac{du_x}{dt}\right)^2 - c_{LA}\left(\frac{du_x}{dx}\right)^2\right] . \end{aligned} \tag{4.24}$$

4.8.1.2 Torsion

The derivation of the Euler-Lagrange equation for the torsional motion is very similar to that for the longitudinal motion. The main difference is that the displacement u_ϕ is normal to the propagation direction x. To obtain the corresponding equations, I need to replace u_x by u_ϕ and $c_{11}(1-\alpha^2)$ by c_{66} in Eqs. (A1)-(A4). The Lagrangian density is then given by

$$\mathcal{L}\left(\frac{du_\phi}{dx}, \frac{du_\phi}{dt}, x, t\right) = T - U = \frac{1}{2}\left[\rho_{2D}\left(\frac{du_\phi}{dt}\right)^2 - c_{66}\left(\frac{du_\phi}{dx}\right)^2\right] 2\pi R\,. \tag{4.25}$$

4.8.1.3 Bending

Bending a nanotube of radius R is equivalent to its transformation to a segment of a nanotorus of radius R_t. Initially, I will assume that $c_{11} = 0$ and $D > 0$ in the given nanotorus segment, so the strain energy would contain only an out-of-plane component. I first consider a straight nanotube of radius R formed by rolling up a plate of width $2\pi R$. The corresponding out-of-plane strain energy per nanotube segment length is

$$U = \frac{1}{2}\frac{D}{R^2}(2\pi R) = \frac{\pi D}{R}\,. \tag{4.26}$$

The corresponding expression for the total out-of-plane strain energy in a nanotorus is [60],

$$U = 2\pi^2 D \frac{R_t^2}{R\sqrt{(R_t + R)(R_t - R)}}\,. \tag{4.27}$$

Divided by the average perimeter length $2\pi R_t$, I obtain the out-of-plane energy of the torus per nanotube segment length

$$U = \pi D \frac{R_t}{R\sqrt{(R_t + R)(R_t - R)}}\,. \tag{4.28}$$

Assuming that the torus radius is much larger than the nanotube radius, $R_t \gg R$, I can Taylor expand U in Eq. (4.28) and neglect higher-order terms in (R/R_t), which leads to

$$U = \frac{\pi D}{R}\left(1 + \frac{1}{2}\left(\frac{R}{R_t}\right)^2\right)\,. \tag{4.29}$$

Comparing the out-of-plane strain energy of a bent nanotube in Eq. (4.29) and that of a straight nanotube in Eq. (4.26), the change in out-of-plane strain energy per segment length associated with bending turns out to be

$$U = \frac{1}{2}\pi D R\left(\frac{1}{R_t}\right)^2\,. \tag{4.30}$$

During the flexural or bending vibration mode, the local curvature $1/R_t = d^2u_z/dx^2$ changes along the tube, yielding the local in-plane strain energy per nanotube segment length of

$$U = \frac{1}{2}\pi DR\left(\frac{d^2u_z}{dx^2}\right)^2 . \tag{4.31}$$

Next, I consider the in-plane component of strain, obtained by assuming $c_{11} > 0$ and $D = 0$ in a given nanotorus segment. There is nonzero strain in a nanotube deformed to a very wide torus with $R_t \gg R$ even if its cross-section and radius R were not to change in this process. The reason is that the wall of the nanotube undergoes stretching along the outer and compression along the inner torus perimeter in this process. This amounts to a total in-plane strain energy [60]

$$U = \frac{\pi^2 c_{11} R^3}{R_t} \tag{4.32}$$

for the entire torus with an average perimeter of $2\pi R_t$ in relation to a straight nanotube of length $2\pi R_t$. Thus, the in-plane strain energy within the torus per segment length is

$$U = \frac{1}{2}\pi c_{11} R^3\left(\frac{1}{R_t}\right)^2 . \tag{4.33}$$

Considering local changes in curvature $1/R_t = d^2u_z/dx^2$ during the bending vibrations of a nanotube, the local in-plane strain energy per nanotube segment length becomes

$$U = \frac{1}{2}\pi c_{11} R^3\left(\frac{d^2u_z}{dx^2}\right)^2 . \tag{4.34}$$

The strain energy in the deformed nanotube per length is the sum of the in-plane strain energy in Eq. (4.34) and the out-of-plane strain energy in Eq. (4.31), yielding

$$U = \frac{1}{2}(\pi c_{11} R^3 + \pi D R)\left(\frac{d^2 u_z}{dx^2}\right)^2 = \frac{1}{2} D_b \left(\frac{d^2 u_z}{dx^2}\right)^2 , \tag{4.35}$$

where

$$D_b = \pi c_{11} R^3 + \pi D R \tag{4.36}$$

is the effective beam rigidity of a corresponding nanowire. The kinetic energy of a bending nanotube or nanowire segment is given by

$$T = \frac{1}{2}\rho_{1D}\left(\frac{du_z}{dt}\right)^2 . \tag{4.37}$$

This leads to the Lagrangian density

$$\begin{aligned} \mathcal{L}\left(\frac{d^2 u_z}{dx^2}, \frac{du_z}{dt}, x, t\right) &= T - U \\ &= \frac{1}{2}\left[\rho_{1D}\left(\frac{du_z}{dt}\right)^2 - \pi c_{11} R^3 \left(1 + \frac{D}{c_{11} R^2}\right)\left(\frac{d^2 u_z}{dx^2}\right)^2\right] . \end{aligned} \tag{4.38}$$

4.8.2 Derivation of Euler-Lagrange Equations of Motion for Deformations of a Nanotube using Hamilton's Principle

4.8.2.1 Stretching

The Euler-Lagrange equation for stretching a tube or a plate is [19]

$$\frac{d}{dt}\left(\frac{\partial \mathcal{L}}{\partial \frac{du_x}{dt}}\right) + \frac{d}{dx}\left(\frac{\partial \mathcal{L}}{\partial \frac{du_x}{dx}}\right) = 0 . \tag{4.39}$$

Inserting the Lagrangian of Eq. (4.24) in the Euler-Lagrange Eq. (4.39) yields the wave equation for longitudinal vibrations of the tubule or the equivalent nanowire

$$2\pi R \rho_{2D} \frac{d^2 u_x}{dt^2} - 2\pi R c_{11} \left(1 - \alpha^2\right) \frac{d^2 u_x}{dx^2} = \rho_{1D} \frac{d^2 u_x}{dt^2} - c_{LA} \frac{d^2 u_x}{dx^2} = 0\,. \tag{4.40}$$

The nanotube radius R drops out and I obtain

$$\rho_{2D} \frac{d^2 u_x}{dt^2} - c_{11} \left(1 - \alpha^2\right) \frac{d^2 u_x}{dx^2} = \rho_{1D} \frac{d^2 u_x}{dt^2} - c_{LA} \frac{d^2 u_x}{dx^2} = 0\,. \tag{4.41}$$

This wave equation can be solved using the ansatz

$$u_x = u_{x,0} e^{i(kx - \omega t)} \tag{4.42}$$

to yield

$$\rho_{2D} \omega^2 = c_{11} \left(1 - \alpha^2\right) k^2 \tag{4.43}$$

for a tubular structure or

$$\rho_{1D} \omega^2 = c_{LA} k^2 \tag{4.44}$$

for an equivalent 1D nanowire. This finally translates to the desired form

$$\omega_{LA} = \sqrt{\frac{c_{LA}}{\rho_{1D}}}\, k = \sqrt{\frac{c_{11}(1 - \alpha^2)}{\rho_{2D}}}\, k\,. \tag{4.45}$$

which is identical to Eq. (4.7).

4.8.2.2 Torsion

The Lagrangian $\mathcal{L}(du_\phi/dx, du_\phi/dt, x, t)$ in Eq. (4.25), which describes the torsion of a tubule, has a similar form as the Lagrangian in Eq. (4.24). To obtain the equations for torsional motion from those for stretching motion, I need to replace u_x by u_ϕ and $c_{11}(1-\alpha^2)$ by c_{66} in Eqs. (4.39)-(4.45). Thus, the frequency of the torsional acoustic mode becomes

$$\omega = \sqrt{\frac{c_{66}}{\rho_{2D}}}k\,, \tag{4.46}$$

which is identical to Eq. (4.8). The torsional frequency is the same as frequency of the shear motion in the equivalent thin plate [19].

4.8.2.3 Bending

The Euler-Lagrange equation for bending a tube or a plate is given by [19]

$$\frac{d}{dt}\left(\frac{\partial\mathcal{L}}{\partial\frac{du_z}{dt}}\right) - \frac{d^2}{dx^2}\left(\frac{\partial\mathcal{L}}{\partial\frac{d^2u_z}{dx^2}}\right) = 0\,. \tag{4.47}$$

Inserting the Lagrangian of Eq. (4.38) for flexural motion in the Euler-Lagrange Eq. (4.47) yields the wave equation for flexual vibrations

$$\rho_{1D}\frac{d^2u_z}{dt^2} + \pi c_{11}R^3\left(1+\frac{D}{c_{11}R^2}\right)\frac{d^4u_z}{dx^4} = \rho_{1D}\frac{d^2u_z}{dt^2} + D_b\frac{d^4u_z}{dx^4} = 0\,. \tag{4.48}$$

This wave equation can be solved using the ansatz

$$u_z = u_{z,0}e^{i(kx-\omega t)} \tag{4.49}$$

to yield

$$\rho_{1D}\omega^2 = \pi c_{11} R^3 \left(1 + \frac{D}{c_{11}R^2}\right) k^4 = D_b k^4 \,. \tag{4.50}$$

This finally translates to the desired form

$$\omega = \sqrt{\frac{\pi c_{11} R^3}{\rho_{1D}} \left(1 + \frac{D}{c_{11}R^2}\right)}\, k^2 = \sqrt{\frac{D_b}{\rho_{1D}}}\, k^2 \,, \tag{4.51}$$

which is identical to Eq. (4.9).

For a liquid-filled nanotube, I only need to replace ρ_{1D} by $\tilde{\rho}_{1D}$ in Eq. (4.51) to get

$$\omega = \sqrt{\frac{\pi c_{11} R^3}{\tilde{\rho}_{1D}} \left(1 + \frac{D}{c_{11}R^2}\right)}\, k^2 = \sqrt{\frac{D_b}{\tilde{\rho}_{1D}}}\, k^2 \,, \tag{4.52}$$

which is identical to Eq. (4.14).

4.8.3 Coupling Between a Travelling Pressure Wave and the RBM in a Liquid-Filled Carbon Nanotube

Next I consider a long-wavelength displacement wave $u_x = u_{x,0} \exp[i(kx - \omega t)]$ of small frequency ω and wave vector k travelling down the liquid column filling a carbon nanotube. I assume the liquid to be compressible but viscosity-free. Thus, the travelling displacement wave will result in a pressure wave $p = p_0 \exp[i(kx - \omega t)]$ that causes radial displacements $r = r_0 \exp[i(kx - \omega t)]$ in the CNT wall. These radial displacements couple the pressure wave in the liquid to the RBM, but not the longitudinal and torsional modes of the CNT.

At small frequencies ω, there will be little radial variation in the pressure. The local

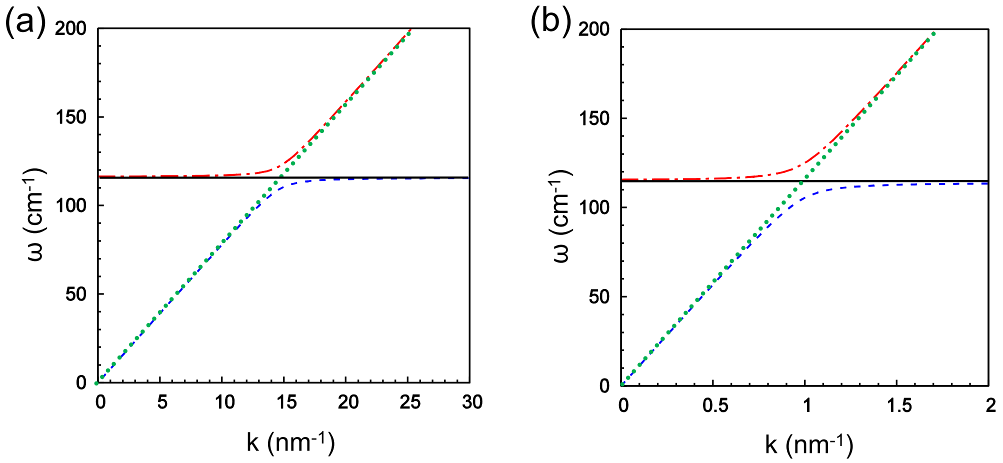

Figure 4.4: Nature and coupling of vibration modes $\omega(k)$ of a carbon nanotube that may be filled with water. (a) Coupling between the dispersionless RBM of a CNT, shown by the black line, and the pressure wave of water enclosed in the CNT, shown by the green dotted line. (b) Coupling between the RBM of a CNT, shown by the black line, and the longitudinal acoustic mode of the CNT, shown by the green dotted line. Results are presented for a CNT with a radius of 1 nm.

compressive strain in the liquid will thus be

$$-\frac{\delta V}{V} = -\left(\frac{\partial u_x}{\partial x} + \frac{2r}{R}\right) \tag{4.53}$$

and the pressure becomes

$$p = -B\frac{\delta V}{V} = -B\left(\frac{\partial u_x}{\partial x} + \frac{2r}{R}\right) . \tag{4.54}$$

Here, B is the bulk modulus of the filling liquid, which I assume is water with $B = 2.2{\cdot}10^9$ Pa.

The local acceleration of water is given by

$$\rho_l \frac{\partial^2 u_x}{\partial t^2} = -\frac{\partial p}{\partial x} \tag{4.55}$$

and the radial acceleration of the CNT is given by

$$\rho_{2D}\frac{\partial^2 r}{\partial t^2} = p - \frac{c_{11}}{R^2} r\,. \tag{4.56}$$

Inserting harmonic solutions for p, u_x and r into Eqs. (4.54)-(4.56), I obtain

$$\begin{pmatrix} 1 & Bik & 2B/R \\ -ik & \rho_l \omega^2 & 0 \\ 1 & 0 & -(c_{11}/R^2 - \rho_{2D}\omega^2) \end{pmatrix} \begin{pmatrix} p_0 \\ u_{x,0} \\ r_0 \end{pmatrix} = 0 \tag{4.57}$$

with the characteristic equation

$$\left(\frac{c_{11}}{R^2} - \rho_{2D}\omega^2\right)\left(k^2 B - \rho_l \omega^2\right) - \rho_l \omega^2 \frac{2B}{R} = 0\,. \tag{4.58}$$

This can be rewritten as

$$\left(\omega_0^2 - \omega^2\right)\left(k^2 v^2 - \omega^2\right) - \omega^2\gamma^2 = 0\,, \tag{4.59}$$

where $\omega_0^2 = c_{11}/(\rho_{2D}R^2)$ and $\gamma^2 = 2B/(\rho_{2D}R)$. For a CNT of radius $R = 1$ nm, I obtain $\omega_0^2 = 474$ ps^{-2} and $\gamma^2 = 5.92$ ps^{-2}.

Solving Eq. (4.59) leads to the dispersion relation $\omega(k)$, which is presented in Fig. 4.4(a). In the following, I focus on the lowest lying branch of the dispersion relation describing a long wavelength, low frequency pressure wave travelling down the liquid column. In this case, I can neglect ω^2 in the first factor of Eq. (4.59) and obtain

$$\omega = \frac{vk}{\sqrt{1 + \frac{\gamma^2}{\omega_0^2}}} \,. \tag{4.60}$$

Considering the filling liquid to be water with the speed of sound $v = \sqrt{B/\rho_l} \approx 1483$ m/s, the velocity of the propagating pressure wave inside the CNT becomes

$$\frac{\omega}{k} = v \frac{1}{\sqrt{1 + \frac{\gamma^2}{\omega_0^2}}} = 1474 \text{ m/s} \,. \tag{4.61}$$

This value is only slightly reduced from that of bulk water because of the relative rigidity of the CNT.

In the corresponding low wavenumber range, the frequency of the RBM is changed to

$$\tilde{\omega}_{RBM} = \omega_{RBM} \sqrt{1 + \frac{\gamma^2}{\omega_{RBM}^2}} \,. \tag{4.62}$$

For a CNT with radius $R = 1$ nm, $(1 + \gamma^2/\omega_{RBM}^2)^{1/2} = (1 + 5.92/474)^{1/2} = 1.006$, yielding only a 0.6% increase in frequency.

The situation is quite different for tubulin microtubules. Assuming a radius of $R = 12.8$ nm, I find $\omega_{RBM} = 0.24$ cm^{-1} corresponding to $\omega_{RBM}^2 = 0.00203$ ps^{-2}. In that case, $(1 + \gamma^2/\omega_{RBM}^2)^{1/2} = (1 + 0.0859/0.00203)^{1/2} = 6.6$. In other words, filling tubulin microtubules with water will increase their RBM frequency by a factor of 6.6.

As seen in the full solution of Eq. (4.59) in Fig. 4.4(a), at $k \approx 15$ nm^{-1}, there is level repulsion and interchange in character between the two dispersion curves. At very much higher frequencies there will be radial modes in the water column that will couple to the

RBM of the CNT. These lie outside the scope of the present treatment.

4.8.4 Coupling Between the LA Mode and the RBM in Carbon Nanotubes

Consider a longitudinal wave travelling along a CNT containing no liquid. The CNT of radius R is aligned along the $x-$direction and can be thought of as a rolled up plate in the $xy-$plane with a width of $2\pi R$ along the $y-$direction. Where the CNT is being locally stretched, it will narrow down and where it is compressed, it will fatten due to the nonzero value of c_{12} reflected in the Poisson ratio. For longitudinal displacement u_x and radial displacement r, the strains will be $\epsilon_{11} = \partial u_x/\partial x$ and $\epsilon_{22} = r/R$.

The strain energy density is then

$$\begin{aligned} U &= \frac{1}{2}\left(c_{11}\epsilon_{11}^2 + c_{11}\epsilon_{22}^2 + 2c_{12}\epsilon_{22}\epsilon_{11}\right) \\ &= \frac{1}{2}c_{11}\left(\left(\frac{\partial u_x}{\partial x}\right)^2 + \left(\frac{r}{R}\right)^2\right) + c_{12}\frac{\partial u_x}{\partial x}\frac{r}{R} \end{aligned} \tag{4.63}$$

and the kinetic energy density is

$$T = \frac{1}{2}\rho_{2D}\left(\left(\frac{\partial u_x}{\partial t}\right)^2 + \left(\frac{\partial r}{\partial t}\right)^2\right). \tag{4.64}$$

There are two Euler-Langrange equations for the radial and the axial motion,

$$\frac{d}{dt}\left(\frac{\partial \mathcal{L}}{\partial(\frac{dr}{dt})}\right) - \frac{\partial \mathcal{L}}{\partial r} = 0 \tag{4.65}$$

and

$$\frac{d}{dt}\left(\frac{\partial\mathcal{L}}{\partial(\frac{du_x}{dt})}\right)+\frac{\partial}{\partial x}\left(\frac{\partial\mathcal{L}}{\partial(\frac{du_x}{dx})}\right)=0\,. \tag{4.66}$$

With the Lagrangian $\mathcal{L} = T - U$ given by Eqs. (4.63)-(4.64), the Euler-Lagrange equations translate to partial differential equations

$$\rho_{2D}\frac{\partial^2 r}{\partial t^2}+c_{11}\frac{r}{R^2}+\frac{c_{12}}{R}\frac{\partial u_x}{\partial x}=0 \tag{4.67}$$

and

$$\rho_{2D}\frac{\partial^2 u_x}{\partial t^2}-c_{11}\frac{\partial^2 u_x}{\partial x^2}-\frac{c_{12}}{R}\frac{\partial r}{\partial x}=0\,. \tag{4.68}$$

Assuming harmonic solutions $u_x = u_{x,0}\exp[i(kx-\omega t)]$ and $r = r_0\exp[i(kx-\omega t)]$, I get

$$\begin{pmatrix} -\rho_{2D}\omega^2+c_{11}/R^2 & ikc_{12}/R \\ -ikc_{12}/R & -\rho_{2D}\omega^2+c_{11}k^2) \end{pmatrix}\begin{pmatrix} r_0 \\ u_{x,0}\end{pmatrix}=0 \tag{4.69}$$

with the characteristic equation

$$\left(\frac{c_{11}}{\rho_{2D}R^2}-\omega^2\right)\left(\frac{c_{11}}{\rho_{2D}}k^2-\omega^2\right)-\frac{c_{12}^2k^2}{{\rho_{2D}}^2R^2}=0\,. \tag{4.70}$$

Solving Eq. (4.70) leads to the dispersion relations $\omega(k)$ that are shown in Fig. 4.4(b) for a CNT with radius $R = 1$ nm, with the values $c_{11}/(\rho_{2D}R^2) = 474$ ps^{-2}, $c_{11}/(\rho_{2D}) = 474$ ps^{-2}nm^2 and $c_{12}^2/(\rho_{2D}^2R^2) = 6434$ nm^{2}ps^{-4}. The results in Fig. 4.4(b) closely resemble those of Ref. [50], obtained using a more complex formalism describing orthotropic elastic cylindrical shells using somewhat different input parameters. Were c_{12} to be zero, then the uncoupled solutions would be the dispersionless RBM of frequency

$$\omega = \frac{1}{R}\sqrt{\frac{c_{11}}{\rho_{2D}}}\,, \tag{4.71}$$

shown by the black solid line in Fig. 4.4(b), and the pure longitudinal mode of velocity

$$v = \frac{\omega}{k} = \sqrt{\frac{c_{11}}{\rho_{2D}}}\,, \tag{4.72}$$

shown by the green dotted line in Fig. 4.4(b).

The coupling term induces level repulsion between the $\omega_{-}(k)$ and $\omega_{+}(k)$ branches, with strong mode hybridization occurring near $k{\approx}1$ nm^{-1}. It is of interest to examine the limiting forms of the two solutions for $k{\rightarrow}0$ and $k{\rightarrow}\infty$.

For $k{\rightarrow}0$, the larger solution $\omega_{+}(k)$ approaches a constant value ω_{+}^{0}. From Eq. (4.70) I obtain

$$\omega_{+}^{0} = \frac{1}{R}\sqrt{\frac{c_{11}}{\rho_{2D}}} + \mathcal{O}\left(k^2\right)\,. \tag{4.73}$$

The lower solution $\omega_{-}(k)$ approaches the value $\omega_{-} = vk$, where v is the velocity of longitudinal mode, modified by its coupling to the RBM. Inserting this in Eq. (4.70) and taking the limit $k{\rightarrow}0$, I obtain

$$v = \frac{\omega}{k} = \sqrt{\frac{c_{11}\left(1-\alpha^2\right)}{\rho_{2D}}}\,, \tag{4.74}$$

where $\alpha = c_{12}/c_{11}$ is the Poisson ratio. The numerical value of the velocity obtained using this expression, v = 21.45 nm/ps, is slightly smaller than the velocity of the longitudinal mode

$$v = \frac{\omega}{k} = \sqrt{\frac{c_{11}}{\rho_{2D}}}\,, \tag{4.75}$$

which turns out to be $v = 21.77$ nm/ps. The 1% reduction by the factor of $\sqrt{1-\alpha^2}$ is caused by the coupling of the longitudinal mode to the RBM.

In the opposite limit $k \rightarrow \infty$, the lower solution $\omega_-(k)$ approaches a value, which is a little below the uncoupled RBM frequency [19] of a nanotube with $R = 1$ nm,

$$\omega = \frac{1}{R}\sqrt{\frac{c_{11}}{\rho_{2D}}} = 117 \text{ cm}^{-1} . \tag{4.76}$$

I can obtain the coupled RBM frequency ω_-^{∞} from Eq. (4.70) by neglecting its value in comparison with $c_{11}k^2/\rho_{2D}$. This yields

$$\omega = \frac{1}{R}\sqrt{\frac{c_{11}\left(1-\alpha^2\right)}{\rho_{2D}}} = 115 \text{ cm}^{-1} . \tag{4.77}$$

The 1% reduction of the RMB frequency in the $k \rightarrow \infty$ limit by the factor of $\sqrt{1-\alpha^2}$ is again caused by the coupling of the longitudinal mode to the RBM.

For $k \rightarrow \infty$, the upper solution approaches the value $\omega_+ = vk$, where v is the velocity of the uncoupled LA mode. Neglecting $c_{11}/(\rho_{2D}R)$ in comparison with v^2k^2 and neglecting k^2 terms in comparison with k^4 terms in Eq. (4.70), I arrive at

$$v = \sqrt{c_{11}/\rho_{2D}} \tag{4.78}$$

with no corrections due to the coupling to the RBM. This was to be expected, since for $kR \gg 1$, this nanotube mode corresponds to the LA mode in a graphene sheet.

Chapter 5

Unusually stable helical coil allotrope of phosphorus

The following discussion is my original contribution to the related publication by Dan Liu, Jie Guan, Jingwei Jiang, and David Tománek, Nano Lett. **16**, 7865-7869 (2016) [61].

5.1 Introduction

Elemental phosphorus has been known for its unusual properties since its isolation as the white phosphorus allotrope [62], a P_4-based molecular solid, in 1669. Other observed allotropes include violet phosphorus [63, 64], also known as Hittorf's metallic phosphorus [65, 66], rather common fibrous red phosphorus [66, 67] with an amorphous structure, and layered black phosphorus [68], known as the most stable crystalline allotrope. Other bulk allotropes, including blue phosphorene, have been predicted [2] and subsequently synthesized [69]. Other structures of elemental phosphorus, which have been studied, include P_n clusters [70–72] and atomically thin P helices, which have been identified as constituents [73] in the complex structure of SnIP. It thus appears quite possible that still more allotropes may be synthesized in the future.

I report here theoretical results that identify an unusually stable helical coil allotrope of phosphorus. The *ab initio* Density Functional Theory calculations indicate that the uncoiled,

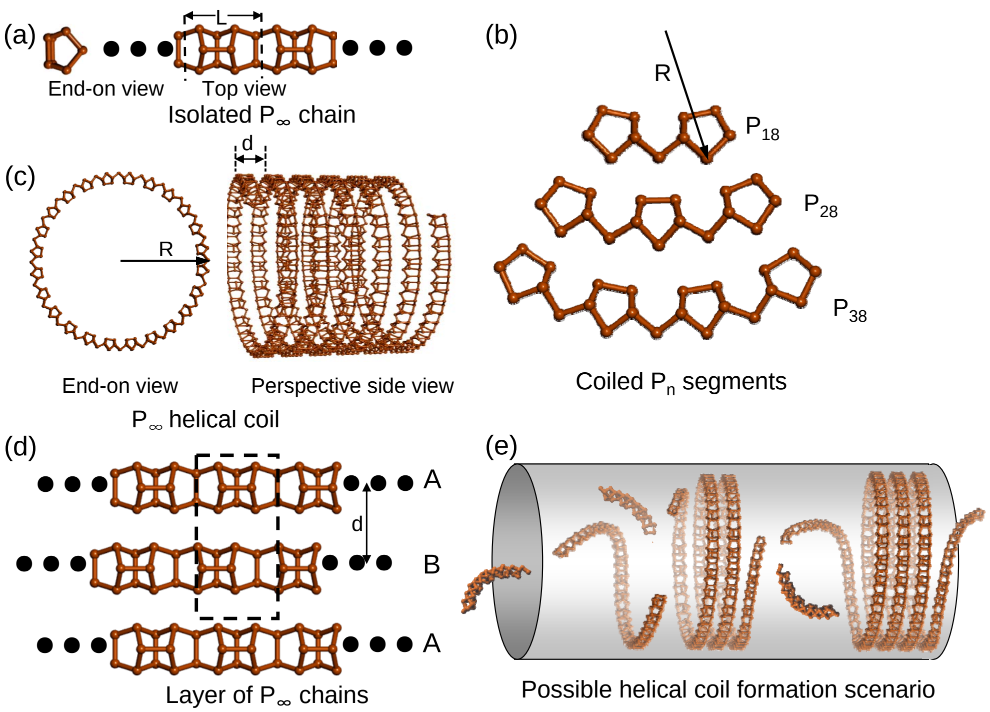

Figure 5.1: (a) Optimum structure of an isolated, straight 1D P_∞ chain with the P_{10} unit cell of length L. (b) Optimized P_{18}, P_{28} and P_{38} segments of the isolated chain, indicating the tendency to form rings with a radius $R\approx 2.4$ nm. (c) The optimum structure of a single coil. (d) Optimum structure of a 2D assembly of P_∞ chains separated by the distance d. (e) Possible scenario for the formation of helical coils by connecting finite-length chain segments inside a cylindrical cavity. The unit cells are indicated by dashed lines in (a) and (d).

isolated straight 1D chain is equally stable as a monolayer of black phosphorus dubbed phosphorene. The coiling tendency and the attraction between adjacent coil segments add an extra stabilization energy of ≈12 meV/atom to the coil allotrope, similar in value to the ≈16 meV/atom inter-layer attraction in bulk black phosphorus. Thus, the helical coil structure is essentially as stable as black phosphorus, the most stable phosphorus allotrope known to date. With an optimum radius of 2.4 nm, the helical coil of phosphorus may fit well and even form inside wide carbon nanotubes.

5.2 Computational methods

Global search for small structural fragments of phosphorus was performed using Adaptive Genetic Algorithms based on a tight-binding Hamiltonian with universal parameters. [74] Suitable structural candidates were then optimized using *ab initio* density functional theory (DFT) as implemented in the SIESTA [13] code to obtain insight into the equilibrium structure, stability and electronic properties of phosphorus structures reported in the main manuscript. All isolated structures, including infinite 1D chains and bent chain segments, have been represented using periodic boundary conditions and separated by a 15 Å thick vacuum region in all directions. I have used the Perdew-Burke-Ernzerhof (PBE) [9] or alternately the Local Density Approximation (LDA) [8, 75] forms of the exchange-correlation functional, norm-conserving Troullier-Martins pseudopotentials [33], and a local numerical double-ζ basis including polarization orbitals. The Brillouin zone of periodic structures has been sampled by a fine grid [34] of 12×1×1 k-points for 1D structures and 12×8×1 k-points for 2D structures. I found the basis, the $k-$point grid, and the mesh cutoff energy of 180 Ry used in the Fourier representation of the self-consistent charge density to be fully converged, providing us with a precision in total energy of 2 meV/atom. All geometries have been optimized using the conjugate gradient method [76] until none of the residual Hellmann-Feynman forces exceeded 10^{-2} eV/Å.

5.3 Results and discussion

The unusually stable structure of a P_{10} cluster and its suitability to link up to an infinite 1D chain was discovered while developing and testing a Genetic Algorithm optimization technique for phosphorus clusters based on a tight-binding formalism [74]. The optimum

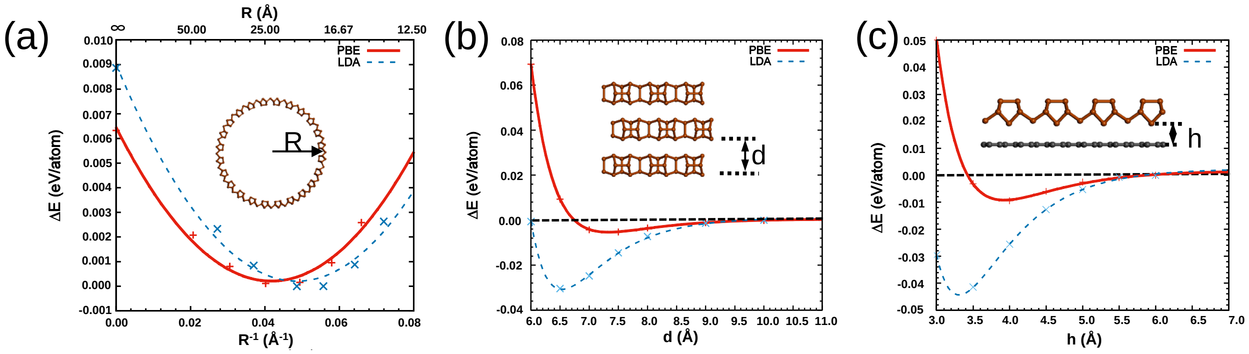

Figure 5.2: (a) Strain energy ΔE per atom as a function of the radius R of an isolated P coil. (b) Inter-chain interaction energy ΔE per atom in a 2D assembly of phosphorus chains, depicted in Fig. 5.1(d), as a function of the inter-chain distance d. (c) Interaction energy ΔE per phosphorus atom between a P chain and a graphene monolayer as a function of the adsorption height h. PBE results are shown by the solid red lines, LDA results by the dashed blue lines.

structure of a P_{10} unit cell in a straight 1D chain, which resembles a narrow tube with a pentagonal cross-section, is shown in Fig. 5.1(a). I notice a structural similarity with fibrous red [66, 67] and violet phosphorus [63–66] structures, which also contain P_{10} subunits in the interlinked chains. The postulated chain structure is also similar to P nanorods [77, 78] and P tubes [79] observed in the AgP_{15} compound. The DFT-PBE calculations indicate a binding energy $E_{coh} = 3.274$ eV/atom for the postulated P_{10} structure with respect to spin-polarized P atoms. This value is only negligibly larger than that of a monolayer of black phosphorus, known as the most stable phosphorus allotrope, with $E_{coh} = 3.273$ eV/atom.

Finite chain segments, shown in Fig. 5.1(b), display a tendency to form coils with an average radius of 2.4 nm. I find this coiling, which had been identified earlier [70, 80], to be associated with an energy gain of 6 meV/atom (PBE) and 9 meV/atom (LDA). Assuming that an ordered P_∞ system may form by connecting finite P_n segments end-to-end, the resulting equilibrium structure will be a helical coil, depicted in Fig. 5.1(c). On a per-atom basis, the elastic strain ΔE in the coil is shown in Fig. 5.2(a) as a function of radius R. The data points are well represented by

$$\Delta E = \frac{1}{2} k \left(\frac{1}{R} - \frac{1}{R_{eq}} \right)^2 , \tag{5.1}$$

where R_{eq} is the equilibrium radius. This expression describes the local strain energy in a finite-length 1D beam thought to be initially aligned with the $x-$direction and deformed to a circular arc of radius R in the $xz-$plane. The local strain is $\sigma = d^2u_z/dx^2 = 1/R$. Should not a straight, but rather a bent beam of radius R_{eq} represent the equilibrium structure, then the local strain would be $\sigma = d^2u_z/dx^2 - 1/R_{eq} = 1/R - 1/R_{eq}$. Equation (5.1) describes the corresponding local strain energy [81]. I find $k = 7.2$ eVÅ^2 for the rigidity of the elastic beam and $R_{eq} = 24$ Å for the optimum radius of curvature based on PBE. The LDA values of $k = 7.5$ eVÅ^2 and $R_{eq} = 21$ Å are in fair agreement with the PBE values.

Same as in the infinite chain, the stability of the helical coil is dominated by the covalent interatomic bonds, which are described well by DFT calculations. The coil is further stabilized by the weak attraction between neighboring strands that is similar in nature to the inter-layer attraction in bulk black phosphorus. As shown in superior Quantum Monte Carlo (QMC) calculations of the latter system [82], the fundamental nature of the inter-layer interaction is rather non-trivial, different from a van der Waals interaction, and not reproduced well by DFT functionals with or without van der Waals corrections. When compared to the more accurate QMC value of 81 meV/atom, the LDA value of 94 meV/atom overestimates and the PBE value of 16 meV/atom underestimates the inter-layer interaction in bulk black phosphorus. I also notice the large ratio of $5 - 6$ between PBE and LDA values for the weak inter-layer interaction. Extrapolating what is known about the interlayer interaction in black phosphorus to the inter-chain interaction in a 2D assembly of chains of Fig. 5.1(d) or the related wall of the helical coil in Fig. 5.1(c), I expect that PBE will also underestimate and LDA overestimate the value of this weak interaction.

In view of the fact that the optimum coil radius is much larger than the chain thickness, the wall of the infinite helical coil in Fig. 5.1(c) is well represented by a 2D assembly of chains of Fig. 5.1(d). I found that the most stable 2D arrangement is one with AB stacking of chains. The inter-chain interaction energy ΔE is displayed as a function of the inter-chain distance d in Fig. 5.2(b). As anticipated above, I expect a large difference between PBE and LDA interaction energies. I obtain the optimum distance $d_{eq} = 7.3$ Å and the interaction energy $\Delta E = 5.3$ meV/atom based on PBE. LDA suggests a smaller separation $d_{eq} = 6.5$ Å and a much larger interaction energy $\Delta E = 30.8$ meV/atom. While still small, the LDA interaction energy is roughly five times higher than the PBE value.

Postulating a new allotrope is of limited use without a plausible formation scenario. I note that previously, the void inside carbon nanotubes has been successfully filled by sublimed C_{60} fullerenes that eventually fused to an inner nanotube [83]. Similarly, functionalized diamondoid molecules were observed to enter the nanotube void, where they converted to carbon chains [84] or diamond nanowires [85]. Inspired by these results, I feel that the most suitable scenario to form a helical coil phosphorus allotrope involves a cylindrical cavity, shown in Fig. 5.1(e).

Suitable cavities with an optimum inner diameter of few nanometers may be found in zeolites or in nanotubes of carbon, BN and other materials. The phosphorus feedstock could be white, red or violet phosphorus that had been sublimed in vacuum, under exclusion of air. The sublimed species would likely be finite-chain segments, shown in Fig. 5.1(b), which may enter at the open end and benefit energetically from the interaction with the inner wall of the cavity. As seen in Fig. 5.2(c), where I consider the related system of an isolated chain

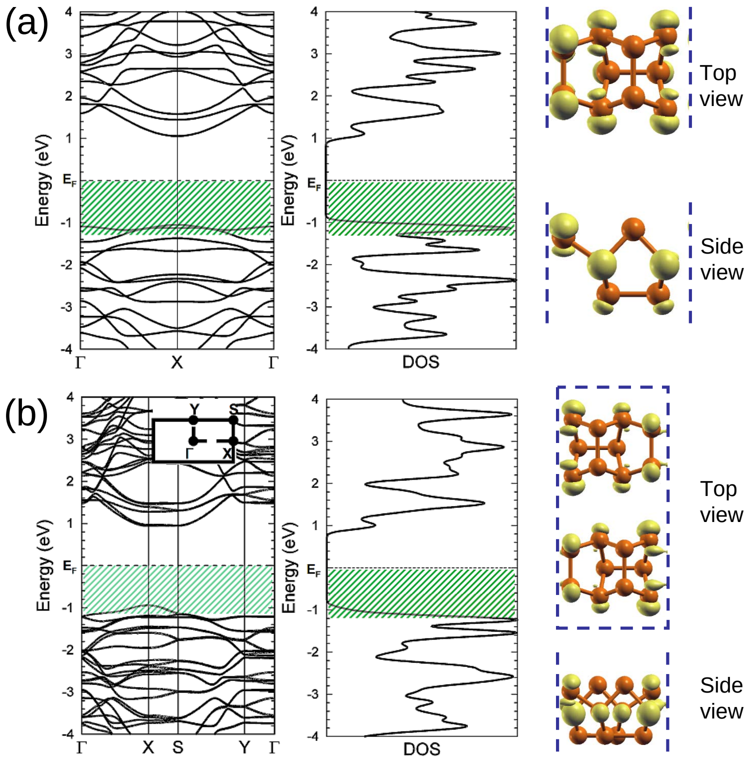

Figure 5.3: Electronic structure of (a) an isolated P chain and (b) a 2D layer of P chains, shown in Figs. 5.1(a) and 5.1(d). Left panels depict the electronic band structure based on PBE and the middle panels the corresponding density of states. The Brillouin zone is shown as inset of the left panel in (b). The right panels depict the charge distribution associated with frontier states in the valence band region, indicated by the green hashed region in (a) and (b), which extends from E_F to 0.2 eV below the top of the valence band. Charge density contours are superposed to structural models, with the unit cells indicated by the dashed lines. Due to differences in the density of states between these systems, the contours are presented at the electron density 0.008 e/Å^3 in (a) and 0.002 e/Å^3 in (b).

on graphene, this interaction is weak and similar in nature to the inter-chain interaction in Fig. 5.2(b). The optimum arrangement is found by inspecting the adsorption energy ΔE as a function of height h in Fig. 5.2(c). For the optimum geometry, I find $\Delta E_{eq} = 9$ meV per P atom at $h_{eq} = 3.9$ Å based on PBE and $\Delta E_{eq} = 44$ meV per P atom at $h_{eq} = 3.3$ Å based on LDA. I notice here again the adsorption energy ratio of ≈5 between LDA and PBE results, consistent with the other results.

Once inside and near the wall of the cylindrical cavity, finite P_n chain fragments will benefit energetically from an end-to-end connection that eliminates open ends. The number of atoms in the finite circular arc, preferentially oriented along the perimeter of the inner cavity, will grow. At the elevated temperatures of subliming phosphorus, the growing P_n ring fragments are very unlikely to interconnect with corresponding segments that contain exactly the right number of atoms, which would complete a ring at the optimum distance to the wall. Much more likely, the last segment to join before possible ring closure will be too long and start the formation of a helical coil. Since transformation of the coil to one or more adjacent rings would require bond breakage within the coil, it is unlikely to happen.

The electronic structure of the new allotrope, similar to that of phosphorene, is of utmost interest [86]. The PBE results for the related phosphorus chains and their 2D assemblies are shown in Fig. 5.3. As seen in Fig. 5.3(a), the P_∞ chain has a direct fundamental band gap of 2.03 eV at X. Similarly, also the 2D chain assembly has a direct band gap of 1.82 eV at X as seen in Fig. 5.3(b). Based on what is known theoretically and experimentally about few-layer phosphorene [86], the PBE band gap values are strongly underestimated in comparison to the experiment.

In view of the fact that phosphorus is typically $p-$doped, I are also interested in the nature of the frontier states in the valence band region. I plotted the charge distribution of these states, covering the energy range between E_F and 0.2 eV below the top of the valence band, in the right panels of Fig. 5.3. Similar to what is known about black phosphorus, I observe lone-pair electron states in the isolated chain in Fig. 5.3(a) that contributes to the electronic inter-chain coupling modifying the band structure, as seen in Fig. 5.3(b). This demonstrated influence of the inter-chain coupling on the electronic structure is a clear evidence that the interaction differs from a purely van der Waals interaction, similar to black phosphorus [82].

In view of the relatively low beam rigidity of the coiling chain, I expect the coils to adjust their radius freely for the optimum fit inside cylindrical cavities. The ability of the helical coil strands to slide past each other allows the helix to adjust to a changing cavity diameter. In view of the favorable inter-chain interaction of 16 meV/atom for an AB stacking in the radial direction, with an optimum inter-chain distance of 0.6 nm based on PBE, I consider it quite possible for a second helix forming inside the outer helix. Considering an outer helical coil at its equilibrium radius $R_{out} = 2.4$ nm, the inner coil should have a radius of $R_{in}{\approx}1.8$ nm. In PBE, the strain energy in the inner structure of < 1 meV/atom according to Fig. 5.2(a) is negligibly small when compared to the additional inter-chain interaction energy of 16 meV/atom. I may even imagine additional helices forming inside the double-helix structure. In view of the low beam rigidity of the chain and the large inter-chain interaction, a structure consisting of nested coaxial coils should be even more stable than bulk black phosphorus, the most stable phosphorus allotrope known to date.

As suggested by the end-on view of a chain in Fig. 5.1(a), the cross-section of the helical coil should appear as lines of pentagons near the walls and along the axis of the cylindrical cavity in Transmission Electron Microscopy (TEM) images. This is very similar to recently observed TEM data [87]. I can imagine left- and right-handed helical coils forming simultaneously and coexisting inside a suitable cylindrical cavity.

As a structural alternative, a black phosphorus monolayer may also roll up to a tube inside a carbon nanotube with a 2.4 nm radius. Assuming an inter-wall distance of 0.5 nm, the radius of the phosphorene nanotube should be $R{\approx}1.9$ nm, and its strain energy should be $\approx$8.6 meV/atom if bent along the soft direction to become an armchair P nanotube, or 42.1 meV/atom if bent along the normal, harder direction [19]. Thus, energetically, a black phosphorus nanotube is not favorable. Also a straight 1D phosphorus chain inside a nanotube should be less stable by > 6 meV/atom than the coiled structure. Thus, I find the coil to be more stable than competing phosphorene nanotube and straight chain structures. Also, assuming that the new phase forms by sublimation of red phosphorus, it will more likely resemble structural elements of red P than the completely different black P.

In layered black phosphorus, the observed bulk band gap value of 0.35 eV is known to increase to 2 eV in the monolayer due to the change in the weak interlayer interaction. PBE calculations underestimate the band gap significantly, suggesting a value of 0.04 eV for the bulk and 0.9 eV for the monolayer. I thus expect also the calculated band gap in isolated chains to lie below the experimental value and to decrease due to inter-chain interaction in 2D chain assemblies. In helical coils, a further reduction, which should furthermore depend on the coil radius, is expected due to improved screening of the electron-hole interaction. In view of this reasoning, it is not surprising that the calculated band gap values lie rather close to the value of 1.95 eV that has been observed in fibrous red phosphorus [88].

Further electronic structure changes induced by coil deformation may open a wide range of applications. Similar to bulk black phosphorus, where changes in the interlayer distance d modify the band gap E_g significantly, I find that axial compression of the coil also modifies the band gap. At the optimum value 0.73 nm for the inter-coil distance d, defined in Fig. 5.2(b), the gap is direct and $E_g = 1.8$ eV according to Fig. 5.3(b). Reducing d to 0.6 nm turns the gap indirect and reduces its value to $\approx$0.8 eV. Further reduction to $d = 0.5$ nm turns the coil metallic. Increasing the inter-chain distance to $d = 0.8$ nm opens the gap to E_g 2.0 eV, while maintaining its direct character. Of course, these changes in the fundamental band gap may only be exploited inside semiconducting nanotubes, such as BN, which have even larger band gaps.

5.4 Summary

In conclusion, I have identified computationally an unusually stable helical coil allotrope of phosphorus. The *ab initio* Density Functional Theory calculations indicate that the uncoiled, isolated straight 1D chain is equally stable as a monolayer of black phosphorus dubbed phosphorene. The coiling tendency and the attraction between adjacent coil segments add an extra stabilization energy of ≈12 meV/atom to the coil allotrope, similar in value to the ≈16 meV/atom inter-layer attraction in bulk black phosphorus. Thus, the helical coil structure is essentially as stable as black phosphorus. In view of the low beam rigidity of the chain and the large inter-chain interaction, a structure consisting of nested coaxial coils should be even more stable than bulk black phosphorus, the most stable phosphorus allotrope known to date. With an optimum radius of 2.4 nm, the helical coil of phosphorus may fit well and even form inside wide carbon nanotubes. I find the coiled P structure to be a semiconductor with a direct gap exceeding 1.8 eV. The size and character of the band gap can further be modified by small structural changes in the coil.

Chapter 6

Microscopic Mechanism of the Helix-to-Layer Transformation in Elemental Group VI Solids

The following discussion is my original contribution to the related publication by Dan Liu, Xianqing Lin and David Tománek, Nano Lett. **18**, 4908-4913 (2018) [89].

6.1 Introduction

After much attention has been devoted to graphene, a 2D allotrope of group IV elemental carbon, scientific interest turned to semiconducting 2D allotropes of group V elements P [86, 90] and As [91,92]. Recent observation of 2D allotropes of group VI elements Se and Te [93–95] came as a surprise, since – unlike group IV and V elemental solids – the bulk structure of Se and Te is not layered, but consists of helical chains of covalently bonded atoms packed in a hexagonal array. For lack of well-defined layers, 2D Se and Te can not be obtained by mechanical exfoliation used in group IV and V systems. Chalcogens are known for a large number of stable allotropes and oxidation states [96]. The latter fact had been identified as the key factor behind the stability of specific 2D allotropes of Se and Te [93]. Still, the

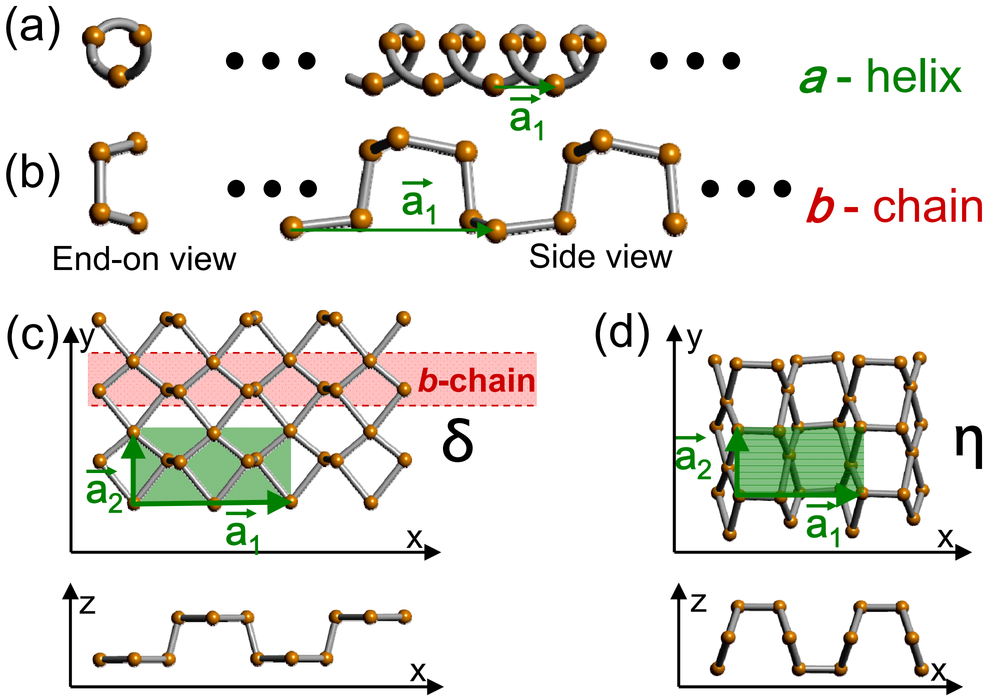

Figure 6.1: Stable 1D and 2D structural allotropes of Se and Te. 1D structures of the (a) *a* helix and (b) *b* chain and their 2D counterparts, the (c) δ and (d) η allotrope. The δ allotrope is a covalently bonded 2D assembly of *b* chains. The unit cells of the 2D structures are highlighted by the transparent green areas in (c) and (d).

strong dissimilarity between the bulk structure containing weakly interacting, intertwined *a* helices and covalently bonded, atomically thin layers raises the intriguing question about the microscopic mechanism behind the transformation from quasi-1D to 2D structures, which has not been addressed yet.

Here I present results of *ab initio* calculations, which help to identify the intermediate steps of the observed transition from *a* helices in the native bulk structure to atomically thin layers of elemental Se and Te [93]. The results unveil the energetics and the intermediate steps encountered during this structural transition. I have discovered an intriguing mechanism that converts an *a* helix to a more stable, previously unknown *b* chain by moving a point-dislocation connecting these two structures. In a zipper-like motion, the *b* chain may reconnect to a previously unknown 2D δ structure, which is unusually stable, similar to the

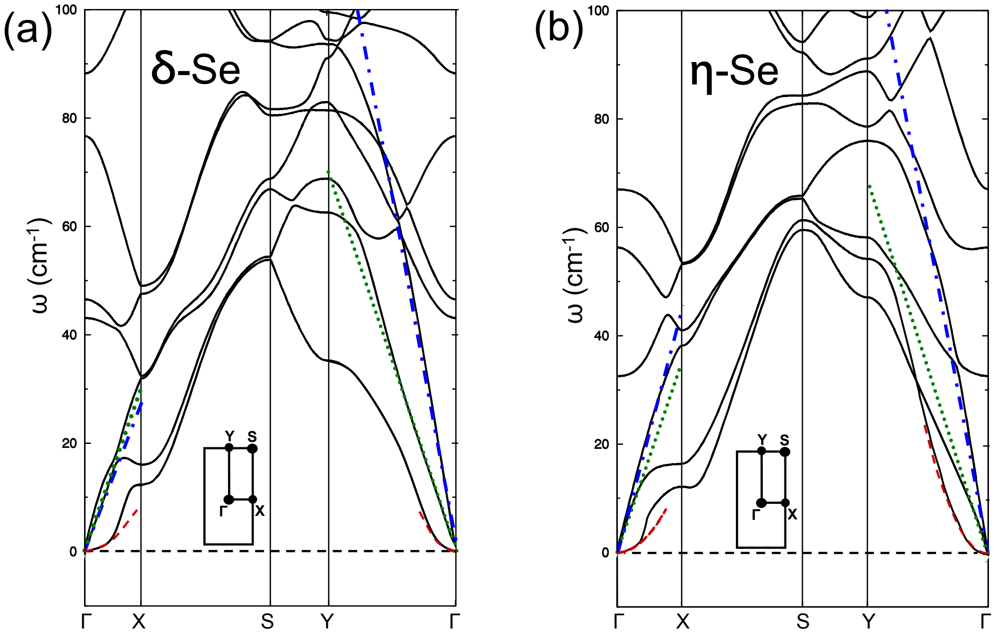

Figure 6.2: Phonon spectra of (a) δ-Se and (b) η-Se calculated using the DFT-LDA energy functional. The Brillouin zones and high-symmetry points are shown schematically in the insets. Continuum elasticity results for long-wavelength longitudinal acoustic modes are shown by the blue dash-dotted lines, for transverse acoustic modes by the dotted green lines, and for flexural modes by the dashed red parabolas.

related η structure. The structural change from the a helix to the 2D δ allotrope is mildly exothermic with -0.17 eV/atom for Se and -0.23 eV/atom for Te. The low number of structural constraints allows the helical structure to exploit many degrees of freedom and thus to lower the activation barriers along the reaction path to $\lesssim$0.3 eV, indicating that the transition may occur at moderate temperatures. The GW quasiparticle calculations of the electronic structure indicate that all quasi-1D and 2D chalcogen allotropes are semiconducting.

6.2 Computational techniques

The calculations of the stability, equilibrium structure, the pathway and dynamics of structural transformations have been performed using density functional theory (DFT) as implemented in the SIESTA [13] and VASP [14, 17] codes. Periodic boundary conditions have been used throughout the study, with monolayers represented by a periodic array of slabs separated by a 30 Å thick vacuum region. I compared results using both the Local Density Approximation (LDA) [8, 75] and the Perdew-Burke-Ernzerhof (PBE) [9] exchange-correlation functionals, since LDA typically overbinds and PBE underbinds. I also checked the importance of van der Waals corrections to the total energy by using the optB86b exchange-correlation functional [97, 98] for selected structures. The SIESTA calculations used norm-conserving Troullier-Martins pseudopotentials [33], a double-ζ basis including polarization orbitals, and a mesh cutoff energy of 180 Ry to determine the self-consistent charge density, which provided us with a precision in total energy of $\lesssim$2 meV/atom. The VASP calculations were performed using the projector augmented wave (PAW) method [17] and 500 eV as energy cutoff. The reciprocal space has been sampled by a fine grid [34] of 10×10 k-points in the 2D Brillouin zones (BZ) of the primitive unit cells of the δ and η structures containing 6 atoms each, and 10 k-points in the BZ of 1D a and b chains with 3- and 6-atom unit cells, respectively. Geometries have been optimized using the conjugate gradient (CG) method [76], until none of the residual Hellmann-Feynman forces exceeded 10^{-2} eV/Å. Microcanonical and canonical MD calculations were performed using 1 fs time steps. Electronic structure has been calculated using the GW quasiparticle approach [99] as implemented in the BerkeleyGW package [100] interfaced with QuantumEspresso [101]. In a periodic arrangement, 1D and 2D structures were separated by 17 Å wide vacuum regions. The Brillouin zone of quasi-1D structures was sampled by $36\times1\times1$ k-points and that of quasi-2D structures by $6\times14\times1$ k-points. I used 10 Ry as energy cutoff for the plane wave expansion of the dielectric matrix. The quasiparticle energies have been determined by considering the lowest 220 unoccupied conduction bands and accounting for all higher-lying bands using the

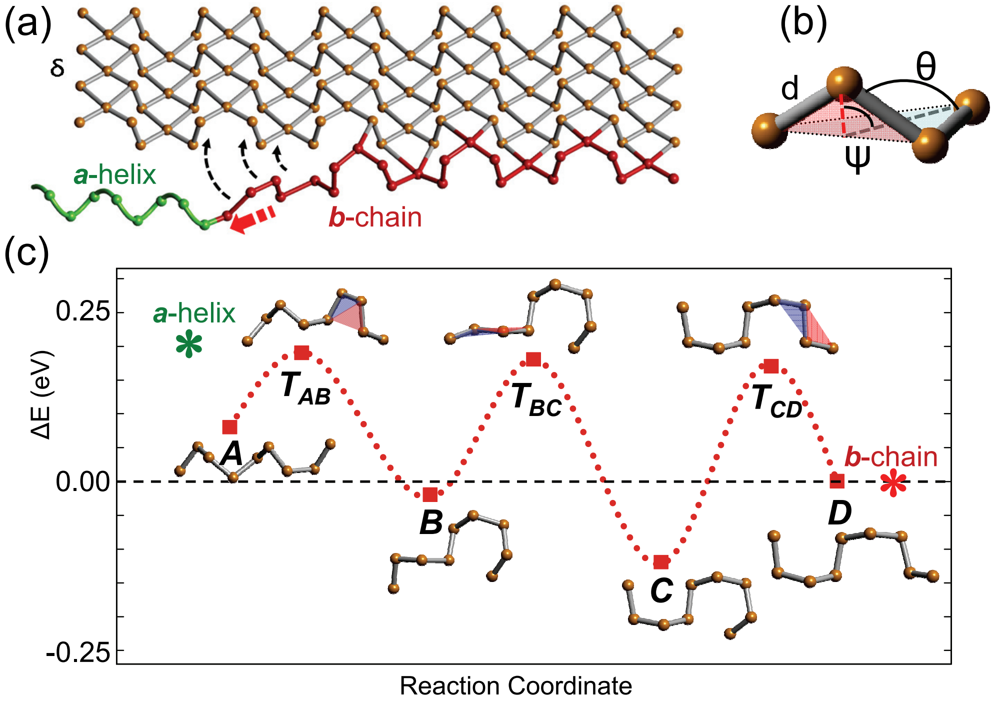

Figure 6.3: (a) Schematic growth mechanism of the energetically stable 2D δ structure by zipper-like attachment of the b chain, which is being formed locally locally at a defect in the native a helix and propagates by dislocation motion. (b) Bond length d, bond angle θ and dihedral angle ψ used to characterize chalcogen structures. (c) DFT-LDA based energy differences ΔE encountered during the stepwise conversion from 1D a-Se to b-Se as a function of the reaction coordinate. The system is represented by a finite Se_9H_2 chain, passivated by hydrogen at both ends, and the total energy is given with respect to the final state. The dotted line is guide to the eye. The energy of a 9-atom long segment of the defect-free infinite a-Se and b-Se chains is indicated by asterisks. Ball-and-stick models show stable Se_9H_2 geometries, labeled by A-D, and the transition states T. Location of the unusually small dihedral angle in the transition states is indicated by shaded triangles.

modified static-remainder approximation [102].

6.3 Results and discussions

Understanding the observed 1D to 2D transformation is an unprecedented challenge due to the large and constantly changing number of degrees of freedom that are actively involved in lowering the activation barriers between intermediate states. In this complex system, the use of common techniques such as the nudged elastic band model becomes a futile

Table 6.1: Cohesive energy E_{coh} of various Se and Te allotropes in [eV/atom] units, obtained using DFT-LDA and DFT-PBE calculations.

		a-helix	b-chain	α	β	γ	δ	η
Se	LDA	3.677	3.700	3.795	3.823	3.569	3.843	3.854
	PBE	3.307	3.327	3.198	3.302	2.953	3.357	3.355
Te	LDA	3.209	3.235	3.479	3.434	3.323	3.443	3.451
	PBE	2.856	2.871	2.904	2.933	2.716	2.940	2.943

endeavor. Restricting the system's freedom invariably increases the activation barriers, incorrectly suggesting that the transformation should not occur under laboratory conditions. I chose a different approach that will be discussed in the following.

Recently observed 2D Se and Te structures [93–95, 103] have been formed by initially evaporating the bulk substances. It is likely that the vapor contained primarily short segments of a helices, shown in Fig. 6.1(a), which constitute the bulk structure. Consequently, I will consider the a helix as the initial structure in the transformation process to 2D structures. I discovered a previously unknown, atomically thin and unusually stable 2D structure of Se and Te, which I call the δ structure, by artificially compressing a 2D assembly of the native a-Se helices in the direction normal to the 2D layer. The 2D δ allotrope, shown in Fig. 6.1(c), emerged after the pressure was released. An impractical, yet computationally feasible way to transform 1D to 2D structures is by artificial confinement in a 2D plane, as shown in Fig. 6.4. The initial structure, depicted in Fig. 6.4(a), consists of a 2D assembly of parallel Se helices separated by $d = 3.83$ Å. The atomic positions in the artificial flat structure shown in Fig. 6.4(b) are obtained by projecting this structure onto a plane. By re-optimizing this structure, I obtained 2D δ-Se, shown in Fig. 6.4(c).

Another previously unknown and stable allotrope, labeled η, is depicted in Fig. 6.1(d). It is related to the δ structure by a series of reflections,while keeping the bond lengths and bond angles constant throughout the structure. The space group of the δ structure is C_{2v}^{4} in the

Schönflies notation and its group number is #28. The space group of the η structure is D_2^2 in the Schönflies notation and its group number is #17. Both groups have only 4 symmetry operations.The structural transformation from the δ to the η structure is depicted in Fig. 6.5. The δ allotrope in Fig. 6.5(a) is transformed to the allotrope in Fig. 6.5(b) by first reflecting the part of the structure on the right of sites $1, 2, 3$ in a plane containing these atoms. This is to be followed by an infinite series analogous reflections involving sites $4, 5, 6$, then $1', 2', 3'$, etc., resulting in a structure reminiscent of a staircase. The structure in Fig. 6.5(b) is transformed to the final η allotrope in Fig. 6.5(c) by an analogous series of reflections. This transformation starts by reflecting the part of the structure on the right of sites $3, 4$ in a plane containing these atoms. This is to be followed by an infinite series analogous reflections involving sites $6, 1'$, then $3', 4'$, etc. A perspective view of the initial δ structure is shown in Fig. 6.5(d) and that of the final η structure in Fig. 6.5(e). Numerical results for the cohesive energies of all known Se and Te allotropes are summarized in Table 6.1.

I studied the stability of the new phases by determining their elastic response and their phonon spectra. Since the 3D elastic modulus tensor is not defined for a truly 2D system, which does not naturally form layered 3D compounds, I have determined the components of the 2D elastic tensor defined earlier [19]. For the δ-phase of Se, I find $c_{11} = 4.97$ N/m, $c_{22} = 20.02$ N/m, $c_{66} = 5.92$ N/m, $D(\Gamma - X) = 0.33$ eV, $D(\Gamma - Y) = 1.15$ eV. For the η-phase of Se, I find $c_{11} = 11.25$ N/m, $c_{22} = 22.71$ N/m, $c_{66} = 7.09$ N/m, $D(\Gamma - X) = 0.39$ eV, $D(\Gamma - Y) = 1.02$ eV. Among others, these elastic constants allow a more accurate representation of low-frequency acoustic modes in the vibrational band structure of the 2D structures, which I present in Fig. 6.2. Due to the similarity of the phonon spectra, I expect the zero-point motion to not to play an important role in the cohesive energy. I find a zero-point energy of 23 meV/atom for β-Se and 24 meV/atom for δ-Se and η-Se, with energy

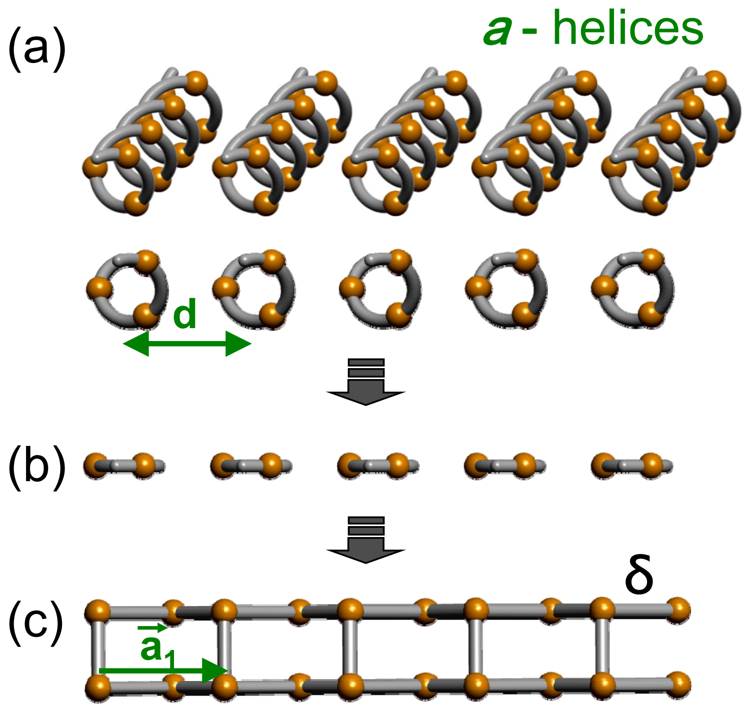

Figure 6.4: Transformation of 1D to 2D structures of elemental Se. (a) Perspective and end-on view of the initial 2D assembly of 1D *a*-chains. (b) End-on view of the structure after artificial confinement to an infinitely thin slab. (c) End-on view of the 2D δ-Se allotrope that formed spontaneously after the structure in (b) was relaxed.

differences of $\lesssim$0.1 meV/atom between the different phases.

In the following, I will first address structures of elemental Se and refer discussion of Te structures for later. The DFT-LDA and DFT-PBE results suggest that δ-Se and η-Se are energetically near-degenerate. The previously introduced [93, 94] β-Se allotrope is less stable than δ-Se by 20 meV/atom (LDA) and 55 meV/atom (PBE) and thus the least stable of the three. Still, in view of the relatively small energy differences and structural similarities, I expect that all these structural allotropes, and possibly even others, may be formed under synthesis conditions at elevated temperatures. In the following, I will focus on the energetically stable δ structure and its microscopic formation mechanism starting from the native a helix structure.

Inspecting the equilibrium structure of δ-Se in Fig. 6.1(c), I found that it can be viewed

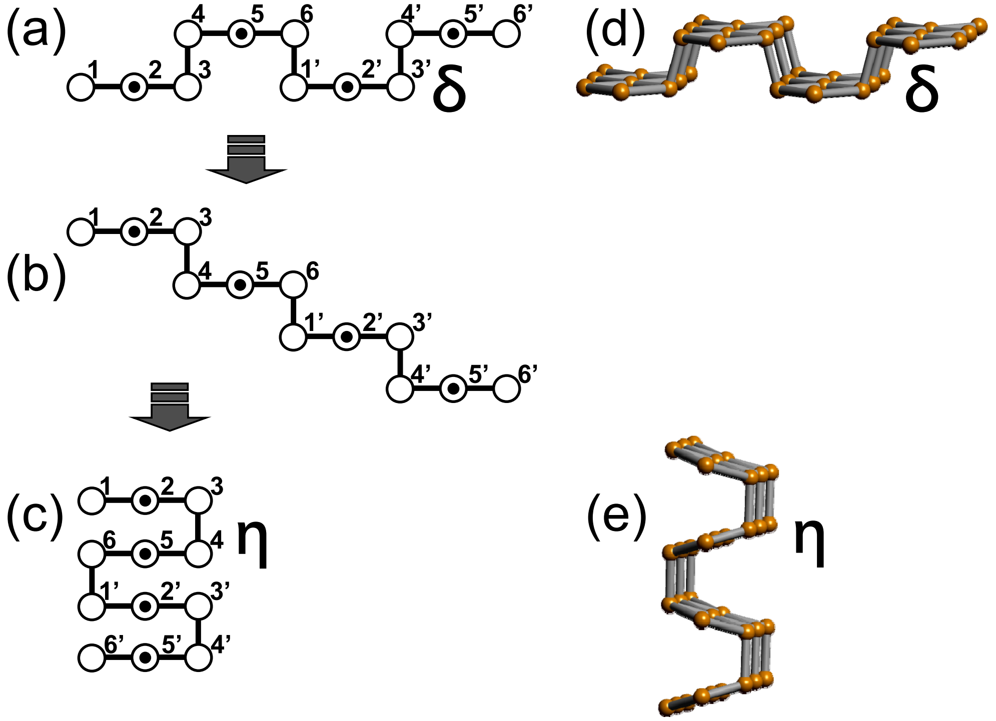

Figure 6.5: Structural transformation between the 2D δ and the η allotropes by a series of reflections in planes normal to the picture plane. (a)-(c) Schematic side view of the initial and intermediate structures. Atoms in a plane normal to the lattice are shown by ◯ and atoms in front of these by ⊙. Atoms in one unit cell are labeled by the numbers $1 - 6$. Primed numbers are used to label atoms in neighboring cells. Perspective views of (d) the initial δ and (e) the final η structure.

as a 2D assembly of 1D chains, which I call b chains. I found the previously unknown b chain, shown in Fig. 6.1(b), to be a stable allotrope of Se, even more stable than the 1D a helix by 23 meV/atom (LDA) and 20 meV/atom (PBE). The b chain may be attached laterally to a semi-infinite δ-Se layer in a zipper-like motion depicted in Fig. 6.3(a). Owing to the multi-valent behavior of the chalcogens [93], this is an activation-free exothermic process that releases 143 meV/atom (LDA) and 30 meV/atom (PBE).

Assuming that b-Se chains, which are entropically favored at high temperatures, are indeed present during the formation of δ-Se, then the only task remaining to understand the entire conversion path from a-Se to δ-Se is locating an energetically favorable pathway for the transformation from the a helix to the b chain. The most plausible transformation begins by connecting the semi-infinite a helix and a b chain end-to-end by a covalent bond, as seen in Fig. 6.3(a). The a-b connection is a dislocation defect or a 0D domain wall that may propagate along the 1D chain, as indicated by the broken arrow in Fig. 6.3(a).For Se, the step-wise a-to-b conversion is exothermic and requires only a finite activation energy to be discussed below. Individual processes within the entire a-to-b-to-δ transformation may occur concurrently, as shown in Fig. 6.3(a).

I noted that observed stable allotropes of Se and Te all share structural commonalities. As defined in Fig. 6.3(b), these include the bond length d(Se)$\approx$2.38 Å and d(Te)$\approx$2.84 Å, the bond angle $\theta\approx100^\circ-130^\circ$, and the dihedral angle $\psi\approx80^\circ-100^\circ$ found experimentally in bulk structures [104–108]. The step-wise dislocation motion corresponds to a series of a-Se to b-Se structural changes at the dislocation, which were studied in finite chain segments containing 12 Se atoms, passivated by hydrogen at both ends. Relaxing the finite segment of a-Se yielded structure A and relaxing the finite b-Se segment resulted in structure D. Interestingly, the infinite a and b chains as well as their finite counterparts A and D displayed very similar structural characteristics as the bulk structures. Later on, I found out that shorter, 9-atom segments shown in Fig. 6.3(c), are sufficient to visualize and understand the step-wise transformations in the 1D structure.

I discovered that the relative stability of the infinite a-Se and b-Se chains, as well as that of the optimized finite segments, can be rationalized in terms of strain originating in the deviation from the optimum bond length $d = 2.36$ Å, bond angle $\theta\approx106^\circ$ and dihedral angle $\psi\approx83^\circ$, defined in Fig. 6.3(b). Most robust of these parameters is the bond length, which is close to its optimum value in all optimized structures. Whereas $\theta = 102^\circ$ and $\psi = 100^\circ$ are constant throughout the unit cell of a-Se, two thirds of the b-Se unit cell display $\theta = 105^\circ$

and $\psi = 83^\circ$, and the rest is characterized by $\theta = 101^\circ$ and $\psi = 100^\circ$. The closer proximity of b-Se to the optimum angles θ and ψ is reflected in its higher stability by 23 meV/atom (LDA) and 20 meV/atom (PBE) with respect to a-Se.

I found that the entire A to D transformation can be accomplished by a sequence of bond rotations or reflection while maintaining the optimum bond lengths d and bond angles θ throughout the structure. The transformation steps only involved changes in one dihedral angle ψ at a time, as shown in Fig. 6.3(c), which required a typical activation energy of $\lesssim$300 meV. The DFT-LDA energies for the process described in Fig. 6.3(c) differ from DFT-PBE results by $\lesssim$30 meV and from van-der-Waals corrected DFT-optB86b results by $\lesssim$25 meV for the entire structure. The similarity in cohesive energies obtained using LDA and PBE is also seen in Table 6.1. I identified two locally stable structures, labeled B and C, along the A to D trajectory. The locally stable states A, B, C and D all displayed near-optimum values of d, θ and ψ throughout the structure. The contiguous trajectory in configurational space contains unstable transition states T_{AB} between A and B, T_{BC} between B and C, and T_{CD} between C and D. I traced back the lower stability of the transition states to one of the dihedral angles being near zero, far from its optimum value. I verified that all transition states T were unstable in the sense that perturbing the $T_{N,N+1}$ structure in whichever way and following up with microcanonical MD calculations or conjugate gradient (CG) optimization always lead to optimum N or $N+1$ geometries and to no other structure. The relative energy and the structure of these states are depicted in Fig. 6.3(c).

The most favorable conversion from the infinite a-helix (related to state A) to the more stable b-chain (related to state D) is a multi-state process that involves intermediate states B and C, as indicated in Fig. 6.6(a). The energetically favored transformation path by dislocation motion along the chain is illustrated schematically in Fig. 6.6(b).For the following discussion, I label individual atoms by numbers in the finite segment of the a-helix structure in Fig. 6.6(c) and in the finite segment of the b-chain structure in Fig. 6.6(d).

I expect the postulated transition process to be just one of many similar transformations in the system that may occur with potentially even lower activation barriers.Results of selected trajectories from the transition points T, identified in Fig. 6.6(c), are presented in Figs. 6.7-6.9 in terms of the dihedral angle ψ and the potential energy E as a function of the number of conjugate gradient (CG) steps or as a function of time in MD simulations. I found it very useful to consider both CG and MD calculations. CG optimization reaches the intermediates states only in case that there are no local minima between the transition states T and the adjacent intermediate states. This limitation is eliminated in MD simulations at the cost of large fluctuations in the potential energy E caused by corresponding fluctuations in the kinetic energy, which increases in time. Of course, I found the total energy to be conserved in the microcanonical MD simulations. Inspection of the results in Fig. 6.7 shows that all trajectories starting in transition point T_{AB}, whether obtained by CG or MD, lead either to the geometry of the adjacent intermediates state A or B. Similarly, in Fig. 6.8, I found all trajectories from T_{BC} to lead either to state B or C. Finally, as seen in Fig. 6.9, I found all trajectories from T_{CD} to lead either to state C or the final state D. The potential energy E has been decreasing along all trajectories starting from the frozen transition state geometry.

Interestingly, I found the interatomic bond distances and bond angles to remain near their optimum values during the entire A-D transformation. The third factor associated with stability, the dihedral angle ψ, was found to change significantly during the process. In all transition-state geometries, I could identify 4-atom segments with a very unfavorable dihedral angle ψ near 0°. Structural evolution of the system from the transition state to

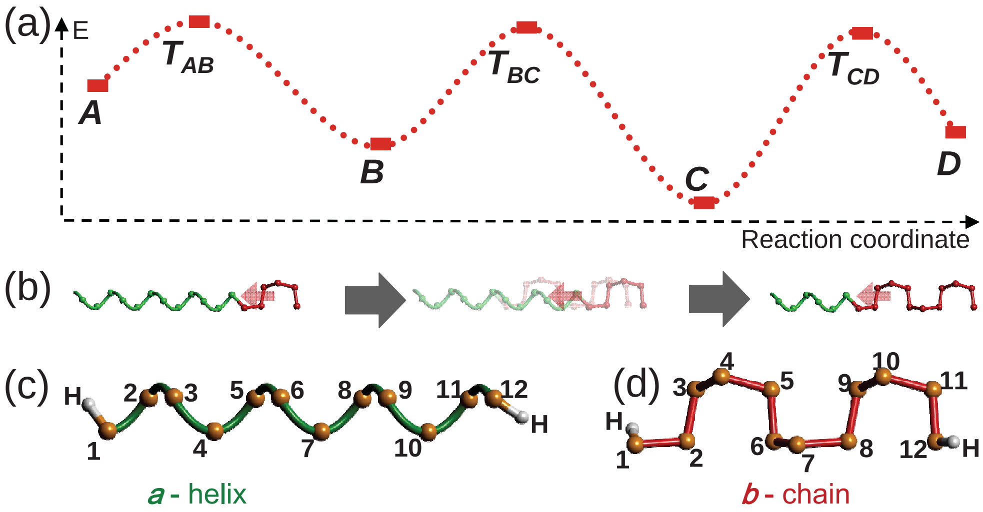

Figure 6.6: (a) Potential energy E as a function of the optimum reaction coordinate during the A-D transformation. (b) Schematic transformation from the a-helix to the b-chain by dislocation motion.Schematic geometry of hydrogen terminated 9-atom segments of (c) the a-helix and (d) the b-chain. Atoms are labeled for later use.

the adjacent intermediate state was in all cases accompanied by a change of the particular dihedral angle ψ towards its optimum value $\approx 83°$. As a matter of fact, I could rationalize the entire transformation from A to D by a sequence of bond rotations.

I should remember that the sequence and energetics of A to D transformations, identified in the finite chain segment, may differ in detail from the corresponding process at a dislocation defect connecting infinite a and b chains, since the free-standing finite structure has fewer constraints than the infinite structure. As seen in Fig. 6.3(c), the net energy gain from the infinite a to the b structure is higher than the energy gain in the finite segment changing from the A to the D structure. As a matter of fact, I should not place too much emphasis on the relative stability of finite A, B, C and D structures, but rather realize that the activation barriers for step-wise structural changes are similar in finite and infinite structures. The energetics and structure of the free-standing finite chain segment will change when connected to a semi-infinite a chain at the one and a semi-infinite b chain at the other

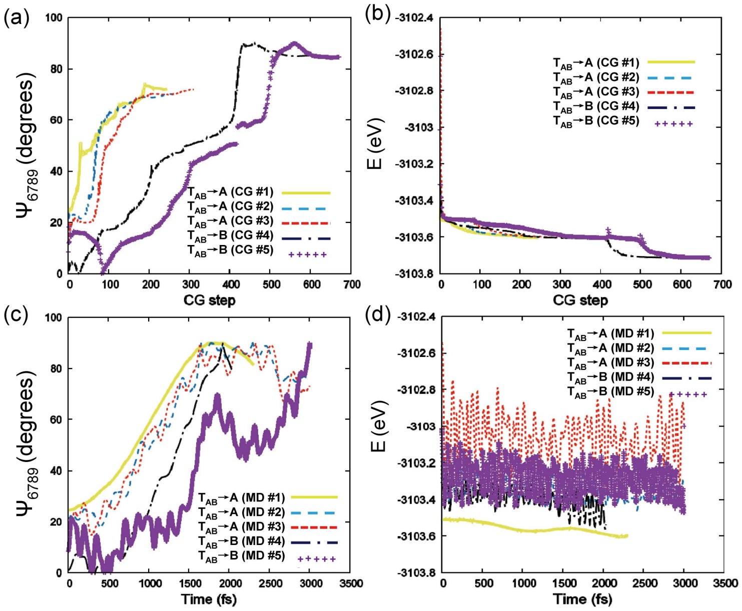

Figure 6.7: (a,c) Dihedral angle ψ and (b,d) potential energy E of the Se system during (a,b) CG optimization and (c,d) MD calculations starting in transition point T_{AB}, identified energetically in Fig. 6.6(a). Atomic positions used to define ψ_{6789} are identified in Fig. 6.6(c) and 6.6(d).

end. Whatever differences in the relative stability of the intermediate states in the infinite or finite segment connecting a and b chains, none will stop the attachment of the b chain to δ-Se that occurs at a significant net energy gain of 143 eV/atom, thus driving the exothermic reaction forward.

Since Te shares the same group VI with Se in the periodic table, I expect the chemical behavior and bonding in the respective elemental solids to be very similar. I found the formation mechanism of the δ allotrope from native a helices via the b chains, discussed above for Se, to be viable for Te as well, with small differences in reaction energies. According to Table 6.1, the a-Te to b-Te conversion is exothermic, releasing 26 meV/atom (LDA) and 15 meV/atom(PBE). Attaching the b chain laterally to a semi-infinite δ-Te layer is also exothermic, releasing 208 meV/atom (LDA) and 69 meV/atom (PBE). As mentioned earlier, also the geometries of the initial, final and intermediate states encountered during the a-Te

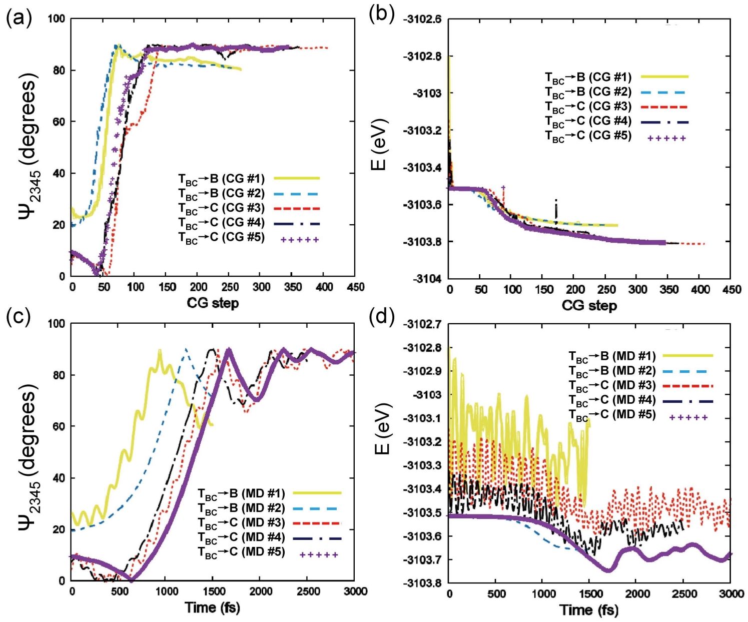

Figure 6.8: (a,c) Dihedral angle ψ and (b,d) potential energy E of the Se system during (a,b) CG optimization and (c,d) MD calculations starting in transition point T_{BC}, identified energetically in Fig. 6.6(a). Atomic positions used to define ψ_{2345} are identified in Fig. 6.6(c) and 6.6(d).

to *b*-Te transformation are similar, the main difference being the Te-Te bond length, which is larger than the value in Se allotropes. Most important, also activation energies of ~0.3 eV are similar in Te and Se.

The electronic band structure of the different 1D and 2D allotropes of Se is shown in Fig. 6.10. The GW results, shown by the solid red lines, are considered a valid counterpart to experimental observation. The LDA results, shown as a matter of reference by the dashed black lines, underestimate the fundamental band gap E_g significantly. Among 1D structures, a-Se in Fig. 6.10(a) has an E_g=5.3 eV wide direct gap at X, and the b-Se in Fig. 6.10(b) has an E_g=5.1 eV wide direct gap at Γ. The GW band gap for a-Se compares favorably with a recently reported E_g=5.46 eV value [109] and a smaller E_g=3.00 eV value [110] obtained using a different approach. δ-Se in Fig. 6.10(c) has an E_g=3.1 eV wide indirect gap, and η-Se in Fig. 6.10(d) has an E_g=2.4 eV wide indirect gap. In general, I see that the band

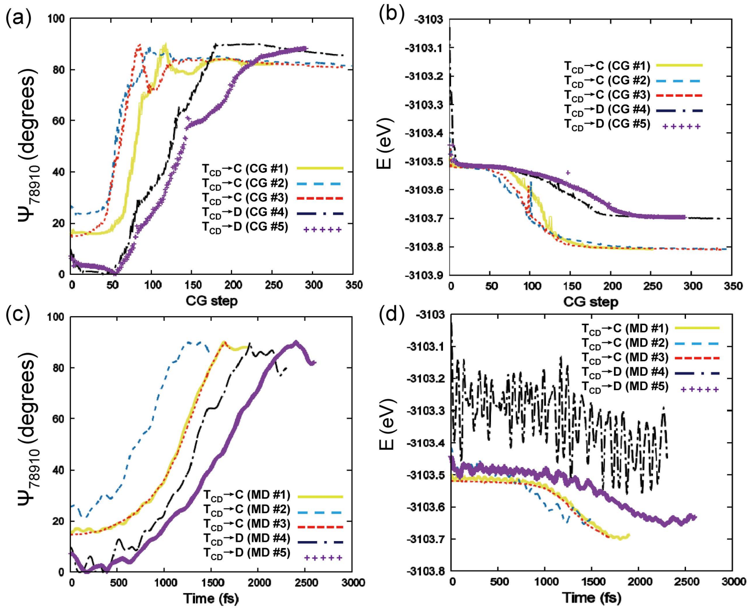

Figure 6.9: (a,c) Dihedral angle ψ and (b,d) potential energy E of the Se system during (a,b) CG optimization and (c,d) MD calculations starting in transition point T_{CD}, identified energetically in Fig. 6.6(a). Atomic positions used to define $\psi_{789,10}$ are identified in Fig. 6.6(c) and 6.6(d).

gaps in 1D structures are significantly larger than in the 2D layers.

The electronic band structure of different 1D and 2D allotropes of Te is displayed in Fig. 6.11. I find the trends and main results for the different Te allotropes to be consistent with those for Se, in particular the band gaps in 1D structures to be much larger than in 2D structures. As seen in Fig. 6.11(a), the band gap of the isolated Te a helix is 1.4 eV wide and indirect. The band gap of the isolated Te b chain, on the other hand, is direct at Γ and 1.5 eV wide, as seen in Fig. 6.11(b). The band structure of 2D δ-Te, shown in Fig. 6.11(c), has an indirect, 0.9 eV wide band gap. Results for the 2D allotrope η-Te, shown in Fig. 6.11(d), indicate a direct, 0.3 eV wide band gap between Γ and Y. These numerical results indicate that the LDA-based band gaps in Te are roughly one third of the LDA values found in Se. As mentioned earlier, while DFT-LDA underestimates band gaps, it still provides useful insight into trends in the electronic structure.

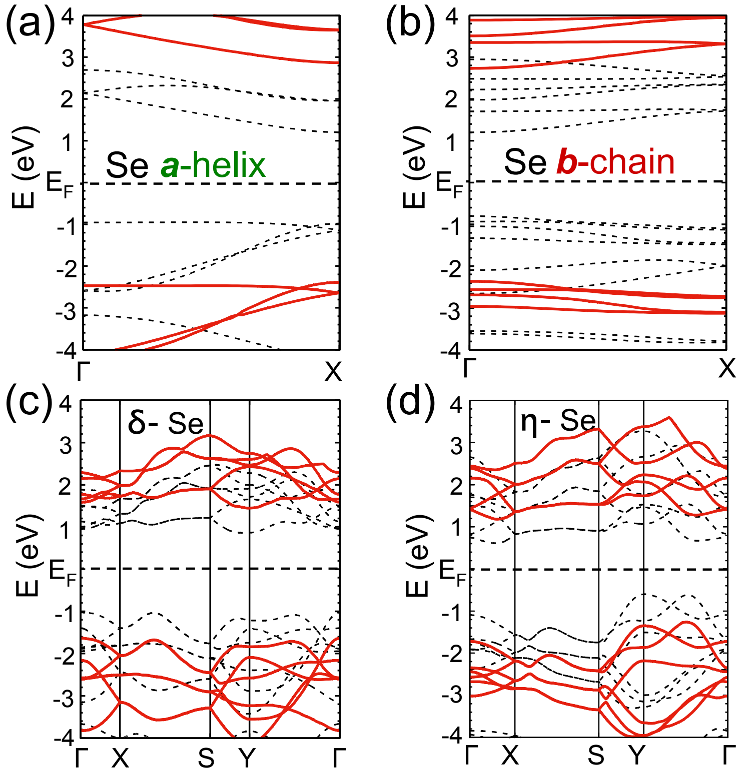

Figure 6.10: Electronic band structure of an isolated (a) a-Se helix, (b) b-Se chain, isolated (c) δ-Se and (d) η-Se monolayers. GW results, shown by solid red lines, are compared to LDA results, shown by the black dashed lines.

Reported experimental results for 2D chalcogen allotropes include a thin layer of a-Se helices on silicon [95], a monolayer of a-Te helices on graphene [103], a substrate-free thin layer of a-Te helices [111], and β-Te, a covalently bonded 2D assembly of a helices [93,94]. A valid question to ask is, why the more stable 2D δ allotrope and the 1D b chain have not been observed. Since interest in group VI elemental 2D structures took off only very recently, it is quite possible that optimum conditions for the synthesis of the proposed allotropes have not been found yet. Established information about 3D chalcogen allotropes consisting of interacting a helices provides only a limited insight into how structures may grow on a 2D substrate. There, the substrate-chalcogen interaction may play a significant role, such as providing extra stabilization of the more reactive b chains over the a helices.

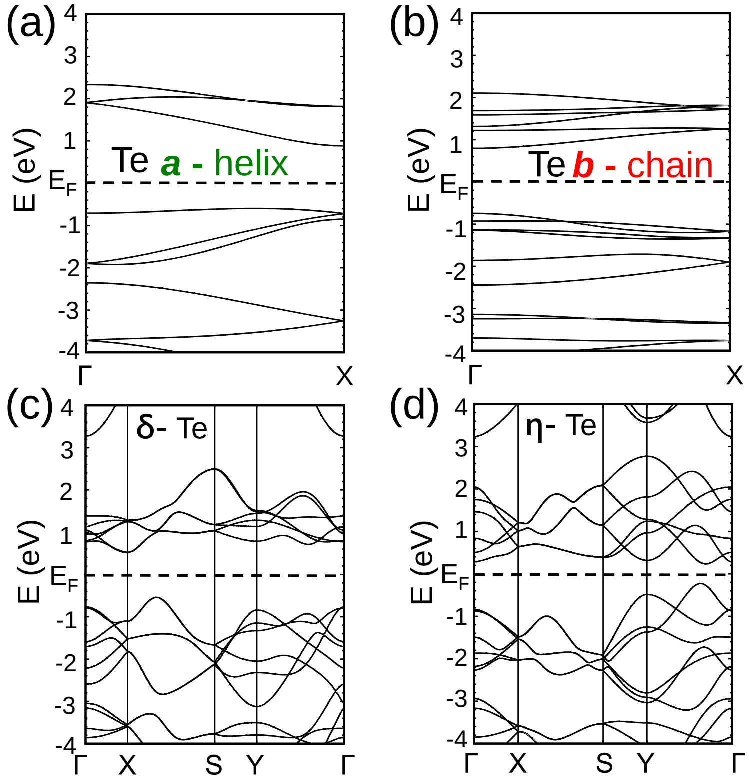

Figure 6.11: Electronic band structure of an isolated (a) a-Te helix, (b) b-Te chain, isolated (c) δ-Te and (d) η-Te monolayers obtained using DFT-LDA.

Without question, the substrate plays a significant role facilitating the 1D to 2D transformation in chalcogen structures. Even a weak adsorbate-substrate interaction will confine condensing chalcogen structures in the 2D space adjacent to the substrate, thus significantly increasing the coalescence rate. To decouple the intrinsic chalcogen reaction energetics from substrate-chalcogen interaction on a particular substrate, I performed all the calculations in vacuum. Specific substrates can be selected that may change the relative stability order in adsorbed chalcogen structures in comparison to such structures in vacuum.

As mentioned before, locating a transformation path in configurational space between very dissimilar structures a and δ, with activation barriers not exceeding $\sim$0.3 eV, is a nontrivial task. So far, state-of-the-art global structural searching techniques were unable to locate such a path or other structures that were very different from the native a helices [93].

I feel that for the time being, understanding the physical origin of strong bonds in terms of d, θ, ψ and locating a pathway along which only the least energy sensitive structural parameter is modified is a more promising approach to understanding the reaction energy. I located such a path from A to D that involves only a sequence of changes in ψ within a 9-atom segment of the chain.

Maybe the most important lesson to learn was that – at least in the class of structures discussed here – releasing structural constraints and increasing the number of degrees of freedom may significantly lower the activation barriers for structural transformations. Even though the initially considered artificial compression of a 2D assembly of a helices with 3 atoms per unit cell to a completely flat structure with 6 degrees of freedom per cell did eventually yield the stable δ allotrope, the energy invested was unphysically high. Allowing for concerted atomic motion in a 9-atom segment with 27 degrees of freedom lowered the activation barriers significantly. In a related scenario of structural phase transitions in monochalcogenindes, artificial spatial constraints [112] were also found to significantly affect the energy barriers and thus the critical temperature [113]. The same behavior can be expected for a wide range of systems undergoing structural phase changes.

6.4 Summary

In summary, based on DFT calculations, I have uncovered the microscopic mechanism of the recently observed structural transition in elemental chalcogens Se and Te from their native bulk structure consisting of a helices to atomically thin 2D layers. I found that the a helices convert to more stable, previously unknown b chains in a multi-step process that involves a point-dislocation motion along the helix. In a zipper-like motion, the b chain reconnects to a related, previously unknown and unusually stable 2D δ structure of Se and Te. The 1D a helix to 2D δ conversion is mildly exothermic with -0.17 eV/atom for Se and -0.23 eV/atom for Te. The high structural flexibility allows the helix to exploit many degrees of freedom and thus significantly lower the activation barriers along the complex reaction path to $\lesssim$0.3 eV, indicating that the conversion may occur at moderate temperatures. In view of the similar stability of the structurally related β, δ and η structures, I expect that all these and maybe even other allotropes should be formed at elevated temperatures. I found all 1D and 2D chalcogen structures to be semiconducting.

Chapter 7

Effect of Net Charge on the Relative Stability of 2D Boron Allotropes

The following discussion is my original contribution to the related publication by Dan Liu and David Tománek, Nano Lett. **19**, 1359-1365 (2019) [114].

7.1 Introduction

Identifying the most stable allotrope of a given compound is one of the key problems in Physics and Chemistry. Whereas charge neutral systems have attracted most attention, notable exceptions are low-dimensional systems that can be charged by extra electrons in specific bulk geometries. Excess of electrons induced by Li intercalation does not affect the honeycomb structure of two-dimensional (2D) graphene layers in graphite intercalation compounds (GICs) [115], but does change the equilibrium structure of MoS_2 monolayers from the 2H to the 1T allotrope [116]. Even though the effect of excess charge on chemical bonding and equilibrium geometry should be general, I expect the most drastic changes to occur in structures of elemental boron that is notorious for its many stable allotropes [117,118]. What appears as frustrated bonding in mostly metallic 2D structures of elemental boron, called borophene, reflects the inability of the element to follow the octet rule of bonding due to its electron deficiency. I speculate that both the electron deficiency and thus the chemical bonding characteristic may be modified by placing a nonzero charge on B atoms. In that case, the most stable borophene structure may differ from a puckered triangular lattice with monatomic vacancies [119–123] or equally stable irregular structures [124–126] identified in the neutral system. Indeed, placing a net charge of $\lesssim$1 e per atom on borophene, provided by an Al(111) substrate [127], or intercalating Mg ions in-between borophene layers in the MgB_2 compound [128], changes the most stable allotrope to a very different honeycomb lattice. Structural changes induced by charging may significantly modify the electronic structure, turning semiconducting 2H-MoS_2 to metallic 1T'-MoS_2 locally [129] and undoped borophene to honeycomb lattices in diborides [130, 131] including MgB_2, which displays superconducting behavior [132].

In this study, I explore the effect of net charge on the bonding character and structural stability of 2D allotropes of boron. The *ab initio* calculations for the neutral system reveal a previously unknown stable 2D ϵ-B structure with a 0.2 eV wide fundamental band gap. I find that the chemical bonding characteristic in this and other boron structures is strongly affected by extra charge, including a 23% lattice constant change in ϵ-B, induced by changing the net charge from 0.25 holes to 0.25 electrons per B atom. Beyond a critical degree of extra electrons near 0.5 electrons/atom, the most stable allotrope changes from ϵ-B to a buckled honeycomb structure. Additional extra electrons, mimicking a transformation of boron to carbon, causes a gradual decrease in the degree of buckling of the honeycomb lattice that can be interpreted as piezoelectric response. I propose that extra electrons can easily be achieved by placing borophene in direct contact with layered electrides such as Ca_2N. In this system, I find that extra electrons accepted by borophene can be doubled by changing from the B/Ca_2N bilayer to the Ca_2N/B/Ca_2N sandwich geometry.

As mentioned above, the vast number of stable neutral 2D borophene allotropes, including

$\alpha-$B, $\beta-$B, $\gamma-$B, $\delta-$B and $\eta-$B structures [119,120], reflects a frustrated bonding character of electron-deficient boron. This element may engage its three valence electrons in only three covalent bonds, resulting in an electron sextet instead of the desirable octet noble-gas configuration. To partly compensate for lack of electrons in the octet configuration, boron atoms often prefer increasing their coordination to six nearest neighbors in the triangular lattice. This is essentially equivalent to adding electrons [133, 134] to the individual atoms that are held together by pure three-center bonding. On the other hand, the stability of the triangular lattice is often enhanced by removing atoms and forming hexagon-shaped monatomic vacancies. This process somehow mimics subtracting electrons while the structure locally converts to a honeycomb lattice, where atoms are held together by two-center bonding. The competition between two-center and three-center bonding has been used to identify the optimum concentration of hexagonal vacancies in the neutral triangular lattice [133, 135, 136], but likely controls also less common neutral structures with four- and five-fold coordinated boron atoms [124, 125]. Biasing this competition by net charge has been shown to affect the fraction of hexagonal vacancies in triangular borophene lattices [137]. Even though extra electrons of B layers has been linked to unexpected superconducting behavior of MgB_2 and found useful to modulate CO_2 capture [138], no systematic attention has been paid to the possibility of deliberately changing the bonding and the equilibrium structure of boron by excess charge.

A viable possibility to significantly dope 2D structures of elemental boron by electrons is to place them in direct contact with electrides including Ca_2N [139, 140] and Y_2C [141]. In these highly electronegative systems with a layered structure, regions of large electron density are found in-between the layers. The charge density in this electron layer amounts to one electron per formula unit in Ca_2N and two electrons per formula unit in Y_2C. The possibility of exfoliation down to a monolayer [139] has been demonstrated in Ca_2N, so that assembly of various vertical heterostructures is possible.

7.2 Computational techniques

The calculations of the stability, equilibrium structure and electronic structure have been performed using density functional theory (DFT) as implemented in the SIESTA [13] code. Periodic boundary conditions have been used throughout the study, with monolayers represented by a periodic array of slabs separated by a 30 Å thick vacuum region. I used the Perdew-Burke-Ernzerhof (PBE) [9] exchange-correlation functional. The SIESTA calculations used norm-conserving Troullier-Martins pseudopotentials [33], a double-ζ basis including polarization orbitals, and a mesh cutoff energy of 250 Ry to determine the self-consistent charge density, which provided us with a precision in total energy of $\lesssim$2 meV/atom. The reciprocal space has been sampled by a fine grid [34] of 4×4 k-points in the 2D Brillouin zones (BZ) of the primitive unit cells of neutral and doped borophene containing 32 atoms, 3×3 k-points in the BZ of supercell of heterostructure of Ca_2N and ϵ_6, and 3×1 k-points in the BZ of supercell of heterostructure of Ca_2N and ϵ_3. Geometries have been optimized using the conjugate gradient (CG) method [76], until none of the residual Hellmann-Feynman forces exceeded 10^{-2} eV/Å.

7.3 Results and discussions

Inspired by the honeycomb structure of the negatively doped boron sublattice found in diborides including MgB_2, I started the investigation of electron doped borophene structures with the honeycomb lattice. To provide substantial configuration freedom for the lattice

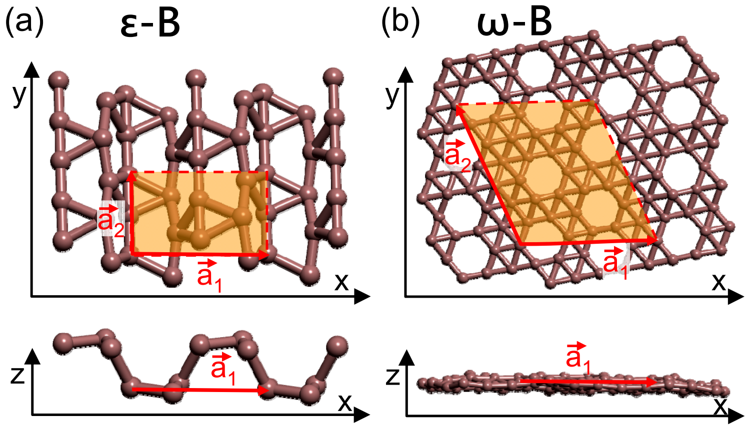

Figure 7.1: Previously unexplored neutral borophene allotropes formed by spontaneous conversion of an artificial honeycomb lattice: (a) ϵ-B and (b) ω-B. The structures are shown in top and side view. The lattice vectors $\vec{a}_1$ and $\vec{a}_2$, shown in red, delimit the highlighted primitive unit cells.

structure, I consider a superlattice with 32 atoms per unit cell and subject all atoms in the supercell to random distortion. To study the effect of extra electrons on the equilibrium structure and the chemical nature of bonding, I changed the degree of extra electrons gradually and optimized each system using the conjugate gradient optimization method.

Starting with no excess charge, I found the neutral honeycomb structure to be unstable and to convert to rather stable allotropes that have not been reported previously. The first allotrope, shown in Fig. 7.1(a) and called ϵ-B, is only 7 meV/atom less stable than the most stable α'-B phase [117] and displays a very uncommon morphology with triangles and pentagons, quite distinct from the well-documented class of triangular lattices with vacancies. The structure shown in Fig. 7.1(b), which I call ω-B, has a very similar morphology to known allotropes containing triangles and hexagons only [119–122], but is 26 meV/atom less stable than α'-B. ϵ-B and ω-B add to the large number of known allotropes, and I expect many more to follow.

Both ϵ-B and ω-B are buckled. Still, I could locate a locally stable, flat counterpart of ω-B, which is 7 meV/atom less stable than ω-B. The cohesive energies of neutral borophene

Table 7.1: Cohesive energy E_{coh} of selected neutral borophene allotropes, obtained using DFT-PBE calculations. n is the number of boron atoms per unit cell and Z is the coordination number of individual atoms in the unit cell.

Allotrope	E_{coh} (eV/atom)	n	Z
ϵ-B	5.699^a	8	4
ω-B	5.680^a	32	4, 5, 6
α'-B	5.706^a	8	5, 6
	5.762^b	8	5, 6
β_{12}-B	5.712^b	5	3, 5, 6
	6.23^c	5	3, 5, 6
δ_6-B	5.662^b	4	6
χ_3-B	5.723^b	4	3, 5
	6.19^c	4	3, 5

[a] Present work.
[b] Reference [117].
[c] Reference [122].

allotropes are compared in Table 7.1.

Next, I added extra 5, 10, 13, 16, 24 and 32 electrons to the 32-atom unit cell with an initial honeycomb arrangements and optimized the geometry. I found the optimum geometries not to depend on initial deformations imposed on the starting structure, which may not be reachable in molecular dynamics trajectories. The optimum boron structures labelled $\epsilon_1 - \epsilon_6$ and their average levels of extra electrons $\langle \Delta Q \rangle$ are displayed in Figs. 7.2(a)-7.2(f).Additional results at the levels of extra electrons of -18 e, -20 e and -28 e in the 32-atom unit cell and the corresponding average charge per boron $\langle \Delta Q \rangle$ are shown in Figure 7.3.I find all these structures to differ significantly from the neutral ϵ-B and ω-B structures in Fig. 7.1, which have been optimized in the same way.

The structure ϵ_1-B in Fig. 7.2(a), which contains triangles, pentagons and hexagons, is reminiscent of ϵ-B, but is completely flat. With increasing extra electrons, the density of pentagons gradually diminishes and eventually vanishes in ϵ_3-B in Fig. 7.2(c), representing the buckled χ_3 phase [117]. At the same time, the density of hexagons increases from ϵ_1-B

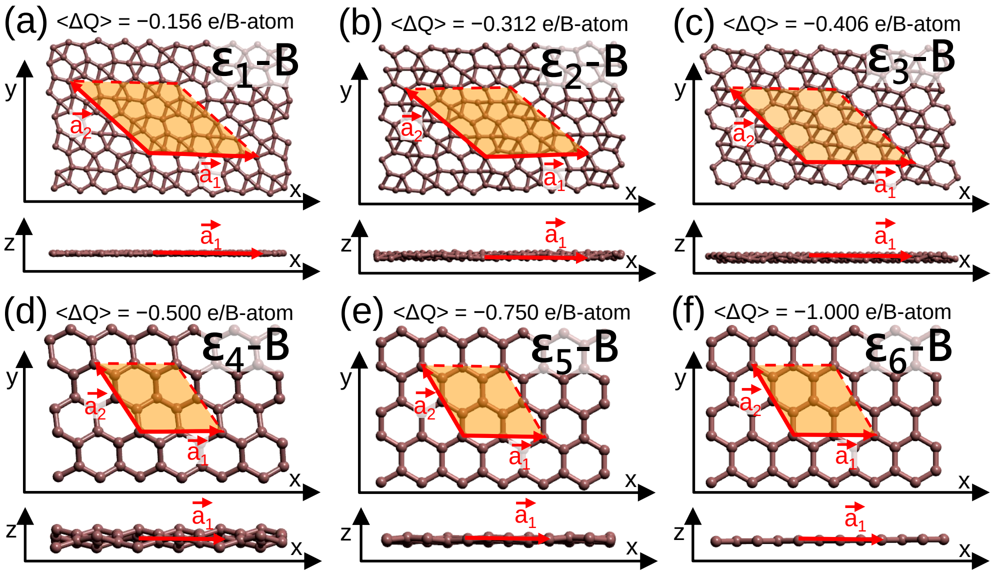

Figure 7.2: Electron doped 2D borophene structures obtained by optimizing a distorted boron honeycomb superlattice with 32 atoms per unit cell. The average excess charge $\langle \Delta Q \rangle$ per boron atom, specified in the panels, increases from (a) ϵ_1-B to (f) ϵ_6-B. The structures are shown in top and side view. The lattice vectors $\vec{a}_1$ and $\vec{a}_2$, shown in red, delimit the highlighted unit cells.

to ϵ_3-B until all other polygons are eliminated in $\epsilon_4 - \epsilon_6$, shown in Figs. 7.2(d)-7.2(f), as the extra electrons exceeds $|\langle \Delta Q \rangle| \gtrsim 0.5$ e/atom. The buckled honeycomb lattice of ϵ_4-B gradually flattens to the graphene-like structure of ϵ_6-B with increasing extra electrons.

The interpretation of these structural changes is rather straight-forward. With one extra electron per atom, boron behaves as sp^2-bonded carbon with four valence electrons, with atoms forming the 2D graphene honeycomb lattice. This structure is rather robust with respect to extra electrons and holes, as evidenced in GIC structures. Similarly, also doped boron should keep its optimum honeycomb lattice structure even if the net charge may be smaller or larger than one extra electron per atom. As seen in Figs. 7.2(d)-7.2(f), the honeycomb structure of borophene, with different degree of buckling, is preferred for the excess charge $\langle \Delta Q \rangle$ ranging between -0.5 and -1.0 e/atom.

To understand the change in the electronic structure that caused a profound structural

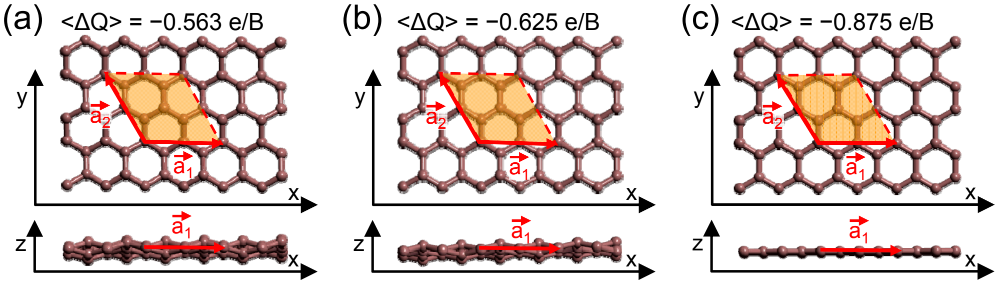

Figure 7.3: Electron doped 2D borophene structures obtained by optimizing a distorted boron honeycomb superlattice with 32 atoms per unit cell. The average excess charge $\langle \Delta Q \rangle$ per boron atom, specified in the panels, increases from (a) to (c). The structures are shown in top view (upper panels) and side view (lower panels). The lattice vectors $\vec{a}_1$ and $\vec{a}_2$, shown in red, delimit the highlighted unit cells.

change from neutral ϵ-B in Fig. 7.1(a) to negatively charged ϵ_6-B$^-$ in Fig. 7.2(f), I first probed the charge density changes $\Delta\rho$ associated with charging. The results for $\Delta\rho$ caused by placing artificially extra electrons on free-standing borophene structures ϵ_3-B and ϵ_6-B are shown in Figs. 7.4(a)-7.4(b). $\Delta\rho$ can be viewed as the crystal counterpart of the Fukui function, and the results indicate that the extra electrons are accommodated in p_z (or π) states normal to the layer, very similar to graphene layers.

A realistic way to provide a high degree of extra electrons, I suggest, is to place borophene layers in contact with the Ca_2N electride. The optimum lattice constant of the triangular lattice of Ca_2N is $a = 3.97$ Å. This layered system has the nominal configuration $[Ca_2N]^+ \cdot e^-$, with layers of Ca_2N separated by layers of excess electrons, and can be exfoliated down to a monolayer chemically [139]. It is to be expected that borophene will be electron doped when placed in the region of excess electrons outside a Ca_2N monolayer. Since I focus on general trends rather than minute details, I studied the charge redistribution using only two prototype structures of doped borophene, namely ϵ_3-B at low- and ϵ_6-B at high-level of extra electrons, in contact with Ca_2N. To determine the degree of extra electrons in borophene caused by a contact to Ca_2N, I inspected the charge redistribution when placing

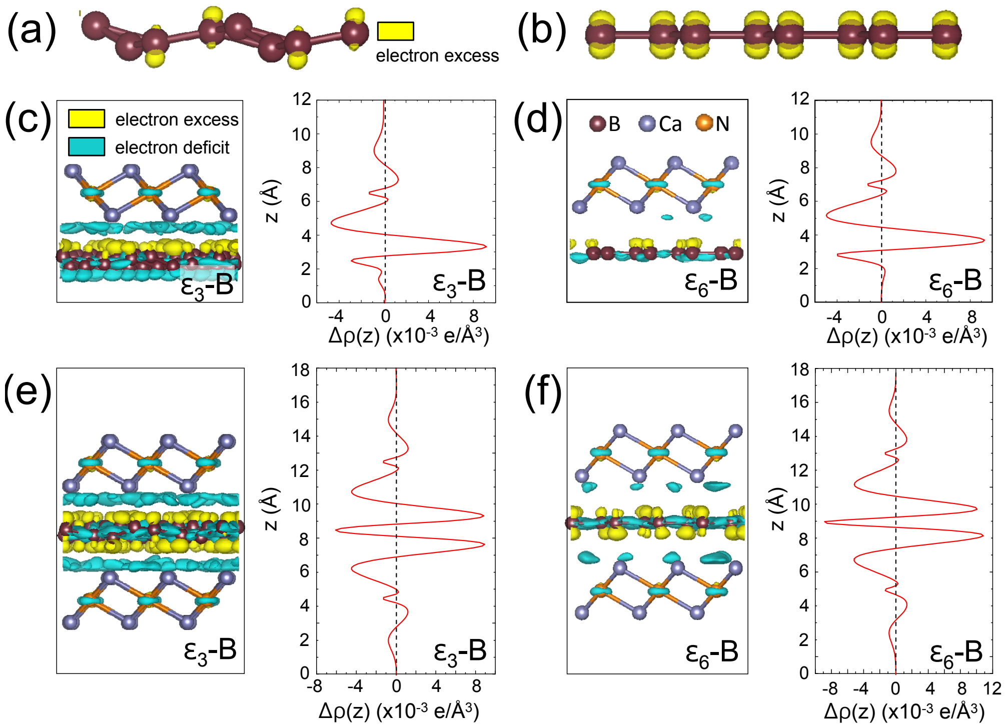

Figure 7.4: Charge redistribution in 2D borophene layers induced by extra electrons or by contact with monolayers of Ca_2N electride. Charge density difference $\Delta\rho$ caused by placing an excess charge (a) $\langle \Delta Q \rangle = -0.406$ e/atom on ϵ_3-B and (b) $\langle \Delta Q \rangle = -1.0$ e/atom on ϵ_6-B. Charge density redistribution $\Delta\rho = \rho(B/Ca_2N) - \rho(B) - \sum \rho(Ca_2N)$ in the bilayer structures (c) ϵ_3-B/Ca_2N and (d) ϵ_6-B/Ca_2N as well as in the sandwich structures (e) Ca_2N/ϵ_3-B/Ca_2N and (f) Ca_2N/ϵ_6-B/Ca_2N. $\Delta\rho$ is shown by isosurfaces bounding regions of electron excess at $+7\times10^{-3}$ e/Å^3 (yellow) and electron deficiency at -2×10^{-3} e/Å^3 (blue). $\langle \Delta\rho(z) \rangle$ is averaged across the $x-y$ plane of the layers.

ϵ_3-B and ϵ_6-B on top of a Ca_2N monolayer or, as in a sandwich geometry, in-between Ca_2N monolayers. The charge density differences caused by electron redistribution in the system are shown in Figs. 7.4(c)-7.4(f).Electron flow from the Ca_2N electride bilayer towards ϵ_3-B is shown in Figure 7.6(a) and towards ϵ_6-B is shown in Figure 7.6(b). The net electron transfer results are similar to those for Ca_2N monolayers in Figure 3 of the main manuscript, namely $\langle \Delta Q \rangle = -0.15$ e/B in ϵ_3-B and $\langle \Delta Q \rangle = -0.20$ e/B in ϵ_6-B. This indicates that the number of Ca_2N layers does not affect the charge transfer to borophene.

I should point out that incommensurate vertical heterostructures formed of doped borophene and Ca_2N layers can not be represented accurately in a periodic structure used in the com-

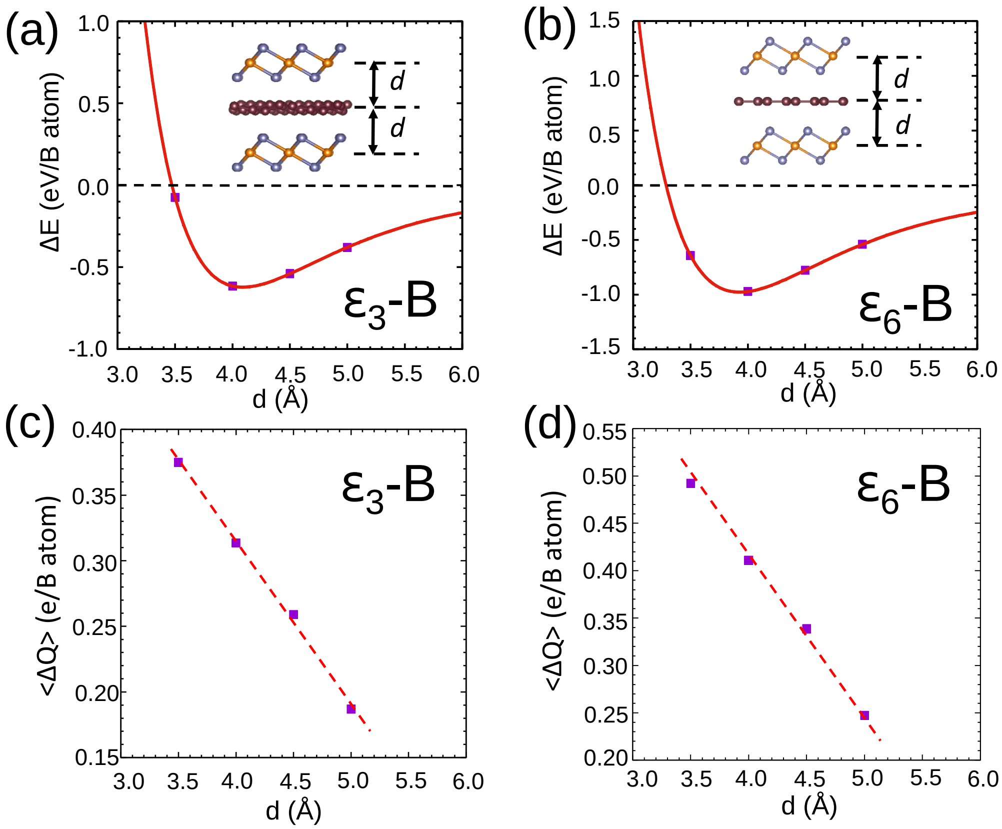

Figure 7.5: Changes in the interlayer interaction energy ΔE and net average charge $\langle \Delta Q \rangle$ on borophene in the Ca_2N/B/Ca_2N sandwich geometry as a function of the interlayer distance d. Results for ϵ_3-B in (a) and (c) are compared to those for ϵ_6-B in (b) and (d).

putational approach. In the calculation, I used the optimum interlayer distance $d = 4.0$ Å in agreement with the results in Figs. 7.5(a) and 7.5(b). I furthermore matched $1{\times}3$ ϵ_3-B supercells with $3{\times}7$ Ca_2N supercells in the ϵ_3-B/Ca_2N superstructure and primitive unit cells of ϵ_6-B with $3{\times}3$ supercells of Ca_2N in the ϵ_6-B/Ca_2N superstructure. The remaining lattice mismatch of $\lesssim$2% was accommodated by averaging the lattice constants of borophene and Ca_2N. Due to this minor lattice distortion, results presented in Figs. 7.4(c)-7.4(f) may differ to a small degree from the charge redistribution in an incommensurate structure. Comparing results for the bilayer in Figs. 7.4(c)-7.4(d) with those in the sandwich structure in Figs. 7.4(e)-7.4(f), I see clearly that borophene receives twice the number of electrons in the sandwich in comparison to the bilayer structure. Specifically, $\langle \Delta Q \rangle$ in ϵ_3-B almost doubles

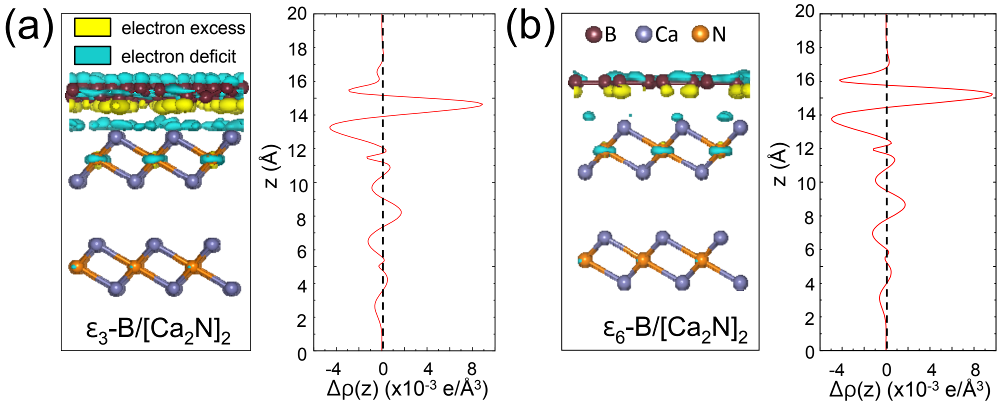

Figure 7.6: Electron flow between borophene and bilayers of the Ca_2N electride. Charge density redistribution $\Delta\rho = \rho(B/[Ca_2N]_2) - \rho(B) - \sum \rho(Ca_2N)$ in (a) ϵ_3-B/$[Ca_2N]_2$ and (b) ϵ_6-B/$[Ca_2N]_2$ triple-layer heterostructures. $\Delta\rho$ is shown by isosurfaces bounding regions of electron excess at $+7\times10^{-3}$ e/Å^3 (yellow) and electron deficiency at -2×10^{-3} e/Å^3 (blue). $\langle\Delta\rho(z)\rangle$ is averaged across the $x-y$ plane of the layers.

from -0.16 e/atom in Fig. 7.4(c) to -0.31 e/atom in Fig. 7.4(e). Similarly, $\langle\Delta Q\rangle$ in ϵ_6-B almost doubles from -0.21 e/atom in Fig. 7.4(d) to -0.41 e/atom in Fig. 7.4(f).

I have evaluated the dependence of the total energy on the interlayer distance d in the Ca_2N/B/Ca_2N sandwich structure for the ϵ_3-B and ϵ_6-B allotropes and present the results in Figs. 7.5(a) and 7.5(b). In both structures, the optimum interlayer distance $d{\approx}4.0$ Å.

There is a significant electron accumulation with a maximum at $d{\approx}3$ Å outside a free-standing Ca_2N electride layer [139], which is accommodated by an adjacent borophene layer. In this case, the net charge on the borophene layer may be changed by changing the interlayer distance d. The results for $\langle\Delta Q\rangle$ as a function of d are presented in Fig. 7.5(c) for ϵ_3-B and in Fig. 7.5(d) for ϵ_6-B sandwiched in-between two Ca_2N layers. I find it interesting that $\langle\Delta Q\rangle$ decreases almost linearly with increasing interlayer distance.

At the equilibrium interlayer distance, I find $\langle\Delta Q\rangle{\approx}-0.31$ e/B-atom in the system with ϵ_3-B and $\langle\Delta Q\rangle{\approx}-0.41$ e/B-atom in the system with ϵ_6-B. The higher value of $\langle\Delta Q\rangle$ in ϵ_6-B is associated with the better ability of this structure to accept electrons.

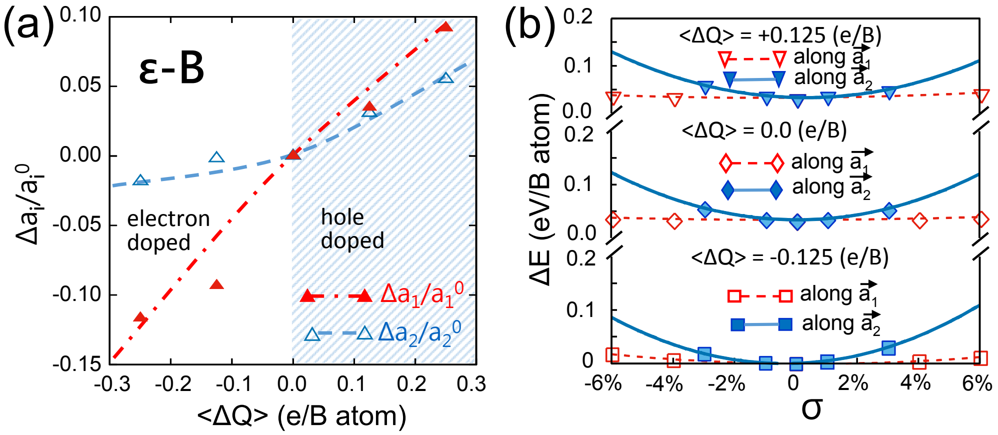

Figure 7.7: Effect of net charge on the equilibrium geometry of ϵ-B. (a) Effect of the net average charge $\langle \Delta Q \rangle$ on the orthogonal lattice constants a_i with $i = 1, 2$. Plotted are charge-induced relative changes $\Delta a_i/a_i^0$, where a_i^0 are the lattice constants in the neutral ϵ-B allotrope. (b) Strain energy ΔE as a function of in-layer strain σ at different levels of extra electrons $\langle \Delta Q \rangle$.

It is well known that in GICs, the net charge transferred from dopant atoms to the graphene layers changes the lattice constant. This change is relatively small, amounting to [142] $\Delta a/a \approx 0.8\%$ in KC_8 with $\langle \Delta Q \rangle \approx -0.125$ e/C-atom. The corresponding results for the effect of extra electrons on the lattice constants in the stable ϵ-B allotrope are shown in Fig. 7.7(a). The lattice changes are anisotropic and larger than found in graphene. I find that extra electrons expands the lattice more along the softer $\vec{a}_1$ direction than along the harder $\vec{a}_2$ direction. At the levels of extra electrons $\langle \Delta Q \rangle \approx -0.3$ to -0.5 e/B-atom discussed above for the $Ca_2N/B/Ca_2N$ heterostructures, the lattice expansion exceeds 10%.

The in-layer stiffness of ϵ-B with neutral, extra electrons and extra holes is addressed in Fig. 7.7(b). I used the shorthand notation 0 for the neutral system, $-$ for $\langle \Delta Q \rangle = -0.125$ e/B and + for $\langle \Delta Q \rangle = +0.125$ e/B. Irrespective of extra electron, the energy change due to in-layer strain σ is much larger along the harder $\vec{a}_2$ direction than along the softer $\vec{a}_1$ direction. In terms of the 2D elastic constants [19], I find for the softer $\vec{a}_1$ direction $c_{11}(-) = 67.99$ N/m, $c_{11}(0) = 18.70$ N/m, and $c_{11}(+) = 29.98$ N/m. Along the harder $\vec{a}_2$

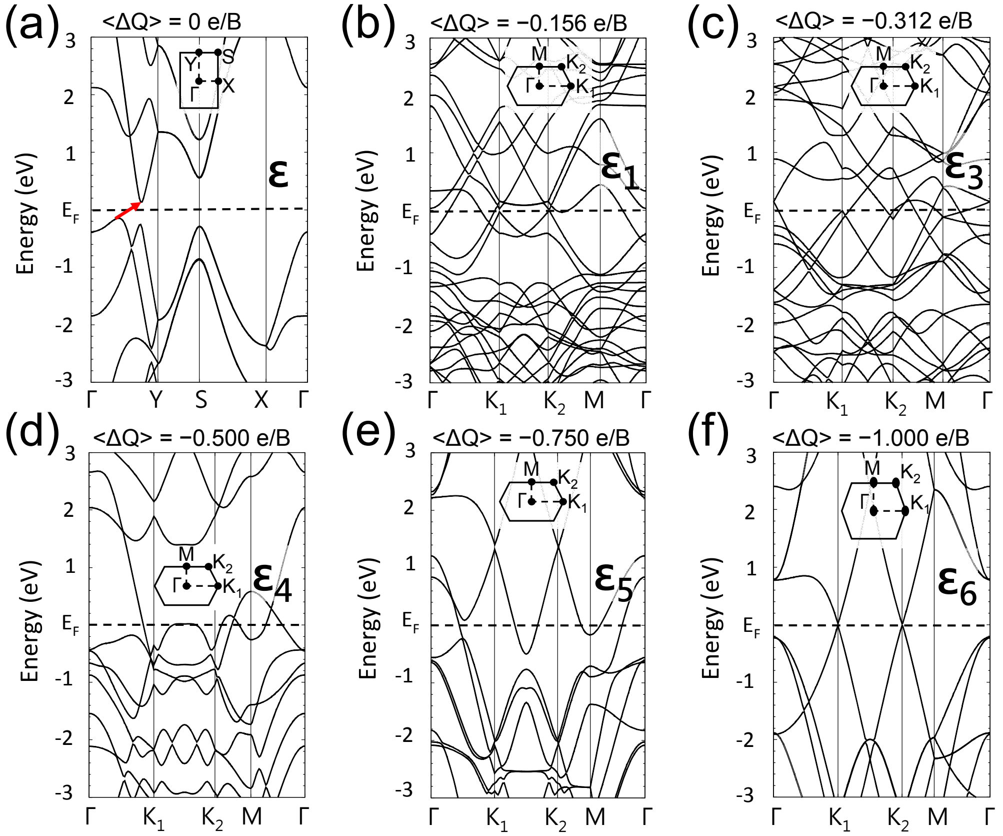

Figure 7.8: Electronic band structure of (a) neutral ϵ-B, (b) ϵ_1-B with $\langle \Delta Q \rangle = -0.156$ e/B, (c) ϵ_3-B with $\langle \Delta Q \rangle = -0.406$ e/B, (d) ϵ_4-B with $\langle \Delta Q \rangle = -0.500$ e/B, (e) ϵ_5-B with $\langle \Delta Q \rangle = -0.750$ e/B, and (f) ϵ_6-B with $\langle \Delta Q \rangle = -1.000$ e/B, calculated using the DFT-PBE functional. The indirect fundamental band gap is indicated by the red arrow in (a).

direction I find $c_{22}(-) = 446.79$ N/m, $c_{22}(0) = 360.52$ N/m, and $c_{22}(+) = 338.58$ N/m.

The electronic band structure of selected boron 2D allotropes discussed in this study is shown in Fig. 7.8. I should note that DFT calculations used in this study do not represent the true quasi-particle band structure and typically underestimate band gaps. With this fact in mind, I find that, according to the PBE results in Fig. 7.8(a), the neutral ϵ-B allotrope of Fig. 7.1(a) is a semiconductor with a small indirect band gap of $E_g = 0.2$ eV. Whereas stretching along the soft $\vec{a}_1$ direction by 4% turns ϵ-B into a direct-gap semiconductor, compressing by 4% along $\vec{a}_1$ causes gap closure. Stretching ϵ-B by 1% along the hard $\vec{a}_2$ direction turns this allotrope metallic, whereas compression by 1% changes the its indirect

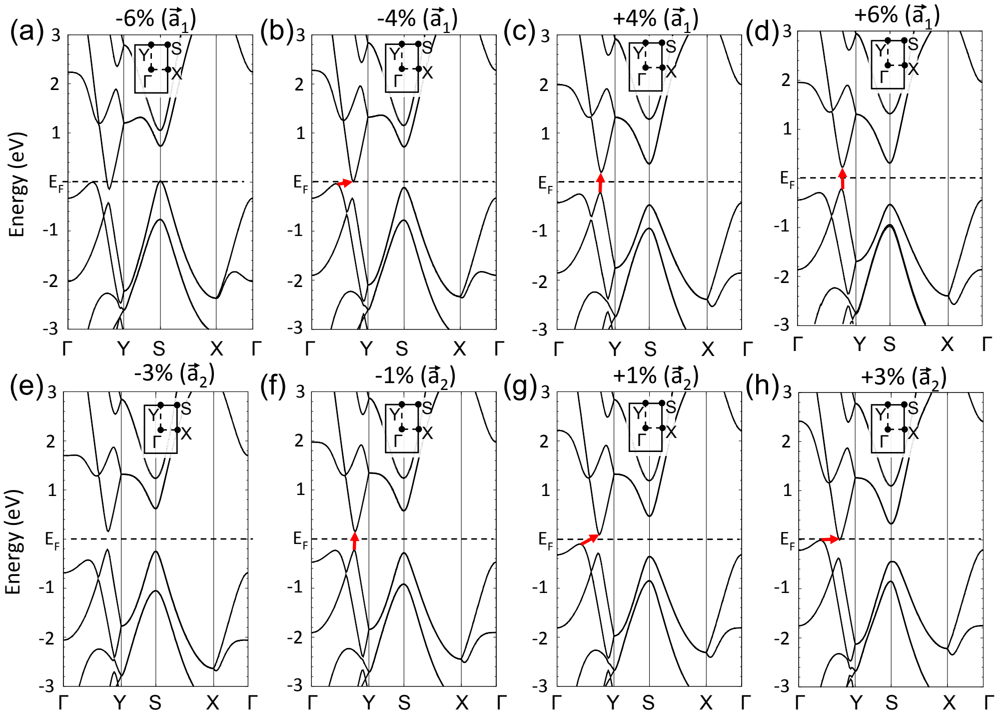

Figure 7.9: Electronic band structure of ϵ-B subject to in-layer strain of (a) -6%, (b) -4%, (c) +4%, and (d) +6% along the $\vec{a}_1$ direction, and (e) -3%, (f) -1%, (g) +1%, and (h) +3% along the $\vec{a}_2$ direction. The fundamental band gap is indicated by the red arrows in semiconducting systems.

gap to a direct gap.The neutral ϵ-borophene monolayer is an indirect-gap semiconductor, as seen in Figure 66(a) of the main manuscript. Its electronic structure changes, however, significantly, when it is subject to in-layer strain, as shown in Figure 7.9. The effect of strain along the softer $\vec{a}_1$ direction is shown in Figures 7.9(a)-7.9(d). The results indicate that compression exceeding 4% closes the gap and turns ϵ-B metallic. Stretching opens the gap and, when in excess of 4%, turns the gap direct. The effect of strain along the harder $\vec{a}_2$ direction is shown in Figures 7.9(e)-7.9(h). The trend is opposite in this case, since it is compression that opens the gap and turns it direct, and stretching beyond 3% turns the system metallic. Ability to tune very narrow band gaps by moderate strain appears very interesting for Terahertz applications.

I find all doped borophene allotropes to be metallic or semi-metallic, as shown in Figs. 7.8(b)-

7.8(f). Inspection of the band structure reveals the formation of a Dirac cone at K_1 and K_2 in the honeycomb structures in ϵ_5-B in Fig. 7.8(e) and in ϵ_6-B in Fig. 7.8(f). The Dirac cone appears ≈1.4 eV above E_F in ϵ_5-B at the level of extra electrons $\langle \Delta Q \rangle = -0.750$ e/B and at E_F in ϵ_6-B at $\langle \Delta Q \rangle = -1.000$ e/B, which mimics the structure and valence charge of graphitic carbon.

The majority of the reported stable structures of neutral 2D borophene were triangular lattices containing arrays of monatomic vacancies, reflecting the frustrated bonding character of electron-deficient boron. When considering the effect of excess charge on the bonding geometry, I observed a transition driven by increasing net negative charge from structures containing triangles and higher polygons, depicted in Fig. 7.1(a) and Figs. 7.2(a)-7.2(c), for $|\langle \Delta Q \rangle| < 0.5$ e/B to all-hexagon structures, depicted in Figs. 7.2(c)-7.2(f), for $|\langle \Delta Q \rangle| > 0.5$ e/B. The highest coordinations number of six that may be achieved in a network of triangles reflects to some degree the vain attempt of neutral boron atoms to satisfy the octet rule. Excess negative charge, with the maximum value $|\langle \Delta Q \rangle| = 1.0$ e/B considered here, offers the ability to satisfy this rule in the honeycomb network of ϵ_6-B in Fig. 7.2(f).

To understand the chemical origin of these structural changes, I need to inspect the charge redistribution caused by extra electrons, corresponding to the Fukui function for a crystal.In parallel to Figure 63(a) and 63(b) of the main manuscript, where I showed the spatial distribution of extra electrons added to two borophene structures, I present in Figure 7.10 corresponding results for the distribution of extra two electron charges added to the 32-atom unit cell of borophene, equivalent to $\langle \Delta Q \rangle = -0.0625$ e/atom. I considered negatively charged structures ϵ_1-B in Figure 7.10(a), ϵ_2-B in Figure 7.10(b), ϵ_3-B in Figure 7.10(c), and ϵ_4-B in Figure 7.10(d). In addition to these structures described in Figure 2 of the main manuscript, I present results for the structure depicted in Figure 7.3(b) in Figure 7.10(e),

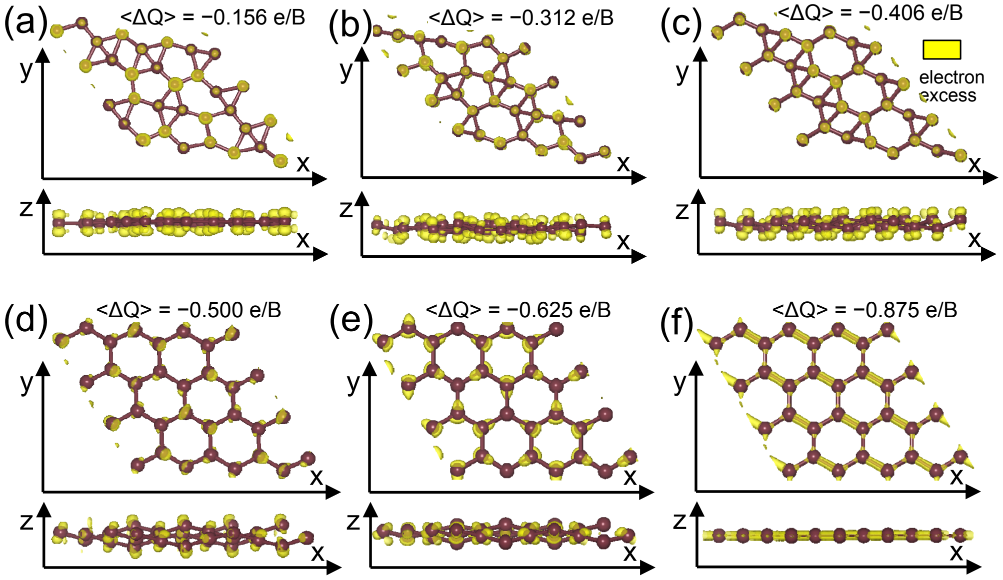

Figure 7.10: Charge density difference $\Delta\rho$ caused by placing an excess charge $\langle \Delta Q \rangle = -0.0625$ e/atom on selected borophene structures characterized in Figure 7.2 of the main manuscript and in Figure 7.3. (a) ϵ_1-B of Figure 7.2(a), (b) ϵ_2-B of Figure 7.2(b), (c) ϵ_3-B of Figure 7.2(c), (d) ϵ_4-B of Figure 7.2(d), as well as B structures shown in (e) Figure 7.3(b) and (f) Figure 7.3(c). $\Delta\rho$ is shown by isosurfaces bounding regions of electron excess at $+2.5\times10^{-3}$ e/Å^3 (yellow).

and for that of Figure 7.3(c) in Figure 7.10(f). The results indicate that the electrons are initially occupying p_z (or π) states, causing increasing buckling, which is evident when comparing the side views in Figures 7.10(a)-7.10(c). After transition to an all-hexagon lattice in Figure 7.10(d), electrons begin gradually occupying σ states, causing flattening of the honeycomb lattice, until the excess charge of one electron per B atom is reached in Figure 7.10(f). Occupation of the σ-states in the bond region even at levels of extra electrons as low as half an electron per boron is facilitated by the fact that the σ band lies much closer to the π band and to the Fermi level than in graphene.

Complementing the results presented in Fig. 7.4 for borophene interacting with Ca_2N, these results suggest that additional electrons are first accommodated in p_z (or π) states normal to the borophene layer, which cause buckling, and then in σ states, which reduce the amount of buckling. Starting with the lightly electron doped ϵ_1-B containing triangles, I observe an increasing degree of buckling with increasing extra electrons up to $|\langle \Delta Q \rangle| \lesssim 0.5$ e/B. At that point, the structure changes to the honeycomb structure mimicking hole-doped graphene. For $|\langle \Delta Q \rangle| > 0.5$ e/B, additional excess charge gets increasingly accommodated in σ states, which are much closer to E_F in borophene than in graphene, causing a reduction of buckling down to zero for $\langle \Delta Q \rangle = -1.0$ e/B.

Assuming that the Ca_2N electride can transfer up to one electron per formula unit to a borophene layer, I can expect the maximum average charge $\langle \Delta Q \rangle$ per boron atom in B/Ca_2N bilayers to range from -0.22 e in ϵ_3-B/Ca_2N to -0.28 e/atom in ϵ_6-B/Ca_2N. The transferred charge may be up to twice as large in Ca_2N/B/Ca_2N sandwich structures. These values are slightly larger, but close to those found in the actual heterostructures, reported in Fig. 7.4. I compared the charge transfer between monolayers and multilayers of the Ca_2N electride in contact with borophene and found essentially no difference. Thus, the number of Ca_2N layers does not affect the maximum value of $\langle \Delta Q \rangle$.

It is not easy to achieve the level of extra electrons $\langle \Delta Q \rangle = -1.0$ e/B by contacting an electronegative material. According to the results for the Ca_2N/B/Ca_2N sandwich structure in Fig. 7.5(d), the Ca_2N electride can provide only up to $\approx$0.4 electrons per boron atom, much less than the desired level of extra electrons of 1 e/B. An alternative to Ca_2N is Y_2C, which can supply twice as many electrons as Ca_2N, but is hard to exfoliate. Assuming maximum charge transfer from Y_2C to borophene, B could receive up to 0.8 electrons in the Y_2C/B/Y_2C heterostructure. Such a large electron transfer should further augment the Coulomb attraction between borophene and Y_2C, thus further deducing the interlayer distance, as seen in Figs. 7.4(a) and 7.4(b), and increase the amount of electron transfer, possibly up to 1.0 e/B.

I have mentioned electronic structure parallels between the honeycomb structure of ϵ_6-B carrying one extra electron per atom and graphene. Even though the system of π electrons near E_F and the Dirac cone in the corner of the Brillouin zone occur in both systems, there are notable differences between the systems. In graphene, the top of the σ-band lies more than 3 eV below E_F, whereas this energy difference is only 0.2 eV in ϵ_6-B. Apparently, the lower core charge of elemental boron is the main reason, why the σ and π bands are energetically closer than in graphene. As mentioned before, this results in an increased role of σ states in electron doped borophene structures.

According to the results in Fig. 7.7(a), changing the level of extra electrons $\langle \Delta Q \rangle$ from -0.25 e to $+0.25$ e results in a 23% increase of the borophene lattice constant a_1. Conversely, I may speculate that changing the lattice constant should modulate the electron transfer from the electride to the borophene layer, thus changing the dipole moment normal to the interface. In that case, an in-plane vibration of the heterostructure will cause this dipole to oscillate and to emit an electromagnetic signal of the same frequency.

Clearly, the most drastic effect of extra electrons is seen in the hexagonal borophene structure stabilized in MgB_2, which is the cause of superconductivity in this system. Extra electrons may also be used as a way to change structures in a predictable way. As an illustration, I find the χ_3-B structure [122], which has been synthesized at 680 K on Ag(111), to be very similar to the electron-doped, buckled ϵ_3-B structure. In that case, a simpler way to fabricate χ_3-B may consist of bringing borophene in contact with an electride, allowing it to relax to ϵ_3-B while electron doped. The final flat structure of χ_3-B may evolve after the electride has been removed. These two examples illustrate new possibilities of using extra electrons to change the structure of boron. Even though extra electrons may have a lesser effect on the equilibrium structure of other systems, the findings about the interplay between structure and excess charge have a general validity.

7.4 Summary

In summary, I have studied the effect of extra electrons on the bonding character and stability of two-dimensional (2D) structures of elemental boron, called borophene, which is known to form many stable allotropes. The *ab initio* calculations for the neutral system have revealed previously unknown stable 2D ϵ-B and ω-B structures in addition to previously reported triangular lattices with monatomic vacancies. I found that the chemical bonding characteristic in this and other boron structures is strongly affected by extra charge, which is first accommodated in the π and subsequently in the σ network of electrons. Beyond a critical degree of extra electrons, the most stable allotrope was found to change from ϵ-B containing triangles and higher polygons to a buckled honeycomb structure. With extra electrons, mimicking a transformation of boron to carbon, causes a gradual decrease in the degree of buckling of the honeycomb lattice that can be interpreted as piezoelectric response. I also found that extra electrons can be achieved by placing borophene in direct contact with layered electrides such as Ca_2N. I found that extra electrons can be doubled to $\approx$0.4 e/B atom by changing from the B/Ca_2N bilayer to the Ca_2N/B/Ca_2N sandwich geometry.

Chapter 8

Towards room-temperature superconductivity in low-dimensional C_{60} nanoarrays: An *ab-initio* study

The following discussion is my original contribution to the related publication by Dogan Erbahar, Dan Liu, Savas Berber and David Tománek, Phys. Rev. B **97**, 140505(R) (2018) [143].

8.1 Introduction

The quest for room-temperature superconductivity has lost nothing of its appeal during the 30-year long intense search following the observation of superconductivity in cuprate perovskites, with the critical temperature T_c rising from the 30-K range in the La-Ba-Cu-O system [144] to 77 K in Y-Ba-Cu-O [145]. Current record T_c values of 133 K in the doped $HgBa_2Ca_2Cu_3O_8$ perovskite [146] and 203 K in sulfur hydride [147] have only been observed under high pressure. Progress in raising T_c significantly further has lagged behind expectations. Whereas the microscopic origin of superconductivity is still being speculated about in high-T_c compounds, the rather high T_c values observed in doped solid C_{60}, possibly even exceeding 60 K [148], results from strong electron-phonon coupling caused by the dynamical Jahn-Teller effect on individual fullerene molecules [149, 150]. In alkali-doped M_3C_{60} molecular solids, T_c could be quantitatively reproduced [149, 150] using the McMillan equation [151]. The key behind a substantial electron-phonon coupling constant is one of its factors, namely a high density of states (DOS) at the Fermi level $N(E_F)$, which depends on the particular element M used to intercalate bulk C_{60}.

Here I propose a way to further increase T_c for superconductivity by increasing $N(E_F)$ and thus the electron-phonon coupling constant λ by reducing the C_{60} coordination number Z in doped low-dimensional C_{60} nanoarrays. I considered intercalation by both electron donors and acceptors, as well as electron doping in a solid formed of La@C_{60} endohedral complexes. I found that $N(E_F)$ increases with decreasing bandwidth of the partly filled h_u HOMO and t_{1u} LUMO derived frontier bands, which may be achieved by reducing the coordination number of C_{60}. Whereas $N(E_F)$ increases significantly by changing from 3D C_{60} crystals to 2D arrays of doped fullerenes intercalated in-between graphene layers, $N(E_F)$ reaches its maximum in doped quasi-1D arrays of C_{60} molecules inside $(10, 10)$ carbon nanotubes (CNTs), forming C_{60}@CNT peapods. Whereas partial filling of the t_{1u}-derived band of C_{60} may be achieved by adsorbing K atoms on the peapod surface, the desired depopulation of the h_u-derived band by adsorbed F is not possible. The results indicate that the highest T_c value approaching room temperature may occur in electron-doped C_{60} peapod arrays or in diluted 3D crystals, where quasi-1D arrangements of C_{60} form percolation paths.

8.2 Computational methods

I performed density functional theory (DFT) calculations to obtain insight into the effect of geometrical arrangement of fullerenes on the electronic structure of C_{60} intercalation compounds. I used the Perdew-Zunger [75] form of the spin-polarized exchange-correlation functional in the local density approximation to DFT, as implemented in the SIESTA code [152], which correctly reproduces the inter-layer spacing and interaction in graphitic structures. The valence electrons were described by norm-conserving Troullier-Martins pseudopotentials [33] with partial core corrections in the Kleinman-Bylander factorized form [153]. I used a double-zeta polarized basis and limited the range of the localized orbitals in such a way that the energy shift caused by their spatial confinement was no more than 10 meV [154]. The Brillouin zone of a 3D lattice of C_{60} molecules was sampled by 10×10×10 k-points, that of a 2D lattice by 10×10 k-points, and that of decoupled 1D chains of C_{60} molecules inside a nanotube by 10 k-points. The DOS was convoluted by 0.02 eV^{-1}. In a periodic arrangement, 1D structures were separated by 15 Å thick vacuum regions and 2D structures by 13 Å thick vacuum regions. The charge density and the potentials were determined on a real-space grid with a mesh cutoff energy of 180 Ry, which was sufficient to achieve a total energy convergence of better than 2 meV/atom.

8.3 Results and discussions

In alkali-doped M_3C_{60} (M=K, Rb, Cs) fcc crystals, superconductivity with $T_c \lesssim 40$ K has been observed [155] and explained by electron-phonon coupling that is modulated by the lattice constant [149,150]. The same behavior is expected to occur in the isoelectronic La@C_{60} that has been isolated from raw soot [156] and found to be stable [157]. When exohedrally doped M_3C_{60} crystals are exposed to ambient or harsh conditions, other than the dopant atoms M may penetrate deep inside the lattice, react with the M atoms and destroy superconductivity. This is much less likely to occur in endohedrally doped La@C_{60} crystals, since the dopant La

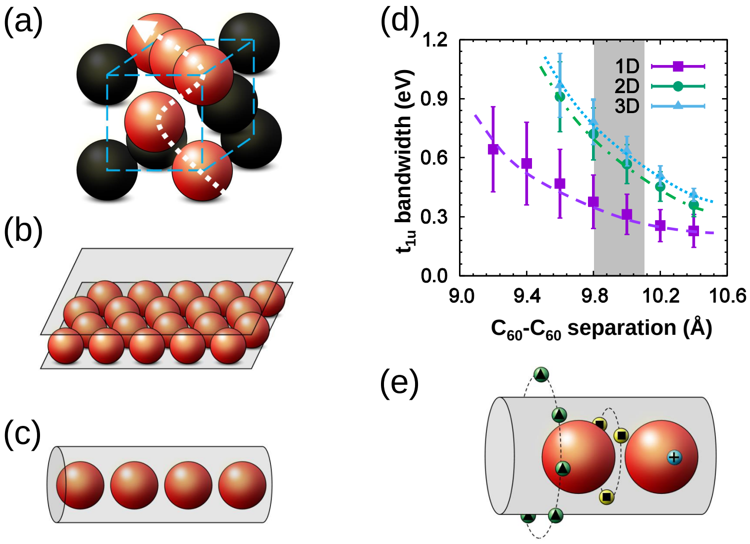

Figure 8.1: Schematic arrangement of C_{60} molecules in (a) a 3D fcc crystal, (b) a 2D triangular lattice, and (c) a 1D array inside a $(10, 10)$ carbon nanotube peapod. (d) Width of the t_{1u}-derived band in a 1D, 2D and 3D arrangement of C_{60} molecules as a function of the C_{60}-C_{60} center-to-center separation d_{cc}. The equilibrium value of d_{cc} depends on the C_{60} orientation and is indicated by the gray strip in (d) for undoped structures. The 'error bars' reflect the effect of changing the C_{60} orientation on the bandwidth. (e) Schematic arrangement of dopant atoms outside the 1D peapod (▲), inside the nanotube but outside the fullerene (■), and inside the fullerene (+). Dark spheres in (a) represent clusters other than C_{60} that separate quasi-1D percolating arrays of fullerenes from the surrounding matrix. The planes in (b) are only a visual aid.

atoms are enclosed inside the protective C_{60} cage. As mentioned above, superconductivity in 3D M_3C_{60} crystals is caused by strong electron-phonon coupling related to a dynamical Jahn-Teller effect on individual C_{60} cages, made possible by retardation. The dominant role of the intercalated alkali atoms is to partly fill the t_{1u} LUMO of C_{60} that broadens to a narrow band in the M_3C_{60} molecular solid. Changes in T_c caused by pressure or changing the element M can be traced back to changes in the electron-phonon coupling constant $\lambda = VN(E_F)$ in the McMillan equation [149–151]. Since the on-ball Bardeen-Pines interaction V does not change, λ is proportional to the C_{60}-projected DOS at the Fermi level $N(E_F)$, which – for electron doping – is roughly inversely proportional to the width of the t_{1u}-derived band. In hole-doped C_{60}, E_F is expected to be lowered into the h_u-derived band with an even higher

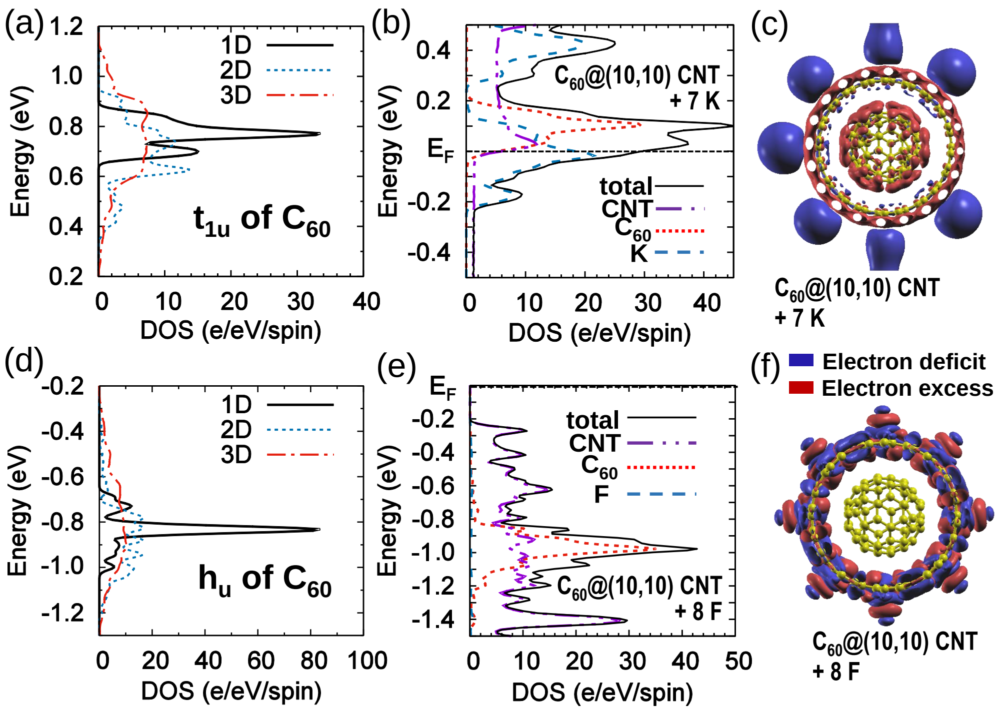

Figure 8.2: Density of states (DOS) and charge redistribution in doped C_{60} crystals. (a) DOS of the t_{1u} LUMO-derived bands of C_{60} in 1D, 2D and 3D periodic C_{60} arrangements for the C_{60}-C_{60} separation $d_{cc} = 9.8$ Å. (b) Total and projected DOS of a C_{60}@$(10, 10)$ CNT peapod doped externally by 7 K donor atoms per C_{60}. (c) Charge density difference $\Delta\rho = \rho_{tot}(C_{60}@CNT{+}7K) - \rho_{tot}(C_{60}@CNT) - \sum_{at} \rho_{tot}(K\ atom)$. (d) DOS of the h_u HOMO-derived bands of C_{60} in 1D, 2D and 3D periodic C_{60} arrangements for the C_{60}-C_{60} separation $d_{cc} = 9.8$ Å. (e) Total and projected DOS of a C_{60}@$(10, 10)$ CNT peapod doped externally by 8 F acceptor atoms per C_{60}. (f) Counterpart of (c) for C_{60}@CNT+8F. In (c) and (f), blue contours for electron deficit are shown for $\Delta\rho = -3.0\times10^{-3}$ e/bohr^3 and red contours for electron excess are shown for $\Delta\rho = +3.0\times10^{-3}$ e/bohr^3. All energies are with respect to E_F.

$N(E_F)$ value, which may be the cause of the high value $T_c \geq 60$ K that has been reported earlier [148].

All experimental strategies used so far to raise T_c have been based on increasing the C_{60}-C_{60} separation d_{cc} in a 3D fcc crystal, which would lower the width of the LUMO- and HOMO-derived bands and thus increase $N(E_F)$ in doped crystals. The approach is quite different [158]: I consider increasing $N(E_F)$ by reducing the number of C_{60} nearest neighbors. As seen in Fig. 8.1(a), this may be achieved simply in a 3D crystal by mixing C_{60}

with clusters of similar size that do not interact with C_{60}, such as BN fullerenes. In this case, the lowered C_{60} coordination number would decrease the width of the t_{1u} and h_u derived bands and thus increase $N(E_F)$ in doped crystals. Other C_{60} arrangements with a lower Z include 2D arrays of C_{60} that could possibly be intercalated in graphite [159,160], as seen in Fig. 8.1(b), or 1D arrays of C_{60} in C_{60}@NT peapods [161–163] shown in in Fig. 8.1(c). As seen in Fig. 8.1(d), the width of the t_{1u}-derived band decreases both with increasing C_{60}-C_{60} separation and with the reduction of dimensionality that translates to the reduction of the coordination number, with 1D arrangements appearing optimal. Since superconductivity is suppressed in truly 1D systems according to the Mermin-Wagner theorem [164], I consider bundles of weakly interacting peapods instead of isolated 1D peapods. As I will show in the following, the mail role of the nanotube in these systems is to provide a suitable enclosure that aligns C_{60} molecules and protects them from the ambient. Due to their weak interaction, bundles of nanotubes have a very similar DOS as isolated nanotubes. Since the same applies to peapods, I will consider an isolated peapod a valid representative of a peapod bundle from the viewpoint of electronic structure.

As indicated in Fig. 8.1(e), peapods with the narrowest bandwidth and potentially highest $N(E_F)$ could be doped by donor or acceptor atoms that may be outside the nanotube, inside the nanotube but outside C_{60}, or inside the C_{60} molecule such as the La@C_{60} metallofullerene [157]. Within the peapod, the C_{60}-C_{60} separation could be further increased by enclosing dopant atoms along with the C_{60} molecules inside the nanotube. For most of this study, I will focus on donor doping, causing partial filling of the t_{1u}-derived band, and will show later that acceptor doping may be hard to achieve.

The DOS shape of the t_{1u} LUMO-derived band in quasi-1D, 2D triangular and 3D fcc lattices of C_{60} is depicted in Fig. 8.2(a) and that of the h_u HOMO-derived band in the same lattices is shown in Fig. 8.2(d). Clearly, the DOS at E_F reaches its maximum near half-filling of these bands in quasi-1D structures. Since the t_{1u} LUMO-derived band holds up to 6 electrons and the h_u HOMO-derived band up to 10 electrons, half-filling of these bands requires either 3 extra electrons for each C_{60} and E_F inside the t_{1u}-derived band, or depletion of 5 electrons from each C_{60} and placing E_F inside the h_u-derived band. Comparing the results in Figs. 8.2(a) and 8.2(d), I note that acceptor doping – if achievable – would result in a significantly higher $N(E_F)$ than donor doping.

The calculated DOS of a C_{60}@$(10,10)$ peapod doped externally by 7 K atoms per C_{60} is shown in Fig. 8.2(b) and the DOS of the corresponding peapod doped externally by 8 F atoms per C_{60} is shown in Fig. 8.2(e). Comparing the partial densities of states in these two cases, I conclude that C_{60}-derived states are barely affected by those of the surrounding nanotube due to a very small hybridization. In the case of donor doping by K depicted in Fig. 8.2(b), I clearly observe partial filling of the t_{1u}-derived band of C_{60} as well as the nearly-free electron bands of the $(10,10)$ nanotube [165]. To get a better feel for the charge flow in the system, I plotted the charge density difference defined by $\Delta\rho = \rho_{tot}(\mathrm{C_{60}@CNT{+}7K}) - \rho_{tot}(\mathrm{C_{60}@CNT}) - \sum_{at} \rho_{tot}(\mathrm{K\ atom})$ in Fig. 8.2(c). Obviously, there is a net electron flow from K atoms to the C_{60}@$(10,10)$ peapod, with the excess charge accommodated both on the C_{60} and the nanotube. Integration of the C_{60}-projected DOS in Fig. 8.2(b) up to E_F indicates a partial population of the t_{1u}-derived band by 0.4 electrons.

The calculated DOS of an acceptor-doped peapod, shown in Fig. 8.2(e), presents a very different picture. I selected F as a suitable electron acceptor due to its high electronegativity. Unlike in previous studies of acceptor-doped C_{60}, where covalently bonded halogen atoms disrupted the π-electron network on the molecules [166], F atoms were bonded on the outside of the nanotube surrounding C_{60} molecules. As expected, I found the h_u-derived band of

C_{60} to be essentially unaffected by the presence of the surrounding nanotube and the 8 F atoms per C_{60} outside the nanotube. Still, the C_{60} molecule remained charge neutral. The h_u-derived narrow band band remained completely filled, located about 1 eV below E_F. I found F atoms to be strongly bonded outside the nanotube, causing pyramidalization of the CNT, disrupting its π-electron network and opening up a gap at the Fermi level, which turned the system into a semiconductor. This can be clearly see when inspecting the charge flow in this system in Fig. 8.2(f). I find that F atoms strongly hybridize with the C atoms of the tube, redistributing the charge only within the F/CNT subsystem, with no effect on the net charge of C_{60}. Since hole doping of C_{60} appears very difficult, I will focus on electron doping of the t_{1u}-derived band of C_{60} chains in the following.

As mentioned earlier, the electronic band structure of C_{60} arrays should depend to a nontrivial degree on the orientation of the C_{60} molecules that will affect the interaction between adjacent molecules [167]. I studied 5 different orientations, identified in Fig. 8.3(a), which result in a different degree of inter-ball hybridization. Since the effect of orientation on the total energy of C_{60} chains amounts to ≤ 2 meV/atom, I expect many C_{60} orientations to coexist within a quasi-1D C_{60} array inside a peapod. The DOS for a chain of C_{60} molecules at different orientations and the C_{60}-C_{60} separation $d_{cc} = 9.8$ Å is shown in Fig. 8.3(b). I note that the maximum DOS value changes significantly with orientation. Therefore, in Fig. 8.3(c), I plotted the range of achievable maxima of $N(E_F)$ as ‘error bars’ for different C_{60}-C_{60} orientations. I find that very high values of $N(E_F)$ may be achieved in 1D chains of C_{60} molecules, since doping further increases C_{60}-C_{60} separations beyond the value found in pristine peapods.

To estimate the critical temperature for superconductivity T_c, I used McMillan’s equation [149–151]

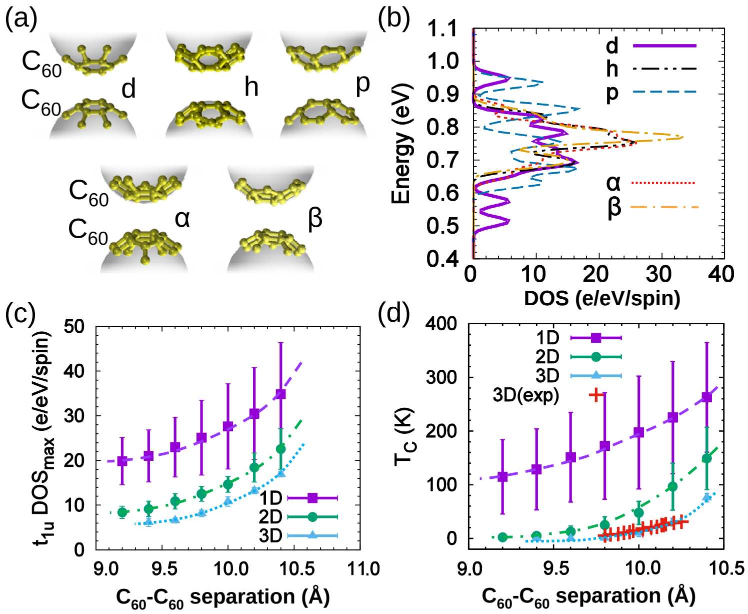

Figure 8.3: Properties of 1D arrays of C_{60} molecules found in CNT peapods. (a) Ball-and-stick models of different atomic arrangements at the C_{60}-C_{60} interface. Considered are double-bonds facing double-bonds (d), hexagons facing hexagons (h), pentagons facing pentagons (p). α and β arrangements are obtained by a 90° rotation of C_{60} molecules in p arrangement about two different axes that are orthogonal to the chain axis and to each other. (b) DOS of the t_{1u} LUMO-derived bands of C_{60} for the C_{60} orientations, defined in (a), at the C_{60}-C_{60} separation $d_{cc} = 9.8$ Å. All energies are with respect to E_F. (c) Maximum DOS value of t_{1u}-derived bands in 1D, 2D and 3D crystals of C_{60}. The 'error bars' reflect the effect of changing the C_{60} orientation. (d) Critical temperature for superconductivity T_c based on the McMillan equation (8.1) and using $N(E_F)$ from (c). The lines in (c) and (d) are guides to the eye.

$$T_c = \frac{\hbar\omega_{log}}{1.2k_B} \exp\left[\frac{-1.04(1+\lambda)}{\lambda - \mu^* - 0.62\lambda\mu^*}\right] . \tag{8.1}$$

This equation describes the solution of the Eliashberg equations in superconductors with a strong electron-phonon coupling ($\lambda \leq 2$) in a semi-empirical way that is physically appealing. It also has been found to correctly reproduce the observed T_c values in M_3C_{60} solids as a function of the C_{60}-C_{60} separation [150], shown by the data points for 3D systems in Fig. 8.3(d). I used the parameters of Ref. [[150]], namely $\hbar\omega_{log}/k_B = 2800$ K, $\mu^* = 0.2$ for the effective mass and $V = 52$ meV for the Bardeen-Pines interaction, which are not affected by the local arrangement of C_{60} molecules. Using $\lambda = VN(E_F)$ for the electron-phonon coupling constant, I were able to convert $N(E_F)$ values for 3D, 2D and quasi-1D systems with different C_{60}-C_{60} distances to potentially achievable T_c values and present the results in Fig. 8.3(d). The estimates indicate that, in the best imaginable scenario, T_c near room temperature may be achievable using bundles of donor-doped peapods.

Clearly, there are limits to the range of C_{60}-C_{60} separations d_{cc} compatible with superconductivity. Increasing d_{cc} decreases the inter-ball hopping integral t, while not affecting the on-ball Coulomb integral U. At large C_{60}-C_{60} separations, the U/t ratio should increase beyond a critical value that would change doped C_{60} from a metal to a Mott-Hubbard insulator [168, 169].

8.4 Summary

In summary, I have proposed a viable way to further increase T_c for superconductivity by increasing the C_{60}-projected density of states (DOS) at the Fermi level $N(E_F)$ and thus the electron-phonon coupling constant in doped low-dimensional C_{60} nanoarrays. I considered intercalation by both electron donors and acceptors, as well as electron doping in a solid formed of La@C_{60} endohedral complexes. I found that $N(E_F)$ increases with decreasing bandwidth of the partly filled h_u HOMO- and t_{1u} LUMO-derived frontier bands, which may be achieved by reducing the coordination number of C_{60}. $N(E_F)$ increases significantly by changing from 3D C_{60} crystals to 2D arrays of doped fullerenes intercalated in-between graphene layers and reaches its maximum in doped quasi-1D arrays of C_{60} molecules inside a (10, 10) carbon nanotube, forming a C_{60}@CNT peapod. Whereas partial filling of the t_{1u}-derived band may be achieved by adsorbing alkali atoms outside the 1D peapod, the desired depopulation of the h_u-derived band could not be achieved by F atoms adsorbed on the nanotube surrounding the C_{60} molecules. The results indicate that the highest T_c values may occur in electron-doped C_{60} peapods or in dilute 3D crystals, where quasi-1D arrangements of C_{60} form percolation paths. Only experimental evidence will show if low-dimensional arrays of doped C_{60} will become superconducting with T_c approaching room temperature, or rather turn to a Mott-Hubbard insulator.

Chapter 9

Shear instability in twisted bilayer graphene

The following discussion is my original contribution to the related publication by Xianqing Lin, Dan Liu and David Tománek, Phys. Rev. B **98**, 195432 (2018) [170].

9.1 Introduction

Theoretically postulated [171–174] drastic changes in the electronic structure at the Fermi level E_F of bilayer graphene (BLG) near the 'magic' twist angle $\theta_m \simeq 1.08^\circ$ have been recently confirmed experimentally [175, 176] and ignited a feverish research effort in twisted BLG (TBLG). Superconductivity [176] and strongly correlated electronic behavior [175], observed at θ_m, are associated with a meV-wide flat band around the Dirac point [171] at E_F with a vanishing density of states (DOS). This flat band, which is formed only within an extremely narrow range $\Delta\theta < 0.1^\circ$ around θ_m, is separated by band gaps above and below from the rest of the electronic spectrum [171, 175–177]. From the viewpoint of atomic structure, nonzero twist causes a Moiré pattern with domains of AB, BA and AA stacking to change rapidly in size especially at small values of the twist angle θ. In view of the unusual sensitivity of the electronic structure to twist angle θ alone, I study here the effect of two other soft deformation modes, namely global shear and atomic relaxation in TBLG. Published data suggest that shear does affect the electronic structure of untwisted and unrelaxed BLG [178], but do not report associated energy changes. Many calculations have explored atomic relaxations in untwisted [179] and twisted BLG and their effect on the electronic structure [180–188], but ignored inhomogeneities in the stacking structure observed by high-resolution transmission electron microscopy (TEM) [5, 189].

Here I combine continuum elasticity theory with a tight-binding description of the electronic structure [190] to study the behavior of BLG under combined twist and shear. I focus on geometries with a twist angle θ near the observed magic angle $\theta_m \approx 1.08^\circ$, where the electronic structure, including the appearance and disappearance of a flat band near E_F as well as band gaps above and below, shows extreme sensitivity to structural deformations. I find TBLG near θ_m to be energetically unstable with respect to global shear by the angle $\alpha \approx 0.08^\circ$. Also, I find that the effect of shear on the electronic structure is as important as that of atomic relaxation. Under optimum global shear, calculated θ_m is reduced by 0.04° and agrees with the observed value.

9.2 Computational methods

I use precise experimental data for monolayer and bilayer graphene as input for the calculations. For unstable geometries, where such data are not available, I use *ab initio* density functional theory (DFT) as implemented in the VASP code [14, 16, 191]. I used projector-augmented-wave (PAW) pseudopotentials [17,18] and the *SCAN+rVV10* exchange-correlation functional [192], which provides a proper description of the van der Waals interaction [193]. I used 800 eV as the electronic kinetic energy cutoff for the plane-wave basis and a total energy difference between subsequent self-consistency iterations below 10^{-5} eV/atom as the criterion for self-consistency. I reached full convergence, since the calculations were limited to very small unit cells of AA- and AB-stacked BLG.

9.3 Results and discussions

9.3.1 Deformation Modes in Bilayer Graphene

The softest deformation modes of BLG are relative translation and rotation of the constituent graphene layers. BLG subject to uniform twist creates a Moiré lattice of equilateral triangles, and rigid displacement only translates this lattice with no effect on the atomic and electronic structure. Atomic relaxations including local bending in TBLG, as well as global shear and stretch of the monolayers, require more energy. Global stretch, which involves bond stretching, is energetically harder than global shear, which involves only bond bending. Global shear creates a stripe pattern of domains [178]. The combination of twist and shear has not been explored so far.

The deformation of BLG under shear and twist is defined in Fig. 9.1(a). In the initially AA-stacked BLG, I define the shear direction within the top layer by the angle β with respect to the armchair direction. After first being sheared by the angle α, the to player is subsequently rotated by the angle θ. The mathematical formulation of the shear-twist deformation in BLG is detailed in the Related Information section. The general Moiré pattern of a sheared and twisted BLG is a lattice asymmetric triangles with AA-stacked regions forming the vertices, as shown schematically in Fig. 9.1(b). The triangular regions of AB and BA stacking between the vertices have no symmetry in general, but become equilateral in the case of pure twist in the BLG associated with $\alpha = 0°$. Figure 9.1(c) contains a reproduction of a dark-field TEM image of the BLG reported in Ref. [5]. The

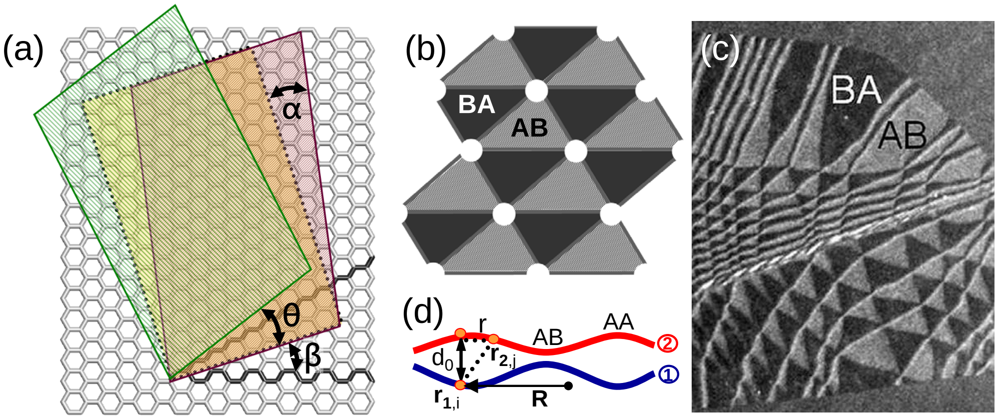

Figure 9.1: Shear and twist in bilayer graphene (BLG). (a) Definition of shear and twist operations in BLG, initially a bilayer in AA stacking indicated by the honeycomb lattice. A rectangular segment of the top layer, with one side closing the angle β with respect to the highlighted armchair direction, is indicated in yellow and surrounded by the dotted line. The segment is first sheared by the angle α and subsequently rotated by the angle θ. (b) Schematic top view of a uniformly twisted and sheared monolayer graphene (MLG) on top of an undeformed MLG. The resulting relaxed Moiré pattern contains regions of AA stacking, highlighted by the white circles, and those of AB or BA stacking. (c) Dark-field TEM image of bilayer graphene reproduced from Ref. [[5]]. (d) Schematic side view of a relaxed sheared and twisted BLG with locally varying stacking.

triangular lattice in this figure is strongly distorted due to inhomogeneous twist and strain. Quantities associated with atomic relaxation are defined in the schematic side view of sheared and twisted BLG in Fig. 9.1(d). The local inter-layer distance d_0 depends on the 2D position vector $\mathbf{R}$ within the BLG plane, which distinguishes regions with different local stacking sequences.

9.3.2 Relaxations in Sheared and Twisted Bilayer Graphene

To quantify the effect of relaxation in the BLG, I consider both in-plane and out-of-plane deformations and calculate changes in the total energy $E_{tot} = E_{el} + E_{int}$ in terms of the elastic deformation energy E_{el} of the individual layers and the interlayer interaction energy E_{int}. The displacement of the atom i at $\mathbf{r}_{n,i}$, defined in Fig. 9.1(d) for layers $n = 1, 2$, is

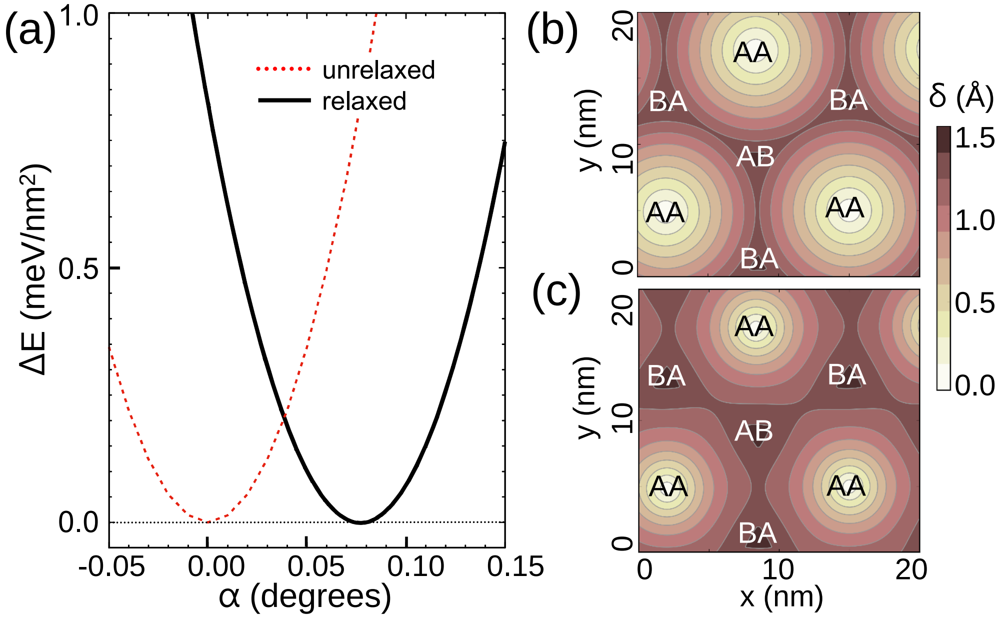

Figure 9.2: (a) Energy difference ΔE caused by shearing the top layer of BLG, which had been twisted by $\theta_m = 1.08°$, by varying the shear angle α along the $\beta = 0°$ direction. Results for the BLG with unrelaxed atomic positions in planar, sheared monolayers are shown by the red dotted line and for the BLG with relaxed atomic positions by the black solid line. Contour plots of the local shift vector length $\delta = |\boldsymbol{\delta}|$ in the BLG structure, which had been twisted by $\theta_m = 1.08°$ and sheared by $\alpha = 0.08°$ along the $\beta = 0°$ direction, (b) in absence and (c) in presence of lattice relaxation.

described by a continuous displacement field with an in-plane component $\mathbf{u}^{(n)}(\mathbf{R})$ and an out-of-plane component $h^{(n)}(\mathbf{R})$. The elastic deformation energy is given by [194]

$$\begin{aligned} E_{el} &= \sum_{n=1}^{2} \int d\mathbf{R} \Bigg\{ \frac{\kappa}{2} \left(\frac{\partial^2 h^{(n)}}{\partial x^2} + \frac{\partial^2 h^{(n)}}{\partial y^2} \right)^2 \\ &+ \frac{\lambda+\mu}{2} \left(\frac{\partial u_x^{(n)}}{\partial x} + \frac{\partial u_y^{(n)}}{\partial y} \right)^2 \\ &+ \frac{\mu}{2} \left[\left(\frac{\partial u_x^{(n)}}{\partial x} - \frac{\partial u_y^{(n)}}{\partial y} \right)^2 + \left(\frac{\partial u_y^{(n)}}{\partial x} + \frac{\partial u_x^{(n)}}{\partial y} \right)^2 \right] \Bigg\}, \end{aligned} \tag{9.1}$$

where the integral extends over the Moiré pattern supercell. I use $\kappa = 1.4$ eV for the flexural rigidity [19], and $\lambda = 4.23$ eV/Å^2 and $\mu = 9.04$ eV/Å^2 for the 2D elastic Lamé factors [188] of graphene.

To calculate the interlayer interaction energy E_{int}, I first characterize the local stacking at position $\mathbf{R} = \mathbf{r}_{1,i}$ of atom i in layer 1, shown in Fig. 9.1(d), by calculating the connection vectors $\mathbf{r}_{2,j} - \mathbf{r}_{1,i}$ to all atoms j of the same sublattice in layer 2 and their projections onto the $x - y$ plane of the lattice. The shortest among these vectors is then called the shift vector [179] $\boldsymbol{\delta}(\mathbf{R})$. With this definition, $|\boldsymbol{\delta}| = 0$ in AA-stacked and $|\boldsymbol{\delta}| = a/\sqrt{3}$ in AB-stacked BLG, where $a = 2.46$ Å is the lattice constant of graphene. The observed interlayer distance in the stable AB-stacked BLG is $d_0^{AB} = 3.35$ Å. The corresponding calculated value for AA-stacked BLG, which is less stable by $\Delta E = 0.38$ eV/nm^2, is $d_0^{AA} = 3.60$ Å.

The interlayer interaction energy depends on the local interlayer separation $d_0(\mathbf{R})$ and the local shift vector $\boldsymbol{\delta}(\mathbf{R})$. Since the Moiré supercells are much larger than the interatomic distance in the twist angle range of interest, both quantities can be represented well by a continuous field. Then, the interlayer interaction energy is given by the integral

$$E_{int} = \int V(\mathbf{R}) d\mathbf{R} \, , \tag{9.2}$$

which extends over the Moiré supercell. I represent the interlayer interaction potential $V(\mathbf{R}) = V[\boldsymbol{\delta}(\mathbf{R}), d_0(\mathbf{R})]$, as well as the quantities d_0 and $\boldsymbol{\delta}$, by a Fourier expansion over the BLG lattice [181], which is detailed in the Related Information section. The expansion requires only few of the shortest reciprocal superlattice vectors of the BLG and is trivial for an untwisted BLG with AA and AB stacking, where $V =$ const. and $V^{AA} - V^{AB} = 0.38$ eV/nm^2.

The optimum geometry of the relaxed BLG that had been subject to global shear and twist is obtained by globally minimizing the total energy, which has been determined using a Fourier expansion detailed in the Related Information section.

Whereas lattice relaxation is driven by energy gain, shear distortion of a monolayer requires energy investment. For a given twist angle θ, it is conceivable that the energy invested in shear may be outweighed by an additional energy gain associated with relaxation to a more favorable structure. This situation is illustrated in Fig. 9.2(a) that shows energy changes in TBLG with $\theta_m = 1.08°$. I found the energy values, which are shown for shear along the $\beta = 0°$ direction, to be nearly identical for shear along $\beta = 30°$, an conclude that the shear energy does not depend on β. When lattice relaxation is suppressed, as shown by the dotted line, the most stable geometry is unsheared with $\alpha = 0°$. When allowing for lattice relaxation, the optimum geometry has acquired a global shear angle $\alpha = 0.08°$.

The absolute value of the local shift vector $\delta = |\boldsymbol{\delta}|$ as a function of $\mathbf{R} = (x, y)$ is shown in Figs. 9.2(b) and 9.2(c) for BLG structures that have been twisted by $\theta_m = 1.08°$ and sheared by the small angle $\alpha = 0.08°$ along the $\beta = 0°$ direction. The corners of the Moiré supercell, shown in white, are the unshifted AA regions with $\delta = 0$. In the unrelaxed structure of Fig. 9.2(b), the energetically favorable regions of AB or BA stacking are rather small. Upon relaxation, these favorable stacking regions increase in size, as seen in Fig. 9.2(c). The effect of relaxation becomes much more visible at smaller twist angles θ associated with very large Moiré domains. As seen in Fig. 9.4, the AB and BA domains then acquire a distinctly triangular shape upon relaxation, which has been observed in TEM images [5,189] including Fig. 9.1(c).

9.3.3 Electronic Structure of Sheared, Twisted and Relaxed Bilayer Graphene

To study the combined effect of shear, twist and atomic relaxation on the electronic structure of BLG, I use an extension of the minimum Hamiltonian [190] that had successfully reproduced the electronic structure of twisted BLG. Due to the high in-plane stiffness and flexural rigidity of graphene, the atomic relaxation is rather small and smooth across the BLG lattice, so that the intra-layer nearest-neighbor Hamiltonian with $V^0_{pp\pi} = 3.09$ eV is not affected. Since the interlayer separation changes between the value d_0^{AA} and d_0^{AB} within each Moiré domain, as seen in Fig. 9.1(d), I modify the expressions for the interlayer hopping in Ref. [[190]] to

$$t(r, \mathbf{R}) = V^0_{pp\sigma}(d_0) e^{-(\sqrt{r^2+d_0^2}-d_0)/\lambda} \frac{d_0^2}{r^2 + d_0^2} \,, \tag{9.3}$$

where

$$V^0_{pp\sigma}(d_0) = V^0_{pp\sigma}(d_0^{AB}) e^{-(d_0-d_0^{AB})/\lambda'} \,. \tag{9.4}$$

In these expressions, the only quantity that depends on the position $\mathbf{R}$ within the layer is the local interlayer separation $d_0 = d_0(\mathbf{R})$, defined in Fig. 9.1(d). For the unrelaxed geometry with $d_0 = d_0^{AB} = \text{const.}$, the values $V^0_{pp\sigma}(d_0^{AB}) = 0.39$ eV, $d_0^{AB} = 3.35$ Å, $\lambda = 0.27$ Å have been established in Ref. [[190]]. I furthermore use the parameter $\lambda' = 0.58$ Å to adequately describe the dependence of $V^0_{pp\sigma}$ on the interlayer separation to match the DFT calculations.

In TBLG, where atomic relaxation has not been considered explicitly in a related previous study [190], I determined the electronic structure at the interlayer distance d_0^{AB} using the same continuum method for the description of eigenstates. In unrelaxed TBLG subject to shear, the interlayer Hamilton matrix elements of Ref. [[190]] are modified as

$$\langle \psi_{1,\eta}(\mathbf{k_1}) | H | \psi_{2,\xi}(\mathbf{k_2}) \rangle = \sum_{\mathbf{G},\mathbf{G'}} \frac{\tilde{t}(|\mathbf{k_1} + \mathbf{G}|)}{\Omega} e^{i(\mathbf{G} \cdot \tau_\eta - \mathbf{G'} \cdot \tau'_\xi)} \delta_{\mathbf{k_2} - \mathbf{k_1}, \mathbf{G} - \mathbf{G'}} \, . \tag{9.5}$$

Here I use η and ξ to represent the two sublattices with the basis vectors $\boldsymbol{\tau}$ in the unsheared bottom layer 1 and $\boldsymbol{\tau'}$ in the top layer 2 that has been sheared and twisted. $\mathbf{k_n}$ is the momentum vector in layer n. $\tilde{t}(k)$ is the 2D Fourier transform of $t(r)$ that is independent of the position within the unrelaxed bilayer, which is kept at the constant optimum interlayer separation d_0^{AB}. $\mathbf{G}$ is the reciprocal lattice vector of the bottom layer 1 and $\mathbf{G'}$ is the reciprocal lattice vector of the sheared and twisted top layer 2. For non-specific values of α, β and θ, the BLG lattice is generally incommensurate, but can be approximated by a commensurate Moiré superlattice with large unit cells.

For small twist angles, the reciprocal lattice vectors of the undeformed bottom layer 1 in Eq. (9.5) can be approximated by $\mathbf{G} = n_1 \mathbf{b}_1 + n_2 \mathbf{b}_2$ and those of the deformed top layer 2 by $\mathbf{G'} = n_1 \mathbf{b}'_1 + n_2 \mathbf{b}'_2$, with n_1 and n_2 being small integers. In these expressions, $\mathbf{b_{1/2}}$ are the two vectors spanning the reciprocal lattice of the bottom layer and $\mathbf{b'}_{\mathbf{1/2}}$ those spanning the reciprocal lattice of the deformed top layer. In relaxed commensurate BLG structures, I do not use Eq. (9.5), but rather diagonalize the tight-binding Hamiltonian directly to obtain the electronic band structure.

The effect of shear and atomic relaxation on the DOS of TBLG subject to twist by the magic angle $\theta_m = 1.08°$ is discussed in Fig. 9.3 for energies close to E_F and in Fig. 9.5 for a wider energy range. The DOS characteristics at θ_m are a narrow 'flat band' around the Dirac point with vanishing DOS at E_F and band gaps above and below. The DOS of unsheared and unrelaxed TBLG in Fig. 9.3(a) is the same as in a previous report [190] for

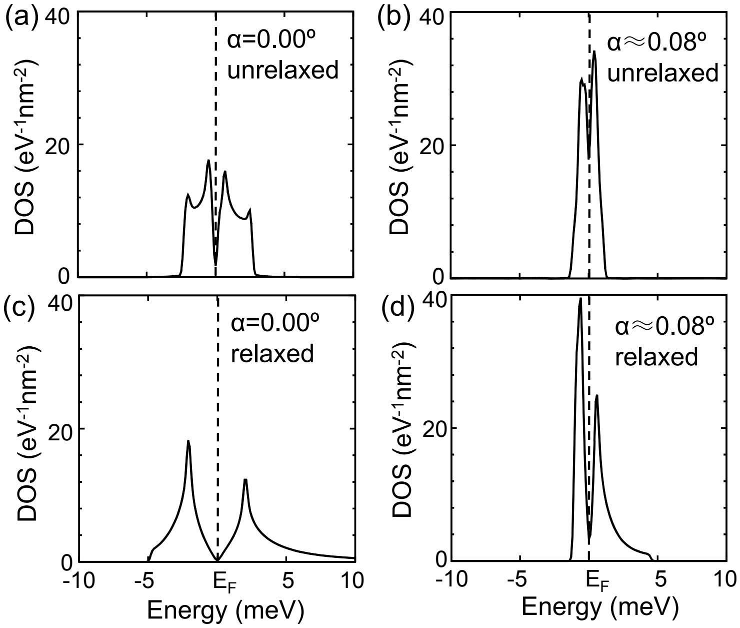

Figure 9.3: Electronic density of states (DOS) in the BLG structure subject to the magic twist angle $\theta_m = 1.08°$. Results for the unsheared structure are shown in panels (a) and (c), and those for the top layer sheared by $\alpha = 0.08°$ along the $\beta = 0°$ direction in (b) and (d). Results for the unrelaxed structure in (a) and (b) are compared to those for the relaxed structure in (c) and (d).

the same structure, where shear and atomic relaxation have not been considered explicitly. Subjecting BLG to global shear by $\alpha = 0.08°$, while suppressing any atomic relaxation, reduces the width of the flat significantly, as seen in Fig. 9.3(b), to almost half its value in unsheared TBLG. This result alone proves that even minor shear plays a significant role in the electronic structure of TBLG. As seen in Fig. 9.3(c), atomic relaxation alone increases the width of the band near E_F significantly with respect to the structure in Fig. 9.3(a) to the degree that the designation 'flat band' is no longer appropriate. Subjecting this relaxed structure to minor shear of $\alpha = 0.08°$, however, narrows down this band to resemble that of Fig. 9.3(a) for TBLG irrespective of shear and relaxation. Thus, taking shear into account is essential to properly identify the θ_m value in relaxed TBLG. I compared the width of the narrow band around E_F for unsheared and sheared TBLG with atomic relaxation. The results, reproduced in Fig. 9.6, suggest that the minimum bandwidth is found at the magic angle $\theta_m = 1.12^\circ$ in relaxed TBLG with suppressed shear. This value is larger than the magic angle value $\theta_m = 1.08^\circ$ that is observed in sheared and relaxed TBLG.

As reported in the discussion of shear in Fig. 9.2(a), the deformation energy ΔE is nearly independent of the shear direction β. Nevertheless, β modifies strongly the shape of the triangles in the Moiré superlattice. Local changes in the shear angle α and direction β are clearly visible in the TEM images of BLG reported in Fig. 9.1(c) and Refs. [[5]] and [[189]]. I also note that the high energy cost of in-layer deformations including shear limits the degree of atomic relaxation. Distributing shear from one to both layers of BLG should cut this energy cost in half in the harmonic regime, thus reducing the limits imposed on atomic relaxation and providing extra energy gain for the system.

9.4 Summary

In conclusion, I studied the effect of combined shear and twist on the energy as well as the atomic and electronic structure of BLG. I found that the observed drastic changes in the electronic structure near the Fermi level, caused by minute changes of the twist angle away from the magic value $\theta_m \approx 1.08^\circ$, are strongly affected by lattice relaxation and global shear. Using precise experimental data for monolayer and bilayer graphene as input in a simplified formalism for the electronic structure and elastic energy, I found TBLG near θ_m to be unstable with respect to global shear by the angle $\alpha \approx 0.08^\circ$. I also found that shear and atomic relaxation modified the electronic structure of TBLG to a similar degree. At optimum global shear, the calculated value of the magic angle θ_m in relaxed TBLG is reduced by 0.04° to agree with the observed value of 1.08°.

9.5 Related Information

9.5.1 Mathematical formulation of the rigid shear-twist deformation in bilayer graphene

Before describing the shear-twist deformation in bilayer graphene (BLG), I need to recall that the honeycomb lattice of graphene consists of two triangular sub-lattices A and B. The Bravais lattice of the bottom layer 1 is spanned by the vectors $\mathbf{a_1} = a(\sqrt{3}/2, -1/2)$ and $\mathbf{a_2} = a(\sqrt{3}/2, 1/2)$ in Cartesian coordinates, where $a = 2.46$ Å is the lattice constant of graphene. The basis vectors of the sublattices are $\boldsymbol{\tau_A} = 0$ and $\boldsymbol{\tau_B} = (\mathbf{a_1} + \mathbf{a_2})/3$. Initially, the top layer 2 of the BLG is on top of layer 1 in AA stacking.

The sheer-twist transformation of the BLG top layer with respect to the bottom layer is shown schematically in Fig. 9.1(a). Pure shear in the graphene top layer by the angle α along the shear direction angle β with respect to the armchair direction is described by the transformation matrix

$$S_\alpha = \begin{pmatrix} 1 - \sin\beta\cos\beta\tan\alpha & (\cos\beta)^2\tan\alpha \\ -(\sin\beta)^2\tan\alpha & 1 + \sin\beta\cos\beta\tan\alpha \end{pmatrix} . \tag{9.6}$$

Pure counter-clockwise twist of the top layer by the angle θ with respect to the bottom layer is described by the unitary transformation matrix

$$T_\theta = \begin{pmatrix} \cos\theta & -\sin\theta \\ \sin\theta & \cos\theta \end{pmatrix} . \tag{9.7}$$

The shear-twist operation transforms the two Bravais lattice vectors $\mathbf{a_j}$ of the top layer to

$\mathbf{a_j'} = T_\theta S_\alpha \mathbf{a_j}$ with $j = 1, 2$. Except for specific values of θ, α and β, the shear-twisted BLG (STBLG) lattice is incommensurate. For small values of θ and α, such an incommensurate structure can be approximated by a commensurate superlattice with with large Moiré supercells. The electronic structure of this system can be obtained to a good accuracy using the continuum method described in Ref. [[190]].

The reciprocal Moiré superlattice is spanned by the two vectors $\mathbf{b_1^{(s)}} = \mathbf{b_2} - \mathbf{b'_2}$ and $\mathbf{b_2^{(s)}} = (\mathbf{b'_1} + \mathbf{b'_2}) - (\mathbf{b_1} + \mathbf{b_2})$. In the notation, $\mathbf{b_j}$ with $j = 1, 2$ are the two vectors spanning the reciprocal lattice of the bottom layer and the primed vectors $\mathbf{b'_j}$ span the reciprocal lattice of the top layer. The two reciprocal lattice vectors $\mathbf{b_1^{(s)}}$ and $\mathbf{b_2^{(s)}}$ define the lattice vectors $\mathbf{a_1^{(s)}}$ and $\mathbf{a_2^{(s)}}$ of the direct Bravais STBLG superlattice. When $\mathbf{a_1^{(s)}}$ and $\mathbf{a_2^{(s)}}$ both belong to the Bravais lattice of the individual layers, STBLG becomes commensurate. This condition is fulfilled when $\mathbf{a_1^{(s)}} = M_1\mathbf{a_1} + N_1\mathbf{a_2}$ and $\mathbf{a_2^{(s)}} = M_2\mathbf{a_1} + N_2\mathbf{a_2}$ with integer values of M_1, N_1, M_2, and N_2.

The supercell area of the sheared top layer remains the same as that of the unsheared bottom layer if $M_2 + N_2 = N_1 - 1$. The quantities M_1, N_1, M_2, and N_2 define uniquely the twist angle θ, the shear angle α and the shear direction angle β of the top layer. One geometry near the first magic angle, characterized by $(M_1, N_1) = (30, 31)$ and $(M_2, N_2) = (-31, 61)$, describes an unsheared twisted BLG layer with $\theta = 1.0845°$ and $\alpha = 0°$. Another similar geometry, characterized by $(M_1, N_1) = (31, 32)$ and $(M_2, N_2) = (-36, 67)$, describes a sheared twisted BLG layer with $\theta = 1.0845°$, $\alpha = 0.0872°$, and $\beta = -0.5423°$. I determine the lattice relaxation and its effect on the electronic structure of the sheared and twisted BLG using the commensurate structures.

9.5.2 Mathematical background of the relaxation treatment in sheared and twisted bilayer graphene

BLG subject to rigid shear and twist, which is characterized by θ, α and β, is further stabilized by atomic relaxation. In the bottom layer 1 with $\theta = \alpha = 0$, the in-plane displacement $\mathbf{u}^{(1)}(\mathbf{R})$ of an atom with respect to its initial position $\mathbf{R}$ can be represented by a Fourier expansion as

$$\mathbf{u}^{(1)}(\mathbf{R}) = \sum_j \tilde{\mathbf{u}}^{(1)}(\mathbf{G}_j^{(s)}) \sin(\mathbf{G_j}^{(s)} \cdot \mathbf{R}) \,. \tag{9.8}$$

The sum extends over all vectors $\mathbf{G_j^{(s)}}$ of the reciprocal Moiré superlattice of the BLG, which is spanned by $\mathbf{b}_1^{(s)}$ and $\mathbf{b}_2^{(s)}$.

In the twisted and sheared top layer 2, the in-plane displacement $\mathbf{u}^{(2)}(\mathbf{R})$ of an atom with respect to its position $\mathbf{R}$ in the unrelaxed, unsheared, but twisted layer can be expressed by

$$\mathbf{u}^{(2)}(\mathbf{R}) = \sum_j \tilde{\mathbf{u}}^{(2)}(\mathbf{G}_j^{(s)}) \sin(\mathbf{G}_j^{(s)} \cdot S_\alpha \mathbf{R}) + S_\alpha \mathbf{R} - \mathbf{R} \,. \tag{9.9}$$

Here, the direction angle β of the shear transformation, defined as S_α in Eq. (9.6), has been rotated by the twist angle θ. I note that atomic displacements described by Eqs. (9.8) and (9.9) maintain the shape and size of the Moiré supercells. In BLG subject to twist angles near $\theta_m = 1.08°$, the summation in Eqs. (9.8) and (9.9) requires only three shortest vectors of the reciprocal Moiré superlattice $\mathbf{G_1^{(s)}} = \mathbf{b}_1^{(s)}$, $\mathbf{G_2^{(s)}} = \mathbf{b}_2^{(s)}$, and $\mathbf{G_3^{(s)}} = -\mathbf{b}_1^{(s)} - \mathbf{b}_2^{(s)}$. In BLG subject to smaller twist angles θ around 0.4°, I include three additional vectors $\mathbf{G_4^{(s)}} = 2\mathbf{b}_1^{(s)}$, $\mathbf{G_5^{(s)}} = 2\mathbf{b}_2^{(s)}$, and $\mathbf{G_6^{(s)}} = -2\mathbf{b}_1^{(s)} - 2\mathbf{b}_2^{(s)}$ for convergence.

Expressions for the in-plane atomic displacements $\mathbf{u}^{(n)}(\mathbf{R})$ in layers $n = 1, 2$ allow us to determine the shift vector $\boldsymbol{\delta}(\mathbf{R})$ at the position $\mathbf{R}$ by

$$\boldsymbol{\delta}(\mathbf{R}) = \left[\mathbf{u}^{(2)}(T_\theta \mathbf{R}) - \mathbf{u}^{(1)}(\mathbf{R})\right] + [T_\theta \mathbf{R} - \mathbf{R}] \ . \tag{9.10}$$

The periodicity of $\mathbf{u}^{(1)}(\mathbf{R})$ and $\mathbf{u}^{(2)}(\mathbf{R})$ of the Moiré superlattice, described by the Fourier sum in Eqs. (9.8) and (9.9), describes the same periodic behavior of $\boldsymbol{\delta}(\mathbf{R})$.

Similarly, the periodicity in the interlayer separation $d_0(\mathbf{R})$ can be evaluated by the Fourier sum

$$d_0(\mathbf{R}) = < d_0 > + \Delta d_0 \sum_{j=1}^{3} \cos(\mathbf{G_j^{(s)}} \cdot \mathbf{R}) \, . \tag{9.11}$$

Here, $< d_0 >$ is the average interlayer distance and Δd_0 describes the modulation of d_0. Since d_0 varies smoothly across the Moiré supercell, an adequate description of $d_0(\mathbf{R})$ can be obtained using only three shortest vectors $\mathbf{G_j^{(s)}}$ of the reciprocal Moiré superlattice defined above for $j = 1 - 3$. Having specified the position dependence of the interlayer distance $d_0(\mathbf{R})$, the out-of-plane displacement $h^{(n)}$ of each individual layer n, used to evaluate E_{el} using Eq. (9.1), is given by

$$h^{(1)}(\mathbf{R}) = \frac{1}{2}\left(-d_0(\mathbf{R}) + 3\Delta d_0 + < d_0 >\right) \quad \text{and} \tag{9.12}$$

$$h^{(2)}(\mathbf{R}) = \frac{1}{2}\left(+d_0(\mathbf{R}) - 3\Delta d_0 - < d_0 >\right) \, . \tag{9.13}$$

With the Fourier expansions of the in-layer displacement $\mathbf{u}^{(n)}(\mathbf{R})$ and the interlayer distance $d_0(\mathbf{R})$, I can determine the elastic energy E_{el} of STBLG using Eq. (9.1).

To determine the interlayer interaction energy E_{int} specified in Eq. (9.2), I have to locate a proper expression for the interlayer interaction potential $V(\mathbf{R})$. Since $V(\mathbf{R})$ is periodic in

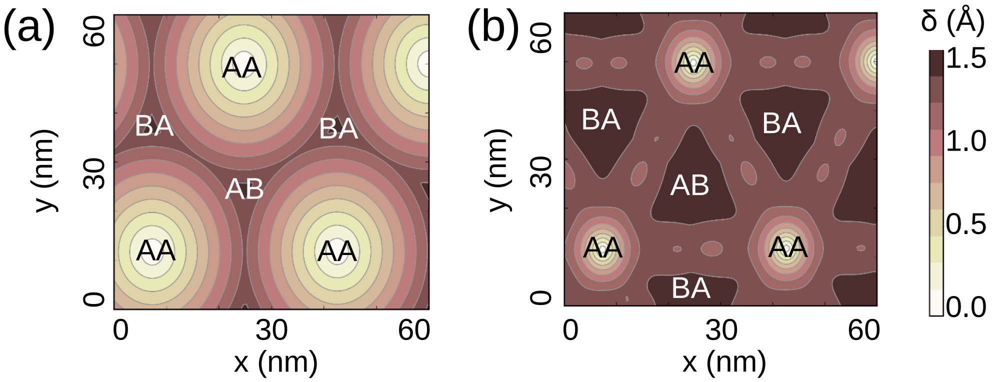

Figure 9.4: Contour plots of the local shift vector length $\delta = |\boldsymbol{\delta}|$ in the BLG structure, which had been twisted by $\theta = 0.4°$ and sheared by $\alpha = 0.08°$ along the $\beta = 0°$ direction, (a) in absence and (b) in presence of lattice relaxation.

STBLG, I can also express it as a Fourier expansion [181]

$$V(\mathbf{R}) = \sum_j \tilde{V}(\mathbf{G}_j^{(s)}) \cos(\mathbf{G_j}^{(s)} \cdot \mathbf{R})\,. \tag{9.14}$$

The sum extends over all vectors $\mathbf{G_j^{(s)}}$ of the reciprocal Moiré superlattice of the BLG. In reality, $V(\mathbf{R}) = V(\boldsymbol{\delta}(\mathbf{R}), d_0(\mathbf{R}))$ depends not on the global position $\mathbf{R}$, but rather the quantities $\boldsymbol{\delta}$ and d_0, which show the same periodicity, as expressed in Eqs. (9.10) and (9.11). Using straight-forward algebra, I arrive at the expression

$$V(\boldsymbol{\delta}, d_0) = V_{AA}(d_0) - 6\Delta V(d_0) + 2\Delta V(d_0) \sum_{j=1}^{3} \cos(\mathbf{G}_j \cdot \boldsymbol{\delta})\,, \tag{9.15}$$

where the sum is limited to the smallest three vectors $\mathbf{G}_1 = \mathbf{b_1}$, $\mathbf{G}_2 = \mathbf{b_2}$, and $\mathbf{G}_3 = -\mathbf{b_1} - \mathbf{b_2}$, since V varies smoothly with $\boldsymbol{\delta}$.

I have used the expression $\Delta V(d_0) = (1/9)[V^{AA}(d_0) - V^{AB}(d_0)]$ for the periodic modulation of V in Eq. (9.15), where $V^{AA}(d_0)$ and $V^{AB}(d_0)$ are the total energies of AA- and AB-stacked BLG per area, which both depend on the interlayer distance d_0. Furthermore, I

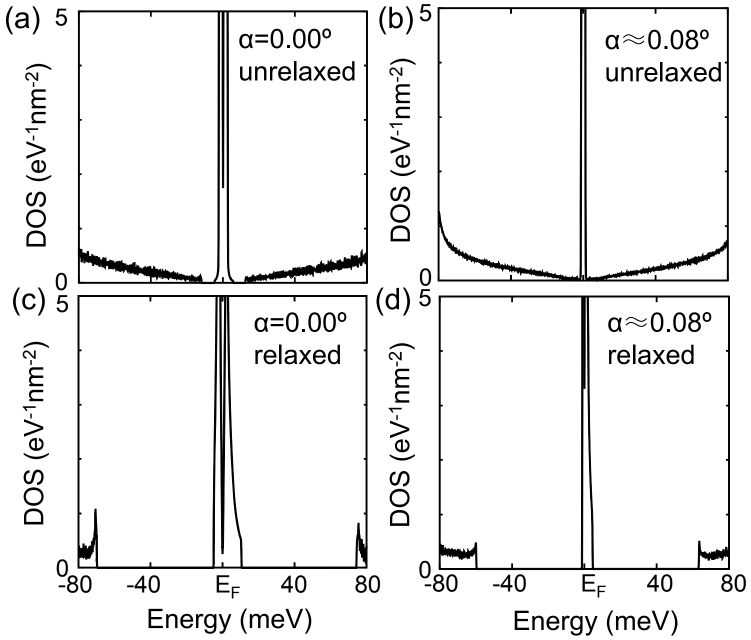

Figure 9.5: Electronic density of states (DOS) in the BLG structure subject to the magic angle twist $\theta_m = 1.08°$. Results for the unsheared structure are shown in panels (a) and (c), and those for the top layer sheared by $\alpha = 0.08°$ along the $\beta = 0°$ direction in (b) and (d). Results for the unrelaxed structure in (a) and (b) are compared to those for the relaxed structure in (c) and (d). The energy scale is extended in comparison to Fig. 9.3.

have set $V^{AA}(d_0^{AA}) = 0$ as a reference value. Using the DFT results, I have fitted $V_{AA}(d_0)$ and $V_{AB}(d_0)$ by third-order polynomials. The expressions in units of eV/Å^2 are $V^{AA}(d_0) = [0.113(d_0 - d_0^{AA})^2 - 0.340(d_0 - d_0^{AA})^3]/\Omega_0$ and $V_{AB}(d_0) = [-0.020 + 0.174(d_0 - d_0^{AB})^2 - 0.224(d_0 - d_0^{AB})^3]/\Omega_0$ when using d_0 in Å units and the value $\Omega_0 = 5.24$ Å^2 for the area of the graphene unit cell.

With expressions for E_{el} and E_{int} in place, I can evaluate the total energy $E_{tot} = E_{el} + E_{int}$ for any BLG geometry. For given global shear characterized by α and β and given global twist given by θ, I can determine the atomic relaxations by globally minimizing the total energy with respect to $\tilde{\mathbf{u}}^{(\mathbf{n})}(\mathbf{G}^{(\mathbf{s})})$, Δd_0 and $< d_0 >$.

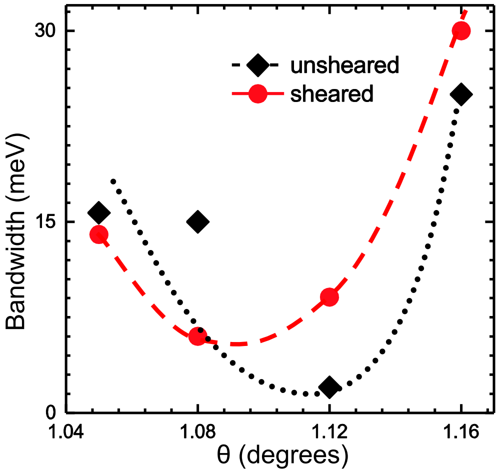

Figure 9.6: The width of the 'flat band' in a relaxed twisted bilayer graphene structure as a function of the twist angle θ. Data points for commensurate, relaxed structures in the vicinity of the observed value $\theta_m = 1.08°$ are presented by the black diamonds (◆) for the unsheared lattice and by the red circles (●) for the structure with the top layer sheared by $\alpha \approx 0.08°$ along the $\beta = 0°$ direction. The dotted and dashed lines are guides to the eye.

9.5.3 Local relaxation in sheared and twisted bilayer graphene

The pattern of the local shift vectors δ depends primarily on the twist angle θ, which determines the domain size. The pattern in the bilayer graphene (BLG) lattice twisted by a very small angle $\theta = 0.4°$ is presented in Fig. 9.4. The domains of the Moiré superlattice are significantly larger than in BLG with the magic twist angle $\theta_m = 1.08°$ discussed earlier. The δ pattern in the larger domains is changed substantially by atomic relaxation. In particular, the domains of AB or BA stacking acquire a distinct triangular character that has been observed in dark-field TEM images [5, 189].

9.5.4 Electronic structure changes in sheared and twisted bilayer graphene

The electronic density of states (DOS) in sheared and twisted BLG is shown in Fig. 9.5 in a larger energy window around E_F than in Fig. 9.3. I note that both atomic relaxation and global shear modify the spectrum of the unsheared and unrelaxed lattice, shown in Fig. 9.5(a), significantly. Band gaps above and below the ‘flat band’ region are significant only in the relaxed structure. Only the DOS of the sheared and relaxed structure in Fig. 9.5(d) displays a combination of a narrow flat band and band gaps above and below.

9.5.5 Value of the magic angle in unsheared and sheared twisted bilayer graphene

Since shear plays an important role in the relaxed twisted bilayer graphene, it is expected to affect the magic angle θ_m as well. In Fig. 9.6 I show the width of the narrow band around E_F as a function of the twist angle θ for both an unsheared BLG and for BLG with its top layer sheared by $\alpha \approx 0.08^\circ$ along the $\beta = 0^\circ$ direction. Only few data points are shown, since only few commensurate structures with reasonably small unit cells exist in the narrow twist angle region shown. I notice that the (first) magic angle, associated with the narrowest bandwidth, occurs at 1.12° in the unsheared and at 1.08° in the globally sheared BLG. The latter value in the sheared lattice agrees well with the observed value [175, 176] $\theta_m(\text{expt}) \approx 1.08^\circ$.

Chapter 10

Two-dimensional Mechanical Metamaterials with Unusual Poisson Ratio Behavior

The following discussion is my original contribution to the related publication by Zhibin Gao, Dan Liu and David Tománek, Phys. Rev. Appl. **10**, 064039 (2018) [195].

10.1 Introduction

There is growing interest in mechanical metamaterials, man-made structures with counter-intuitive mechanical properties [196]. Unlike in ordinary uniform materials, deformations in such metamaterials derive from the geometry of the assembly rather than the elastic properties of the components. This behavior is scale independent, covering structures from the macro- to the nanoscale. Most attention in this respect seems to be drawn by the Poisson ratio ν [197], the negative ratio of lateral to applied strain. Ordinary materials with typical values $0 < \nu < 0.5$ contract laterally when stretched, with unusually large values reported for cellular materials [198]. Auxetic metamaterials with $\nu < 0$, on the other hand, expand in both directions when stretched [198–202] leading to advanced functionalities [203,204]. Auxetic systems with macroscopic components have been utilized for shock absorption in automobiles [205], in high-performance clothing [206–208], in bioprostheses [209] and stents [210] in medicine, and for strain amplification [211]. Auxetic 2D mechanical metamaterials with nanostructured components, some of which have been described previously [212–215], may find their use when precise micromanipulation of 2D structures including bilayer graphene is required [176].

Here I report the design of 2D mechanical metamaterials that may be deformed substantially at little or no energy cost. Unlike origami- and kirigami-inspired metamaterials, which derive their functionality from folding a 2D material into the third dimension [216–219], the structures I describe are confined to a plane during deformation. Such confinement may be achieved by a strong attraction to a planar substrate or in a sandwich geometry. Specifically, I consider infinite assemblies of rigid isosceles triangles hinged in their corners on the macro-scale [220] and polymerized phenanthrene molecules forming 'porous graphene' on the nano-scale. In these and in a large class of related structures, consisting of connected and near-rigid isosceles triangles, the Poisson ratio ν diverges at particular strain values. ν also changes its magnitude and sign, and displays a 'shape memory' effect in a specific range of deformations, meaning that this quantity depends on previously applied strain. The corresponding results are scale invariant.

10.2 Computational methods

I have studied the electronic and structural properties as well as the deformation energy of polyphenanthrene dubbed 'porous graphene' using *ab initio* density functional theory (DFT) as implemented in the VASP code [14, 16, 191]. I represented this 2D structure by

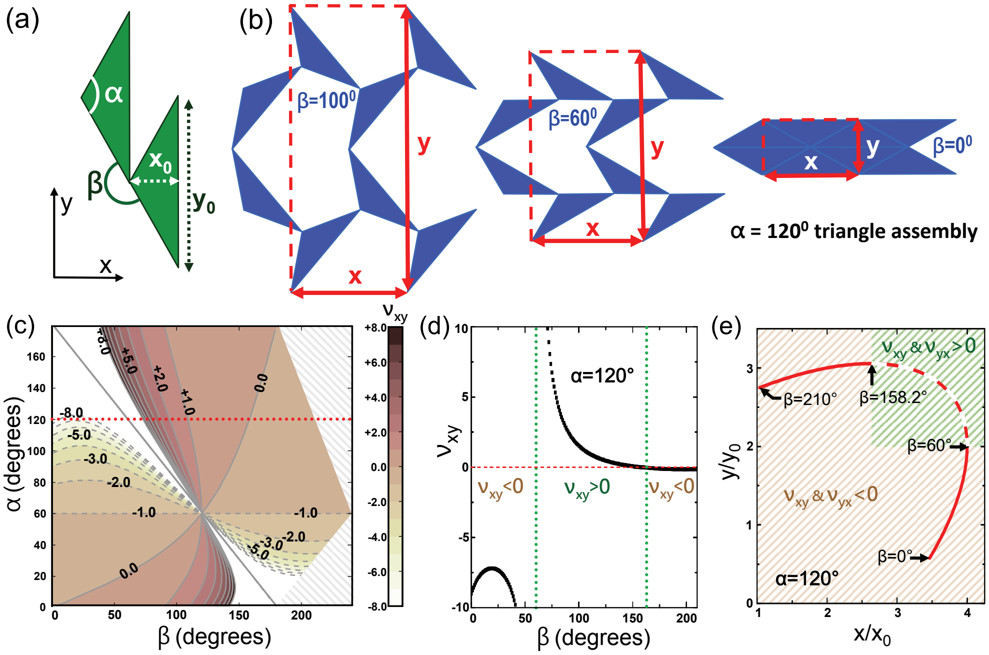

Figure 10.1: Deformations in a 2D assembly of rigid isosceles triangles. (a) Adjacent triangles with opening angle α and mutual orientation defined by the closing angle β, hinged tip-to-corner, forming the primitive unit cell. The triangle height x_0 and the length y_0 of its base define the horizontal and vertical length scales. (b) Snap shots of the $\alpha = 120^\circ$ triangle assembly for different values of β. The conventional rectangular unit cell is twice the size of the primitive unit cell. (c) Contour plot of the Poisson ratio $\nu_{xy} = -(dy/y)/(dx/x)$ as a function of α and β. The dotted red line highlights behavior of the $\alpha = 120^\circ$ triangle assembly. (d) Poisson ratio ν_{xy} as a function of β in the $\alpha = 120^\circ$ system. (e) Changes in the scaled width x/x_0 and height y/y_0 of the conventional unit cell for $\alpha = 120^\circ$ caused by changing the angle β.

imposing periodic boundary conditions in all directions and separating individual layers by a vacuum region of 20 Å. I used projector-augmented-wave (PAW) pseudopotentials [17,18] and the Perdew-Burke-Ernzerhof (PBE) [9] exchange-correlation functional. The Brillouin zone of the conventional unit cell of the 2D structure has been sampled by an 5×3×1 k-point grid [34]. I used 500 eV as the electronic kinetic energy cutoff for the plane-wave basis and a total energy difference between subsequent self-consistency iterations below 10^{-4} eV as the criterion for reaching self-consistency. All geometries have been optimized using the conjugate-gradient method [76], until none of the residual Hellmann-Feynman forces

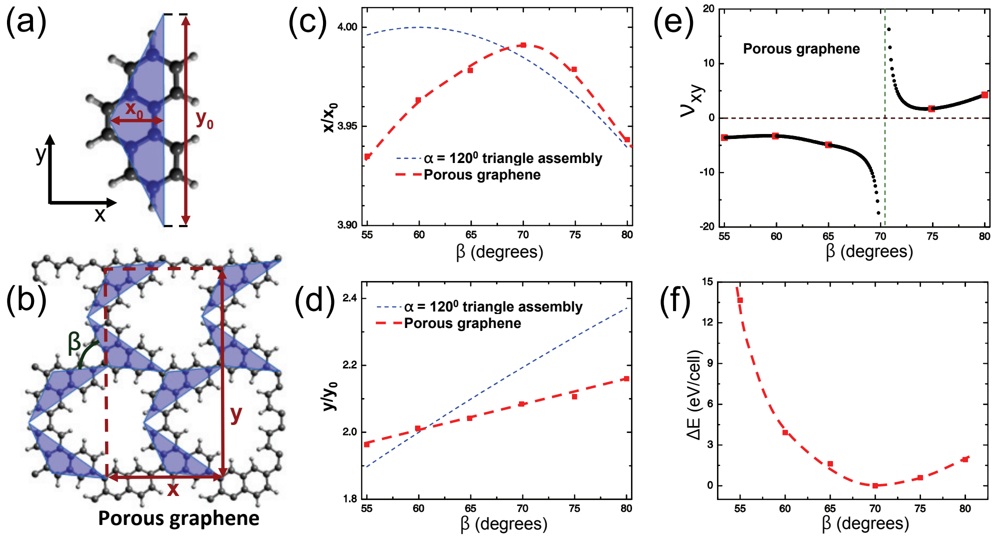

Figure 10.2: Deformations in porous graphene, a phenanthrene-based 2D mechanical metamaterial. (a) Structure of the $C_{14}H_{10}$ phenanthrene molecule and its relation to an isosceles $\alpha = 120°$ triangle of Fig. 10.1. (b) Equilibrium structure of 2D porous graphene consisting of polymerized phenanthrene molecules with $\beta = 70°$. Saturating hydrogen atoms are shown by the lighter and smaller spheres. Changes in the scaled width x/x_0 (c) and height y/y_0 (d) of the conventional unit cell in the triangle assembly and porous graphene as a function of the closing angle β. (e) Poisson ratio ν_{xy} in porous graphene as a function of β. (f) Strain energy in the $C_{56}H_{28}$ conventional unit cell as a function of β. The dashed and dotted lines connecting data points for porous graphene in (c)-(f) are guides to the eye.

exceeded 10^{-2} eV/Å.

10.3 Results and discussions

Figure 10.1 depicts the macro-scale 2D mechanical metamaterial I consider, namely an infinite assembly of rigid isosceles triangles hinged in the corners and described using periodic boundary conditions. There are two identical triangles with different orientation in the primitive unit cell of the lattice, as seen in Fig. 10.1(a). The conventional unit cell, shown in Fig. 10.1(b), is rectangular and twice the size of the primitive unit cell. The deformation behavior of such constrained lattices of polygons including rectangles [221] and connected bars, some of which display a Poisson ratio that changes sign, value, and even diverges, has been described and classified earlier [220,222]. In the system, structural changes are regulated by the only independent variable, the angle β. The full range of β is $0 \leq \beta \leq \alpha + 180°$ for $\alpha \leq 60°$ and $0 \leq \beta \leq 270° - \alpha/2$ for $\alpha \geq 60°$. Since there is no energy involved when changing β, the structure maintains its geometry after deformation. Snap shots of the triangle assembly and the conventional unit cell at different values of β, shown in Fig. 10.1(b), illustrate the unusual flexibility of the system.

For a system of triangles aligned with the Cartesian coordinate system as shown in Fig. 10.1(a), I can determine the strain in the y-direction in response to strain applied along the x-direction. The negative ratio of these strains is the Poisson ratio ν_{xy}, which is given by

$$\nu_{xy} = -\frac{dy/y}{dx/x} = \frac{\cos(\frac{\alpha}{2})\sin(\frac{\beta}{2}) - 3\sin(\frac{\alpha}{2})\cos(\frac{\beta}{2})}{\cos(\frac{\alpha}{2})\cos(\frac{\beta}{2}) + 3\sin(\frac{\alpha}{2})\sin(\frac{\beta}{2})} \tan\left(\frac{\alpha+\beta}{2}\right). \tag{10.1}$$

Dependence of ν_{xy} on α and β is presented as a contour plot in Fig. 10.1(c). Several aspects of this result are noteworthy when inspecting the behavior of $\nu_{xy}(\beta)$ for a constant value of the opening angle α. With the exception of $\alpha = 60°$ describing equilateral triangles [223,224], ν_{xy} changes magnitude and sign with changing β. Presence of the tangent function in Eq. (10.1) causes ν_{xy} to diverge to $\pm\infty$ for $\beta_{crit}(\nu_{xy}) = 180° - \alpha$, with $\beta_{crit}(\nu_{xy}) = 60°$ for $\alpha = 120°$. For $\alpha > 60°$, ν_{xy} changes sign twice across the full range of β values, as shown in Fig. 10.1(d) for $\alpha = 120°$. The condition for the divergence of $\nu_{yx} = 1/\nu_{xy}$, describing strain in the x-direction in response to strain applied in the y-direction, is $\tan(\beta_{crit}(\nu_{yx})/2) = 3\tan(\alpha/2)$. For $\alpha = 120°$, ν_{yx} will diverge at $\beta_{crit}(\nu_{yx}) = 158.2°$.

Maybe the most unexpected aspect of the result is the ‘shape memory’ effect displayed by both ν_{xy} and ν_{yx} if the angle β becomes a hidden variable in the system. To explain what I mean, I first inspect the $(x(\beta)/x_0, y(\beta)/y_0)$ trajectory given by

$$\frac{x}{x_0} = 2\left[\tan\left(\frac{\alpha}{2}\right)\cos\left(\frac{\beta}{2}\right) + \sin\left(\frac{\beta}{2}\right)\right] , \tag{10.2}$$

$$\frac{y}{y_0} = 3\sin\left(\frac{\beta}{2}\right) + \cot\left(\frac{\alpha}{2}\right)\cos\left(\frac{\beta}{2}\right) . \tag{10.3}$$

The $(x(\beta)/x_0, y(\beta)/y_0)$ trajectory, describing the changing shape of the unit cell, is shown for $\alpha = 120°$ in Fig. 10.1(e), and for other values of α in Fig. 10.4 in the Related Information section. The sign of the slope of the trajectory, opposite to the sign of ν_{xy} and ν_{yx}, changes twice as the structure unfolds with increasing β. Regions of positive and negative ν_{xy} and ν_{yx}, delimited by the above-mentioned critical values $\beta_{crit}(\nu_{xy})$ for ν_{xy} and $\beta_{crit}(\nu_{yx})$ for ν_{yx}, are distinguished graphically in Fig. 10.1(e). For any x in the range $3.46 < x/x_0 < 4.00$, there are two different values of y associated with different values of β and different signs of ν_{xy}. Similarly, for any y in the range $2.75 < y/y_0 < 3.06$, there are two different solutions for x associated with different values of β and different signs of ν_{yx}.

Let us now consider a macroscopic piece of 'material' consisting of hinged triangles, which are so small that their mutual orientation cannot be made out. With no information about the deformation history, the material may exhibit either a positive or a negative Poisson ratio. The *only* way to change the material so that it would exhibit a definite positive or negative sign of the Poisson ratio is to subject it to a sequence of deformations. Assume that this material is first stretched to its maximum along a given direction such as x. Subsequent stretching along a direction normal to the first will result in a positive, subsequent compression in a negative Poisson ratio. I may say that the system retains a memory of previous deformations.

What happens microscopically can be clearly followed in Fig. 10.1(e). Even though the value of β is hidden, I know that it becomes 60° for maximum stretch along x and 158.2° for maximum stretch along y. Subsequent deformation normal to the first direction then dictates the sign of ν. This behavior derives from the nonlinearity in the system and, in some aspect, parallels the behavior of shape memory alloys.

Whereas macroscopic triangular assemblies with various values of α will find their use in particular applications, I turn the interest to 2D nanostructures that can be formed by coordination chemistry and macromolecular assembly. Microstructures including colloidal Kagomé lattices [225–227] and graphitic nanostructures [228,229] including polyphenylene [230], sometimes dubbed nanoporous graphene, have been synthesized, but do not display a negative Poisson ratio. In the following, I focus on polyphenanthrene, a 2D structure of phenanthrene molecules shown in Fig. 10.2(a). There is a strong similarity between this molecule and $\alpha = 120°$ triangles depicted in Fig. 10.1. In particular, 2D assemblies of structures in Figs. 10.1(a) and 10.2(a) display strong similarities in their Poisson ratio behavior discussed below.

The calculated equilibrium structure of 2D porous graphene formed of polymerized phenanthrene molecules with the optimum angle $\beta = 70°$, shown in Fig. 10.2(b), illustrates the relationship between this structure and the $\alpha = 120°$ triangle assembly. The unusual flexibility of polyphenanthrene is owed to the connection of phenanthrene molecules by strong C-C σ bonds, which are also responsible for the strength and flexibility of polyethylene. The DFT calculations indicate only small structural distortions of the phenanthrene molecules, which nevertheless break their initial mirror symmetry.

In Fig. 10.2(c) I compare changes in the scaled width x/x_0 of the conventional unit cell as a function of the closing angle β for the assembly of triangles and for porous graphene. The corresponding changes in the scaled height y/y_0 are shown in Fig. 10.2(d) in the same

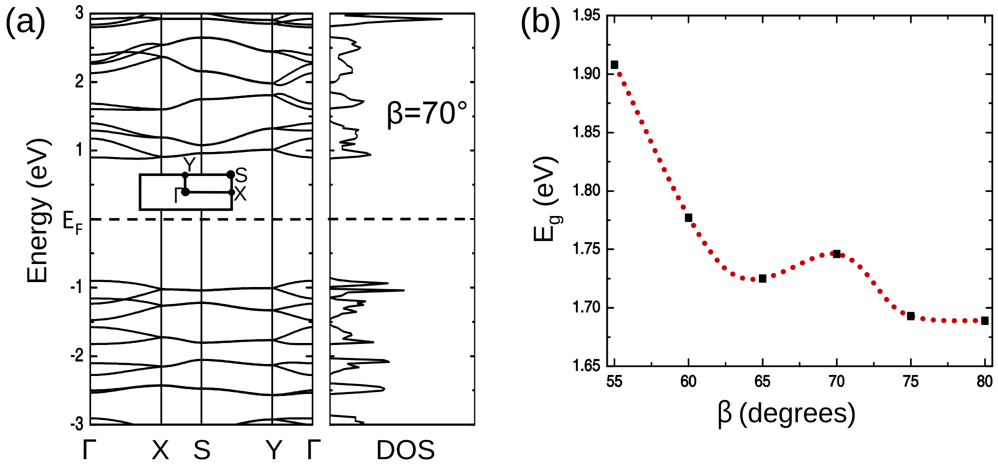

Figure 10.3: Electronic structure of porous graphene, a phenanthrene-based 2D mechanical metamaterial, based on DFT-PBE calculations. (a) Band structure of the equilibrium structure with $\beta = 70°$ obtained using the rectangular $C_{56}H_{28}$ unit cell. High-symmetry points in the rectangular Brillouin zone are shown in the inset. (b) Fundamental band gap E_g as a function of the angle β.

range of β values. Interestingly, $x(\beta)/x_0$ reaches its maximum at $\beta_{crit}(\nu_{xy})$ for both systems, whereas $y(\beta)/y_0$ increases monotonically with increasing β. According to the definition of the Poisson ratio $\nu_{xy} = -(dy/y)/(dx/x)$, ν_{xy} diverges at $\beta_{crit}(\nu_{xy}) = 60°$ in the triangular assembly, as seen in Fig. 10.1(d). Similarly, ν_{xy} diverges at $\beta_{crit}(\nu_{xy}) = 70°$ in porous graphene, as shown in Fig. 10.2(e). The slope of $x(\beta)/x_0$ changes sign at β_{crit}, resulting in $\nu_{xy} < 0$ for $\beta < \beta_{crit}(\nu_{xy})$ and $\nu_{xy} > 0$ for $\beta > \beta_{crit}(\nu_{xy})$ in both systems.

The energy investment ΔE associated with deforming the polyphenanthrene structure is shown in Fig. 10.2(f). The results were obtained by optimizing the structure for selected values of the angle β that defines the relative orientation of the two inequivalent phenanthrene molecules in the unit cell. With $\beta{\approx}70°$ representing the structural optimum, I found that changing β by $\pm 10°$ required $\Delta E < 3$ eV per unit cell, corresponding to an energy investment of only ≈50 meV per C atom, about 1% of the bond breaking energy. Thus, the polyphenanthrene structure is rather soft and represents a valid counterpart to the isoenergetic model system of Fig. 10.1.

Phenanthrene is a tricyclic organic molecule with a 3.36 eV wide DFT-PBE gap between the lowest unoccupied molecular orbital (LUMO) and the highest occupied molecular orbital (HOMO). When polymerized to the 2D polyphenanthrene structure depicted in Fig. 10.2(b), the HOMO broadens to the valence and the LUMO to the conduction band. This is seen in Fig. 10.3(a), which depicts the band structure and the density of states of the optimum geometry of polyphenanthrene with $\beta = 70^\circ$, with the Brillouin zone shown in the inset. The DFT-PBE results indicate that the fundamental band gap E_g is reduced from the molecular value to 1.75 eV in the equilibrium structure of the layer, but still does not vanish for $55^\circ < \beta < 80^\circ$. The gap is near-direct due to the flatness of bands, and decreases from 1.9 eV at $\beta = 55^\circ$ to 1.7 eV at $\beta = 80^\circ$. I should remember that Kohn-Sham eigenvalues in all DFT calculations including ours do not correctly represent the electronic structure and typically underestimate the band gaps.

The decrease of E_g and its dependence on β upon polymerization is caused by the presence of covalent C-C bonds that connect individual phenanthrene molecules elastically and electronically. Unfolding of the polyphenanthrene structure with increasing angle β rotates individual phenanthrene molecules and modifies the bonding at the connection between adjacent monomers, causing the the electronic structure to depend on β. The range of deformations in polyphenanthrene is smaller than in triangular assemblies due to the steric hindrance caused by hydrogen termination. In absence of planar confinement, phenanthrene molecules rotate out-of-plane at large tensile strain values not considered here.

Elastic response of materials is commonly described by elastic constants constituting the elastic matrix, which describe stress-strain relationships and thus contain energy in their dimension. The Poisson ratio is fundamentally different. It is a dimensionless quantity that describes deformations induced by strain, independent of the energy cost. According to its definition in Eq. (10.1), it depends on the choice of the coordinate system. The trace of the strain matrix, however, which describes the fractional change of the area induced by the mechanism, is independent of the choice of coordinates and could couple naturally to external fields such as pressure.

I believe that changes in pore size caused by the deformation of the 2D unit cell may find their use in tunable sieving in a layered system [231, 232], including application in desalination membranes. 2D mechanical metamaterials may also find unusual applications in micro-manipulation. In particular, a 2D layer in partial contact with an in-plane junction of 2D metamaterials with different values of ν, including $\nu > 0$ and $\nu < 0$, may experience a torque normal to the plane when in-plane strain is applied at the junction of the 2D systems. Also the observation of strain-related electronic structure changes in polyphenanthrene opens new possibilities. Since polyphenanthrene and a wide range of porous graphene structures can be viewed as a system of covalently connected quantum dots, in-layer strain may be used to tune the coupling between such quantum dots and thus change the electronic structure of the system.

10.4 Summary

In summary, I have designed 2D mechanical metamaterials that may be deformed substantially at little or no energy cost. Unlike origami- and kirigami-based mechanical metamaterials that derive their functionality from folding a 2D material to the third dimension, the structures I design are confined to a plane during deformation. In reality, such confinement may be achieved by a strong attraction to a planar substrate or in a sandwich geometry. On the macro-scale, the structures I describe are assemblies of rigid isosceles triangles hinged in their corners. Their nanoscale counterpart are molecules such as phenanthrene that may be polymerized using coordination chemistry or macromolecular assembly to form specific geometries with a porous graphene structure. In these and in a large class of related structures, consisting of connected and near-rigid isosceles triangles confined to a plane, the Poisson ratio ν diverges for particular strain values. ν also changes its magnitude and sign, depending on the applied uniaxial strain, and displays a shape memory effect with respect to the deformation history.

10.5 Related Information

10.5.1 Deformation behavior in 2D isosceles triangle assemblies

As discussed earlier, for a given value y of the unit cell height in a 2D assembly of isosceles triangles with $\alpha > 60°$, I can find two different values x of the unit cell width, with the two structures displaying opposite signs of ν. Similarly, I can find two different values y for a given value of x, with the two structures displaying opposite signs of ν. This unusual behavior results from the presence of a hidden variable, the relative triangle orientation β, and causes ν to depend not only on the overall sample shape, but also the history of the system. The unfolding of an assembly of triangles with $\alpha = 120°$ and its history dependence has been characterized by the $x - y$ trajectory in Fig. 10.1(e) in the range of accessible β angles.

$x - y$ trajectories for several values of α are shown in Fig. 10.4. The particular shape of these $x - y$ trajectories indicates that also for opening angles other than $\alpha = 120°$ discussed above, the value and sign of ν may depend on sample history. Only in the specific case of

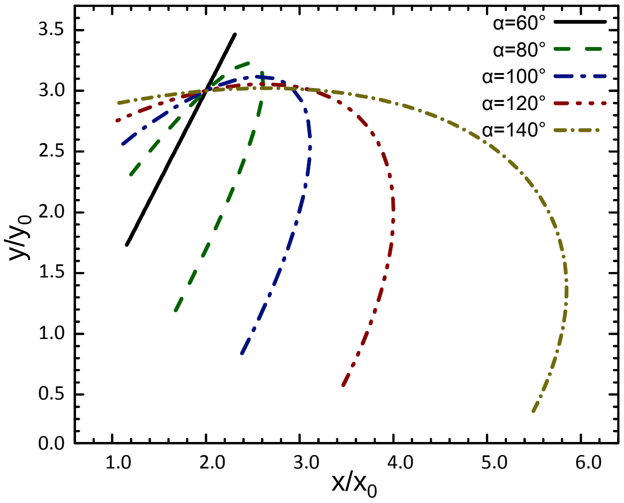

Figure 10.4: Changes in the scaled width x/x_0 and height y/y_0 of the conventional unit cell for different values of the opening angle α as a function of the closing angle β. The relevant quantities are defined in Fig. 10.1.

equilateral triangles with $\alpha = 60°$, discussed in the following, the $y-x$ trajectory in Fig. 10.4 is linear and ν is history independent.

10.5.2 Deformations in a 2D assembly of rigid equilateral triangles

I mentioned above that the behavior of $\alpha = 60°$ triangle systems, depicted in Fig. 10.5, is unique among the 2D assemblies of corner-sharing isosceles triangles. As discussed in the main manuscript and above, the Poisson ratio changes drastically for triangle systems with opening angle α other than 60°. While hinged equilateral triangles gradually unfold when β increases, the width x of the unit cell remains proportional to its height y, resulting in a constant, β-independent Poisson ratio $\nu_{xy} = -1$, as noted earlier [223, 224]. For the particular angle $\beta = 120°$, the structure of the assembly resembles the Kagomé lattice.

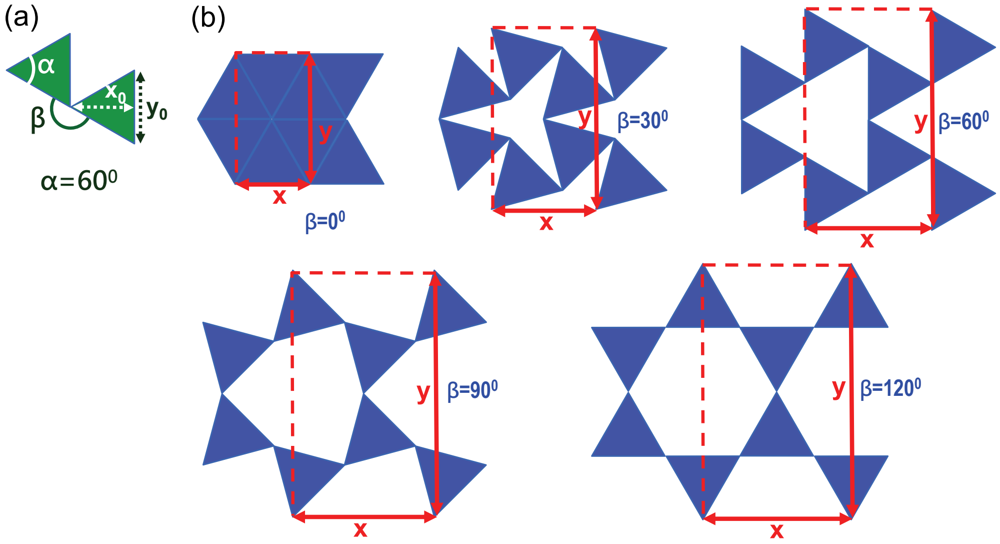

Figure 10.5: Deformations in a 2D assembly of rigid equilateral triangles. (a) Adjacent triangles with mutual orientation defined by the closing angle β, hinged at the corners, forming the primitive unit cell. The triangle height x_0 and the length y_0 of its base define the horizontal and vertical length scales. (b) Snap shots of the triangle assembly for different values of β. The conventional unit cells of width x and height y are indicated.

Chapter 11

Conclusions

Low-dimensional materials have been attracting unusual attention due to their exotic properties and their potential application in miniaturized devices. The vision of what is desirable and possible and what is not requires physical understanding first, provided by theory and quantified by numerical calculation. It is important to recognize that each approach has its limitations. As an example, atomistic calculations are limited in their prediction of long-wavelength acoustic phonon modes due to the required large supercell sizes and often produce numerical artifacts. Applying the continuum elasticity approach to low-dimensional systems appears as a promising alternative to address this problem. This approach does not depend on supercells, is universal and efficient. It is interesting that results for graphene and black phosphorene obtained using this approach agree with available observed spectra and cover a substantial part of the Brillouin zone centered at the Γ-point.

To achieve progress in nanoscience and nanotechnology, searching for low-dimensional materials with promising properties is a key prerequisite. Since the explosion of interest in graphene, there has been significant progress in developing computational approaches for low-dimensional nanomaterials. Besides black phosphorene, which is the most stable 2D allotrope of phosphorus, I have identified in this thesis an equally stable 1D structure that prefers to bend. Long segments, formed from sublimed red phosphorus inside a carbon nanotube, like to form coils. Since the coil stability is almost independent of the radius, nested coils should be formed, as confirmed by high-resolution transmission electron microscopy.

Despite extensive experimental efforts to synthesize 2D allotropes of other elements except for few studies of group VI elements. What we know about Se or Te, both bulk materials are composed by 1D helices. I started from the 1D helices and proposed a way to transform the helices to a stable 2D allotrope by searching the high-dimensional configuration space for the optimum microscopic reaction path. Following this path, the activation barriers have been reduced to below 0.3 eV, which is sufficiently low to allow a synthesis.

What has been underestimated in many studies is the potential effect of net charge on the relative stability of structural allotropes. I found that elemental boron is very sensitive to net charge and that stable 2D allotropes of charged boron are very different from neutral boron. Gradually increasing the electron concentration in a 2D geometry causes boron to behave more and more like carbon. With one excess electron per boron atom, the optimum structure becomes a honeycomb lattice and the electronic structure resembles that of graphene, including the occurrence of a Dirac cone at a corner of the Brillouin zone. In this study, and in the general situation necessitating excess electrons, a 2D electride appears to be the most promising option to supply the extra charge.

A key objective in the field of superconductors is to increase the critical temperature T_c to hopefully near the room temperature. In an alkali-doped C_{60} crystal, reducing the dimension from the 3D fcc structure in the bulk to a quasi-1D structure inside a nanotube causes a significant increase in the density of states at the Fermi level, which may increase T_c to possibly even room temperature.

Availability of high-quality graphene monolayers has ignited broad interest in graphene-inspired 2D nanomaterials. A graphene bilayer has one additional degree of freedom that had been overlooked in the past, namely relative twist. I have found that twisted bilayer graphene is unstable with respect to in-plane shear and out-of-plane atomic relaxation. The emergence of an ultra-narrow band near the Fermi level at the 'magic angle' is likely responsible for the observed superconductivity in this system. The honeycomb structure of graphitic carbon is also found in many organic molecules that may be interconnected to a contiguous 2D layer that may be viewed as a metamaterial that can be deformed. Tailoring the deformation affects not only the electronic structure, but also the mechanical behavior. I have studied a particular 2D porous graphene system, namely a phenanthrene-based 2D metamaterial, which exhibits an unusual behavior of the Poisson ratio ν. Applying in-layer strain, I have found that ν may change its sign and even diverge at specific in-layer deformations.

BIBLIOGRAPHY

BIBLIOGRAPHY

[1] L. Wirtz and A. Rubio, *The phonon dispersion of graphite revisited*, Solid State Commun. **131**, 141 (2004).

[2] Z. Zhu and D. Tománek, *Semiconducting layered blue phosphorus: A computational study*, Phys. Rev. Lett. **112**, 176802 (2014).

[3] A. M. Rao, E. Richter, S. Bandow, B. Chase, P. C. Eklund, K. A. Williams, S. Fang, K. R. Subbaswamy, M. Menon, A. Thess, R. E. Smalley, G. Dresselhaus, and M. S. Dresselhaus, *Diameter-Selective Raman Scattering from Vibrational Modes in Carbon Nanotubes*, Science **275**, 187 (1997).

[4] D. Tománek, *Guide Through the Nanocarbon Jungle*, IOP Publishing, Bristol, UK, 2014.

[5] J. S. Alden, A. W. Tsen, P. Y. Huang, R. Hovden, L. Brown, J. Park, D. A. Muller, and P. L. McEuen, *Strain solitons and topological defects in bilayer graphene*, Proc. Natl. Acad. Sci. U.S.A. **110**, 11256 (2013).

[6] M. Born and R. Oppenheimer, *Zur Quantentheorie der Molekeln*, Annalen der Physik **389**, 457 (1927).

[7] W. Kohn and L. J. Sham, *Self-Consistent Equations Including Exchange and Correlation Effects*, Phys. Rev. **140**, A1133 (1965).

[8] D. M. Ceperley and B. J. Alder, *Ground State of the Electron Gas by a Stochastic Method*, Phys. Rev. Lett. **45**, 566 (1980).

[9] J. P. Perdew, K. Burke, and M. Ernzerhof, *Generalized Gradient Approximation Made Simple*, Phys. Rev. Lett. **77**, 3865 (1996).

[10] S. Grimme, J. Antony, S. Ehrlich, and H. Krieg, *A consistent and accurate ab initio parametrization of density functional dispersion correction (DFT-D) for the 94 elements H-Pu*, The Journal of Chemical Physics **132**, 154104 (2010).

[11] J. Klimeš, D. R. Bowler, and A. Michaelides, *Chemical accuracy for the van der Waals density functional*, J. Phys.: Cond. Matt. **22**, 022201 (2010).

[12] J. Klimeš, D. R. Bowler, and A. Michaelides, *Van der Waals density functionals applied to solids*, Phys. Rev. B **83**, 195131 (2011).

[13] E. Artacho, E. Anglada, O. Dieguez, J. D. Gale, A. Garcia, J. Junquera, R. M. Martin, P. Ordejon, J. M. Pruneda, D. Sanchez-Portal, and J. M. Soler, *The SIESTA method; developments and applicability*, J. Phys. Cond. Mat. **20**, 064208 (2008).

[14] G. Kresse and J. Furthmüller, *Efficient iterative schemes for ab initio total-energy calculations using a plane-wave basis set*, Phys. Rev. B **54**, 11169 (1996).

[15] G. Kresse and J. Hafner, *Ab initio molecular dynamics for liquid metals*, Phys. Rev. B **47**, 558 (1993).

[16] G. Kresse and J. Hafner, *Ab initio molecular-dynamics simulation of the liquid-metal–amorphous-semiconductor transition in germanium*, Phys. Rev. B **49**, 14251 (1994).

[17] G. Kresse and D. Joubert, *From ultrasoft pseudopotentials to the projector augmented-wave method*, Phys. Rev. B **59**, 1758 (1999).

[18] P. E. Blöchl, *Projector augmented-wave method*, Phys. Rev. B **50**, 17953 (1994).

[19] D. Liu, A. G. Every, and D. Tománek, *Continuum approach for long-wavelength acoustic phonons in quasi-two-dimensional structures*, Phys. Rev. B **94**, 165432 (2016).

[20] B. Peng, H. Zhang, H. Shao, Y. Xu, R. Zhang, and H. Zhu, *The electronic, optical, and thermodynamic properties of borophene from first-principles calculations*, J. Mater. Chem. C **4**, 3592 (2016).

[21] W. Yu, Z. Zhu, C.-Y. Niu, X. Cai, and W.-B. Zhang, *Atomically thin binary V-V compound semiconductor: a first-principles study*, arXiv:1510.04108v5 (2016).

[22] A. K. Majee and Z. Aksamija, *Length divergence of the lattice thermal conductivity in suspended graphene nanoribbons*, Phys. Rev. B **93**, 235423 (2016).

[23] A. E. H. Love, *A treatise on the mathematical theory of elasticity*, Cambridge University Press, Cambridge, UK, 1927.

[24] A. Maznev and A. Every, *Focusing of Acoustic Modes in Thin Anisotropic Plates*, Acta Acustica **3**, 387 (1995).

[25] P. Malekzadeh, M. G. Haghighi, and M. Shojaee, *Nonlinear free vibration of skew nanoplates with surface and small scale effects*, Thin-Walled Structures **78**, 48 (2014).

[26] Q. Lu and R. Huang, *Nonlinear Mechanics of Single-Atomic-Layer Graphene Sheets*, Int. J. Appl. Mech. **1**, 443 (2009).

[27] P. Lambin, *Elastic Properties and Stability of Physisorbed Graphene*, Appl. Sci. **4**, 282 (2014).

[28] B. Arash and Q. Wang, *A Review on the Application of Nonlocal Elastic Models in Modeling of Carbon Nanotubes and Graphenes*, pages 57–82, Springer International Publishing, Cham, 2014.

[29] A. H. Castro Neto, F. Guinea, N. M. R. Peres, K. S. Novoselov, and A. K. Geim, *The electronic properties of graphene*, Rev. Mod. Phys. **81**, 109 (2009).

[30] P. M. Chaikin and T. C. Lubensky, *Principles of Condensed Matter Physics*, Cambridge University Press, Cambridge, UK, 1995.

[31] D. Nelson, T. Piran, and S. Weinberg, *Statistical mechanics of membranes and surfaces*, World Scientific, Singapore, second edition, 2004.

[32] H. Suzuura and T. Ando, *Phonons and electron-phonon scattering in carbon nanotubes*, Phys. Rev. B **65**, 235412 (2002).

[33] N. Troullier and J. L. Martins, *Efficient pseudopotentials for plane-wave calculations*, Phys. Rev. B **43**, 1993 (1991).

[34] H. J. Monkhorst and J. D. Pack, *Special points for Brillouin-zone integrations*, Phys. Rev. B **13**, 5188 (1976).

[35] K. V. Zakharchenko, M. I. Katsnelson, and A. Fasolino, *Finite Temperature Lattice Properties of Graphene beyond the Quasiharmonic Approximation*, Phys. Rev. Lett. **102**, 046808 (2009).

[36] A. Politano, A. R. Marino, D. Campi, D. Farías, R. Miranda, and G. Chiarello, *Elastic properties of a macroscopic graphene sample from phonon dispersion measurements*, Carbon **50**, 4903 (2012).

[37] R. Jishi, L. Venkataraman, M. Dresselhaus, and G. Dresselhaus, *Phonon modes in carbon nanotubules*, Chem. Phys. Lett. **209**, 77 (1993).

[38] J. Guan, Z. Zhu, and D. Tománek, *High Stability of Faceted Nanotubes and Fullerenes of Multiphase Layered Phosphorus: A Computational Study*, Phys. Rev. Lett. **113**, 226801 (2014).

[39] D. Tomanek, W. Zhong, and E. Krastev, *Stability of multishell fullerenes*, Phys. Rev. B **48**, 15461 (1993).

[40] D. Liu, A. G. Every, and D. Tománek, *Long-wavelength deformations and vibrational modes in empty and liquid-filled microtubules and nanotubes: A theoretical study*, Phys. Rev. B **95**, 205407 (2017).

[41] A. Jorio, M. Dresselhaus, and G. Dresselhaus, *Carbon Nanotubes: Advanced Topics in the Synthesis, Structure, Properties and Applications*, Number 111 in Topics in Applied Physics, Springer, Berlin, 2008.

[42] G. Overney, W. Zhong, and D. Tomanek, *Structural rigidity and low-frequency vibrational modes of long carbon tubules*, Z. Phys D: Atoms, Molecules and Clusters **27**, 93 (1993).

[43] V. Sazonova, Y. Yaish, H. Üstünel, D. Roundy, T. A. Arias, and P. L. McEuen, *A tunable carbon nanotube electromechanical oscillator*, Nature **431**, 284 (2004).

[44] Q. Wang and V. K. Varadan, *Vibration of carbon nanotubes studied using nonlocal continuum mechanics*, Smart Mater. Struct. **15**, 659 (2006).

[45] R. F. Gibson, E. O. Ayorinde, and Y.-F. Wen, *Vibrations of carbon nanotubes and their composites: A review*, Comp. Sci. Technol. **67**, 1 (2007).

[46] M. Roukes, *Plenty of room, indeed*, Sci. Am. **285**, 48 (2001).

[47] M. Ling, L. Hui-Jun, H. Yi, Z. Xiang, H. Cheng-Zheng, and S. Jing, *Phonon dispersion relations and soft modes of 4 Å carbon nanotubes*, Chinese Phys. B **19**, 016301 (2010).

[48] X. S. Qian, J. Q. Zhang, and C. Q. Ru, *Wave propagation in orthotropic microtubules*, J. Appl. Phys. **101**, 084702 (2007).

[49] Y. M. Sirenko, M. A. Stroscio, and K. W. Kim, *Elastic vibrations of microtubules in a fluid*, Phys. Rev. E **53**, 1003 (1996).

[50] C. Wang, C. Ru, and A. Mioduchowski, *Vibration of microtubules as orthotropic elastic shells*, Physica E **35**, 48 (2006).

[51] H. M. Lawler, J. W. Mintmire, and C. T. White, *Helical strain in carbon nanotubes: Speed of sound and Poisson ratio from first principles*, Phys. Rev. B **74**, 125415 (2006).

[52] E. Secchi, S. Marbach, A. Niguès, D. Stein, A. Siria, and L. Bocquet, *Massive radius-dependent flow slippage in carbon nanotubes*, Nature **537**, 210 (2016).

[53] A. Politano, A. R. Marino, D. Campi, D. Farías, R. Miranda, and G. Chiarello, *Elastic properties of a macroscopic graphene sample from phonon dispersion measurements*, Carbon **50**, 4903 (2012).

[54] Q. Lu, M. Arroyo, and R. Huang, *Elastic Bending Modulus of Monolayer Graphene*, J. Phys. D: Appl. Phys. **42**, 102002 (2009).

[55] D. Sánchez-Portal, E. Artacho, J. M. Soler, A. Rubio, and P. Ordejón, *Ab initio structural, elastic, and vibrational properties of carbon nanotubes*, Phys. Rev. B **59**, 12678 (1999).

[56] J. Maultzsch, H. Telg, S. Reich, and C. Thomsen, *Radial breathing mode of single-walled carbon nanotubes: Optical transition energies and chiral-index assignment*, Phys. Rev. B **72**, 205438 (2005).

[57] P. Venier, A. C. Maggs, M.-F. Carlier, and D. Pantaloni, *Analysis of microtubule rigidity using hydrodynamic flow and thermal fluctuations.*, J. Biol. Chem. **269**, 13353 (1994).

[58] H. Felgner, R. Frank, and M. Schliwa, *Flexural rigidity of microtubules measured with the use of optical tweezers*, J. Cell Sci. **109**, 509 (1996).

[59] M. Kikumoto, M. Kurachi, V. Tosa, and H. Tashiro, *Flexural rigidity of individual microtubules measured by a buckling force with optical traps*, Biophys. J. **90**, 1687 (2006).

[60] C. Chuang, J. Guan, D. Witalka, Z. Zhu, B.-Y. Jin, and D. Tománek, *Relative stability and local curvature analysis in carbon nanotori*, Phys. Rev. B **91**, 165433 (2015).

[61] D. Liu, J. Guan, J. Jiang, and D. Tománek, *Unusually Stable Helical Coil Allotrope of Phosphorus*, Nano Lett. **16**, 7865 (2016).

[62] Elemental phosphorus was first extracted from human urine by German alchemist Hennig Brand around 1669.

[63] H. Thurn and H. Krebs, *Crystal Structure of Violet Phosphorus*, Angew. Chem. Internat. Edit. **5**, 1047 (1966).

[64] H. Thurn and H. Krebs, *Über Struktur und Eigenschaften der Halbmetalle. XXII. Die Kristallstruktur des Hittorfschen Phosphors*, Acta Crystallogr. Sect. B **25**, 125 (1969).

[65] W. Hittorf, *Zur Kenntnis des Phosphors*, Annalen der Physik und Chemie **202**, 193 (1865).

[66] M. Ruck, D. Hoppe, B. Wahl, P. Simon, Y. Wang, and G. Seifert, *Fibrous Red Phosphorus*, Angew. Chem. Int. Ed. **44**, 7616 (2005).

[67] R. Hultgren, N. S. Gingrich, and B. E. Warren, *The Atomic Distribution in Red and Black Phosphorus and the Crystal Structure of Black Phosphorus*, J. Chem. Phys. **3**, 351 (1935).

[68] P. W. Bridgman, *Two new Modifications of Phosphorus*, J. Am. Chem. Soc. **36**, 1344 (1914).

[69] J. L. Zhang, S. Zhao, C. Han, Z. Wang, S. Zhong, S. Sun, R. Guo, X. Zhou, C. D. Gu, K. D. Yuan, Z. Li, and W. Chen, *Epitaxial Growth of Single Layer Blue Phosphorus: A New Phase of Two-Dimensional Phosphorus*, Nano Lett. **16**, 4903 (2016).

[70] M. Haeser, U. Schneider, and R. Ahlrichs, *Clusters of phosphorus: a theoretical investigation*, J. Am. Chem. Soc. **114**, 9551 (1992).

[71] R. O. Jones and G. Seifert, *Structure of phosphorus clusters using simulated annealing. II.* P_9, P_{10}, P_{11}, *anions* P_4^{2-}, P_{10}^{2-}, P_{11}^{3-}, *and cations* P_n^+ *to* $n = 11$, J. Chem. Phys **96**, 7564 (1992).

[72] G. Seifert and R. O. Jones, *Structure of phosphorus clusters by simulated annealing*, Z. Phys. D **26**, 349 (1993).

[73] D. Pfister, K. Schäfer, C. Ott, B. Gerke, R. Pöttgen, O. Janka, M. Baumgartner, A. Efimova, A. Hohmann, P. Schmidt, S. Venkatachalam, L. van Wüllen, U. Schürmann, L. Kienle, V. Duppel, E. Parzinger, B. Miller, J. Becker, A. Holleitner, R. Weihrich, and T. Nilges, *Inorganic Double Helices in Semiconducting SnIP*, Adv. Mater. , 9783 (2016).

[74] D. Liu, J. Jiang, G. B. King, K. Moskovtsev, and D. Tomanek, in preparation.

[75] J. P. Perdew and A. Zunger, *Self-interaction correction to density-functional approximations for many-electron systems*, Phys. Rev. B **23**, 5048 (1981).

[76] M. R. Hestenes and E. Stiefel, *Methods Of Conjugate Gradients For Solving Linear Systems*, J. Res. Natl. Bur. Stand. **49**, 409 (1952).

[77] A. Pfitzner, M. F. Bräu, J. Zweck, G. Brunklaus, and H. Eckert, *Phosphorus Nanorods-Two Allotropic Modifications of a Long-Known Element*, Angew. Chem. Int. Ed. **43**, 4228 (2004).

[78] F. Bachhuber, J. von Appen, R. Dronskowski, P. Schmidt, T. Nilges, A. Pfitzner, and R. Weihrich, *The Extended Stability Range of Phosphorus Allotropes*, Angew. Chem. Int. Ed. **53**, 11629 (2014).

[79] C. Grotz, K. Schäfer, M. Baumgartner, R. Weihrich, and T. Nilges, *One-Dimensional* P_{15}*- Tubes in Layered Semiconducting* AgP_{15}, Inorg. Chem. **54**, 10794 (2015).

[80] A. J. Karttunen, M. Linnolahti, and T. A. Pakkanen, *Icosahedral and Ring-Shaped Allotropes of Phosphorus*, Chem. Eur. J. **13**, 5232 (2007).

[81] A. Maceri, *Theory of Elasticity*, Springer, Berlin, 2010.

[82] L. Shulenberger, A. D. Baczewski, Z. Zhu, J. Guan, and D. Tomanek, *The Nature of the Interlayer Interaction in Bulk and Few-Layer Phosphorus*, Nano Lett. **15**, 8170 (2015).

[83] S. Bandow, M. Takizawa, K. Hirahara, M. Yudasaka, and S. Iijima, *Raman scattering study of double-wall carbon nanotubes derived from the chains of fullerenes in single-wall carbon nanotubes*, Chem. Phys. Lett. **337**, 48 (2001).

[84] J. Zhang, Y. Feng, H. Ishiwata, Y. Miyata, R. Kitaura, J. E. P. Dahl, R. M. K. Carlson, H. Shinohara, and D. Tománek, *Synthesis and Transformation of Linear Adamantane Assemblies inside Carbon Nanotubes*, ACS Nano **6**, 8674 (2012).

[85] J. Zhang, Z. Zhu, Y. Feng, H. Ishiwata, Y. Miyata, R. Kitaura, J. E. P. Dahl, R. M. K. Carlson, N. A. Fokina, P. R. Schreiner, D. Tománek, and H. Shinohara, *Evidence of diamond nanowires formed inside carbon nanotubes from diamantane dicarboxylic acid*, Angew. Chem. Int. Ed. **52**, 3717 (2013).

[86] H. Liu, A. T. Neal, Z. Zhu, Z. Luo, X. Xu, D. Tomanek, and P. D. Ye, *Phosphorene: An Unexplored 2D Semiconductor with a High Hole Mobility*, ACS Nano **8**, 4033 (2014).

[87] Jinying Zhang (private communication).

[88] G. Fasol, *Time-resolved luminescence study of amorphous phosphorus: temperature and excitation energy dependences*, J. Phys. C: Solid State Phys. **18**, 1729 (1985).

[89] D. Liu, X. Lin, and D. Tománek, *Microscopic Mechanism of the Helix-to-Layer Transformation in Elemental Group VI Solids*, Nano Lett. **18**, 4908 (2018).

[90] L. Li, Y. Yu, G. J. Ye, Q. Ge, X. Ou, H. Wu, D. Feng, X. H. Chen, and Y. Zhang, *Black phosphorus field-effect transistors*, Nature Nanotech. **9**, 373 (2014).

[91] O. Osters, T. Nilges, F. Bachhuber, F. Pielnhofer, R. Weihrich, M. Schöneich, and P. Schmidt, *Synthesis and Identification of Metastable Compounds: Black Arsenic-Science or Fiction?*, Angew. Chem. Int. Ed. **51**, 2994 (2012).

[92] M. Pumera and Z. Sofer, *2D Monoelemental Arsenene, Antimonene, and Bismuthene: Beyond Black Phosphorus*, Advanced Materials **29**, 1605299 (2017).

[93] Z. Zhu, X. Cai, S. Yi, J. Chen, Y. Dai, C. Niu, Z. Guo, M. Xie, F. Liu, J.-H. Cho, Y. Jia, and Z. Zhang, *Multivalency-Driven Formation of Te-Based Monolayer Materials: A Combined First-Principles and Experimental study*, Phys. Rev. Lett. **119**, 106101 (2017).

[94] J. Chen, Y. Dai, Y. Ma, X. Dai, W. Ho, and M. Xie, *Ultrathin β-tellurium layers grown on highly oriented pyrolytic graphite by molecular-beam epitaxy*, Nanoscale **9**, 15945 (2017).

[95] J. Qin, G. Qiu, J. Jian, H. Zhou, L. Yang, A. Charnas, D. Y. Zemlyanov, C.-Y. Xu, X. Xu, W. Wu, H. Wang, and P. D. Ye, *Controlled Growth of a Large-Size 2D Selenium Nanosheet and Its Electronic and Optoelectronic Applications*, ACS Nano **11**, 10222 (2017).

[96] N. N. Greenwood and A. Earnshaw, *Chemistry of the Elements*, pages 645–662, Butterworth-Heinemann, second edition, 1997.

[97] J. Klimeš, D. R. Bowler, and A. Michaelides, *Chemical accuracy for the van der Waals density functional*, J. Phys.: Cond. Matt. **22**, 022201 (2010).

[98] J. Klimeš, D. R. Bowler, and A. Michaelides, *Van der Waals density functionals applied to solids*, Phys. Rev. B **83**, 195131 (2011).

[99] M. S. Hybertsen and S. G. Louie, *Electron correlation in semiconductors and insulators: Band gaps and quasiparticle energies*, Phys. Rev. B **34**, 5390 (1986).

[100] J. Deslippe, G. Samsonidze, D. A. Strubbe, M. Jain, M. L. Cohen, and S. G. Louie, *BerkeleyGW: A massively parallel computer package for the calculation of the quasiparticle and optical properties of materials and nanostructures*, Comp. Phys. Commun. **183**, 1269 (2012).

[101] P. Giannozzi, S. Baroni, N. Bonini, M. Calandra, R. Car, C. Cavazzoni, D. Ceresoli, G. L. Chiarotti, M. Cococcioni, I. Dabo, A. D. Corso, S. de Gironcoli, S. Fabris, G. Fratesi, R. Gebauer, U. Gerstmann, C. Gougoussis, A. Kokalj, M. Lazzeri, L. Martin-Samos, N. Marzari, F. Mauri, R. Mazzarello, S. Paolini, A. Pasquarello, L. Paulatto, C. Sbraccia, S. Scandolo, G. Sclauzero, A. P. Seitsonen, A. Smogunov, P. Umari, and R. M. Wentzcovitch, *QUANTUM ESPRESSO: a modular and open-source software project for quantum simulations of materials*, J. Phys.: Cond. Matter **21**, 395502 (2009).

[102] J. Deslippe, G. Samsonidze, M. Jain, M. L. Cohen, and S. G. Louie, *Coulomb-hole summations and energies for GW calculations with limited number of empty orbitals: A modified static remainder approach*, Phys. Rev. B **87**, 165124 (2013).

[103] X. Huang, J. Guan, Z. Lin, B. Liu, S. Xing, W. Wang, and J. Guo, *Epitaxial Growth and Band Structure of Te Film on Graphene*, Nano Lett. **17**, 4619 (2017).

[104] P. J. Brown and J. B. Forsyth, *The Crystal Structure and Optical Activity of Tellurium*, Acta Crystallogr. A **52**, 408 (1996).

[105] P. Cherin and P. Unger, *Two-dimensional refinement of the crystal structure of tellurium*, Acta Crystallogr. **23**, 670 (1967).

[106] R. D. Burbank, *The crystal structure of α-monoclinic selenium*, Acta Crystallogr. **4**, 140 (1951).

[107] C. Adenis, V. Langer, and O. Lindqvist, *Reinvestigation of the structure of tellurium*, Acta Crystallogr. C **45**, 941 (1989).

[108] J. C. Jamieson and D. B. Mcwhan, *Crystal strucutre of tellurium at high pressures*, J. Chem. Phys. **43**, 1149 (1965).

[109] E. Andharia, T. P. Kaloni, G. J. Salamo, S.-Q. Yu, H. O. Churchill, and S. Barraza-Lopez, *Quasi-particle bandgap and excitonic properties of selenium atomic chains*, (2017).

[110] B. Tuttle, S. Alhassan, and S. Pantelides, *Computational Predictions for Single Chain Chalcogenide-Based One-Dimensional Materials*, Nanomaterials **7**, 115 (2017).

[111] Y. Du, G. Qiu, Y. Wang, M. Si, X. Xu, W. Wu, and P. D. Ye, *One-Dimensional van der Waals Material Tellurium: Raman Spectroscopy under Strain and Magneto-Transport*, Nano Lett. **17**, 3965 (2017).

[112] R. Fei, W. Kang, and L. Yang, *Ferroelectricity and Phase Transitions in Monolayer Group-IV Monochalcogenides*, Phys. Rev. Lett. **117**, 097601 (2016).

[113] M. Mehboudi, B. M. Fregoso, Y. Yang, W. Zhu, A. van der Zande, J. Ferrer, L. Bellaiche, P. Kumar, and S. Barraza-Lopez, *Structural Phase Transition and Material Properties of Few-Layer Monochalcogenides*, Phys. Rev. Lett. **117**, 246802 (2016).

[114] D. Liu and D. Tománek, *Effect of Net Charge on the Relative Stability of 2D Boron Allotropes*, Nano Lett. **19**, 1359 (2019).

[115] M. S. Dresselhaus and G. Dresselhaus, *Intercalation compounds of graphite*, Adv. Phys. **30**, 139 (1981).

[116] M. A. Py and R. R. Haering, *Structural destabilization induced by lithium intercalation in MoS_2 and related compounds*, Can. J. Phys. **61**, 76 (1983).

[117] X. Wu, J. Dai, Y. Zhao, Z. Zhuo, J. Yang, and X. C. Zeng, *Two-Dimensional Boron Monolayer Sheets*, ACS Nano **6**, 7443 (2012).

[118] A. Quandt and I. Boustani, *Boron Nanotubes*, ChemPhysChem. **6**, 2001 (2005).

[119] M. H. Evans, J. D. Joannopoulos, and S. T. Pantelides, *Electronic and mechanical properties of planar and tubular boron structures*, Phys. Rev. B **72**, 045434 (2005).

[120] J. Kunstmann and A. Quandt, *Broad boron sheets and boron nanotubes: An ab initio study of structural, electronic, and mechanical properties*, Phys. Rev. B **74**, 035413 (2006).

[121] A. J. Mannix, X.-F. Zhou, B. Kiraly, J. D. Wood, D. Alducin, B. D. Myers, X. Liu, B. L. Fisher, U. Santiago, J. R. Guest, M. J. Yacaman, A. Ponce, A. R. Oganov, M. C. Hersam, and N. P. Guisinger, *Synthesis of borophenes: Anisotropic, two-dimensional boron polymorphs*, Science **350**, 1513 (2015).

[122] B. Feng, J. Zhang, Q. Zhong, W. Li, S. Li, H. Li, P. Cheng, S. Meng, L. Chen, and K. Wu, *Experimental realization of two-dimensional boron sheets*, Nat. Chem. **8**, 563 (2016).

[123] Z. Zhang, E. S. Penev, and B. I. Yakobson, *Two-dimensional boron: structures, properties and applications*, Chem. Soc. Rev. **46**, 6746 (2017).

[124] X.-F. Zhou, X. Dong, A. R. Oganov, Q. Zhu, Y. Tian, and H.-T. Wang, *Semimetallic Two-Dimensional Boron Allotrope with Massless Dirac Fermions*, Phys. Rev. Lett. **112**, 085502 (2014).

[125] X.-F. Zhou, A. R. Oganov, X. Shao, Q. Zhu, and H.-T. Wang, *Unexpected Reconstruction of the α-Boron (111) Surface*, Phys. Rev. Lett. **113**, 176101 (2014).

[126] F. Ma, Y. Jiao, G. Gao, Y. Gu, A. Bilic, Z. Chen, and A. Du, *Graphene-like Two-Dimensional Ionic Boron with Double Dirac Cones at Ambient Condition*, Nano Lett. **16**, 3022 (2016).

[127] W. Li, L. Kong, C. Chen, J. Gou, S. Sheng, W. Zhang, H. Li, L. Chen, P. Cheng, and K. Wu, *Experimental realization of honeycomb borophene*, Sci. Bull. **63**, 282 (2018).

[128] E. Nishibori, M. Takata, M. Sakata, H. Tanaka, T. Muranaka, and J. Akimitsu, *Bonding Nature in MgB_2*, J. Phys. Soc. Japan **70**, 2252 (2001).

[129] R. Kappera, D. Voiry, S. E. Yalcin, B. Branch, G. Gupta, A. D. Mohite, and M. Chhowalla, *Phase-engineered low-resistance contacts for ultrathin MoS_2 transistors*, Nat. Mater. **13**, 1128 (2014).

[130] P. G. Perkins, The electronic structure of the hexaborides and the diborides, in *Boron and Refractory Borides*, edited by V. Matkovich, chapter 3, pages 31–51, Springer, Berlin, 1977.

[131] A. N. Kolmogorov and S. Curtarolo, *Theoretical study of metal borides stability*, Phys. Rev. B **74**, 224507 (2006).

[132] J. Nagamatsu, N. Nakagawa, T. Muranaka, Y. Zenitani, and J. Akimitsu, *Superconductivity at 39 K in magnesium diboride*, Nature **410**, 63 (2001).

[133] H. Tang and S. Ismail-Beigi, *Novel Precursors for Boron Nanotubes: The Competition of Two-Center and Three-Center Bonding in Boron Sheets*, Phys. Rev. Lett. **99**, 115501 (2007).

[134] H. Tang and S. Ismail-Beigi, *Self-doping in boron sheets from first principles: A route to structural design of metal boride nanostructures*, Phys. Rev. B **80**, 134113 (2009).

[135] H. Tang and S. Ismail-Beigi, *First-principles study of boron sheets and nanotubes*, Phys. Rev. B **82**, 115412 (2010).

[136] N. Karmodak and E. D. Jemmis, *The Role of Holes in Borophenes: An Ab Initio Study of Their Structure and Stability with and without Metal Templates*, Angew. Chem. Int. Ed. **56**, 10093 (2017).

[137] T. Tarkowski, J. A. Majewski, and N. G. Szwacki, *Energy decomposition analysis of neutral and negatively charged borophenes*, FlatChem **7**, 42 (2018).

[138] X. Tan, H. A. Tahini, and S. C. Smith, *Borophene as a Promising Material for Charge-Modulated Switchable CO_2 Capture*, ACS Appl. Mater. Interfaces **9**, 19825 (2017).

[139] D. L. Druffel, K. L. Kuntz, A. H. Woomer, F. M. Alcorn, J. Hu, C. L. Donley, and S. C. Warren, *Experimental Demonstration of an Electride as a 2D Material*, J. Am. Chem. Soc. **138**, 16089 (2016).

[140] K. Lee, S. W. Kim, Y. Toda, S. Matsuishi, and H. Hosono, *Dicalcium nitride as a two-dimensional electride with an anionic electron layer*, Nature **494**, 336 (2013).

[141] X. Zhang, Z. Xiao, H. Lei, Y. Toda, S. Matsuishi, T. Kamiya, S. Ueda, and H. Hosono, *Two-Dimensional Transition-Metal Electride Y_22C*, Chem. Mater. **26**, 6638 (2014).

[142] D. E. Nixon and G. S. Parry, *The expansion of the carbon-carbon bond length in potassium graphites*, J. Phys. C: Solid State Phys. **2**, 1732 (1969).

[143] D. Erbahar, D. Liu, S. Berber, and D. Tománek, *Towards room-temperature superconductivity in low-dimensional* C_{60} *nanoarrays: An ab initio study*, Phys. Rev. B **97**, 140505 (2018).

[144] J. G. Bednorz and K. A. Müller, *Possible High T_c Superconductivity in the Ba-La-Cu-O System*, Z. Phys. B **64**, 189 (1986).

[145] M. K. Wu, J. R. Ashburn, C. J. Torng, P. H. Hor, R. L. Meng, L. Gao, Z. J. Huang, Y. Q. Wang, and C. W. Chu, *Superconductivity at 93 K in a new mixed-phase Y-Ba-Cu-O compound system at ambient pressure*, Phys. Rev. Lett. **58**, 908 (1987).

[146] C. W. Chu, L. Gao, F. Chen, Z. J. Huang, R. L. Meng, and Y. Y. Xue, *Superconductivity Above 150 K In HgBa2Ca2Cu3O8+Delta at High Pressures*, Nature **365**, 323 (1993).

[147] A. Drozdov, M. Eremets, I. Troyan, V. Ksenofontov, and S. Shylin, *Conventional superconductivity at 203 Kelvin at high pressures in the sulfur hydride system*, Nature **525**, 73 (2015).

[148] L. Song, K. Fredette, D. Chung, and Y. Kao, *Superconductivity in interhalogen-doped fullerenes*, Solid State Commun. **87**, 387 (1993).

[149] M. Schluter, M. Lannoo, M. Needels, G. A. Baraff, and D. Tomanek, *Electron-phonon coupling and superconductivity in alkali-intercalated* C_{60} *solid*, Phys. Rev. Lett. **68**, 526 (1992).

[150] M. Schluter, M. Lannoo, M. Needels, G. A. Baraff, and D. Tomanek, *Superconductivity in alkali intercalated* C_{60}, J. Phys. Chem. Solids **53**, 1473 (1992).

[151] W. L. McMillan, *Transition Temperature of Strong-Coupled Superconductors*, Phys. Rev. **167**, 331 (1968).

[152] J. M. Soler, E. Artacho, J. D. Gale, A. García, J. Junquera, P. Ordejón, and D. Sánchez-Portal, *The SIESTA method for ab initio order-N materials simulation*, J. Phys: Cond. Mat. **14**, 2745 (2002).

[153] L. Kleinman and D. M. Bylander, *Efficacious form for model pseudopotentials*, Phys. Rev. Lett. **48**, 1425 (1982).

[154] E. Artacho, D. Sánchez-Portal, P. Ordejón, A. García, and J. M. Soler, *Linear-Scaling ab-initio Calculations for Large and Complex System*, Phys. Stat. Sol. **215**, 809 (1999).

[155] A. F. Hebard, M. J. Rosseinsky, R. C. Haddon, D. W. Murphy, S. H. Glarum, T. T. M. Palstra, A. P. Ramirez, and A. R. Kortan, *Superconductivity at 18 K in potassium-doped C60*, Nature **350**, 600 (1991).

[156] H. Shinohara (private communication).

[157] J. Guan and D. Tománek, *Can* CF_3*-functionalized La@*C_{60} *be isolated experimentally and become superconducting?*, Nano Lett. **17**, 3402 (2017).

[158] R. F. Service, *Nanotube 'Peapods' Show Electrifying Promise*, Science **292**, 45 (2001).

[159] S. Saito and A. Oshiyama, *Design of* C_{60}*-graphite cointercalation compounds*, Phys. Rev. B **49**, 17413 (1994).

[160] M. Fuhrer, J. Hou, X.-D. Xiang, and A. Zettl, C_{60} *intercalated graphite: Predictions and experiments*, Solid State Commun. **90**, 357 (1994).

[161] S. Okada, *Energetics and electronic structures of potassium-intercalated* C_{60} *peapods*, Phys. Rev. B **72**, 153409 (2005).

[162] V. Timoshevskii and M. Côté, *Doping of C_{60}-induced electronic states in BN nanopeapods: Ab initio simulations*, Phys. Rev. B **80**, 235418 (2009).

[163] T. Koretsune, S. Saito, and M. L. Cohen, *One-dimensional alkali-doped* C_{60} *chains encapsulated in BN nanotubes*, Phys. Rev. B **83**, 193406 (2011).

[164] N. D. Mermin and H. Wagner, *Absence of Ferromagnetism or Antiferromagnetism in One- or Two-Dimensional Isotropic Heisenberg Models*, Phys. Rev. Lett. **17**, 1133 (1966), and *ibid.* **17**, 1307 (1966)(E).

[165] S. Okada, S. Saito, and A. Oshiyama, *Energetics and Electronic Structures of Encapsulated C_{60} in a Carbon Nanotube*, Phys. Rev. Lett. **86**, 3835 (2001).

[166] Y. Miyamoto, A. Oshiyama, and S. Saito, *Halogen doping in solid C_{60}*, Solid State Commun. **82**, 437 (1992).

[167] M. P. Gelfand and J. P. Lu, *Orientational Disorder and Electronic States in* C_{60} *and A_3C_{60}, where A is an Alkali Metal*, Phys. Rev. Lett. **68**, 1050 (1992).

[168] A. Y. Ganin, Y. Takabayashi, P. Jeglič, D. Arčon, A. Potočnik, P. J. Baker, Y. Ohishi, M. T. McDonald, M. D. Tzirakis, A. McLennan, G. R. Darling, M. Takata, M. J. Rosseinsky, and K. Prassides, *Polymorphism control of superconductivity and magnetism in Cs_3C_{60} close to the Mott transition*, Nature **466**, 221 (2010).

[169] Y. Nomura, S. Sakai, M. Capone, and R. Arita, *Unified understanding of superconductivity and Mott transition in alkali-doped fullerides from first principles*, Science Adv. **1**, e1500568 (2015).

[170] X. Lin, D. Liu, and D. Tománek, *Is Twisted Bilayer Graphene Stable under Shear?*, Phys. Rev. B **98**, 195432 (2018).

[171] R. Bistritzer and A. H. MacDonald, *Moiré bands in twisted double-layer graphene*, Proc. Natl. Acad. Sci. U.S.A. **108**, 12233 (2011).

[172] E. Suárez Morell, J. D. Correa, P. Vargas, M. Pacheco, and Z. Barticevic, *Flat bands in slightly twisted bilayer graphene: Tight-binding calculations*, Phys. Rev. B **82**, 121407 (2010).

[173] J. M. B. Lopes dos Santos, N. M. R. Peres, and A. H. Castro Neto, *Continuum model of the twisted graphene bilayer*, Phys. Rev. B **86**, 155449 (2012).

[174] S. Fang and E. Kaxiras, *Electronic structure theory of weakly interacting bilayers*, Phys. Rev. B **93**, 235153 (2016).

[175] Y. Cao, V. Fatemi, A. Demir, S. Fang, S. L. Tomarken, J. Y. Luo, J. D. Sanchez-Yamagishi, K. Watanabe, T. Taniguchi, E. Kaxiras, R. C. Ashoori, and P. Jarillo-Herrero, *Correlated insulator behaviour at half-filling in magic-angle graphene superlattices*, Nature **556**, 80 (2018).

[176] Y. Cao, V. Fatemi, S. Fang, K. Watanabe, T. Taniguchi, E. Kaxiras, and P. Jarillo-Herrero, *Unconventional superconductivity in magic-angle graphene superlattices*, Nature **556**, 43 (2018).

[177] Y. Cao, J. Y. Luo, V. Fatemi, S. Fang, J. D. Sanchez-Yamagishi, K. Watanabe, T. Taniguchi, E. Kaxiras, and P. Jarillo-Herrero, *Superlattice-Induced Insulating States and Valley-Protected Orbits in Twisted Bilayer Graphene*, Phys. Rev. Lett. **117**, 116804 (2016).

[178] P. San-Jose, J. González, and F. Guinea, *Non-Abelian Gauge Potentials in Graphene Bilayers*, Phys. Rev. Lett. **108**, 216802 (2012).

[179] A. M. Popov, I. V. Lebedeva, A. A. Knizhnik, Y. E. Lozovik, and B. V. Potapkin, *Commensurate-incommensurate phase transition in bilayer graphene*, Phys. Rev. B **84**, 045404 (2011).

[180] K. Uchida, S. Furuya, J.-I. Iwata, and A. Oshiyama, *Atomic corrugation and electron localization due to Moiré patterns in twisted bilayer graphenes*, Phys. Rev. B **90**, 155451 (2014).

[181] S. Zhou, J. Han, S. Dai, J. Sun, and D. J. Srolovitz, *Van der Waals bilayer energetics: Generalized stacking-fault energy of graphene, boron nitride, and graphene/boron nitride bilayers*, Phys. Rev. B **92**, 155438 (2015).

[182] M. M. van Wijk, A. Schuring, M. I. Katsnelson, and A. Fasolino, *Relaxation of Moiré patterns for slightly misaligned identical lattices: graphene on graphite*, 2D Mater. **2**, 034010 (2015).

[183] S. Dai, Y. Xiang, and D. J. Srolovitz, *Twisted Bilayer Graphene: Moiré with a Twist*, Nano Lett. **16**, 5923 (2016).

[184] S. K. Jain, V. Juričić, and G. T. Barkema, *Structure of twisted and buckled bilayer graphene*, 2D Materials **4**, 015018 (2017).

[185] N. N. T. Nam and M. Koshino, *Lattice relaxation and energy band modulation in twisted bilayer graphene*, Phys. Rev. B **96**, 075311 (2017).

[186] K. Zhang and E. B. Tadmor, *Structural and electron diffraction scaling of twisted graphene bilayers*, J. Mech. Phys. Solids **112**, 225 (2018).

[187] F. Gargiulo and O. V. Yazyev, *Structural and electronic transformation in low-angle twisted bilayer graphene*, 2D Mater. **5**, 015019 (2018).

[188] S. Carr, D. Massatt, S. B. Torrisi, P. Cazeaux, M. Luskin, and E. Kaxiras, *Relaxation and Domain Formation in Incommensurate 2D Heterostructures*, (2018).

[189] H. Yoo, K. Zhang, R. Engelke, P. Cazeaux, S. H. Sung, R. Hovden, A. W. Tsen, T. Taniguchi, K. Watanabe, G.-C. Yi, M. Kim, M. Luskin, E. B. Tadmor, and P. Kim, *Atomic reconstruction at van der Waals interface in twisted bilayer graphene*, (2018).

[190] X. Lin and D. Tománek, *Minimum model for the electronic structure of twisted bilayer graphene and related structures*, Phys. Rev. B **98**, 081410 (2018).

[191] G. Kresse and J. Furthmüller, *Efficiency of ab-initio total energy calculations for metals and semiconductors using a plane-wave basis set*, Computat. Mater. Sci. **6**, 15 (1996).

[192] H. Peng, Z.-H. Yang, J. P. Perdew, and J. Sun, *Versatile van der Waals Density Functional Based on a Meta-Generalized Gradient Approximation*, Phys. Rev. X **6**, 041005 (2016).

[193] J. Klimeš, D. R. Bowler, and A. Michaelides, *Van der Waals density functionals applied to solids*, Phys. Rev. B **83**, 195131 (2011).

[194] P. L. de Andres, F. Guinea, and M. I. Katsnelson, *Bending modes, anharmonic effects, and thermal expansion coefficient in single-layer and multilayer graphene*, Phys. Rev. B **86**, 144103 (2012).

[195] Z. Gao, D. Liu, and D. Tománek, *Two-Dimensional Mechanical Metamaterials with Unusual Poisson Ratio Behavior*, Phys. Rev. Applied **10**, 064039 (2018).

[196] K. Bertoldi, V. Vitelli, J. Christensen, and M. van Hecke, *Flexible mechanical metamaterials*, Nature Rev. Mater. **2**, 17066 (2017).

[197] G. N. Greaves, A. Greer, R. Lakes, and T. Rouxel, *Poisson's ratio and modern materials*, Nat. Mater. **10**, 823 (2011).

[198] L. J. Gibson, M. F. Ashby, G. Schajer, and C. Robertson, *The mechanics of two-dimensional cellular materials*, Proc. R. Soc. Lond. A **382**, 25 (1982).

[199] R. Lakes, *Foam structures with a negative Poisson's ratio*, Science **235**, 1038 (1987).

[200] R. Lakes, *Advances in negative Poisson's ratio materials*, Adv. Mater. **5**, 293 (1993).

[201] R. H. Baughman and D. S. Galvão, *Crystalline networks with unusual predicted mechanical and thermal properties*, Nature **365**, 735 (1993).

[202] A. Alderson, *A triumph of lateral thought*, Chemistry & Industry **17**, 384 (1999).

[203] H. Mitschke, J. Schwerdtfeger, F. Schury, M. Stingl, C. Körner, R. F. Singer, V. Robins, K. Mecke, and G. E. Schröder-Turk, *Finding Auxetic Frameworks in Periodic Tessellations*, Adv. Mater. **23**, 2669 (2011).

[204] Z. Gao, X. Dong, N. Li, and J. Ren, *Novel two-dimensional silicon dioxide with in-plane negative Poisson's ratio*, Nano Lett. **17**, 772 (2017).

[205] F. Scarpa, C. W. Smith, W. Miller, K. Evans, and R. Rajasekaran, Vibration damping structures, U.S. Patent US 2012/0315456 A1, 2012.

[206] A. Papadopoulou, J. Laucks, and S. Tibbits, *Auxetic materials in design and architecture*, Nature Rev. Mater. **2**, 17078 (2017).

[207] Y. Chen, T. Li, F. Scarpa, and L. Wang, *Lattice Metamaterials with Mechanically Tunable Poisson's Ratio for Vibration Control*, Phys. Rev. Applied **7**, 024012 (2017).

[208] T. M. Cross, K. W. Hoffer, D. P. Jones, P. B. Kirschner, E. Langvin, and J. C. Meschter, Auxetic structures and footwear with soles having auxetic structures, U.S. Patent US 9,402,439 B2, 2016.

[209] F. Scarpa, *Auxetic materials for bioprostheses [In the Spotlight]*, IEEE Signal Process. Mag. **25**, 128 (2008).

[210] R. Hengelmolen, Auxetic tubular liners, U.S. Patent US 2006/0129227 A1, 2006.

[211] R. H. Baughman, J. M. Shacklette, A. A. Zakhidov, and S. Stafström, *Negative Poisson's ratios as a common feature of cubic metals*, Nature **392**, 362 (1998).

[212] S. Shan, S. H. Kang, Z. Zhao, L. Fang, and K. Bertoldi, *Design of planar isotropic negative Poisson's ratio structures*, Extreme Mech. Lett. **4**, 96 (2015).

[213] D. H. Boal, U. Seifert, and J. C. Shillcock, *Negative Poisson ratio in two-dimensional networks under tension*, Phys. Rev. E **48**, 4274 (1993).

[214] K. Wojciechowski, *Two-dimensional isotropic system with a negative Poisson ratio*, Phys. Lett. A **137**, 60 (1989).

[215] J. N. Grima and K. E. Evans, *Self expanding molecular networks*, Chem. Commun. **16**, 1531 (2000).

[216] M. Schenk and S. D. Guest, *Geometry of Miura-folded metamaterials*, Proc. Natl. Acad. Sci. USA **110**, 3276 (2013).

[217] H. Yasuda and J. Yang, *Reentrant Origami-Based Metamaterials with Negative Poisson's Ratio and Bistability*, Phys. Rev. Lett. **114**, 185502 (2015).

[218] A. Rafsanjani and K. Bertoldi, *Buckling-Induced Kirigami*, Phys. Rev. Lett. **118**, 084301 (2017).

[219] J. N. Grima, S. Winczewski, L. Mizzi, M. C. Grech, R. Cauchi, R. Gatt, D. Attard, K. W. Wojciechowski, and J. Rybicki, *Tailoring Graphene to Achieve Negative Poisson's Ratio Properties*, Adv. Mater. **27**, 1455 (2015).

[220] S. D. Guest and J. W. Hutchinson, *On the determinacy of repetitive structures*, J. Mech. Phys. Solids **51**, 383 (2003).

[221] J. N. Grima, A. Alderson, and K. E. Evans, *Auxetic behaviour from rotating rigid units*, Phys. stat. sol. (b) **242**, 561 (2005).

[222] G. W. Milton, *Complete characterization of the macroscopic deformations of periodic unimode metamaterials of rigid bars and pivots*, J. Mech. Phys. Solids **61**, 1543 (2013).

[223] J. N. Grima, R. Jackson, A. Alderson, and K. E. Evans, *Do zeolites have negative Poisson's ratios?*, Adv. Mater. **12**, 1912 (2000).

[224] K. Sun, A. Souslov, X. Mao, and T. C. Lubensky, *Surface phonons, elastic response, and conformal invariance in twisted kagome lattices*, Proc. Natl. Acad. Sci. USA **109**, 12369 (2012).

[225] Q. Chen, S. C. Bae, and S. Granick, *Directed self-assembly of a colloidal kagome lattice*, Nature **469**, 381 (2011).

[226] H. Maeda, R. Sakamoto, and H. Nishihara, *Coordination Programming of Two-Dimensional Metal Complex Frameworks*, Langmuir **32**, 2527 (2016).

[227] R. Sakamoto, K. Takada, T. Pal, H. Maeda, T. Kambe, and H. Nishihara, *Coordination nanosheets (CONASHs): strategies, structures and functions*, Chem. Commun. **53**, 5781 (2017).

[228] M. Treier, C. A. Pignedoli, T. Laino, R. Rieger, K. Müllen, D. Passerone, and R. Fasel, *Surface-assisted cyclodehydrogenation provides a synthetic route towards easily processable and chemically tailored nanographenes*, Nature Chem. **3**, 61 (2011).

[229] C. Moreno, M. Vilas-Varela, B. Kretz, A. Garcia-Lekue, M. V. Costache, M. Paradinas, M. Panighel, G. Ceballos, S. O. Valenzuela, D. Peña, and A. Mugarza, *Bottom-up synthesis of multifunctional nanoporous graphene*, Science **360**, 199 (2018).

[230] M. Bieri, M. Treier, J. Cai, K. Ait-Mansour, P. Ruffieux, O. Groning, P. Groning, M. Kastler, R. Rieger, X. Feng, K. Müllen, and R. Fasel, *Porous graphenes: two-dimensional polymer synthesis with atomic precision*, Chem. Commun. **45**, 6919 (2009).

[231] C. Schumacher, S. Marschner, M. Cross, and B. Thomaszewski, *Mechanical Characterization of Structured Sheet Materials*, ACM Trans. Graph. **37**, 148:1 (2018).

[232] D. Attard, A. R. Casha, and J. N. Grima, *Filtration Properties of Auxetics with Rotating Rigid Units*, Materials **11**, 725 (2018).